Synthese und Charakterisierung *E*/*Z*-photoisomerisierbarer Inhibitoren zur reversiblen Modulation der Deacetylase-Aktivität von Sirtuinen

Inauguraldissertation
zur
Erlangung des akademischen Grades eines
Doktors der Naturwissenschaften
(Dr. rer. nat.)
der
Mathematisch-Naturwissenschaftlichen Fakultät
der
Universität Greifswald

vorgelegt von
Christoph Werner Grathwol
geboren am 20.05.1988
in Donaueschingen

Greifswald, Juni 2020

Dekan: Prof. Dr. Gerald Kerth

Erstgutachter: Prof. Dr. Andreas Link

Zweitgutachter: Prof. Dr. Tanja Schirmeister

Tag der Disputation: 01.09.2020

Inhaltsverzeichnis

Abkürzungsverzeichnis

Ac	Acetyl
ACN	Acetonitril
ADP	Adenosindiphosphat
AS	Aminosäure
Asp	Asparaginsäure
ATP	Adenosintriphosphat
NAD^+	Nicotinamidadenindinukleotid (oxidierte Form)
Bn	Benzyl
CI	Konischer Übergang
C-RAF	*Rapidly accelerated fibrosarcoma C*
D	Debye (Elektrisches Dipolmoment)
DCM	Dichlormethan
DMF	*N*,*N*-Dimethylformamid
DMSO	Dimethylsulfoxid
DNA	Desoxyribonukleinsäure
DIPEA	*N*,*N*-Diisopropylethylamin (IUPAC: *N*-Ethyldiisopropylamin)
Et	Ethyl
FP	Fluoreszenzpolarisation
GPCR	G-Protein-gekoppelter Rezeptor
GSH	Glutathion
H	Histon
HAc	Essigsäure
HATU	*O*-(7-Azabenzotriazol-1-yl)-*N*,*N*,*N′*,*N′*-tetramethyluronium-hexafluorophosphat
HDAC	Histondeacetylase
His	Histidin
HPLC	Hochleistungsflüssigkeitschromatographie
HTS	Hochdurchsatz-Screening
IC_{50}	Inhibitorische Konzentration für 50% Hemmung
K	Lysin
Kat.	Katalysator
KDAC	Lysindeacetylase
k. I.	Keine Inhibition
LC	Flüssigkeitschromatographie
LED	Lichtemittierende Diode
Lys	Lysin
MeOH	Methanol
MS	Massenspektrometrie

NF-κB	*Nuclear factor "kappa-light-chain-enhancer" of activated B-cells*
o-	ortho
*O*AADPR	*O*-Acetyl-ADP-Ribose
ONyl	4-Oxononanoyl
Oxone	Kaliumperoxomonosulfat
Ph	Phenyl
PCL	Photochromer Ligand
PSD	Photostationäre Verteilung
PSS	Photostationärer Zustand
RGB	Rot Grün Blau
RING	*Really interesting new gene*
ROS	Reaktive Sauerstoffspezies
SAR	Struktur-Wirkungs-Beziehung
Sir	*Silent information regulator*
Sir2p	*Silent information regulator 2 protein*
SirReal	*Sirtuin-rearranging ligand*
S_N2	Bimolekulare nukleophile Substitution
TEA	Triethylamin
TFA	Trifluoroessigsäure
THF	Tetrahydrofuran
Tol	Tolyl
u. I.	Unspezifische Interaktion
UV	Ultraviolett
Vis	Sichtbar (englisch *visible*)
Z	Benzyloxycarbonyl-Gruppe
ZMAL	Z-(ε-Acetyl)lysin-7-amino-4-methylcumarin

1 Einleitung

1.1 Photopharmakologie: Wirkstoffselektivität im Scheinwerferlicht

Die Photopharmakologie ist eine noch recht junge Disziplin der Arzneimitteltherapie, bei der Licht als Instrument genutzt wird, um Arzneistoffe gezielt zu aktivieren bzw. zu deaktivieren.[1,2] Damit soll die Target-Selektivität von Wirkstoffen gesteigert, unerwünschte Nebenwirkungen verhindert und die systemische Toxizität von Arzneistoffen reduziert werden. Weiterhin dienen photopharmakologische Wirkstoffe als interessantes Werkzeug für die Erforschung biologischer Targets, da in Echtzeit verfolgt werden kann, wie sich eine veränderte Aktivität des Targets auf die Zelle oder den jeweiligen Signalweg auswirkt.[3]

Von zentraler Bedeutung in der Photopharmakologie ist die Entwicklung photochromer Liganden (PCL). Durch Integration molekularer Photoschalter in Wirkstoffstrukturen entstehen Liganden, deren Aktivität sich durch Bestrahlung mit Licht geeigneter Wellenlänge beeinflussen lässt.[4,5] Licht bietet als regulierendes Instrument hierbei entscheidende Vorteile, da es nicht-invasiv und mit einer hohen sowohl räumlichen als auch zeitlichen Präzision verabreicht werden kann.[4] Im Gegensatz zu UV-Strahlung ist sichtbares Licht in Abhängigkeit von Wellenlänge und Intensität weitestgehend unschädlich für zelluläre Bestandteile. Noch energieärmere Infrarotstrahlung kann als „unsichtbares Reagenz“ ohne Kontamination des untersuchten Systems oder behandelten Gewebes eingesetzt werden.[6]

1.1.1 Molekulare Photoschalter

Molekulare Photoschalter sind Verbindungen, die sich durch Bestrahlung mit Licht einer definierten Wellenlänge reversibel isomerisieren lassen.[7] Neben der geometrischen Form des Moleküls kann sich dabei sowohl dessen Polarität als auch Flexibilität verändern, sodass sich die Verbindung zwischen mindestens zwei physikochemisch voneinander verschiedenen Formen hin- und herschalten lässt. Unter Lichtausschluss liegt der molekulare Photoschalter in seiner thermodynamisch stabilsten Form vor. Der Gleichgewichtszustand, der sich während der Bestrahlung zwischen dem thermodynamisch günstigeren Isomer und dessen Photoisomer einstellt, wird photostationärer Zustand (PSS) genannt. Bei vorliegender Metastabilität des entstandenen Photoisomers bildet sich nach Unterbrechung der Bestrahlung über einen bestimmten Zeitraum wieder der thermische Gleichgewichtszustand aus. Dieser Zeitraum kann je nach Photoschalter einige Pikosekunden bis hin zu mehreren Jahren betragen. Im Falle thermisch stabiler PSS findet eine Rückreaktion ausschließlich photochemisch statt.[8,9] Da die Aktivität eines Wirkstoffs in direkter Beziehung zu dessen Struktur, Konformation und Elektronenverteilung steht, erlauben derartige Photoisomerisierungen eine lichtabhängige Modulation der Zielstruktur.[10,11]

Inzwischen ist ein großes Repertoire an Strukturen bekannt, die als molekulare Photoschalter verwendet werden können.[3,12,13] Die dabei stattfindenden photochemischen Reaktionen umfassen die *E*/*Z*-Photoisomerisierung von Doppelbindungen und intramolekulare Photozyklisierungsreaktionen (Tab. 1). Vier photophysikalische Eigenschaften können zur weiteren Charakterisierung des jeweiligen Photoschalters herangezogen werden: (a) die zur Photoisomerisierung benötigte Wellenlänge, (b) die thermische Stabilität der PSS, (c) die photostationäre Verteilung der Photoisomere (PSD) sowie (d) die Ermüdungsbeständigkeit bzw. chemische Stabilität des Photoschalters.[6,14]

Tab. 1: Eine Auswahl verschiedener molekularer Photoschalter.

Klasse	Lichtinduzierte Isomerisierung
Azobenzene	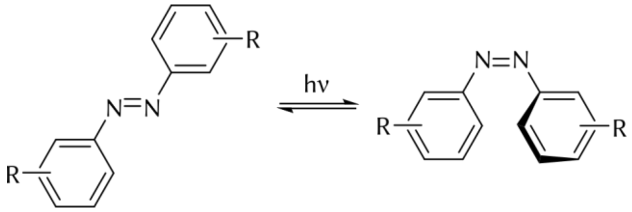
Stilbene	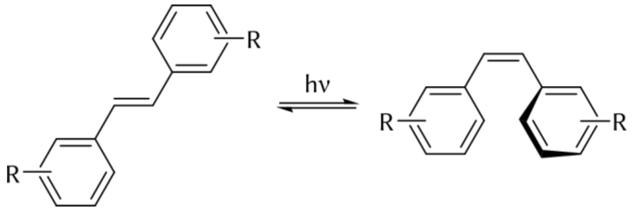
Diarylethene (X = S, O, NMe, SO_2)	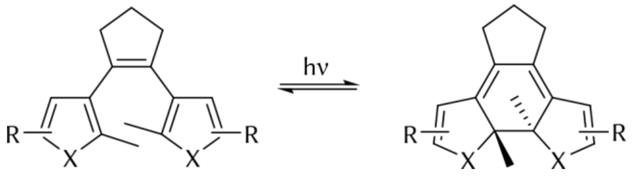
Fulgide (X = O, NR; Y = O, S)	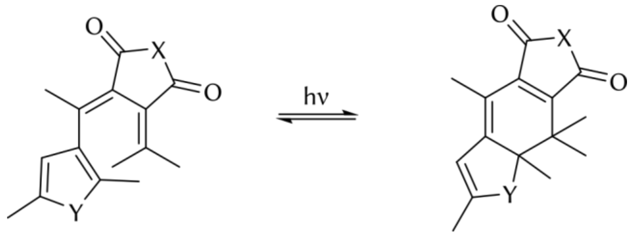

1.1.2 Azobenzene

Azobenzene sind die wohl am besten untersuchten und im pharmakologischen Kontext am häufigsten verwendeten molekularen Photoschalter.[13] Durch UV-Strahlung (λ = 320 nm) lässt sich das thermodynamisch stabilere *E*-Azobenzen in das metastabile *Z*-Azobenzen umwandeln, dabei beträgt die Energiedifferenz zwischen beiden Isomeren 58 kJ·mol^{-1}.[15] Durch die Photoisomerisierung verändern sich sowohl die Molekülform als auch die Polarität. So besitzt *Z*-Azobenzen zwei um 42–57° zueinander gedrehte Ringebenen und ein Dipolmoment von 3 D, wohingegen *E*-Azobenzen planar ist und kein Dipolmoment aufweist.[16,17]

Das UV/Vis-Spektrum von *E*-Azobenzen zeigt typischerweise zwei Absorptionsmaxima (Abb. 1).[18–21] Die intensive Bande im UV-Bereich (λ = 320 nm) stellt einen symmetrieerlaubten π→π*-Übergang dar.[18,22] Absorption eines Photons dieser Wellenlänge überführt *E*-Azobenzen aus dessen elektronischem Grundzustand S_0 in den zweiten angeregten Singulett-Zustand S_2.[23] Das schwächere Absorptionsmaximum im sichtbaren Bereich (λ = 450 nm) entsteht hingegen durch einen symmetrieverbotenen n→π*-Übergang und regt *E*-Azobenzen in den ersten Singulett-Zustand S_1 an.[24] Im UV/Vis-Spektrum des *Z*-Azobenzens erscheint der π→π*-Übergang schwächer sowie blauverschoben (λ = 270 nm), wohingegen der n→π*-Übergang im sichtbaren Bereich (λ = 450 nm) intensiver ist als der entsprechende Übergang im Spektrum des *E*-Azobenzens. Ausgehend von beiden angeregten Zuständen (S_1 und S_2) findet eine *E*/*Z*-Isomerisierung statt. Allerdings läuft die Umwandlung aus S_1 unter höherer Quantenausbeute ab als aus S_2.[25]

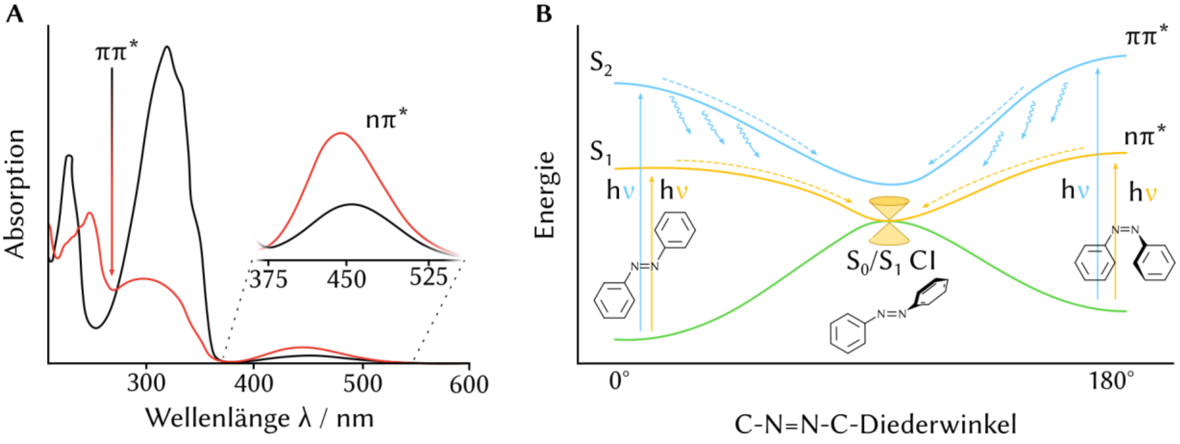

Abb. 1: A) UV/Vis-Spektrum von *E*-Azobenzen (schwarz) und *Z*-Azobenzen (rot). B) Photochemischer Reaktionsverlauf der *E*/*Z*-Photoisomerisierung von Azobenzen. Ein konischer Übergang (CI) zwischen der S_1- und S_0-Potentialhyperfläche erlaubt eine Relaxation in den Grundzustand unter Isomerisierung.

Für die Photoisomerisierung existieren zwei grundlegende Mechanismen (Abb. 2): (a) Rotation und (b) Inversion.[26] Der Rotationsmechanismus verläuft über eine Änderung des C-N=N-C-Diederwinkels, wohingegen der N=N-C-Bindungswinkel konstant bei 120° bleibt.[27,28] Der Inversionsmechanismus beschränkt sich im Gegensatz dazu auf eine Bewegung innerhalb der C-N=N-C-Ebene. Einer der beiden N=N-C-Bindungswinkel öffnet sich in diesem Fall vollständig und führt zu einem Übergangszustand mit einem sp-hybridisiertem Azo-Stickstoffatom.[29] Auf diesen beiden grundlegenden Mechanismen basieren zwei weitere Variationen: (c) die konzertierte Inversion beider N=N-C Gruppen unter Bildung eines vollständig linearen Übergangszustandes sowie (d) eine Kombination aus Rotations- und Inversionsbewegung.[23]

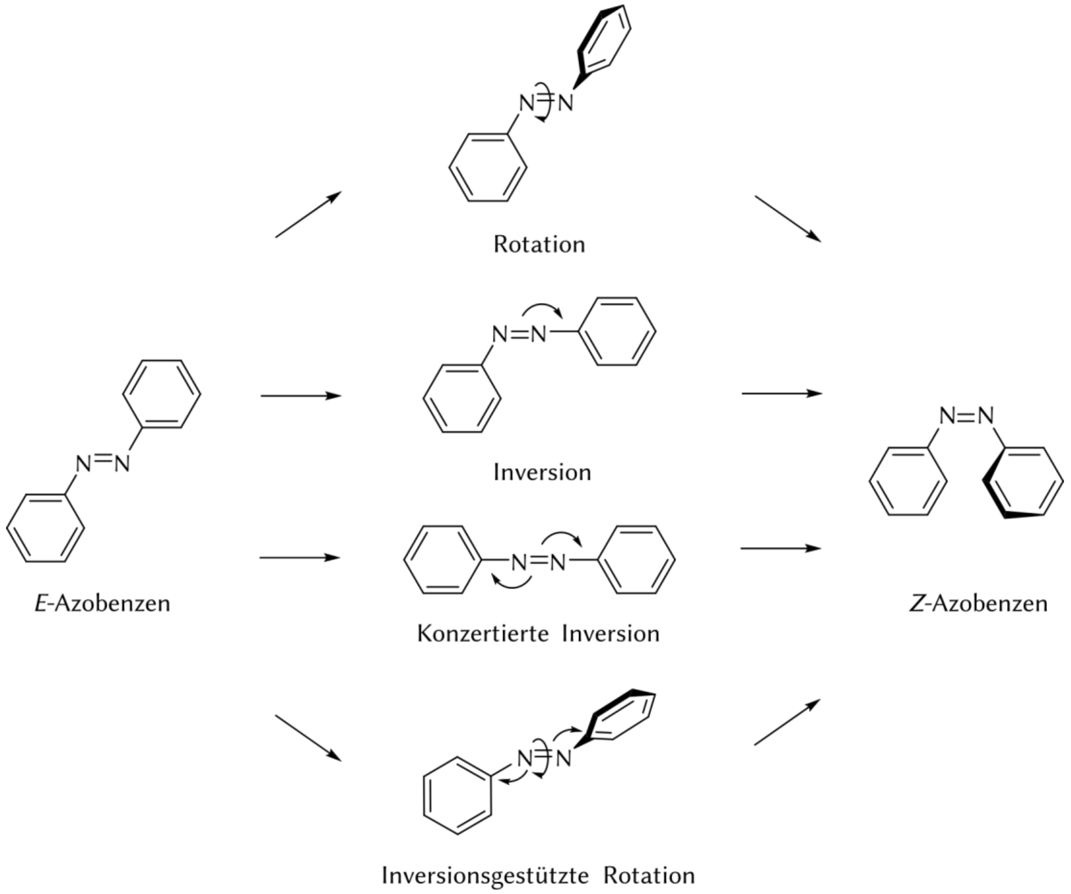

Abb. 2: Postulierte Mechanismen für die *E*→*Z*-Photoisomerisierung von Azobenzen. Der Rotationsmechanismus beinhaltet eine Änderung des C-N=N-C-Diederwinkels, wohingegen der N=N-C-Bindungswinkel konstant bei 120° bleibt. Der Inversionsmechanismus beschränkt sich auf eine Bewegung in der C-N=N-C-Ebene. Bei konzertierter Inversion ändern sich beide N=N-C-Bindungswinkel gleichzeitig. Der inversionsgestützte Rotationsmechanismus wird durch Rotationsbewegungen dominiert und durch zusätzliche Inversionsbewegungen beider N=N-C-Bindungswinkel unterstützt.

Ein solcher inversionsgestützter Rotationsmechanismus gilt inzwischen als gesichert für die Umwandlung von *E*-Azobenzen zu *Z*-Azobenzen ausgehend von S_1.[30,31] Eine Kombination aus Rotations- und Inversionsbewegungen führen auf der S_1-Potentialhyperfläche zu einem konischen Übergang (CI) zwischen dem ersten angeregten Singulett-Zustand S_1 und dem Singulett-Grundzustand S_0, über welchen das angeregte *E*-Azobenzen unter Isomerisierung relaxieren kann (Abb. 1).[30,32] Ein ähnliches Verhalten wird für eine

Relaxation aus S_2 diskutiert. Allerdings ist aus diesem Zustand auch ein nicht-produktiver CI zugänglich, der ohne Isomerisierung zum Grundzustand zurückführt, was die geringeren Quantenausbeuten nach S_2-Anregung erklärt.[33,34]

Die Aktivierungsenergie der thermischen *Z*→*E*-Isomerisierung in Azobenzen beträgt etwa 95 $kJ \cdot mol^{-1}$.[35] In Azobenzen und der Mehrheit seiner Derivate verläuft die thermische Rückreaktion verhältnismäßig langsam nach einem Inversionsmechanismus. So beträgt die Halbwertszeit der thermischen *Z*→*E*-Isomerisierung von Azobenzen in Lösung bei Raumtemperatur zwei Tage.[23,36] Der mechanistische Verlauf wird jedoch durch vorhandene Substituenten und das umgebende Lösungsmittel beeinflusst. Elektronendonatoren in *ortho*- bzw. *para*-Stellung zur Azogruppe (2-/4-NR_2, 2-/4-OR) erhöhen die Elektronendichte im π*-Molekülorbital und verringern die Energiebarriere für eine thermische Rückreaktion, wodurch sich der Prozess beschleunigt.[37,38] Dieser Effekt verstärkt sich in polaren Lösungsmitteln.[39] Die thermische Rückreaktion in diesen Derivaten kann je nach Substitution bzw. Lösungsmittel variieren und nach einem langsameren Inversions- oder einem schnellen Rotationsmechanismus verlaufen.[40] Bei nicht vollständig alkylierten Substituenten in *ortho*- bzw. *para*-Position wird die thermische Stabilität des *Z*-Isomers zusätzlich durch intra- bzw. intermolekulare Wasserstoffbrückenbindungen oder Tautomerisierung reduziert.[41–44]

1.1.3 Stilbene

Wie die N,N-Doppelbindung der Azofarbstoffe lässt sich die C,C-Doppelbindung der Stilbene durch UV-Strahlung ($\lambda = 300$ nm) isomerisieren.[45] Eine Rotation um die zentrale C,C-Doppelbindung überführt *E*-Stilben nach photochemischer Anregung in das *Z*-Isomer. Letzteres nimmt im Gegensatz zum planaren *E*-Stilben eine propellerähnliche Konformation ein, in welcher die von den Ringen aufgespannten Ebenen um 30–50° zueinander verdreht sind.[46,47]

Zur thermischen *Z*→*E*-Isomerisierung aus dem Singulett-Grundzustand S_0 muss eine recht hohe Energiebarriere von bis zu 190 $kJ \cdot mol^{-1}$ überwunden werden. Sie entspricht einem Übergangszustand mit einem Diederwinkel der zentralen Doppelbindungsebene von 90°. Bei Raumtemperatur kann eine *E*/*Z*-Isomerisierung angesichts dieser hohen Barriere vernachlässigt werden.[13,48] Nach photochemischer Anregung in den ersten angeregten Singulett-Zustand S_1 nimmt der Doppelbindungscharakter der zentralen C,C-Doppelbindung jedoch stark ab, wodurch eine Rotation um diese Bindung erleichtert wird.[48,49] Bei einem Diederwinkel von 90° kann das Konformationsisomer durch innere Konversion aus S_1 in den Singulett-Grundzustand S_0 wechseln und schließlich mit jeweils gleicher Wahrscheinlichkeit entweder zum *E*- oder *Z*-Azobenzen relaxieren.[50,51]

1.1.4 Diarylethene und Fulgide

Diarylethene und Fulgide sind strukturell verwandt und gehen beide aufgrund ihrer Hexatrien-Teilstruktur intramolekulare Photozyklisierungsreaktionen ein.[7] Im Falle heterozyklischer Diarylethene mit Furyl- oder Thiophenylresten auf beiden Seiten der zentralen Doppelbindung sind beide Photoisomere thermisch stabil und können nur photochemisch ineinander überführt werden.[52] Gleiches gilt für Fulgide, vorausgesetzt die C-Atome der Doppelbindungen sind vollständig substituiert und das Fulgid besitzt Heteroaromaten (Furyl- oder Thiophenfulgide).[53–56] Die Verwendung von Diarylethenen und Fulgiden als molekulare Photoschalter beruht hauptsächlich auf den strukturellen Unterschieden zwischen „offener“ und „geschlossener“ Form. Die Starrheit des Moleküls nimmt durch die lichtinduzierte Zyklisierung bedeutend zu, wohingegen sich die Polarität nur geringfügig ändert.[6]

1.2 Sirtuine: Homologe des *Silent Information Regulator 2 Proteins*

Sirtuine bilden eine Enzymfamilie aus der Gruppe der Lysin-Deacetylasen (KDACs). Sie katalysieren die Deacetylierung von N^{ε}-Acetyl-lysin-Seitenketten zahlreicher Substratproteine unter Verwendung von NAD^+ als Cofaktor. Namensgeber dieser Enzymfamilie ist das Gen *Sir2* (*silent information regulator 2*) der Hefe *Saccharomyces cerevisiae*. *Sir2* codiert für die Histon-Deacetylase Sir2p, die an der Stilllegung von Genabschnitten beteiligt ist, welche unter anderem Einfluss auf den Paarungstyp der Hefezellen nehmen.[57,58] Homologe des Sir2p sind evolutionär stark konserviert und kommen in Organismen aller drei Domänen des Lebens vor. Sirtuine, auch *Sir2-like proteins* genannt, lassen sich entsprechend ihrer phylogenetischen Verwandtschaft in fünf Kategorien (I, II, III, IV und U) einteilen.[59,60] Der Mensch besitzt sieben Sirtuin-Isotypen (Sirt1–7), die den Sirtuin-Familien I–IV angehören. Die Klasse U enthält hingegen ausschließlich Sirtuine der Bakterien und Archeen.[60] Innerhalb der Zelle verteilen sich die humanen Sirtuine auf drei Kompartimente: Sirt1 wird zusammen mit den Isotypen Sirt6 und Sirt7 dem Zellkern bzw. Nukleolus zugeschrieben, wohingegen Sirt2 das dominierende Sirtuin des Cytoplasmas ist. Die Isotypen Sirt3–5 werden üblicherweise als mitochondriale Sirtuine bezeichnet.[61] Abhängig vom Zelltyp und Zellzyklus pendeln Sirt1 und Sirt2 zwischen Zellkern und Cytoplasma.[62,63] Im Falle des Sirt3 wird von zwei Isofomen berichtet, die sich in unterschiedlichen Kompartimenten aufhalten: Eine unprozessierte Form mit voller Länge (lSirt3) befindet sich im Zellkern und eine weitere, am N-terminalen Ende verkürzte Form (sSirt3), in den Mitochondrien.[64,65] Ebenso existieren von Sirt7 zwei Isoformen unterschiedlicher Länge. Das Protein voller Länge (lSirt7) ist Teil des Cytoplasmas, die kürzere Form (sSirt7) beschränkt sich hingegen auf den Nukleolus.[66]

Neben deren Lokalisation innerhalb der Zelle unterscheiden sich die humanen Sirtuine auch in ihrer enzymatischen Aktivität. Die Isotypen Sirt1–3 sind phylogenetisch eng miteinander verwandt (Klasse I) und besitzen eine hohe Deacetylase-Aktivität. Im Gegensatz dazu ist die Deacetylase-Aktivität der übrigen Isotypen eher schwach ausgeprägt.[67–73] Obwohl Sirtuine im Allgemeinen zu den Protein-Deacetylasen zählen, beschränkt sich deren katalytische Aktivität nicht nur auf Deacetylierungsvorgänge. So deacyliert Sirt5 Malonyl-, Succinyl- und Glutaryllysine deutlich effizienter als Acetyllysine.[74–76] Sirt6 zeigt hingegen eine hohe Demyristoylaseaktivität.[77,78] Letzteres wird insbesondere auch bei Sirt2 beobachtet.[79] Sirt4 besitzt neben einer schwachen Deacetylase-Aktivität eine ausgeprägte Lipoamidase-Aktivität und wie auch Sirt6 eine Mono-ADP-Ribosyltransferaseaktivität.[67,71,80] Im Folgenden liegt der Fokus auf der Deacetylase-Aktivität der Klasse I Sirtuine Sirt1–3.

1.2.1 Physiologische Funktionen im humanen Organismus

Die Lokalisation der Sirtuine innerhalb der Zelle spiegelt deren physiologische Funktionen wieder. So deacetylieren Sirt1 und Sirt2 zahlreiche nukleäre und cytosolische Substrate, wohingegen Sirt3 vornehmlich die Deacetylierung metabolischer Enzyme des Mitochondriums katalysiert. Aufgrund ihres breiten Substratspektrums sind die Isotypen Sirt1–3 an der Regulation zahlreicher zellulärer Prozesse wie der Gentranskription, des Zellzyklus, der Apoptose und des Energiestoffwechsels beteiligt.[60,61]

Die im menschlichen Genom codierten Histondeacetylasen (HDAC) werden auf vier große Familien aufgeteilt. Sirtuine, welche die dritte HDAC-Familie darstellen, heben sich aufgrund ihres NAD^+-basierten Reaktionsmechanismus von den übrigen sogenannten „klassischen HDACs“ (Kategorie I, II und IV) ab, die einen Zn^{2+}-abhängigen Hydrolysemechanismus aufweisen. Durch die Deacetylierung spezifischer Lysinreste von Histonproteinen beeinflussen Sirt1–3 die Struktur des betroffenen Chromatin-Bereichs und regulieren so die Expression darin enthaltener Gene.[81,82] Aufgrund der Deacetylierung steigt sowohl die Affinität der DNA zu assoziierten Histonen als auch die Affinität der DNA-Histonkomplexe (Nucleosomen) zueinander, sodass sich eine dichtere Packung des Chromatins ergibt und die Transkription von Genen verhindert wird.[83]

Im Cytosol ist Sirt2 üblicherweise mit dem Mikrotubuli-Netzwerk assoziiert und deacetyliert die α-Untereinheit des heterodimeren Tubulinproteins (α-/β-Tubulin). Der Acetylierungsgrad der Mikrotubuli hat dabei Einfluss auf deren Flexibilität und Widerstandsfähigkeit und spielt eine wichtige Rolle bei der Regulation des Zellzyklus.[84–86]

Der Einfluss von Sirt1–3 auf die Apoptose ist komplex. So zeigen sich abhängig vom Zelltyp sowohl pro-apoptotische als auch anti-apoptotische Effekte.[87–89] Unter anderem verursachen Sirt1 und Sirt2 eine anti-apoptotische Wirkung durch die Deacetylierung und der damit ausgelösten Deaktivierung des Tumorsuppressors p53.[90–93] Entsprechend konnte eine gesteigerte Apoptose von Krebszellen durch eine pharmakologische Inhibition von Sirt1 hervorgerufen werden.[94–96] Andererseits zeigten Sirt1 und Sirt2 auch pro-apoptotische Effekte durch die Inaktivierung des Transkriptionsfaktors NF-κB und der sich daraus ergebenden verringerten Cytokin-Freisetzung.[87,89,97,98] Der anti-apoptotische Effekt von Sirt3 basiert auf der Deacetylierung und Aktivierung mitochondrialer Enzyme, welche reaktive Sauerstoffspezies (ROS) abbauen und so die Zelle vor oxidativem Stress schützen.[99–104] Gleichzeitig wurde aber auch von pro-apoptotischen Effekten durch Sirt3 berichtet.[105,106]

Aufgrund ihrer Abhängigkeit von NAD^+ ist die Sirtuin-Aktivität indirekt verknüpft mit dem Energiestatus der Zelle. Allerdings nehmen Sirtuine auch direkten Einfluss auf den Glukose- und Fettstoffwechsel der Zelle.[107] Unter Kalorienrestriktion forcieren Sirt1–3 die

Gluconeogenese durch Aktivierung verschiedener Transkriptionsfaktoren und metabolischer Enzyme.[108–110] Weiterhin wird von einem positiven Einfluss von Sirt1–3 auf die glukoseabhängige Insulinsekretion berichtet.[108,111–113] Die Rolle von Sirt2 als Insulinsensitizer ist allerdings gewebespezifisch.[114] Bezüglich des Fettstoffwechsels zeigt sich durch eine gesteigerte Aktivität von Sirt1–3 unter Kalorienrestriktion eine vermehrte Lipolyse in weißem Fettgewebe und eine Induktion der β-Oxidation.[115–120]

Über viele unterschiedliche Wirkmechanismen nimmt die Deacetylase-Aktivität der Isotypen Sirt1–3 auch Einfluss auf neuronale Prozesse und hat insbesondere Auswirkung auf die neurotoxische Wirkung von Proteinen wie α-Synuclein, Huntingtin, Tau und β-Amyloiden. Auch in diesem Zusammenhang wird jedoch von einem ambivalenten Verhältnis zwischen Sirtuin-Aktivität und neuroprotektiver Wirkung berichtet.[121,122]

1.2.2 Mechanismus der Sirtuin-katalysierten Transacetylierung

Der Mechanismus der Sirtuin-katalysierten Deacetylierung unterscheidet sich deutlich von der Zn^{2+}-katalysierten Deacetylierung klassischer HDACs. Wohingegen klassische HDACs unter Abspaltung von Acetat deacetylieren, übertragen Sirtuine die Acetylgruppe des Substrats auf NAD^+, wobei Nicotinamid und 2′-*O*-Acetyl-ADP-ribose (2′-*O*AADPR) als Nebenprodukte gebildet werden.[123–126] Daher handelt es sich weniger um eine Deacetylierung als vielmehr um eine Transacetylierung. Voraussetzung für die Katalyse ist, dass Substrat und Cofaktor an das Enzym gebunden sind. Die Reihenfolge ist hierbei entscheidend: Die initiale Bindung des Proteinsubstrats induziert eine Konformationsänderung des Enzyms.[127,128] Nur durch diese Konformationsänderung erfolgt die Bindung des Cofaktors in einer produktiven Orientierung, welche die Katalyse der Transacetylierung ermöglicht.[129,130]

Im ersten Schritt der Katalyse findet ein nukleophiler Angriff des Amid-Sauerstoffatoms der N^{ε}-Acetyl-lysin-Seitenkette am C1′ der Nicotinamidribose statt.[131,132] In einer S_N2-ähnlichen nukleophilen Substitution bildet sich unter Freisetzung von Nicotinamid ein α-1′-*O*-Alkylimidat als erstes Zwischenprodukt (Abb. 3).[133–135] Die 2′-OH-Gruppe des α-1′-*O*-Alkylimidats wird durch einen konservierten Histidinrest im aktiven Zentrum der Sirtuine für einen intramolekularen nukleophilen Angriff am Iminium-Kohlenstoffatom aktiviert und bildet eine bizyklische Verbindung als zweites Zwischenprodukt.[136] Nach Freisetzung des deacetylierten Substrats entsteht ein bizyklisches Carbenium-Ion, welches von einem Wassermolekül angegriffen wird und 2′-*O*AADPR als Produkt der enzymatischen Reaktion liefert.[137] Durch eine nicht-enzymatische Umesterung bildet sich ein Gleichgewicht zwischen 2′- und 3′-*O*AADPR. Beide Verbindungen wirken als sekundäre Botenstoffe und nehmen beispielsweise Einfluss auf das Überleben der Zelle unter oxidativem Stress oder die Stabilität von Heterochromatin.[138] Das im ersten Schritt der Katalyse freigesetzte Nicotinamid dient hingegen dem Sirtuin selbst als physiologischer Feedback-Inhibitor. Tatsächlich handelt es sich bei Nicotinamid um einen pan-Sirtuin-Inhibitor. Nach Freisetzung kann es durch erneute Bindung an das Sirtuin die entsprechende Rückreaktion zu NAD^+ auslösen und so die Katalyse hemmen.[129,139]

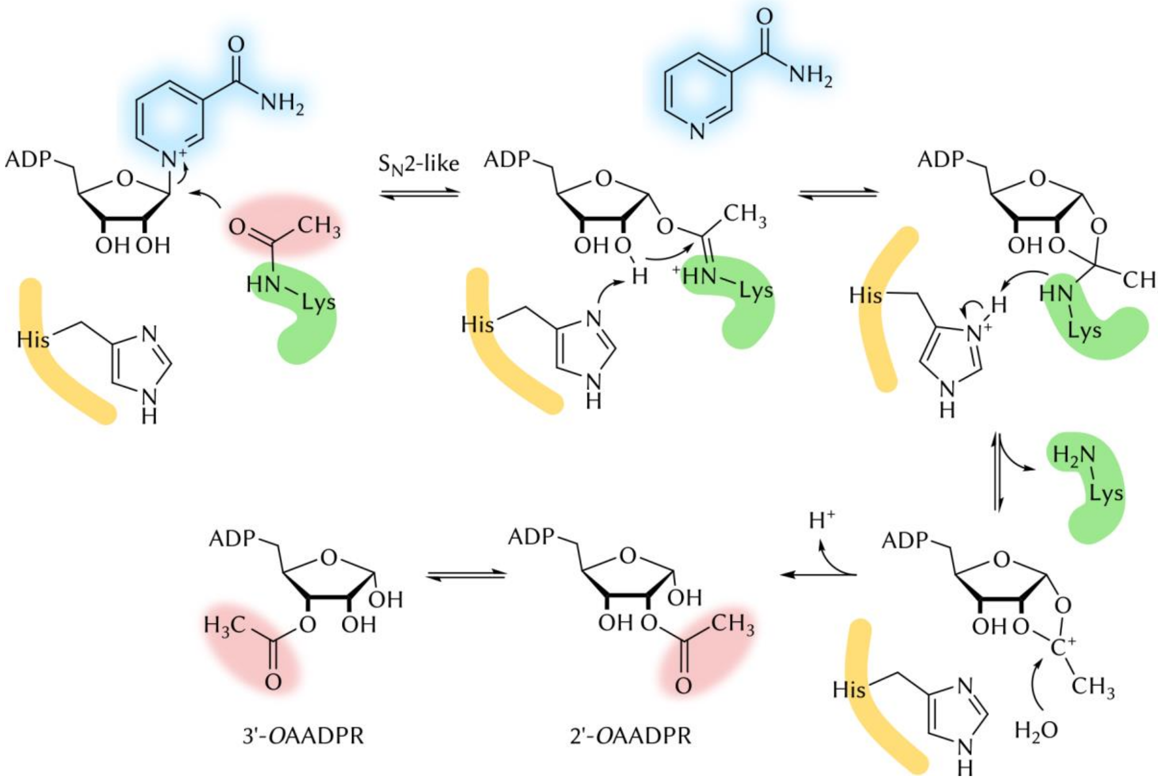

Abb. 3: Mechanismus der Sirtuin-katalysierten Deacetylierung. Die Acetylgruppe (rot) eines Substratproteins (grün) wird unter Bildung von Nicotinamid (blau) und 2′-*O*AADPR auf den Cofaktor NAD$^+$ übertragen. Ein konservierter Histidinrest im katalytischen Zentrum der Sirtuine (gelb) ist an der Katalyse beteiligt.

1.2.3 Struktureller Aufbau der Sirtuine

Mit Ausnahme der Isoenzyme Sirt4 und Sirt7 sind inzwischen Röntgenkristallstrukturen aller humanen Sirtuine verfügbar. Aus dem Vergleich dieser Strukturen lässt sich ein allgemeiner Aufbau ableiten: Das Kernsegment aus circa 275 Aminosäuren ist unter den Sirtuinen stark konserviert und teilt sich in zwei globuläre Subdomänen (Abb. 4).[140] Bei der größeren der beiden Subdomänen handelt es sich um eine Rossmann-Faltung, bestehend aus einem sechssträngigen parallelen β-Faltblatt, das zwischen zwei Flächen mehrerer α-Helices liegt.[127] Diese Supersekundärstruktur dient typischerweise der Bindung von Dinukleotiden wie NAD$^+$.[141,142] Die kleinere und strukturell variablere Subdomäne enthält ein Zn^{2+}-bindendes Modul, das in seiner Topologie einer RING-Fingerdomäne ähnelt.[127] Obwohl das koordinierte Zn^{2+} im Gegensatz zu den HDACs der Klassen I, II und IV nicht am Katalyse-Mechanismus teilnimmt, ist es für die Funktionalität der Sirtuine unentbehrlich.[143] Beide globulären Domänen werden über vier Polypeptidschleifen miteinander verbunden und bilden zusammen eine große Furche, welche die Bindungsstellen für NAD$^+$ und den acylierten Lysinrest des Substratproteins enthält.[61]

Nach Bindung von Substrat und Cofaktor schließt sich die Furche durch eine Drehbewegung der kleineren Domäne hin zur großen Domäne. Die offene Konformation geht auf diese Weise in die geschlossene, produktive Konformation über und bildet einen hydrophoben Kanal um die acylierte Lysinseitenkette.[140,144] In dieser Konformation lässt sich die NAD$^+$-Bindestelle in drei Bereiche einteilen: Ausgehend von der Bindungsstelle der ADP-Ribose-Teilstruktur (A-Site) folgen die Bindungsstellen der Nicotinamid-Ribose-Teilstruktur (B-Site) und des Nicotinamid-Restes (C-Site).[127] Im Falle von Sirt2 existiert nahe der C-Site eine weitere hydrophobe Tasche, die der Bindung langer Fettsäureketten dient.[144] Diese sogenannte „Selectivity Pocket" ist spezifisch für Sirt2 und eignet sich zur Etablierung isotypspezifischer Wechselwirkungen.[145]

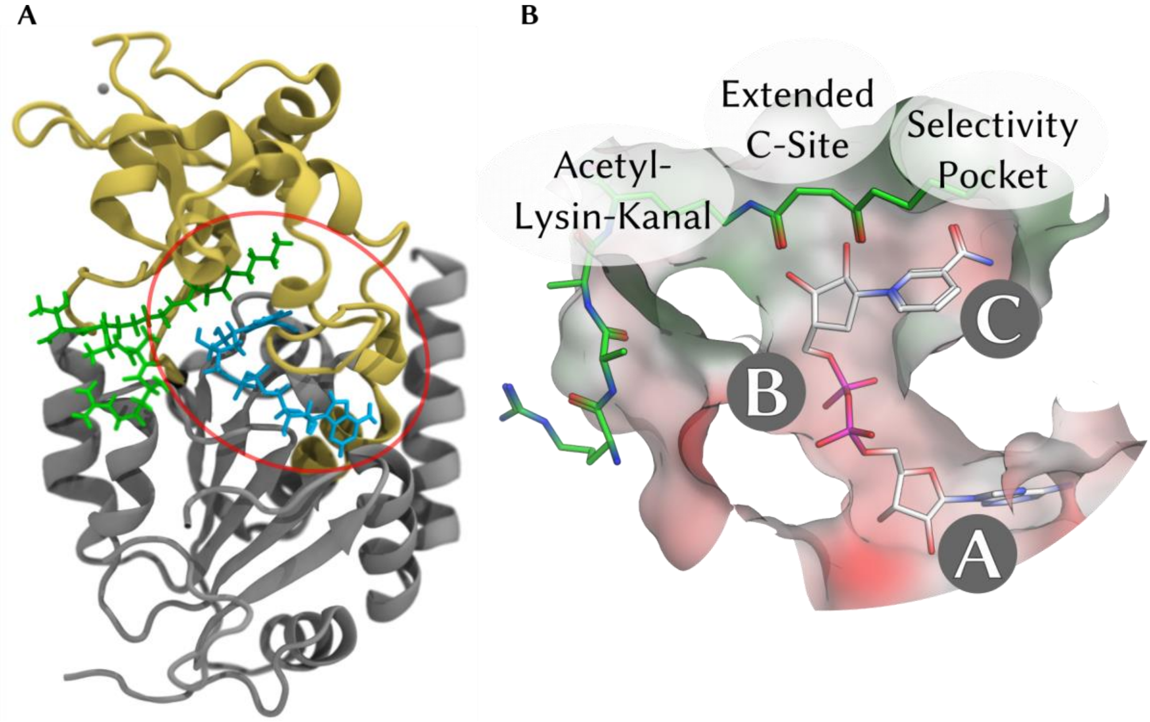

Abb. 4: A) Humanes Sirt2 (AS34–356) in geschlossener Konformation im Komplex mit H3K23(4-ONyl)-Peptid (grün) und carba-NAD$^+$ (blau) auf Basis der Kristallstruktur 5g4c.pdb. Die große globuläre Domäne (grau) enthält eine Rossmann-Faltung, die als Dinukleotid-Bindemotiv dient. Die kleine Domäne (gelb) enthält ein Zn^{2+}-bindendes Motiv, das einer RING-Finger Domäne ähnelt. B) Oberflächenrepräsentation des aktiven Zentrums (grün: hydrophob; rot: hydrophil). Gekennzeichnet sind die Bindetaschen des Cofaktors NAD$^+$ und des Proteinsubstrats.

1.2.4 Sirtuin-spezifische Hemmstoffe

Im Gegensatz zu den Inhibitoren der klassischen HDACs, die bereits etablierte Arzneistoffe in der Krebstherapie sind, wurde bisher noch kein Sirtuin-Inhibitor als Arzneistoff zugelassen.[66] Grund dafür war lange Zeit das Fehlen potenter und selektiver Wirkstoffkandidaten. Die Aufklärung von Struktur und Katalysemechanismus der Sirtuine sowie das Screening verschiedener Substanzbibliotheken lieferten inzwischen jedoch einige vielversprechende Kandidaten.[146,147]

Nicotinamid selbst kann als Mechanismus-basierter Sirtuin-Inhibitor betrachtet werden. Auch wenn es mit einem IC_{50} von 50–184 µM nur eine vergleichsweise geringe inhibitorische Aktivität gegenüber den verschiedenen Sirtuinen aufweist, diente es bereits häufig als Fragment zur Auffindung und Entwicklung potenter Sirtuin-Inhibitoren.[148] Bereits 2005 ging der hochaktive Sirt1-Inhibitor Selisistat (**I**) aus einem Hochdurchsatz-Screening (HTS) hervor.[149] Bei Selisistat handelt sich um ein Indol-Derivat mit einer anellierten

Cyclohexancarboxamid-Struktur, welche das Nicotinamid nachahmt (Abb. 5). Durch Bindung von **I** an die C-Site hält es Sirt1 in seiner geschlossenen Konformation und verhindert so die Freisetzung von 2′-*O*AADPR aus dem katalytischen Zentrum. Mit einem IC_{50} von 98 nM zählt Selisistat bis heute zu den potentesten Sirt1-Inhibitoren. Die pharmakologischen Effekte wurden in verschiedenen *in vivo*-Studien untersucht und erwiesen sich als positiv, vor allem in der Therapie der Chorea Huntington. Darauffolgende klinische Tests bestätigten Selisistat als wirksamen und gut verträglichen Arzneistoff (Klinische Studien: NCT01521832 bzw. NCT01485952). Klinische Langzeitstudien (Phase III) stehen derzeit noch aus.[150,151]

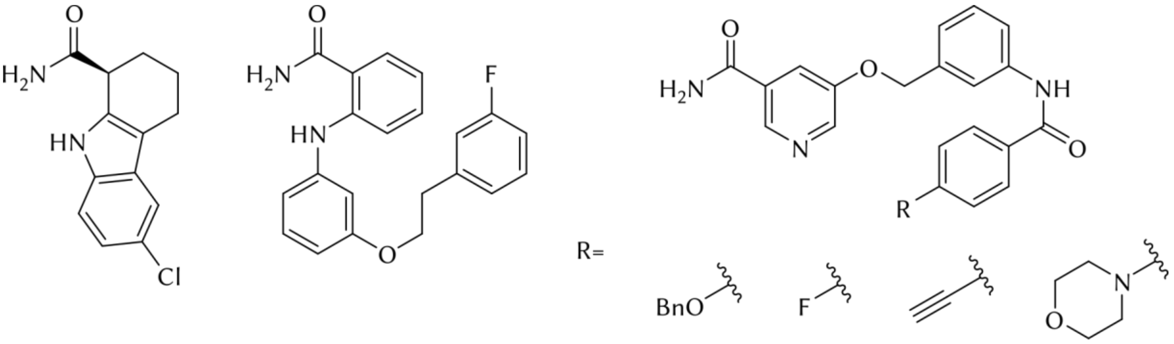

	I	II	III	IV	V	VI
Sirt1	0,098	> 300	> 200	10,1	3,0	6,6
Sirt2	19,6	0,57	0,14	0,075	0,041	0,017
Sirt3	48,7	> 300	> 200	3,39	3,20	1,87

Abb. 5: Strukturen und IC_{50}-Werte (µM) selektiver Sirtuin-Inhibitoren mit Nicotinamid-imitierenden Strukturmotiven.

Nicotinamid oder Nicotinamid-ähnliche Fragmente werden auch in einigen hochselektiven Sirt2-Inhibitoren verwendet. Dazu zählen beispielsweise das 2-Anilinobenzamid **II** sowie die 5-Benzyloxynicotinamide **III–VI**. Wie durch Docking-Studien angedeutet wurde, bindet das Benzamid-Motiv der Verbindung **II** vermutlich außerhalb der C-Site im äußeren Bereich der Substratbindungsstelle und dient daher nicht zur Imitation des Nicotinamids.[152] Die Selektivität von **II** gegenüber Sirt2 basiert vermutlich auf der Bindung des fluorierten Phenethylrests an eine hydrophobe Tasche außerhalb des katalytischen Zentrums von Sirt2, welche in Sirt1 zwar auch vorhanden ist, allerdings deutlich kleiner ausfällt.[152] Im Falle der Verbindungen **III–VI** wiesen Docking-Studien auf eine Bindung des Nicotinamid-Rests an die C-Site von Sirt2 hin.[153] Weitere Wechselwirkungen wurden mit der Substrat-bindenden Region von Sirt2 angedeutet. Durch Kompetitionsstudien mit NAD^+ und dem Peptidsubstrat wurden beide Bindungsstellen experimentell verifiziert.[153] Allerdings liefert der vorgeschlagene Bindungsmodus keine ausreichende Erklärung für die beobachtete Isotyp-Selektivität der 5-Benzyloxynicotinamide, da insbesondere Sirt1–3 in den betreffenden Bereichen eine hohe Sequenzhomologie aufweisen.[153] Die biologische Aktivität beider Verbindungen konnte durch eine Zunahme von acetyliertem α-Tubulin in Zellversuchen bestätigt werden.[152–155]

Einen besonderen Stellenwert unter den selektiven Sirt2-Inhibitoren nehmen die SirReals ein, die ebenfalls aus dem Screening einer Substanzbibliothek hervorgingen (Abb. 6).[156,157] Röntgenstrukturanalysen enthüllten einen außergewöhnlichen Bindungsmodus für SirReal2 (**VII**), das eine Umlagerung des aktiven Zentrums von Sirt2 auslöst und das Enzym trotz gleichzeitiger Bindung von Substrat und Cofaktor in seiner offenen Konformation hält und auf diese Weise die Katalyse verhindert.[156] Die hohe Aktivität und Selektivität von **VII** wird vermutlich durch eine besondere Flexibilität von Sirt2 im verlängerten Bereich der C-Site („Extended C-Site") und durch Bindung an die Selectivity Pocket verursacht.[145]

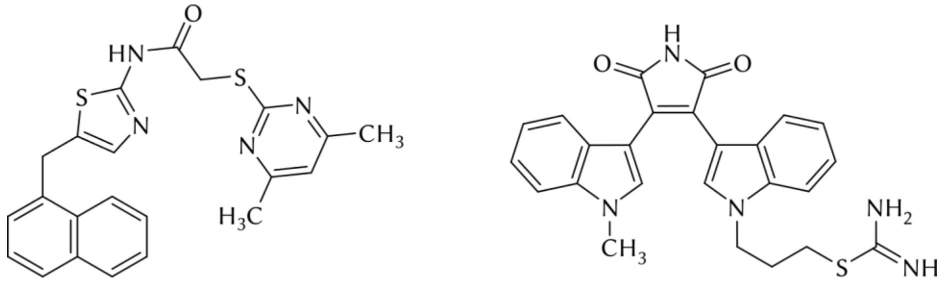

	VII	**VIII**
Sirt1	> 140	3,5
Sirt2	0,14	0,8
Sirt3	> 140	3,7

Abb. 6: Strukturen und IC_{50}-Werte (µM) des selektiven Sirt2-Inhibitors SirReal2 (**VII**) und des PKC-Inhibitors Ro31-8220 (**VIII**).

Aufgrund struktureller Überschneidungen zwischen NAD^+ und ATP besitzen einige ATP-imitierende Kinase-Inhibitoren auch eine inhibitorische Aktivität gegenüber Sirtuinen. So wurde Ro31-8220 (**VIII**) zwar ursprünglich als Inhibitor der Proteinkinase C (PKC) entwickelt, im Rahmen eines Screenings allerdings ebenfalls als potenter, unselektiver Sirtuin-Inhibitor identifiziert (Abb. 6).[158–160]

1.3 Zielsetzung

Innerhalb der letzten zehn Jahre seit ihrer Entstehung erlebt die Photopharmakologie eine rasante Entwicklung. Die Möglichkeit, die Wirkung biologisch aktiver Substanzen durch externe Lichtstimuli zu beeinflussen und so eine präzise Kontrolle über spezifische biochemische Prozesse im Inneren der Zelle zu erlangen, ist von enormem Potential für die Arzneistoffforschung und Pharmakotherapie. Intensive Forschung auf diesem Gebiet hat inzwischen photochrome Liganden für verschiedenste Targets hervorgebracht, darunter zahlreiche Enzyme,[161] Ionenkanäle,[162] GPCRs,[163] Transportproteine[164,165] sowie Komponenten des Cytoskeletts.[166]

Aufgrund der zentralen Bedeutung der Sirtuine bei der Regulation verschiedener zellulärer Prozesse stellen Modulatoren dieser Enzymfamilie vielversprechende potentielle Wirkstoffe in der Therapie von malignen Neoplasien[95,96] und neurodegenerativen Erkrankungen wie Morbus Alzheimer,[167–169] Morbus Parkinson[170–172] oder Chorea Huntington[173–175] dar. Ferner scheinen Sirtuin-Modulatoren hilfreich in der Vorbeugung und Behandlung metabolischer

Krankheiten wie Typ II-Diabetes mellitus[176], Adipositas[177] und damit assoziierten Folgeerkrankungen.[178,179] Aufgrund der komplexen und teilweise zellspezifischen Funktion der Sirtuine ist eine Kontrolle über die Aktivität ihrer Modulatoren besonders wünschenswert.

Ziel dieser Arbeit war die Synthese, Charakterisierung und Testung selektiver Sirtuin-Inhibitoren, deren biologische Aktivität durch Lichtstimuli reversibel beeinflusst werden sollte. Als Ausgangspunkt des Forschungsprojekts diente die stilbenoide Verbindung **IX**, die aus dem Screening einer Kinase-Inhibitor-Bibliothek als moderat aktiver Sirtuin-Inhibitor mit schwach ausgeprägter Selektivität hervorging (Abb. 7).[180] Zunächst sollte das Potential stilbenoider Verbindungen bezüglich ihrer Eignung als PCL in einem biologischen Kontext untersucht und nötigenfalls optimiert werden.

Die Azologisierung biologisch aktiver Verbindungen ist ein häufig verwendetes Prinzip im Design von PCLs. Sie beschreibt den Austausch strukturell ähnlicher Motive durch Diazenogruppen und ermöglicht somit das Einfügen einer photosensitiven Gruppe unter Beibehaltung der Molekülgeometrie und meist auch der biologischen Aktivität.[181] Die Verbindungen **IX** sowie die strukturell nahestehenden 5-Benzyloxynicotinamide von Ai *et al.* (**III**–**VI**) stellen in dieser Hinsicht aussichtsreiche Kandidaten dar. Durch Ersetzen der C,C-Doppelbindung in **IX** bzw. der *N*-Arylamid-Bindung in **III**–**VI** durch eine N,N-Doppelbindung sollten die Leitstrukturen in Azofarbstoffe umgewandelt werden. Die potentiellen Photoschalter sollten weiterhin durch strukturelle Modifikationen hinsichtlich ihrer photophysikalischen Eigenschaften sowie biologischen Aktivität optimiert werden.

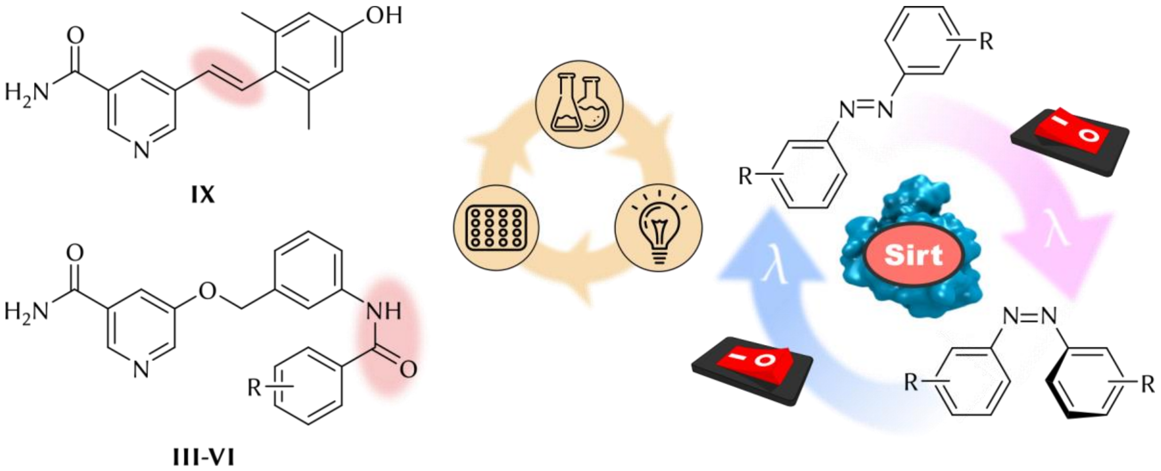

Abb. 7: Auf Grundlage der Leitstrukturen **III**–**VI** und **IX** sollen potente und selektive Sirtuin-Photoschalter entwickelt werden. Dazu sollen die Leitstrukturen durch einen iterativen Prozess aus chemischer Synthese, photochemischer Charakterisierung und biologischer Evaluation hinsichtlich ihrer photophysikalischen Eigenschaften und Target-Affinität optimiert werden.

2 Methoden und Ergebnisse

2.1 Synthese *E*/*Z*-photoisomerisierbarer Sirtuin-Inhibitoren

Die im Rahmen dieser Arbeit dargestellten Sirtuin-Inhibitoren lassen sich auf drei Substanzklassen aufteilen: (a) Analoga der Leitstruktur **IX** mit Styrylpyridin-Kern, (b) 5-Phenylazonicotinamide basierend auf Leitstruktur **IX** sowie (c) Azobenzen-Derivate der Leitstrukturen **III**–**VI**.

2.1.1 Synthese von Styrylpyridinen

Verschieden substituierte Styrylpyridine wurden ausgehend von 5-Bromnicotinamid (**1a**) bzw. 5-Bromnicotinsäuremethylester (**1b**) in ein bis drei Schritten dargestellt (Schema 1). Die Heck-Kupplung zu den jeweiligen Styrylpyridinen erfolgte dabei sowohl unter Verwendung von 3-Brompyridinen (**1a**, **1b**) als auch 3-Vinylpyridinen (**2a**, **2b**). Letztere waren durch Suzuki-Miyaura- bzw. Stille-Kupplung aus den entsprechenden 3-Brompyridinen direkt zugänglich.[182,183] Tendenziell lieferten 3-Brompyridine im Vergleich zu 3-Vinylpyridinen höhere Ausbeuten in der Heck-Reaktion.[184] Im Allgemeinen waren die Ausbeuten in diesem Schritt jedoch unbefriedigend. Angesichts der ausreichenden Gesamtausbeuten wurde auf eine weitere Optimierung der Reaktionsbedingungen verzichtet.

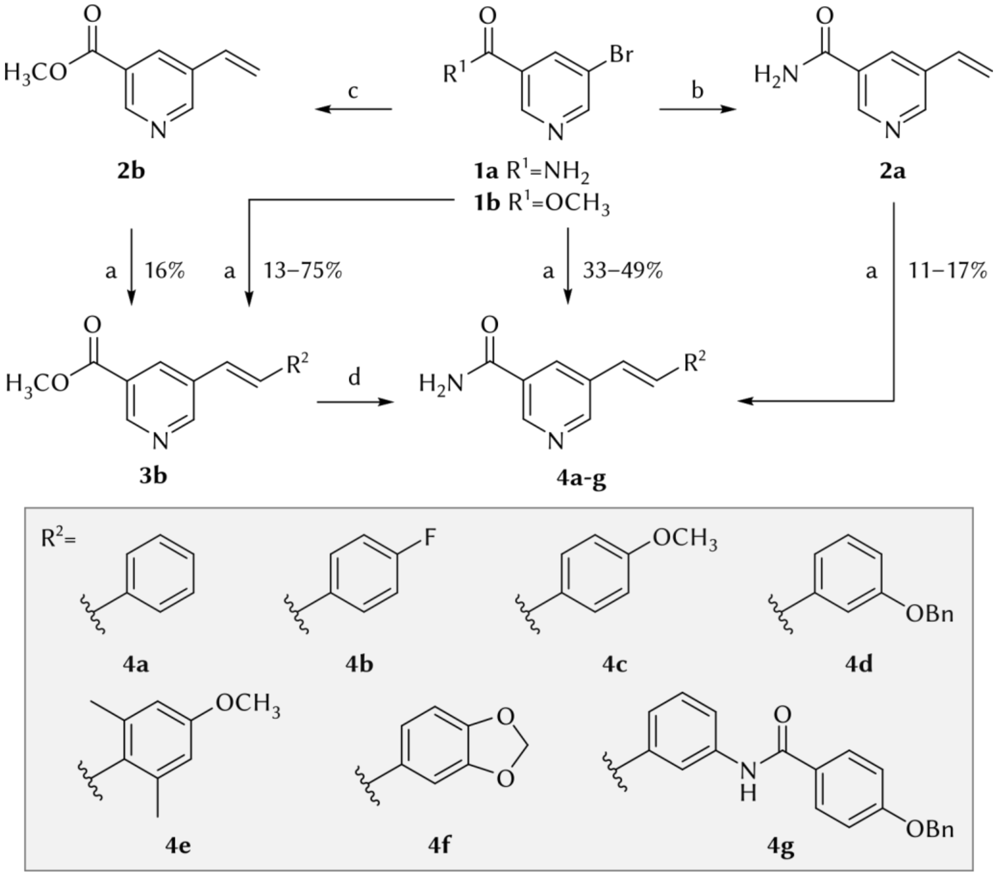

Schema 1: a) Pd-Kat., P(*o*-Tol)$_3$, TEA, DMF, 120–140 °C, 1–24 h; b) Kaliumvinyltrifluoroborat, Cs_2CO_3, $PdCl_2(PPh_3)_2$, ACN, H_2O, 120 °C, 1,5 h, 78%; c) Tributylvinylzinn, $Pd(PPh_3)_4$, Toluen, 110 °C, 3 h, 76%; d) NH_3, MeOH, 40 °C, 72 h, 87–95%.

Neben den Styrylpyridinen **4a–g** wurden zwei starre bzw. „überbrückte“ Derivate (**5a**, **5b**) in einer Suzuki-Reaktion von **1a** mit 2-Naphthalinboronsäure bzw. (3,4-Dihydronaphthalin-2-yl)boronsäure dargestellt (Schema 2). Anhand von **5a** und **5b** sollte untersucht werden, inwiefern die freie Rotation des Phenylrings einen Einfluss auf die biologische Aktivität der Styrylpyridine hat.

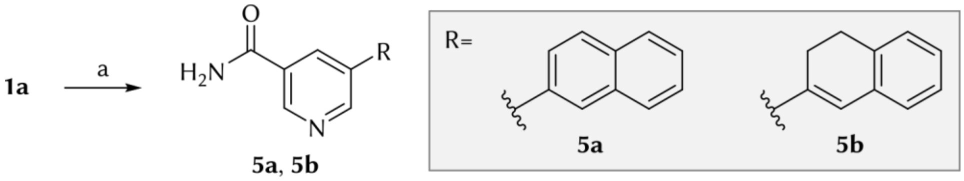

Schema 2: a) Boronsäure, Pd(PPh$_3$)$_4$, Na$_2$CO$_3$, DMF, H$_2$O, Mikrowellenreaktor, 150 °C, 15 min, 43–64%.

2.1.2 Synthese von 5-Phenylazonicotinamiden

Eine Sammlung verschiedener 5-Phenylazonicotinamide wurde in einer zweistufigen Synthese ausgehend von 5-Aminonicotinsäuremethylester (**6**) dargestellt (Schema 3). Durch Diazotierung konnte **6** in das entsprechende Diazoniumsalz überführt werden und in einer anschließenden Azokupplung zu **7a–f** reagieren. Ammonolyse der Methylester **7a–f** lieferte im letzten Schritt die Nicotinamid-Derivate **8a–f**. Da Diazoniumsalze als schwache Elektrophile nur mit besonders elektronenreichen Aromaten reagieren, waren durch direkte Azokupplung von **6** nur Phenol- (**4a–d**) und Anilin-Derivate (**4e**, **4f**) zugänglich.[185]

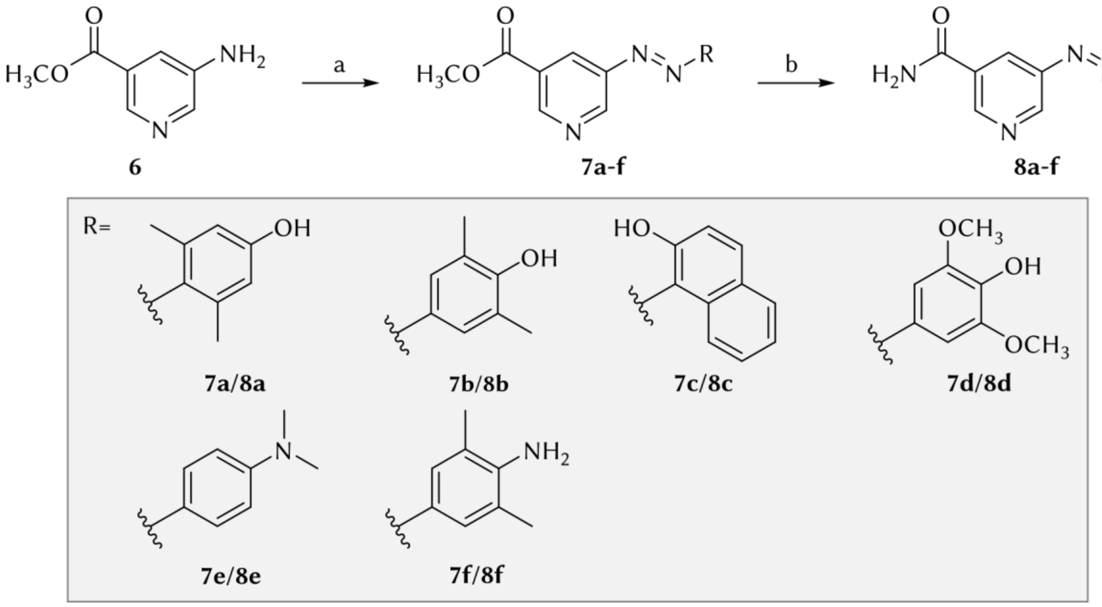

Schema 3: a) 1. NaNO$_2$, HCl, H$_2$O, 0 °C; 2. Ar-OH oder Ar-NR$_2$, H$_2$O, 0–21 °C, 31–65%; b) NH$_3$, MeOH, 24–96 h, 89–100%.

Die Umsetzung der primären aromatischen Aminogruppe der Nicotinsäureester **7f** bzw. **10** mit Säurechloriden einiger aliphatischer bzw. aromatischer Carbonsäuren lieferte nach abschließender Ammonolyse des Nicotinsäureesters die Nicotinamide **9a–k** (Schema 4). Wegen sterischer Hinderung der primären aromatischen Aminogruppe durch die beiden benachbarten Methylgruppen in **7f** bzw. **10** verlief die nukleophile Substitution trotz Verwendung hochreaktiver Säurechloride vergleichsweise langsam. Auch nach Reaktionszeiten von mehreren Tagen sowie einem bis zu 1,5-fachem Überschuss des Säurechlorids wurde keine vollständige Umsetzung erreicht.

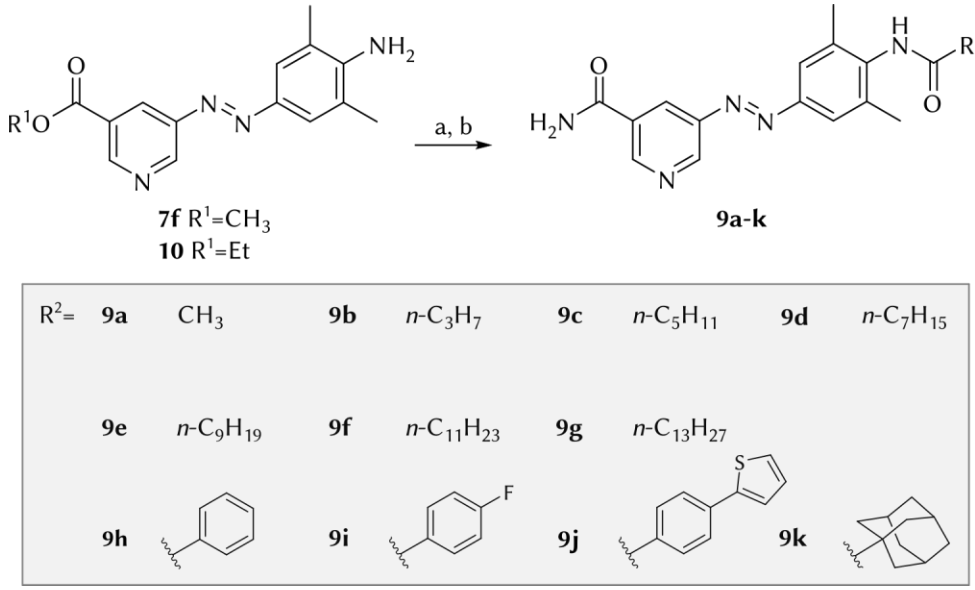

Schema 4: a) Carbonsäurechlorid, Pyridin oder DIPEA, THF, 0–21 °C, 24–72 h, 26–76%; b) NH_3, MeOH, 24–96 h, 64–100%.

Eine Derivatisierung der Carboxamid-Gruppe der Nicotinamid-Teilstruktur zu *N*-Alkylamiden wurde ausgehend von 5-Aminonicotinsäureethylester (**10**) in zwei Stufen durchgeführt (Schema 5). Analog zur Synthese von **7f** wurde **10** zunächst diazotiert und in einer Azokupplung mit 2,6-Dimethylanilin zu **11** umgesetzt. Anstelle einer Ammonolyse erfolgte nun im letzten Schritt eine Aminolyse zu den *N*-Alkylamiden **12a–d** durch verschiedene primäre Alkylamine. Methylester wie **7f** ließen sich nicht durch primäre Alkylamine zu *N*-Alkylamiden umsetzen.

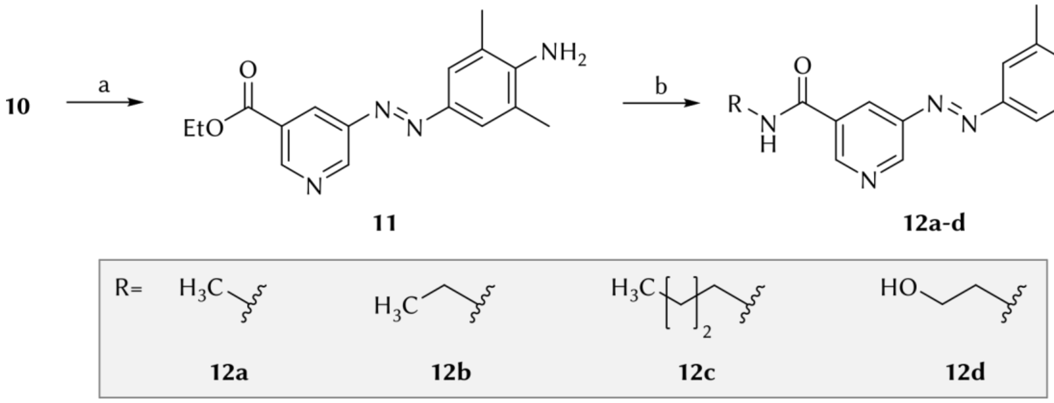

Schema 5: a) 1. NaNO$_2$, HCl$_{aq}$, H$_2$O, 0 °C; 2. 2,6-Dimethylanilin, HCl$_{aq}$, H$_2$O, 0° C, 38%; b) R-NH$_2$, MeOH, 40–110 °C, 96 h, 88–98%.

Unter Anwendung der Mills-Reaktion ließen sich auch weniger elektronenreiche Aromaten zu Azofarbstoffen umsetzen (Schema 6).[185–188] So lieferte die Kondensation von **6** mit den aromatischen Nitrosoverbindungen **14a**–**e** in Essigsäure weitere Methylester (**15a**–**e**), die durch Ammonolyse im letzten Reaktionsschritt zu den Nicotinamiden **16a**–**e** reagierten. Die aromatischen Nitrosoverbindungen **14a**–**e** ließen sich durch Oxidation mittels Kaliumperoxomonosulfat (Oxone) aus den entsprechenden primären aromatischen Aminen **13a**–**e** darstellen.[189] Verbindung **6** konnte auf diese Weise jedoch nicht in die entsprechende Nitrosoverbindung überführt werden, da vermutlich stattdessen das Pyridin-*N*-oxid gebildet wurde.

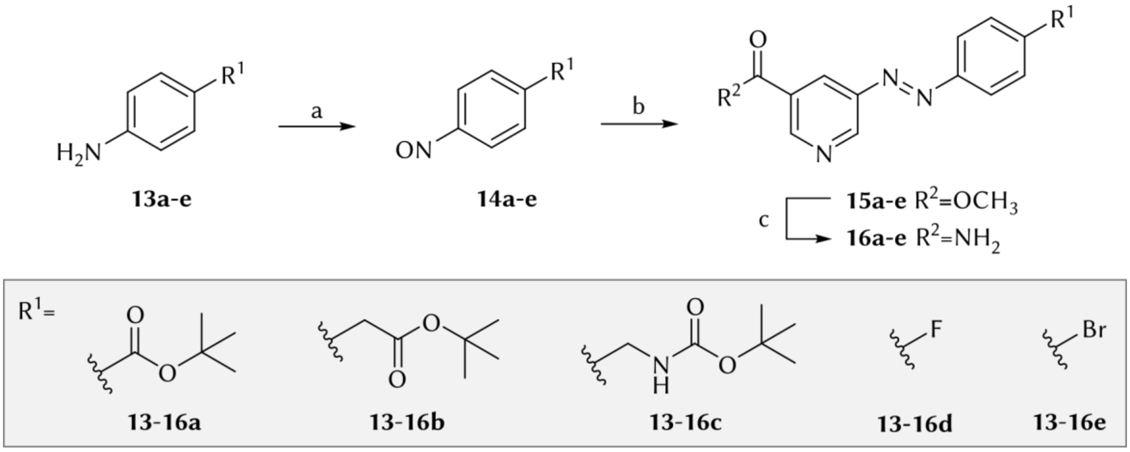

Schema 6: a) Oxone, DCM, H$_2$O, 4–48 h; b) **6**, HAc, 40 °C, 2–14 Tage, 7–43% über zwei Stufen; c) NH$_3$, MeOH, 96 h, 64–100%.

Ausgehend von **15a**, **15c** und **15e** wurden durch weitere Derivatisierung die Nicotinamid-Derivate **16f–i** erhalten (Schema 7). Nach saurer Spaltung der *tert*-Butyl-basierten Schutzgruppen in **15a** und **15c** konnte die freigelegte Carbonsäure bzw. Aminogruppe unter intermediärer Bildung eines Aktivesters bzw. durch Umsetzung mit einem Säurechlorid zum Amid **15f** bzw. **15g** umgewandelt werden. Arylbromid **15e** erlaubte hingegen die Kupplung terminaler Alkine nach Sonogashira und lieferte die Verbindungen **15h** und **15i**, die wie auch **15f** und **15g** nach Ammonolyse die Nicotinamide **16f–i** lieferten.[190]

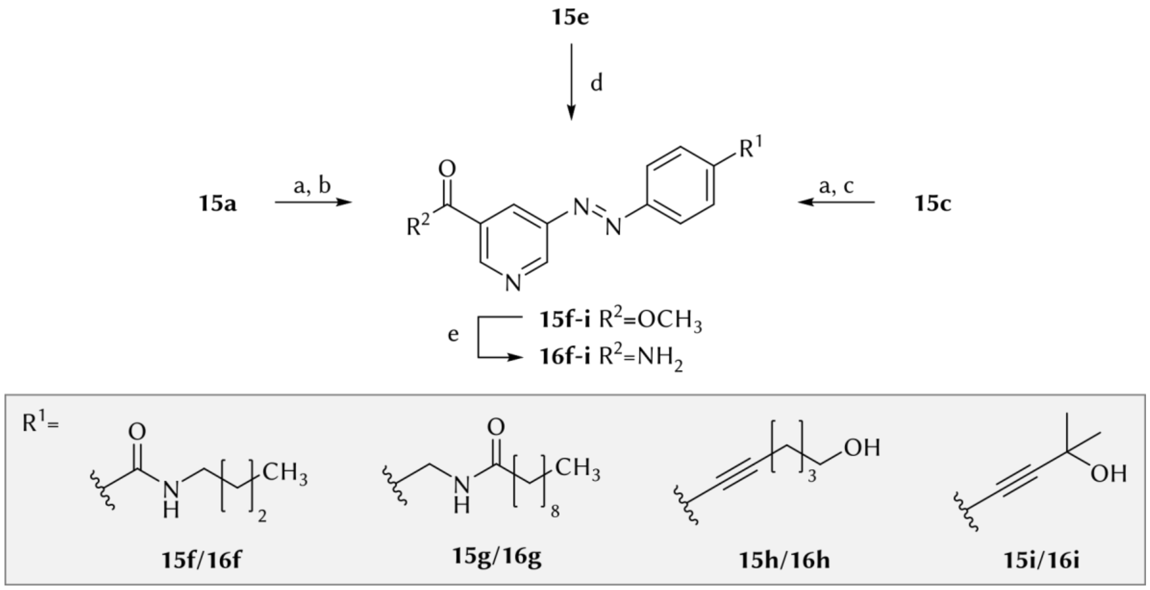

Schema 7: a) TFA, DCM, 12 h, 100% b) *n*-Butylamin, HATU, DIPEA, DMF, 16 h, 56%; c) Decanoylchlorid; DIPEA, THF, 80%; d) Terminales Alkin, $Pd(PPh_3)_4$, CuI, TEA, THF oder DCM, 50–85 °C, 24 h, 20%; e) NH_3, MeOH, 96 h, 97–100%.

2.1.3 Synthese von Azobenzenen

Auf Grundlage der 5-Benzyloxynicotinamide (**III**–**VI**) wurden einige analoge Azobenzen-Derivate dargestellt (Schema 8). Entsprechend der Originalpublikation erfolgte die Synthese ausgehend von 5-Hydroxynicotinsäuremethylester (**17**).[153] Verbindung **17** wurde zunächst durch 3-Nitrobenzylbromid alkyliert und der erhaltene Nitroaromat **18** zum Anilin-Derivat **19** reduziert. Abweichend von der ursprünglich publizierten Darstellungsmethode wurde in dieser Arbeit Raney-Nickel/H_2 statt $NiCl_2$/$NaBH_4$ zur Reduktion des Nitroaromaten **18** eingesetzt. Die Ausbeute an **19** wurde hierdurch marginal verbessert (85% statt 80%). In einer Mills-Reaktion konnte **19** schließlich zu den Azobenzenen **20a**–**d** umgesetzt werden, die nach Ammonolyse die Nicotinamide **21a**–**d** ergaben.

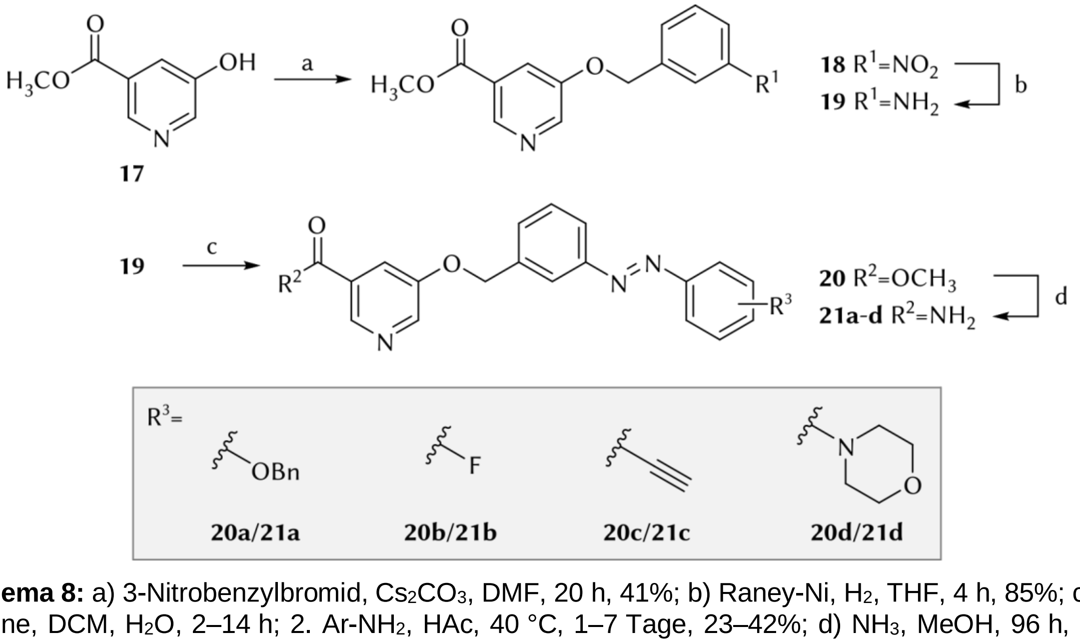

Schema 8: a) 3-Nitrobenzylbromid, Cs_2CO_3, DMF, 20 h, 41%; b) Raney-Ni, H_2, THF, 4 h, 85%; c) 1. Oxone, DCM, H_2O, 2–14 h; 2. Ar-NH_2, HAc, 40 °C, 1–7 Tage, 23–42%; d) NH_3, MeOH, 96 h, 91–100%.

2.2 Photochemische Charakterisierung

Das Verhalten der synthetisierten Photoschalter unter Lichteinfluss wurde *via* UV/Vis-Spektroskopie bzw. Hochleistungsflüssigkeitschromatographie (HPLC) untersucht. Als Lichtquellen dienten hierbei ein UV-Crosslinker, ausgestattet mit sechs UV-Lampen (8 W, UV-B: λ_{max} = 254 nm; UV-A: λ_{max} = 365 nm) sowie ein RGB-LED-Streifen mit 64 LEDs (blau: λ_{max} = 452 nm; grün: λ_{max} = 500 nm; rot: λ_{max} = 630 nm). Die Aufnahme der UV/Vis-Spektren erfolgte in gelöster Form (DMSO/H_2O) bei einer Konzentration von 50 µM, was der Größenordnung der folgenden Aktivitätsbestimmungen in den biochemischen Assays entspricht (vgl. 2.3). Verlässliche HPLC-Chromatogramme wurden hingegen nur bei höher konzentrierten Proben erhalten. In diesem Fall erfolgte Bestrahlung und Messung von methanolischen Lösungen bei einer Konzentration von 1 mM (HPLC) bzw. 10 mM (HPLC-MS).

2.2.1 Photochemie der Styrylpyridine

Die Photochemie der Styrylpyridine wurde stellvertretend anhand der Verbindungen **4a** und **4e** untersucht. Bei Bestrahlung (λ_{max} = 254 nm) von **4a** traten drastische Veränderungen im UV/Vis-Spektrum auf, welche sich weder photochemisch noch thermisch (unter Standardbedingungen) umkehren ließen. Auch im Falle der Verbindung **4e** konnte das ursprünglich aufgenommene UV/Vis-Spektrum nicht wiederhergestellt werden. Mittels HPLC-MS sowie dem Vergleich experimenteller UV/Vis-Spektren aus den LC-Läufen mit simulierten UV/Vis-Spektren potentieller Nebenprodukte wurden insbesondere für **4a** irreversible Nebenreaktionen angezeigt (Manuskript I). Benzo[*h*]chinolin **22** ließ sich anhand einer dargestellten Referenzprobe zweifelsfrei als eines der Nebenprodukte nachweisen (Schema 9).

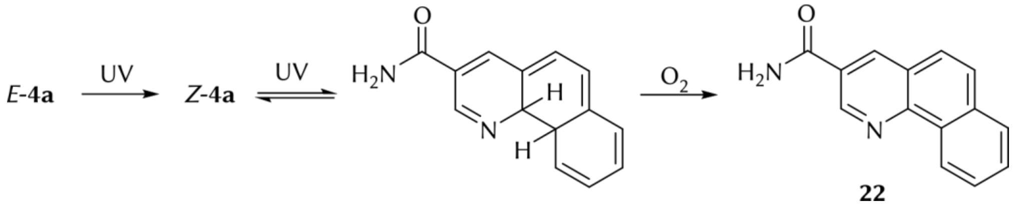

Schema 9: Durch Bestrahlung mit Licht der Wellenlänge 254 nm lässt sich die stilbenoide Verbindung **4a** aus dem thermodynamisch stabileren *E*-Isomer in das *Z*-Isomer umwandeln. Dieses reagiert in einer intramolekularen Photozyklisierungsreaktion mit anschließender Oxidation unter Anwesenheit von Sauerstoff weiter zum Benzo[*h*]chinolin **22**.

2.2.2 Photochemie der Phenylazopyridine und Azobenzene

Von den dargestellten Azofarbstoffen ließ sich die Photoisomerisierung der Verbindungen **9a**–**k**, **16a**–**i** sowie **21a**–**c** näher untersuchen. Die Verbindungen **8a**–**f**, **12a**–**d** sowie **21d** besaßen aufgrund ihrer Substituenten (2-/4-OH- bzw. 4-NR_2) kurzlebige PSS, die anhand der verfügbaren Methoden nicht erfasst werden konnten.

Eine Abschätzung der thermischen Stabilität der PSS erfolgte durch eine photometrische Bestimmung der Reaktionskinetik der thermischen *Z*→*E*-Isomerisierung. Dazu wurde zunächst das Absorptionsmaximum des *E*-Isomers (λ^{Δ}_{max}) bestimmt. Im Anschluss wurde die Probe bestrahlt (λ_{max} = 365 nm) und die Zunahme der Absorption bei λ^{Δ}_{max} über die Zeit verfolgt. Durch nicht-lineare Regression der Messwerte ließ sich die Halbwertszeit der thermischen Reaktion als Maß der PSS Stabilität berechnen (Abb. 8).

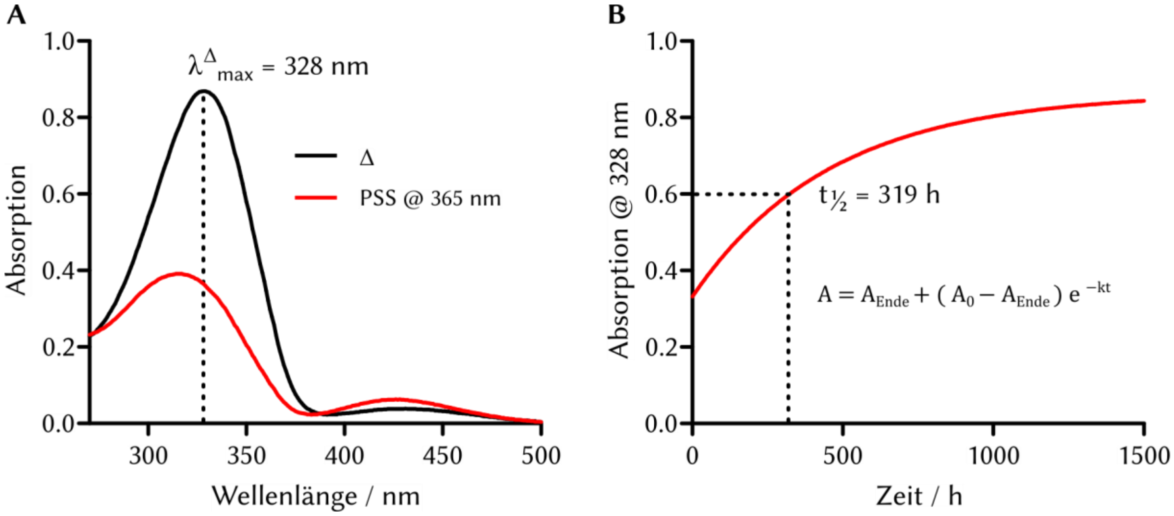

Abb. 8: A) UV/Vis-Spektren der Verbindung **16c** im thermischen Gleichgewicht (Δ, schwarz) sowie im PSS nach Bestrahlung mit Licht einer Wellenlänge von 365 nm (rot); B) Die Zunahme der Absorption bei λ = 328 nm wird über den zeitlichen Verlauf der thermischen Rückreaktion im Dunkeln verfolgt. Nicht-lineare Regression der Messwerte nach einer exponentiellen Annäherungsfunktion ergibt eine Halbwertszeit der Reaktion ($t_{½}$) von 319 h.

Die PSD der Photoschalter in den PSS nach Bestrahlung mit UV-Licht (λ_{max} = 365 nm) bzw. blauem Licht (λ_{max} = 452 nm) wurde durch Auftrennung der Photoisomere mittels HPLC und anschließender relativer Integration der beiden Signale ermittelt (Abb. 9).

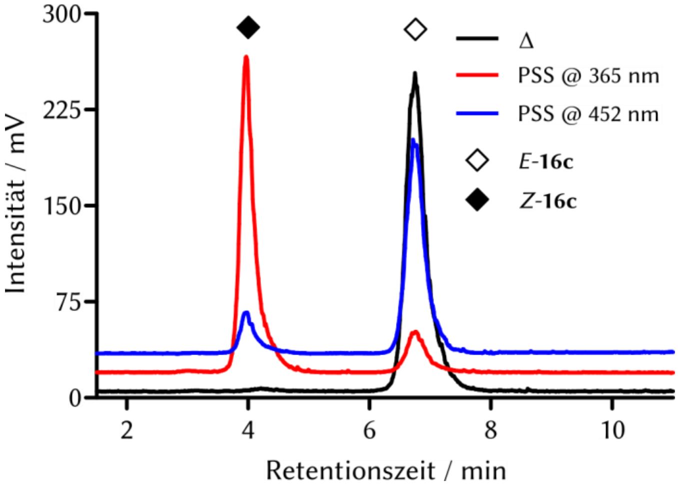

Abb. 9: HPLC-Chromatogramm der Verbindung **16c** im thermischen Gleichgewicht (Δ) sowie im PSS nach Bestrahlung mit Licht einer Wellenlänge von 365 nm bzw. 452 nm. Relative Integration der Signale ergab die PSD der jeweiligen PSS.

Die Verbindungen **16c**, **16g** und **21a** wurden neben ihres Einflusses auf die Aktivität der isolierten Enzyme Sirt1–3 auch hinsichtlich ihrer biologischen Aktivität gegenüber Zellen untersucht (vgl. 2.3.2). Um sicherzustellen, dass die chromophore Azogruppe auch innerhalb des reduktiven Milieus einer Zelle funktional bleibt, wurde die chemische Stabilität dieser Verbindungen gegenüber Glutathion (GSH) mittels HPLC-Analysen untersucht. Dazu wurden die Verbindungen gelöst (90% MeOH in H_2O (v/v), 1 mM) und mit GSH (5 mM) bei Raumtemperatur für 24 h inkubiert. Anschließend wurde die Funktionsfähigkeit des Photoschalters durch Bestrahlung (λ_{max} = 365 nm bzw. 452 nm) getestet (Abb. 10).

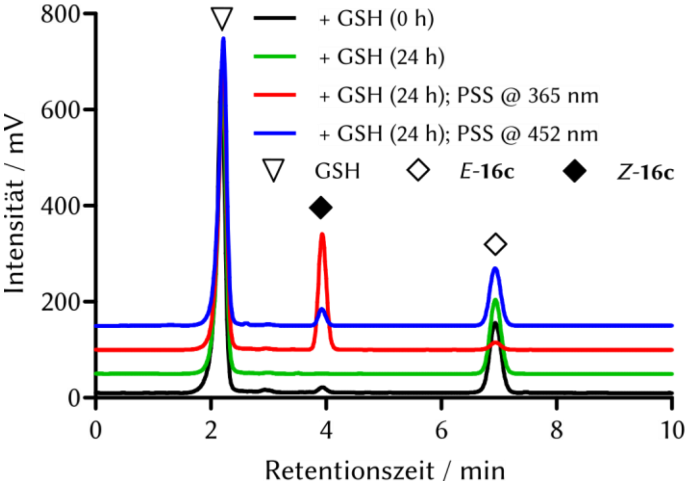

Abb. 10: Stabilität der Verbindung **16c** in Gegenwart von GSH (5 mM). Auch nach 24 h Inkubation bei Raumtemperatur lässt sich **16c** durch Bestrahlung isomerisieren.

Tabelle 1 fasst die Ergebnisse der photophysikalischen Untersuchungen zusammen. Abgesehen von **16d** wurden alle dargestellten Azofarbstoffe in Manuskript III publiziert. Die photophysikalischen Eigenschaften der Verbindung **16d** sind hingegen in Manuskript I beschrieben.

Tabelle 1: Zusammenfassung der photophysikalischen Eigenschaften der Verbindungen **9a-k**, **16ai** sowie **21a-c**.

Substanz	λ^{Δ}_{max} [nm]	$t_{½}$ [h]	PSD @ 365 nm [% *E*-Isomer]	PSD @ 452 nm [% *E*-Isomer]
9a[a]	329	6	12	90
9b[a]	332	8	10	86
9c[b]	339	16	9	87
9d[c]	345	21	9	88
9e[c]	344	22	10	90
9f[c]	346	21	10	91
9g[c]	345	26	14	87
9h[b]	337	0,7	14	91
9i[b]	337	0,6	12	91
9j[b]	330	0,6	29	93
9k[b]	339	7	14	89
16a[b]	325	176	31	94
16b[b]	332	23	6	90
16c[a]	329	319	11	86
16d[a]	324	300	16	75
16e[a]	332	220	9	91
16f[b]	326	254	40	89
16g[c]	333	102	5	79
16h[b]	355	48	25	89
16i[b]	350	79	23	92
21a[b]	352	33	4	80
21b[b]	324	166	2	83
21c[b]	340	63	14	85

Bestimmung von λ^{Δ}_{max} bzw. $t_{½}$ erfolgte in [a] 5% DMSO/H_2O (v/v); [b] 50% DMSO/H_2O; [c] 90% DMSO/H_2O.

2.3 Bestimmung der biologischen Aktivität

2.3.1 Fluoreszenz-basierter Aktivitätsassay (ZMAL-Assay)

Der Einfluss der synthetisierten Verbindungen auf die Deacetylase-Aktivität der humanen Sirtuine Sirt1–3 wurde in einem homogenen fluoreszenzbasierten Enzym-Assay unter Verwendung des künstlichen Substrats Z-(ε-Acetyl)lysin-7-amino-4-methylcumarin (ZMAL), ermittelt.[191] Die Durchführung des Assays erfolgte in der Arbeitsgruppe von Prof. Dr. Manfred Jung an der Albert-Ludwigs-Universität Freiburg.

Durch Vergleich der umgesetzten Substratmenge unter Inhibition mit einer DMSO-Kontrolle wurde die prozentuale Inhibition bei verschiedenen Konzentrationen bestimmt. In einem Aktivitätsscreening erfolgte eine Bestimmung zunächst bei Konzentrationen von 100 µM, 50 µM bzw. 10 µM. IC_{50}-Werte wurden in Doppelmessungen für Verbindungen ermittelt, welche bei einer Konzentration von 10 µM mindestens eine 70%ige Hemmung der Enzymaktivität zeigten.

Um den Einfluss der Photoisomerisierung auf die Affinität der Sirtuin-Inhibitoren zu untersuchen, wurden betreffende Verbindungen in gelöster Form (DMSO) vor der Aktivitätsbestimmung im ZMAL-Assay bestrahlt (λ = 365 nm, 5 min). Die biologische Aktivität des photoisomerisierten Inhibitors wurde schließlich unter Lichtausschluss bestimmt und mit einer nicht bestrahlten Messung verglichen. Im Falle irreversibler Nebenreaktionen unter Bestrahlung (vgl. 2.2.1) oder ungenügender PSS-Stabilität in wässriger Umgebung wurde auf eine Bestimmung unter vorheriger Bestrahlung verzichtet.

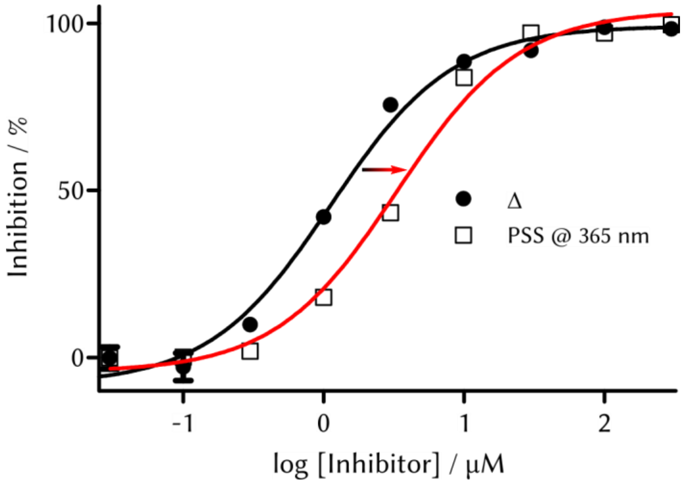

Abb. 11: Konzentrations-Wirkungs-Kurve und nicht-lineare Regression von **16c** gegenüber dem humanen Sirt2 im thermischen Gleichgewicht (Δ) sowie im PSS nach Bestrahlung mit Licht einer Wellenlänge von 365 nm.

Tabelle 2: Inhibitorische Aktivitäten bei gegebener Inhibitorkonzentration bzw. angegeben als IC_{50} (µM) gegenüber den humanen Sirtuin-Isotypen Sirt1–3.

Substanz	Sirt1	Sirt2	Sirt3
X	27% @ 50 µM	24,6 ± 2,8	41,7 ± 2,0
4a	71% @ 10 µM	8,7 ± 0,2	89% @ 50 µM
4b	51% @ 100 µM	6,6 ± 0,5	7,5 ± 0,9
4c	51% @ 10 µM	64% @ 10 µM	90% @ 50 µM
4d	61% @ 50 µM	69% @ 50 µM	60% @ 50 µM
4e	26% @ 50 µM	21% @ 10 µM	79% @ 50 µM
4f	52% @ 50 µM	62% @ 50 µM	87% @ 50 µM
4g	k. I.	9% @ 10 µM	k. I.
5a	k. I.	48% @ 10 µM	38% @ 50 µM
5b	k. I.	45% @ 10 µM	38% @ 50 µM
7f	k. I.	k. I.	k. I.
8a	14% @ 50 µM	7,9 ± 0,6	9,5 ± 0,9
8b	19% @ 50 µM	10,8 ± 0,6	7,9 ± 0,5
8c	k. I.	55% @ 10 µM	64% @ 10 µM
8d	10% @ 10 µM	62% @ 10 µM	39% @ 50 µM
8e	17% @ 10 µM	54% @ 10 µM	66% @ 10 µM
8f	47% @ 100 µM	5,8 ± 0,7	9,4 ± 0,7
11	k. I.	k. I.	k. I.
12a	33% @ 100 µM	45% @ 100 µM	45% @ 100 µM
12b	k. I.	16% @ 10 µM	11% @ 10 µM
12c	k. I.	17% @ 10 µM	11% @ 10 µM
12d	k. I.	43% @ 100 µM	43% @ 100 µM
21d	k. I.	49% @ 10 µM	33% @ 10 µM
22	k. I.	k. I.	k. I.

Tabelle 3: Inhibitorische Aktivitäten bei gegebener Inhibitorkonzentration bzw. angegeben als IC_{50} (µM) gegenüber den humanen Sirtuin-Isotypen Sirt1–3 im thermischen Gleichgewicht (Δ) sowie im PSS nach Bestrahlung bei einer Wellenlänge von 365 nm.

Substanz	**Sirt1**		**Sirt2**		**Sirt3**	
	Δ	**PSS @ 365 nm**	Δ	**PSS @ 365 nm**	Δ	**PSS @ 365 nm**
9a	k. I.	k. I.	17% @ 10 µM	11% @ 10 µM	68% @ 100 µM	52% @ 100 µM
9b	k. I.	k. I.	30% @ 10 µM	4% @ 10 µM	80% @ 100 µM	52% @ 100 µM
9c	k. I.	k. I.	40% @ 10 µM	24% @ 10 µM	20% @ 10 µM	3% @ 10 µM
9d	k. I.	k. I.	44,0 ± 9,5	7,9 ± 0,7	u. I.	u. I.
9e	k. I.	k. I.	26% @ 10 µM	78% @ 10 µM	u. I.	u. I.
9f	k. I.	k. I.	46% @ 10 µM	65% @ 10 µM	u. I.	u. I.
9g	k. I.	k. I.	2,2 ± 0,3	0,9 ± 0,2	u. I.	u. I.
9h	k. I.	k. I.	27% @ 100 µM	52% @ 100 µM	k. I.	32% @ 100 µM
9i	k. I.	k. I.	15% @ 10 µM	15% @ 10 µM	k. I.	k. I.
9j	k. I.	k. I.	80% @ 100 µM	59% @ 100 µM	u. I.	u. I.
9k	k. I.	k. I.	43% @ 100 µM	71% @ 100 µM	k. I.	k. I.
16a	k. I.	7% @ 10 µM	6,0 ± 1,1	6,8 ± 0,4	42% @ 10 µM	45% @ 10 µM
16b	35% @ 100 µM	44% @ 100 µM	3,9 ± 0,2	6,9 ± 0,6	58% @ 10 µM	30% @ 10 µM
16c	k. I.	6% @ 10 µM	0,88 ± 0,06	2,8 ± 0,1	1,1 ± 0,2	4,0 ± 0,7
16d	35% @ 100 µM	19% @ 100 µM	18,9 ± 1,4	24,1 ± 1,7	27,5 ± 3,4	29,9 ± 2,1
16e	k. I.	47% @ 100 µM	7,5 ± 0,5	8,4 ± 0,9	8,2 ± 1,4	13,0 ± 2,2
16f	k. I.	10% @ 10 µM	51% @ 10 µM	61% @ 10 µM	54% @ 10 µM	49% @ 10 µM
16g	k. I.	k. I.	36,6 ± 9,3	1,6 ± 0,2	k. I.	k. I.
16h	60% @ 100 µM	54% @ 100 µM	7,2 ± 0,5	11,8 ± 1,0	64% @ 10 µM	22% @ 10 µM
16i	k. I.	k. I.	15,2 ± 1,8	37,5 ± 5,2	42% @ 10 µM	18% @ 10 µM
21a	k. I.	k. I.	0,70 ± 0,21	1,6 ± 0,2	23% @ 10 µM	24% @ 10 µM
21b	k. I.	k. I.	3,2 ± 0,5	6,4 ± 0,5	34% @ 10 µM	47% @ 10 µM
21c	45% @ 100 µM	62% @ 100 µM	u. I.	6,2 ± 0,5	u. I.	17,2 ± 1,57

2.3.2 Fluoreszenzpolarisations(FP)-basierter Bindungsassay

Ein Fluoreszenzpolarisations(FP)-basierter Bindungsassay auf Grundlage eines von SirReal2 (**VI**) abgeleiteten Fluorophors wurde verwendet, um die Bindungsstellen der Inhibitoren innerhalb des aktiven Zentrums von Sirt2 näher zu bestimmen.[180] Durchführung des Assays erfolgte in der Arbeitsgruppe von Prof. Dr. Manfred Jung an der Albert-Ludwigs-Universität Freiburg. Eine Inhibition von Sirt2 im FP-basierten Bindungsassay zeigt die Verdrängung der fluoreszenzmarkierten SirReal-Sonde an und deutet auf einen vergleichbaren Bindungsmodus des Inhibitors.

Tabelle 4: Sirt2-Aktivitätshemmung (ZMAL-Assay) bzw. Bindungshemmung (FP-Assay) bei gegebener Inhibitorkonzentration (%) bzw. angegeben als IC_{50} (µM).

Substanz	Konzentration [µM]	Sirt2-Aktivitätshemmung ZMAL-Assay [%/µM]	Sirt2-Bindungshemmung FP-Assay [%/µM]
X		24,6 ± 2,8	16,5 ± 3,5
4a	100	8,7 ± 0,2	61
	10		n. I.
4b	100	92	40
	10	62	21
8c	100	65	k. I.
	10	55	k. I.
8f	100	99	98
	10	64	46
9a	100	69	65
	10	21	3

2.3.3 Zell-basierter Aktivitätsassay

Die Durchführung des Zell-basierten Aktivitätsassays wurde in der Arbeitsgruppe von Prof. Dr. J. Bednarski an der Universität Greifswald durchgeführt. Die Untersuchung erfolgte an der Blasenkrebszelllinie RT-4, da diese unter den verfügbaren Zelllinien die stärkste Expression von Sirt2 aufwies. Die Ermittlung der Expressionsprofile bezüglich der humanen Sirtuine Sirt1–3 in verschiedenen Krebszelllinien ist Bestandteil von Manuskript IV. Die Zellen wurden mit den zu testenden Substanzen bei einer Konzentration von 50 µM für 24 h bei 37 °C und 5% CO_2 vorinkubiert und anschließend geerntet, durch Ultraschallbehandlung lysiert und die entsprechenden Proteine mittels Western-Blot analysiert. Zur Bestimmung der biologischen Aktivität dienten folgende zelluläre Target-Proteine: Die Histonproteine H3 und deren acetylierte Produkte H3K9Ac und H3K56Ac, H4 und H4K8Ac sowie acetyliertes und gesamtes α-Tubulin (K40Ac).

In vorläufigen Untersuchungen erfolgte eine Bestimmung der biologischen Aktivität lediglich für die Verbindungen **16c**, **16g** und **21a** nach vorheriger fünfminütiger Bestrahlung mit UV-Licht (λ = 365 nm). Keine der drei Verbindungen beeinflusste die Gesamtmenge an Histon H3 bzw. α-Tubulin, jedoch zeigte sich jeweils eine schwache Zunahme an Histon H4. Die

24-stündige Exposition von RT-4 Zellen mit **16c** und **16g** führte zu einer Hyperacetylierung der Histone H3 (H3K9Ac und H3K56Ac) sowie H4 (H4K8Ac). Im Gegensatz dazu hatte keine der Verbindungen einen Einfluss auf den Acetylierungsgrad von α-Tubulin. Eine biologische Aktivität von **21a** konnte im zellbasierten Assay nicht nachgewiesen werden (Manuskript III).

2.3.4 Kombinationseffekte mit verschiedenen Zytostatika

Der Einfluss einiger dargestellter Verbindungen (**4a**, **8a**, **8b**, **8e**, **8f**, **9g** und **9h**) auf die zytotoxische Wirkung der etablierten Zytostatika Cisplatin, Lomustin und Topotecan wurde in der Arbeitsgruppe von Prof. Patrick J. Bednarski an der Universität Greifswald untersucht. Als Maß der Zytotoxizität diente die in einem Kristallviolett-Assay gemessene Proliferationsinhibition (ausgedrückt als IC_{50}) von SiSo-Zellen (Cervixkarzinom-Zelllinie). Zunächst wurde die zytotoxische Konzentration für jeden einzelnen Inhibitor bestimmt. Anschließend erfolgte eine Bestimmung der IC_{50} der Zytostatika in Kombination mit den jeweiligen Inhibitor-Konzentrationen, die selbst keine Hemmung der Proliferation in der Zelllinie zeigte. Der Quotient aus den IC_{50}-Werten unter Kombination (Inhibitor + Zytostatikum) und der Kontrolle (Zytostatikum alleine) ergab schließlich den Kombinationseffekt CIC (Manuskript IV).

Verbindung **8a** besaß als einzige der getesteten Sirtuin-Inhibitoren einen messbaren Einfluss auf die Proliferation von SiSo-Zellen (IC_{50} = 10,8 µM). Die restlichen Inhibitoren zeigten unterhalb einer Konzentration von 100 µM keine zytotoxische Wirkung. Die Kombinationsstudien erfolgten daher für **8a** bei einer Konzentration von 5 µM, für **4a**, **8b**, **8e**, **8f**, **9g** und **9h** hingegen bei einer Konzentration von 50 µM.

Die Verbindungen **4a**, **8b** und **8f** steigerten die zytotoxische Wirkung von Cisplatin als auch von Lomustin signifikant um näherungsweise 100% (Cisplatin: CIC = 0,43, 0,61 bzw. 0,57; Lomustin: CIC = 0,50, 0,47 bzw. 0,59). Im Falle von Topotecan zeigte sich in Kombination mit allen getesteten Inhibitoren außer **9g** eine gesteigerte Zytotoxizität (CIC: 0,52–0,79).

3 Diskussion

Photoschaltbare Sirtuin-Inhibitoren stellen interessante Werkzeuge für die weitere Erforschung der Sirtuin-Biochemie dar und könnten beispielsweise als hochselektive Zytostatika mit geringen Nebenwirkungen in der Krebstherapie Verwendung finden. Dementsprechend besteht an deren Erforschung und Entwicklung ein großes Interesse. So wurden auf diesem Gebiet bereits bedeutende Fortschritte durch König *et al.* erzielt: Auf Grundlage der Leitstruktur Ro31-8220 (**VII**) wurden photochrome Diarylmaleimide und Indolylfulgide dargestellt, die unter Bestrahlung teilweise reversible intramolekulare Photozyklisierungsreaktionen eingingen.[192,193] Insbesondere im Falle der Indolylfulgide konnte ein reversibler, lichtabhängiger Einfluss der Photozyklisierung auf die Deacetylase-Aktivität von Sirt2 nachgewiesen werden. Violettes Licht (λ = 400 nm) führte zur Bildung der „geschlossenen“ Form, welche eine mindestens 17-fach reduzierte inhibitorische Aktivität aufwies im Gegensatz zu der „offenen“ Form (geschlossen: IC_{50} = 30 µM; offen: IC_{50} > 500 µM). Die Reaktion ließ sich unter grünem Licht (λ = 590 nm) umkehren.

Im Kontrast zu den oben genannten Verbindungen, deren Affinitätsunterschiede im Wesentlichen durch eine veränderte Molekülflexibilität hervorgerufen wird, dienen bei allen in dieser Arbeit beschriebenen Verbindungen die *E*/*Z*-Photoisomerisierung von Doppelbindungen und die damit einhergehenden Veränderungen der Molekülgeometrie und Polarität als zugrundeliegendes Prinzip des molekularen Photoschalters.

3.1 Styrylpyridine als molekulare Photoschalter

Eine *E/Z*-Photoisomerisierung von C,C-Doppelbindungen findet in verschiedenen synthetischen als auch natürlichen Photoschaltern statt. Dazu zählen beispielsweise das Carotinoid Retinal, welches im Sehprozess an der Übersetzung von Lichtreizen in elektrochemische Signale beteiligt ist oder synthetische, sterisch überfrachtete Alkene in sogenannten „molekularen Motoren“.[194,195] Die Untersuchung des photochemischen Verhaltens der dargestellten Styrylpyridine wird in Manuskript I behandelt. Es zeigten sich bedeutende Nachteile in ihrem Gebrauch als molekulare Photoschalter. Dazu zählen die Bildung photochemischer Nebenprodukte, die Irreversibilität der *E*→*Z*-Photoisomerisierung sowie die vergleichsweise geringen Polaritätsunterschiede der Photoisomere. Die Bildung von Nebenprodukten unter Bestrahlung führt in erster Linie zu einem schleichenden Verlust der photochromen Eigenschaften der Verbindung. Ferner gehen auch von den entstandenen Nebenprodukten unvorhergesehene und potentiell toxische Wirkungen aus. Auch wenn die Bildung von Nebenprodukten durch geeignete Substitution des Styrylpyridin-Kerns weitestgehend verhindert werden konnte (vgl. 2.1.1, Verbindung **4e**), ließ sich die *E*→*Z*-Photoisomerisierung nicht umkehren. Beide Photoisomere unterschieden sich nur geringfügig in ihrem Absorptionsverhalten und besaßen im UV/Vis-Bereich jeweils nur ein Absorptionsmaximum, das in Lage und Extinktion nahezu identisch war. Eine selektive Anregung nur eines der beiden Photoisomere war mit den vorhandenen Instrumenten daher nicht realisierbar. Unter Bestrahlung (λ = 254 nm) kam es daher zur

Einstellung eines PSS mit nahezu gleichmäßiger Verteilung der Photoisomere.[196] Die thermische *Z*→*E*-Isomerisierung ist wiederum aufgrund der hohen Aktivierungsenergie bei Raumtemperatur zu vernachlässigen.[48] Zwar wurde berichtet, dass eine reversible *E*/*Z*-Photoisomerisierung von Stilbenen durch Derivatisierung zu Cyanostilbenen ermöglicht wird. Allerdings ist auch bei dieser Substanzklasse die Effektivität der Photoisomerisierung gering und eine Verwendung in biologischen Systemen eher ungeeignet.[197,198] Die in den HPLC-Untersuchungen beobachteten Retentionszeiten der *E*- bzw. *Z*-Styrylpyridine lassen weiterhin auf geringe Polaritätsunterschiede zwischen den Photoisomeren schließen. Bei einer Verwendung als photochrome Liganden könnte sich dies nachteilig auf die Affinitätsunterschiede der Photoisomere auswirken. Der Stytylpyridin-Kern stellte sich daher als ungeeignet für die Entwicklung photochromer Sirtuin-Inhibitoren heraus. Nach dem Azologisierungsprinzip sollte sich **IX** jedoch in einen Azofarbstoff mit vergleichbarer biologischer Aktivität umwandeln lassen. Die Synthese und Untersuchung der entsprechenden Verbindungen ist in Manuskript III beschrieben.

3.2 Konkurrierende Bildung von Nebenprodukten

Obwohl die dargestellten Styrylpyridine nicht als reversibel photoschaltbare Sirtuin-Inhibitoren eingesetzt werden konnten, war das durch Bestrahlung von **4a** gebildete Nebenprodukt **22** aus mehreren Gründen eine interessante Verbindung. Abgesehen von der allgemeinen Bedeutung von Chinolinen[199,200] und Benzochinolinen[201,202] als Strukturmotive in Natur- und Arzneistoffen, besaß **22** eine starke strukturelle Ähnlichkeit zum hochpotenten Sirt1-Inhibitor Selisistat (**I**). Es wurde daher eine entsprechende Aktivität der Verbindung gegenüber Sirt1 vermutet. Tatsächlich ließ sich für **22** jedoch an keinem der Klasse I-Sirtuine eine inhibitorische Aktivität nachweisen (Manuskript I). Ursachen dafür könnten neben der nicht vollständig deckungsgleichen Anordnung des kondensierten Ringsystems außerdem eine ungünstige Orientierung der Carboxamid-Gruppe sein: Eine Röntgenstrukturanalyse enthüllte **22** im Gegensatz zu **I** als vollständig planares Molekül. Eine detaillierte Analyse der Kristallstruktur wurde in Manuskript II veröffentlicht. In der Kristallstruktur von Verbindung **22** deutete eine außergewöhnlich lange Carbonylbindung auf eine Beteiligung der Gruppe am aromatischen Resonanzsystem hin. Dies legt nahe, dass die Carboxamid-Gruppe auch in Lösung nur eine eingeschränkte Rotationsfreiheit besitzt. Im Falle von **I** scheint die Orientierung der Carboxamid-Gruppe jedoch von essentieller Bedeutung für die Affinität zu Sirt1 zu sein: In einer Kristallstruktur von Sirt1, NAD^+ und einem Analogon der Verbindung **I** ist die Carbonylgruppe des Carboxamids rechtwinklig zur Indol-Ebene orientiert und bildet zwei Wasserstoffbrücken zu einer Asparaginsäureseitenkette im Inneren des aktiven Zentrums.[203] Das vorhandene Stereozentrum bestimmt weiterhin, auf welcher Seite der Indol-Ebene sich die Carboxamid Gruppe befindet, wobei nur das *S*-Enantiomer biologische Aktivität besitzt.[204] Folglich bestehen trotz der augenscheinlichen Ähnlichkeit von **22** mit **I** bedeutende strukturelle Unterschiede zwischen diesen beiden Verbindungen.

Die Tatsache, dass **22** im Gegensatz zu **4a** keine biologische Aktivität besaß, stützte allerdings die Annahme, dass sich Styrylpyridine bzw. analoge Azofarbstoffe durch *E*→*Z*-Photoisomerisierung von einer aktiven in eine inaktive Form überführen lassen. Bei dieser Hypothese muss allerdings berücksichtigt werden, dass ein Vergleich von **22** mit einem *Z*-Stilben als sehr vage gilt, da die Ringebenen der *Z*-Stilbene und *Z*-Azobenzene nicht koplanar, sondern zueinander verdreht vorliegen.[16,46,47]

3.3 Azofarbstoffe als molekulare Photoschalter

Dem Azologisierungsprinzip entsprechend, führte ein Austauschen der Stilben-C,C-Doppelbindung in Leitstruktur **IX** durch eine N,N-Doppelbindung zu heteroaromatischen Analoga des häufig in photochromen Liganden verwendeten Azobenzen-Photoschalters. Zusätzlich wurden durch Ersatz der *N*-Phenylamidbindungen in den Leitstrukturen **III**–**VI** auch Azobenzen-Photoschalter (ohne Heteroaromat) dargestellt. Die Beschreibung der photochemischen und photophysikalischen Eigenschaften ist Teil sowohl von Manuskript I als auch Manuskript III.

Verglichen mit den Azobenzen-Photoschaltern sind die heteroaromatischen Abkömmlinge bisher wenig erforscht.[14] Tatsächlich bieten heteroaromatische Azofarbstoffe jedoch verschiedene Vorteile: Zunächst erweitert sich der chemische Spielraum wesentlich unter Verwendung heteroaromatischer Strukturmotive. Besonders für die Entwicklung photochromer Arzneistoffe sind heteroaromatische Komponenten unverzichtbar. Darüber hinaus verbessern sich durch deren Einsatz die pharmakokinetischen Eigenschaften der oft stark lipophilen Azobenzen-Photoschalter. Schließlich gewähren Heteroaromaten, in Ergänzung zu den bereits erwähnten Substituenteneffekten (vgl. 1.1.2), eine weitere Einflussmöglichkeit auf die photophysikalischen Eigenschaften des Photoschalters.[14]

Als Photoschalter unterscheiden sich die dargestellten Azofarbstoffe zunächst in der thermischen Stabilität ihrer PSS. So trat in polaren Lösungsmitteln (DMSO/H_2O) nach Bestrahlung der Verbindungen **8a**–**f**, **12a**–**d** und **21d** eine schnelle, thermische Isomerisierung des *Z*-Isomers auf, wohingegen die Verbindungen **9a**–**k**, **16a**–**i** sowie **21a**–**c** metastabile *Z*-Isomere mit Halbwertszeiten im Bereich von etwa einer bis mehreren hundert Stunden aufwiesen (vgl. Tabelle 1). Die Geschwindigkeit der thermischen *Z*→*E*-Isomerisierung spielt eine zentrale Rolle für die Kompatibilität des Photoschalters zur jeweiligen Verwendung.[181] So können kurzlebige PSS zur Modulation schnell ablaufender Prozesse wie beispielsweise der neuronalen Signalerzeugung und -weiterleitung von Vorteil sein. Hingegen sind Photoschalter mit langlebigen PSS bei der Modulation „langsamer“ Prozesse wie etwa des Stoffwechsels in den meisten Fällen gebräuchlicher, da so keine dauerhafte Bestrahlung notwendig ist, um den Photoschalter im jeweiligen PSS zu halten.

Eine große Bedeutung kommt auch der PSD zu. Diese drückt aus, wie effizient die Photoisomerisierung unter Bestrahlung verläuft. Optimalerweise lässt sich ein Photoschalter unter Bestrahlung mit einer bestimmten Wellenlänge vollständig von einem

Photoisomer in das andere umwandeln. Welchen Anteil die Photoisomere am jeweiligen PSS haben, wird durch die relative Lage ihrer Absorptionsmaxima sowie deren Extinktion bestimmt. Eine vollständige Umwandlung von einem Photoisomer in das andere wird beobachtet, wenn eines der Photoisomere bei einer bestimmten Wellenlänge möglichst stark absorbiert, wohingegen das andere Isomer für Strahlung dieser Wellenlänge transparent ist.[181] Daraus ergibt sich, dass nur ein Isomer selektiv zur Photoisomerisierung angeregt wird.[205,206] Der Großteil der in dieser Arbeit dargestellten Azofarbstoffe zeigte hohe prozentuale Anteile eines der beiden Photoisomere in den PSS nach Bestrahlung mit Strahlung der Wellenlänge 365 nm bzw. 452 nm (vgl. Tabelle 1). Bei lediglich fünf Verbindungen (**9j**, **16a**, **16f**, **16h** und **16i**) lag der Anteil des *E*-Isomers am PSS nach Bestrahlung mit UV-Strahlung bei 365 nm über 15%. Auf der anderen Seite lieferte eine Bestrahlung mit blauem Licht (452 nm) eine PSD mit durchschnittlich 88%iger Beteiligung des *E*-Isomers. Im Allgemeinen erzielt eine effiziente Photoisomerisierung deutliche Effekte, vorausgesetzt die Photoisomere unterscheiden sich zusätzlich auch in ihrer Affinität zum Target. Allerdings kann aufgrund der meist nicht-linearen Beziehungen zwischen Dosis und Effekt auch die Photoisomerisierung eines Photoschalters mit geringen Unterschieden in der PSD zu Unterschieden in der Target-Aktivität führen. Dies trifft insbesondere im Falle steiler sigmoidaler Konzentrations-Wirkungs-Beziehungen zu.[6]

Viele Azofarbstoffe besitzen in der thermodynamisch stabileren *E*-Konfiguration eine ausgeprägte Lipophilie, die besonders bei der Entwicklung photochromer Arzneistoffe häufig zu Problemen führt.[181,207] Bei einem Großteil der dargestellten Azofarbstoffe löste die geringe Polarität des jeweiligen *E*-Isomers eine Aggregation der Verbindungen unter den Lösungsmittelbedingungen des Enzymassays (5% DMSO in H_2O) aus. Da durch Aggregation auch die Photoisomerisierung der Verbindungen gehemmt wurde, musste der DMSO-Anteil in diesen Fällen zur Untersuchung der photochemischen Eigenschaften erhöht werden. Es kann daher nicht davon ausgegangen werden, dass die in Tabelle 1 angegebenen Parameter auf die Situation im Enzymassay zutrifft. Allerdings ließ sich so eine Abschätzung des Verhaltens der Verbindungen in Anwesenheit von Wasser treffen. Tatsächlich ließen sich von den in Tabelle 1 aufgeführten Verbindungen lediglich **9a**, **9b** sowie **16c–e** unter den Lösungsmittelverhältnissen des Enzymassays photoisomerisieren. Das zusätzliche Einfügen polarer Gruppen war hingegen u. a. aufgrund der geringen thermischen Stabilität der PSS der resultierenden Substanzen nicht möglich (siehe Verbindungen **8a–f**, **12a–d**, **21d**).

3.4 Optimierung der inhibitorischen Aktivität

Anhand einer kleinen Bibliothek verschiedener Analoga der Leitstruktur **X** sollte der Einfluss unterschiedlicher Substituenten auf die inhibitorische Aktivität und Selektivität der Verbindungen untersucht werden. Sie werden in Manuskript I beschrieben. Einige der dort veröffentlichten Styrylpyridine besaßen insbesondere gegenüber den Sirtuinen Sirt2 und Sirt3 eine verbesserte inhibitorische Aktivität mit einem IC_{50}-Wert im einstelligen mikromolaren Konzentrationsbereich. Eine Isoenzym-selektive Inhibition wurde jedoch nicht erreicht. Tatsächlich verschlechterte sich das Selektivitätsprofil im Vergleich zur Leitstruktur sogar. So zeigten insbesondere **4a–c** auch eine deutliche Aktivität gegenüber Sirt1. Der FP-basierte Bindungsassay deutete außerdem an, dass die Verbindungen **4a** und **4b** gegenüber Sirt2 einen von der Leitstruktur **IX** abweichenden Bindungsmodus aufwiesen. Interessanterweise ließ sich die Selektivität der Verbindungen durch eine Rigidisierung der Stilben-Doppelbindung verbessern. Die entsprechenden Verbindungen **5a** und **5b** zeigten im Gegensatz zu **4a** keine Aktivität gegenüber Sirt1 und verloren auch gegenüber Sirt3 an Wirkung. Auf die Synthese weiterer Styrylpyridine wurde jedoch angesichts der geringen Eignung dieser Substanzgruppe als molekulare Photoschalter verzichtet. Eine weitere Optimierung der biologischen Aktivität erfolgte an den entsprechenden Azofarbstoff-Derivaten der Leitstruktur **IX**. Sie wird in Manuskript III beschrieben.

Im direkten Azo-Analogon **8a** blieb das Selektivitätsprofil der Leitstruktur **IX** erhalten. Die inhibitorische Aktivität stieg sogar durch den Austausch der C,C-Doppelbindung in den einstelligen mikromolaren Bereich. Das Azologisierungsprinzip ließ sich daher erfolgreich auf **IX** anwenden. Aufgrund der Nicotinamid-Teilstruktur lag die Vermutung nahe, dass die Verbindungen **8a–f** wie Nicotinamid selbst an die C-Site des aktiven Zentrums der Sirtuine binden. Zusätzlich erhärtete sich dieser Verdacht durch die Verbindungen **12a–d**, da eine Derivatisierung der primären Amidgruppe des Nicotinamids zu einer drastischen Abnahme der Aktivität führte. Da die C-Site innerhalb des hochkonservierten aktiven Zentrums der Sirtuine liegt, war es nicht überraschend, dass die geringen strukturellen Unterschiede zwischen den Verbindungen **8a–f** keinen wesentlichen Einfluss auf das Selektivitätsprofil der Inhibition nahmen. Die Präferenz für die Isoenzyme Sirt2 und Sirt3 im Vergleich zu Sirt1 lässt sich hingegen durch deren phylogenetischen Verwandtschaftsgrad erklären (Sirt1: Klasse Ia; Sirt2 und Sirt3: Klasse Ib).[60] So sind die Sequenzhomologien zwischen Sirt2 und Sirt3 stärker ausgeprägt als im Vergleich zu Sirt1. Die Bindung an Sirt2 wurde im Falle der Verbindungen **8f** und **9a** jedoch nicht in der C-Site, sondern in der Nähe der Selectivity Pocket lokalisiert (vgl. Tabelle 4). Da diese Tasche zur Aufnahme langer Fettsäureketten dient, wurden entsprechende Derivate der Verbindungen **8f** bzw. **9a** synthetisiert, um Wechselwirkungen mit dieser Sirt2-spezifischen Tasche zu etablieren. Wie erwartet, verursachte das Anfügen langer Fettsäureketten eine hochselektive Sirt2-Inhibition (**16g**). Die ausgeprägte Lipophilie der Verbindungen führte allerdings auch zu unspezifischen Wechselwirkungen insbesondere mit Sirt3. Weiterhin kann davon ausgegangen werden, dass die effektive Konzentration derartig lipophiler Verbindungen in wässriger Umgebung aufgrund von Aggregation bzw. Präzipitation wesentlich geringer ist, sodass die Verbindungen tatsächlich eine höhere Affinität zu Sirt2 aufweisen sollten, als aus den berechneten IC_{50}-Werten hervorgeht. Diese Vermutung bestätigte sich durch den Einfluss der *E*→*Z*-Photoisomerisierung auf die inhibitorische Aktivität (vgl. 3.5).

Im Falle der Leitstruktur **V** ließ sich das Azologisierungsprinzip weniger erfolgreich anwenden. Dies spiegelte sich in den deutlichen Unterschieden zwischen den IC_{50}-Werten der publizierten 5-Amidobenzylnicotinamide **III–VI** (vgl. 1.2.4) und denen ihrer analogen

Azo-Derivate **21a–d** wieder. Zwar muss berücksichtigt werden, dass die Aktivitätsbestimmung von **III–VI** nicht unter Verwendung desselben Enzymassays erfolgte, allerdings lassen sich derart große Abweichungen dadurch nicht ausreichend erklären. Eine mögliche Ursache zeichnete sich an Verbindung **21d** ab. Offensichtlich kam es aufgrund der geringen Löslichkeit der Verbindungen zu unspezifischen Wechselwirkungen mit den Enzymen Sirt2 und Sirt3. Es ist daher sehr wahrscheinlich, dass der Austausch der Amidbindung in **V** durch die Azogruppe in **21c** zu einer erheblichen Reduktion der Wasserlöslichkeit führte und dementsprechend, wie bereits bei **16g** und anderen lipophilen Verbindungen beobachtet, in wässriger Umgebung eine geringere effektive Konzentration vorherrscht, was wiederum zu einer verminderten biologischen Aktivität führt.

3.5 Einfluss der Photoisomerisierung auf die biologische Aktivität

Die unter Tabelle 3 dargestellten IC_{50}-Werte der verschiedenen Inhibitoren im thermischen Gleichgewicht bzw. PSS nach Bestrahlung (λ_{max}=365 nm) müssen mit Blick auf die Lipophilie der Substanzen interpretiert werden. So zeigen sich die größten Affinitätsunterschiede bei jenen Substanzen, die aufgrund langer Alkylketten eine besonders hohe Lipophilie aufweisen. Dazu zählen insbesondere die Verbindungen **9d** und **16g**. Durch Bestrahlung stieg deren inhibitorische Aktivität um das 6- bzw. 23-Fache. Interessanterweise zeigte sich eine Zunahme der inhibitorischen Aktivität durch *E*→*Z*-Photoisomerisierung ausschließlich bei Verbindungen mit eindeutig lipophilen Eigenschaften (**9d–h**, **9k**, **16g**, **21c**). Eine Erklärung liefert die höhere Polarität des *Z*-Isomers und eine damit einhergehende bessere Löslichkeit in polaren Medien: Wird ein lipophiler Azofarbstoff vor Zugabe in das wässrige Medium in sein *Z*-Isomer überführt, so ist der Anteil an gelöster bzw. nicht aggregierter Substanz höher, was folglich zu einer höheren biologischen Aktivität führt. Sobald die Verbindung allerdings wieder zur *E*-Form isomerisiert, ob thermisch oder photochemisch induziert, kommt es zur Bildung inaktiver Aggregate, die keine erneute Aktivierung erlauben. Die geringe Löslichkeit einiger Verbindungen führte insbesondere bei Sirt3 zu unspezifischen Wechselwirkungen. Im Falle von **21c** ließ sich dies durch eine vorherige Bestrahlung verhindern. Obwohl es sich hierbei um ein interessantes Phänomen mit potentieller Bedeutung für die Verabreichung unpolarer Arzneistoffe handelt, entspricht es offensichtlich nicht dem Sinn eines reversibel steuerbaren Sirtuin-Photoschalters. Die Verbindungen **9a**, **9b** sowie **16c–e** bildeten unter den Lösungsmittelbedingungen des Enzymassays keine Aggregate. Allerdings unterschieden sich die biologischen Aktivitäten der Photoisomere in diesen Fällen nur wenig. Die Verbindung **16c** repräsentierte in dieser Hinsicht das Maximum mit einer Verringerung des IC_{50}-Wertes um das Dreifache. Obwohl inzwischen einige photochrome Liganden 10–50-fache Aktivitätsunterschiede aufweisen, sind schwächer ausgeprägte IC_{50}-Verhältnisse eher die Regel.[206] Ausgedehnte SAR-Studien und genaue Kenntnisse über den Bindungsmodus der Substanzen können hilfreich sein, um hinsichtlich des IC_{50}-Verhältnisses zwischen den Photoisomeren bessere Ergebnisse zu erzielen.[181,208,209]

3.6 Therapeutisches Potential der dargestellten Inhibitoren

Eine Verwendung der synthetisierten Verbindungen als Sirtuin-Photoschalter *in vivo* ist aus verschiedenen Gründen nicht möglich. Die zur *E*→*Z*-Photoisomerisierung benötigte UV-Strahlung stellt dabei eine wesentliche Ursache dar. Um physiologisch kompatibel zu sein, sollte sich der Photoschalter mittels Wellenlängen anregen lassen, die keine toxische Wirkung auf zelluläre Strukturen haben. Bekannterweise kann UV-Strahlung jedoch zur Schädigung von Geweben führen und aufgrund seiner kanzerogenen Wirkung die Entstehung von Karzinomen begünstigen.[210] Weiterhin sollte die verwendete Strahlung eine ausreichende Gewebepenetration aufweisen, um bis zu dem Krankheitsherd vorzudringen. Insbesondere bei Strahlung im UV- oder hochfrequenten, sichtbaren Spektralbereich kommt es zu einer starken Streuung und Absorption durch endogene Chromophore.[211] Im Wellenlängenbereich von 350–650 nm besitzt rotes Licht ($\lambda = 350$ nm) mit 4–5 mm die größte Penetrationstiefe. UV-Licht ($\lambda = 350$ nm) zeigt hingegen nahezu keine Gewebepenetration.[212] Allerdings könnten tiefere Gewebeschichten oder innere Körperoberflächen auch durch alternative Lichtzuführungsmethoden wie Endoskope oder faseroptische Instrumente erreicht werden.[211,213–216] Weiterhin ließe sich durch eine geeignete Derivatisierung des Azofarbstoffes die Anregungswellenlänge vom UV- in den niederfrequenten sichtbaren Spektralbereich bzw. den IR-Bereich verschieben, wie es bereits anhand verschiedener Verbindungen beschrieben wurde.[217–219] Einen bedeutenderen Nachteil stellt hingegen die geringe Löslichkeit der Verbindungen dar. Insbesondere die Notwendigkeit langer Alkylketten für eine selektive Inhibition von Sirt2 gestaltet eine Optimierung hin zu hydrophileren Derivaten ausgesprochen schwierig. Bei hydrophileren Derivaten war hingegen das Verhältnis zwischen den IC_{50}-Werten der Photoisomere schwach ausgeprägt, sodass eine Photoisomerisierung *in vivo* vermutlich zu keinen erkennbaren Effekten führen würde.

Dennoch wurden selektive und aktive Substanzen erhalten, die sich jenseits einer Verwendung als photochrome Liganden zur Inhibition von Sirtuinen *in vivo* eignen. So wurde für die Verbindungen **16c** und **16g** eine biologische Aktivität gegenüber der Blasenkrebszelllinie RT-4 nachgewiesen (Manuskript III). Eine vorherige *E*→*Z*-Photoisomerisierung wurde durchgeführt, um die Wasserlöslichkeit der Verbindung **16g** zu steigern. Da bisher keine Untersuchungen im thermischen Gleichgewicht durchgeführt wurden, kann der Einfluss der Photoisomerisierung auf die biologische Aktivität im Zell-basierten Aktivitätsassay nicht diskutiert werden. Aufgrund ihres Selektivitätsprofils wurde für **16c** und **16g** eine Hyperacetylierung von Sirt2- bzw. Sirt3-spezifischen Substraten erwartet. Dazu zählen die acetylierten Histonproteine H4K16Ac sowie u. a. H3K9, H3K56 und spezifisch für Sirt2 das cytosolische α-Tubulin (K40Ac).[65,81,82,220–223] Tatsächlich ließ sich eine Hyperacetylierung von H3K9 und H3K56 nachweisen. Daraus lässt sich zunächst ableiten, dass **16c** und **16g** zellgängig sind. Im Gegensatz dazu zeigte Verbindung **21a** trotz einer hohen Aktivität im ZMAL-Assay keine Aktivität im Zell-basierten Assay, sodass vermutet werden kann, dass diese Substanz ihren Wirkort im Inneren der Zelle nicht erreicht. Weiterhin wurde eine Hyperacetylierung von H4K8 beobachtet, wohingegen

H4K16 und α-Tubulin von **16c** und **16g** unbeeinflusst blieben. Auch bei einigen hochpotenten und Sirt2-selektiven SirReals konnte durch Western-Blot-Technik eine Hyperacetylierung von α-Tubulin nicht nachgewiesen werden.[156] Allerdings legt die Hyperacetylierung von H4K8 die Vermutung nahe, dass **16c** und **16g** einen zusätzlichen oder alternativen Wirkmechanismus innerhalb der Zelle haben, da bisher nicht von einem Einfluss der Sirtuine auf Lysin 8 in Histon H4 berichtet wurde. Angesichts der Tatsache, dass die Verbindungen **16c** und **16g** auf Basis des schwach aktiven C-RAF-Kinaseinhibitors **IX** entwickelt wurden, ist ein zusätzlicher Wirkmechanismus nicht unwahrscheinlich. Eine Wechselwirkung mit C-RAF oder anderen Kinasen wurde bisher allerdings nicht untersucht.

Eine vielversprechende Eigenschaft mit potentiell therapeutischem Nutzen war der verstärkende Effekt einiger Verbindungen auf die Zytotoxizität der Zytostatika Cisplatin, Lomustin und Topotecan (Manuskript IV). Offensichtlich hatten insbesondere die Verbindungen **4a**, **8a** und **8f** eine proapoptotische Wirkung auf die untersuchte SiSo-Zelllinie. Unter zytotoxischem Stress, ausgelöst durch die oben genannten Zytostatika, kam es daher bereits bei nicht-toxischen Konzentrationen der Zytostatika zur Auslösung des programmierten Zelltods. Angesichts der mangelnden Target-Selektivität der untersuchten Inhibitoren lässt sich diese proapoptotische Wirkung sehr wahrscheinlich nicht auf einen bestimmten Wirkmechanismus zurückführen. Allerdings ist bekannt, dass auch die Inhibition bestimmter Sirtuin-Isotypen einen proapoptotischen Effekt auf die Zelle haben kann (vgl. 1.2.1).[90–93,95]

Es bestehen einige nicht unberechtigte Vorbehalte, was den Gebrauch von Azofarbstoffen in der medizinischen Therapie betrifft. So besitzen einige Azofarbstoffe, wie beispielsweise Methylgelb, Anilingelb sowie Sudan I, III und IV nachgewiesenermaßen ein starkes karzinogenes Potential.[224] Einige Azofarbstoffe werden außerdem durch bakterielle Azoreduktasen der Darmflora zu toxischen aromatischen Aminen metabolisiert.[225] Allerdings finden sich auch einige zugelassene Arzneistoffe wie Sulfasalazin, Phenazopyridin oder Sulfamidochrysoidin unter den bekannten Azofarbstoffen, sodass nicht auf eine generelle Toxizität dieser Verbindungsklasse geschlossen werden darf.[181]

4 Literaturverzeichnis

(1) Brieke, C.; Rohrbach, F.; Gottschalk, A.; Mayer, G.; Heckel, A. Light-controlled tools. *Angew. Chem. Int. Ed.* **2012**, *51*, 8446–8476.

(2) Brieke, C.; Rohrbach, F.; Gottschalk, A.; Mayer, G.; Heckel, A. Lichtgesteuerte Werkzeuge. *Angew. Chem.* **2012**, *124*, 8572–8604.

(3) Szymański, W.; Beierle, J. M.; Kistemaker, H. A. V.; Velema, W. A.; Feringa, B. L. Reversible photocontrol of biological systems by the incorporation of molecular photoswitches. *Chem. Rev.* **2013**, *113*, 6114–6178.

(4) Young, D. D.; Deiters, A. Photochemical control of biological processes. *Org. Biomol. Chem.* **2007**, *5*, 999–1005.

(5) Deiters, A. Principles and applications of the photochemical control of cellular processes. *ChemBioChem* **2010**, *11*, 47–53.

(6) Velema, W. A.; Szymanski, W.; Feringa, B. L. Photopharmacology: beyond proof of principle. *J. Am. Chem. Soc.* **2014**, *136*, 2178–2191.

(7) Feringa, B. L.; Browne, W. R.: *Molecular switches*; Wiley-VCH-Verl.: Weinheim, 2011.

(8) Nishimura, N.; Sueyoshi, T.; Yamanaka, H.; Imai, E.; Yamamoto, S.; Hasegawa, S. Thermal Cis -to- Trans Isomerization of Substituted Azobenzenes II. Substituent and Solvent Effects. *Bull. Chem. Soc. Jpn.* **1976**, *49*, 1381–1387.

(9) Talaty, E. R.; Fargo, J. C. Thermal cis–trans-isomerization of substituted azobenzenes: a correction of the literature. *Chem. Commun. (London)* **1967**, *0*, 65–66.

(10) Lerch, M. M.; Hansen, M. J.; van Dam, G. M.; Szymanski, W.; Feringa, B. L. Emerging Targets in Photopharmacology. *Angew. Chem. Int. Ed.* **2016**, *55*, 10978–10999.

(11) Lerch, M. M.; Hansen, M. J.; van Dam, G. M.; Szymanski, W.; Feringa, B. L. Neue Ziele für die Photopharmakologie. *Angew. Chem.* **2016**, *128*, 11140–11163.

(12) Cheng, H.; Yoon, J.; Tian, H. Recent advances in the use of photochromic dyes for photocontrol in biomedicine. *Coord. Chem. Rev.* **2018**, *372*, 66–84.

(13) Cameron, D.; Eisler, S. Photoswitchable double bonds: Synthetic strategies for tunability and versatility. *J. Phys. Org. Chem.* **2018**, *31*, e3858.

(14) Crespi, S.; Simeth, N. A.; König, B. Heteroaryl azo dyes as molecular photoswitches. *Nat. Rev. Chem.* **2019**, *3*, 133–146.

(15) García-Iriepa, C.; Marazzi, M.; Frutos, L. M.; Sampedro, D. *E*/*Z* photochemical switches: syntheses, properties and applications. *RSC Adv.* **2013**, *3*, 6241.

(16) Duarte, L.; Fausto, R.; Reva, I. Structural and spectroscopic characterization of *E*- and *Z*-isomers of azobenzene. *Phys. Chem. Chem. Phys.* **2014**, *16*, 16919–16930.

(17) Hartley, G. S.; Le Fèvre, R. J. W. 119. The dipole moments of *cis*- and *trans*-azobenzenes and of some related compounds. *J. Chem. Soc.* **1939**, *0*, 531–535.

(18) Lenci, F.; Horspool, W. *CRC Handbook of Organic Photochemistry and Photobiology, Volumes 1 & 2,* CRC Press, 2003.

(19) Lin, S. H.; Villaeys, A. A.; Fujimura, Y. *Adv. Multi-Photon Processes Spectrosc.* **2004**, *16*.

(20) Hamm, P.; Ohline, S. M.; Zinth, W. Vibrational cooling after ultrafast photoisomerization of azobenzene measured by femtosecond infrared spectroscopy. *J. Chem. Phys.* **1997**, *106*, 519–529.

(21) Dürr, H.; Bouas-Laurent, H., Eds. *Photochromism: Molecules and systems*; Elsevier: Amsterdam, **2006**.

(22) Forber, C. L.; Kelusky, E. C.; Bunce, N. J.; Zerner, M. C. Electronic spectra of *cis*- and *trans*-azobenzenes: consequences of *ortho* substitution. *J. Am. Chem. Soc.* **1985**, *107*, 5884–5890.

(23) Bandara, H. M. D.; Burdette, S. C. Photoisomerization in different classes of azobenzene. *Chem. Soc. Rev.* **2012**, *41*, 1809–1825.

(24) Cusati, T.; Granucci, G.; Persico, M.; Spighi, G. Oscillator strength and polarization of the forbidden n-pi* band of *trans*-azobenzene: a computational study. *J. Chem. Phys.* **2008**, *128*, 194312.

(25) Bortolus, P.; Monti, S. *Cis-trans* photoisomerization of azobenzene. Solvent and triplet donors effects. *J. Phys. Chem.* **1979**, *83*, 648–652.

(26) Zhu, M.; Zhou, H. Azobenzene-based small molecular photoswitches for protein modulation. *Org. Biomol. Chem.* **2018**, *16*, 8434–8445.

(27) Magee, J. L.; Shand, W.; Eyring, H. Non-adiabatic Reactions. Rotation about the Double Bond. *J. Am. Chem. Soc.* **1941**, *63*, 677–688.

(28) Wei-Guang Diau, E. A New *Trans*-to-*Cis* Photoisomerization Mechanism of Azobenzene on the S1 (n,π*) Surface. *J. Phys. Chem. A* **2004**, *108*, 950–956.

(29) Rau, H.; Lueddecke, E. On the rotation-inversion controversy on photoisomerization of azobenzenes. Experimental proof of inversion. *J. Am. Chem. Soc.* **1982**, *104*, 1616–1620.

(30) Nenov, A.; Borrego-Varillas, R.; Oriana, A.; Ganzer, L.; Segatta, F.; Conti, I.; Segarra-Marti, J.; Omachi, J.; Dapor, M.; Taioli, S.*; et al.* UV-Light-Induced Vibrational Coherences: The Key to Understand Kasha Rule Violation in *trans*-Azobenzene. *J. Phys. Chem. Lett.* **2018**, *9*, 1534–1541.

(31) Tavadze, P.; Avendaño Franco, G.; Ren, P.; Wen, X.; Li, Y.; Lewis, J. P. A Machine-Driven Hunt for Global Reaction Coordinates of Azobenzene Photoisomerization. *J. Am. Chem. Soc.* **2018**, *140*, 285–290.

(32) Ishikawa, T.; Noro, T.; Shoda, T. Theoretical study on the photoisomerization of azobenzene. *J. Chem. Phys.* **2001**, *115*, 7503–7512.

(33) Xu, C.; Le Yu; Gu, F. L.; Zhu, C. Probing the π → π* photoisomerization mechanism of *trans*-azobenzene by multi-state ab initio on-the-fly trajectory dynamics simulations. *Phys. Chem. Chem. Phys.* **2018**, *20*, 23885–23897.

(34) Le Yu; Xu, C.; Zhu, C. Probing the π→π* photoisomerization mechanism of *cis*-azobenzene by multi-state ab initio on-the-fly trajectory dynamics simulation. *Phys. Chem. Chem. Phys.* **2015**, *17*, 17646–17660.

(35) Brown, E. V.; Granneman, G. R. *Cis-trans* isomerism in the pyridyl analogs of azobenzene. Kinetic and molecular orbital analysis. *J. Am. Chem. Soc.* **1975**, *97*, 621–627.

(36) Dokić, J.; Gothe, M.; Wirth, J.; Peters, M. V.; Schwarz, J.; Hecht, S.; Saalfrank, P. Quantum chemical investigation of thermal *cis*-to-*trans* isomerization of azobenzene derivatives: substituent effects, solvent effects, and comparison to experimental data. *J. Phys. Chem. A* **2009**, *113*, 6763–6773.

(37) Whitten, D. G.; Wildes, P. D.; Pacifici, J. G.; Irick, G. Solvent and substituent on the thermal isomerization of substituted azobenzenes. Flash spectroscopic study. *J. Am. Chem. Soc.* **1971**, *93*, 2004–2008.

(38) Blevins, A. A.; Blanchard, G. J. Effect of Positional Substitution on the Optical Response of Symmetrically Disubstituted Azobenzene Derivatives. *J. Phys. Chem. B* **2004**, *108*, 4962–4968.

(39) Serra, F.; Terentjev, E. M. Effects of Solvent Viscosity and Polarity on the Isomerization of Azobenzene. *Macromolecules* **2008**, *41*, 981–986.

(40) Wang, L.; Wang, X. An ab initio study of stable conformation and thermal isomerization of *p*-aminoazobenzene. *J. Mol. Struct.: THEOCHEM* **2007**, *806*, 179–186.

(41) Emond, M.; Le Saux, T.; Maurin, S.; Baudin, J.-B.; Plasson, R.; Jullien, L. 2-Hydroxyazobenzenes to tailor pH pulses and oscillations with light. *Chemistry* **2010**, *16*, 8822–8831.

(42) Kojima, M.; Nebashi, S.; Ogawa, K.; Kurita, N. Effect of solvent on *cis*-to-*trans* isomerization of 4-hydroxyazobenzene aggregated through intermolecular hydrogen bonds. *J. Phys. Org. Chem.* **2005**, *18*, 994–1000.

(43) Gabor, G.; Frei, Y. F.; Fischer, E. Tautomerism and geometric isomerism in arylazophenols and naphthols. IV. Spectra and reversible photoreactions of *m*- and *p*-hydroxyazobenzene. *J. Phys. Chem.* **1968**, *72*, 3266–3272.

(44) Sawicki, E. Physical Properties of Aminoazobenzene Dyes. VI. Intramolecular Hydrogen Bonding and Tautomerism in 4-Hydroxyazobenzene Derivatives and Higher Homologs 1. *J. Org. Chem.* **1957**, *22*, 743–745.

(45) Waldeck, D. H. Photoisomerization dynamics of stilbenes. *Chem. Rev.* **1991**, *91*, 415–436.

(46) Molina, V.; Merchán, M.; Roos, B. O. A theoretical study of the electronic spectrum of *cis*-stilbene. *Spectrochim. Acta Part A* **1999**, *55*, 433–446.

(47) Arenas, J. F.; Tocon, I. L.; Otero, J. C.; Marcos, J. I. A Priori Scaled Quantum Mechanical Vibrational Spectra of *trans*- and *cis*-Stilbene. *J. Phys. Chem.* **1995**, *99*, 11392–11398.

(48) Han, W.-G.; Lovell, T.; Liu, T.; Noodleman, L. Density Functional Studies of the Ground- and Excited-State Potential-Energy Curves of Stilbene *cis-trans* Isomerization. *ChemPhysChem* **2002**, *3*, 167–178.

(49) Beveridge, D. L.; Jaffé, H. H. The electronic structure and spectra of *cis*- and *trans*-stilbene. *J. Am. Chem. Soc.* **1965**, *87*, 5340–5346.

(50) Kovalenko, S. A.; Dobryakov, A. L.; Ioffe, I.; Ernsting, N. P. Evidence for the phantom state in photoinduced *cis-trans* isomerization of stilbene. *Chem. Phys. Lett.* **2010**, *493*, 255–258.

(51) Orlandi, G.; Palmieri, P.; Poggi, G. An ab initio study of the *cis-trans* photoisomerization of stilbene. *J. Am. Chem. Soc.* **1979**, *101*, 3492–3497.

(52) Irie, M. Diarylethenes for Memories and Switches. *Chem. Rev.* **2000**, *100*, 1685–1716.

(53) Yokoyama, Y. Fulgides for Memories and Switches. *Chem. Rev.* **2000**, *100*, 1717–1740.

(54) Darcy, P. J.; Heller, H. G.; Strydom, P. J.; Whittall, J. Photochromic heterocyclic fulgides. Part 2. Electrocyclic reactions of (*E*)-α-2,5-dimethyl-3-furylethylidene(alkyl-substituted methylene)succinic anhydrides. *J. Chem. Soc. Perkin Trans. 1* **1981**, 202–205.

(55) Heller, H. G.; Oliver, S. Photochromic heterocyclic fulgides. Part 1. Rearrangement reactions of (*E*)-α-3-furylethylidene(isopropylidene)succinic anhydride. *J. Chem. Soc. Perkin Trans. 1* **1981**, 197–201.

(56) Santiago, A.; Becker, R. S. Photochromic fulgides. Spectroscopy and mechanism of photoreactions. *J. Am. Chem. Soc.* **1968**, *90*, 3654–3658.

(57) Ivy, J. M.; Klar, A. J.; Hicks, J. B. Cloning and characterization of four SIR genes of Saccharomyces cerevisiae. *Mol. Cell. Biol.* **1986**, *6*, 688–702.

(58) Rine, J.; Herskowitz, I. Four genes responsible for a position effect on expression from HML and HMR in Saccharomyces cerevisiae. *Genetics* **1987**, *116*, 9–22.

(59) Frye, R. A. Phylogenetic classification of prokaryotic and eukaryotic Sir2-like proteins. *Biochem. Biophys. Res. Commun.* **2000**, *273*, 793–798.

(60) Greiss, S.; Gartner, A. Sirtuin/Sir2 phylogeny, evolutionary considerations and structural conservation. *Mol. Cells* **2009**, *28*, 407–415.

(61) Wang, Y.; He, J.; Liao, M.; Hu, M.; Li, W.; Ouyang, H.; Wang, X.; Ye, T.; Zhang, Y.; Ouyang, L. An overview of Sirtuins as potential therapeutic target: Structure, function and modulators. *Eur. J. Med. Chem.* **2019**, *161*, 48–77.

(62) Tanno, M.; Sakamoto, J.; Miura, T.; Shimamoto, K.; Horio, Y. Nucleocytoplasmic shuttling of the NAD$^+$-dependent histone deacetylase SIRT1. *J. Biol. Chem.* **2007**, *282*, 6823–6832.

(63) North, B. J.; Verdin, E. Interphase nucleo-cytoplasmic shuttling and localization of SIRT2 during mitosis. *PloS one* **2007**, *2*, e784.

(64) Schwer, B.; North, B. J.; Frye, R. A.; Ott, M.; Verdin, E. The human silent information regulator (Sir)2 homologue hSIRT3 is a mitochondrial nicotinamide adenine dinucleotide-dependent deacetylase. *J. Cell Biol.* **2002**, *158*, 647–657.

(65) Scher, M. B.; Vaquero, A.; Reinberg, D. SirT3 is a nuclear NAD$^+$-dependent histone deacetylase that translocates to the mitochondria upon cellular stress. *Genes Dev.* **2007**, *21*, 920–928.

(66) Schiedel, M.; Robaa, D.; Rumpf, T.; Sippl, W.; Jung, M. The Current State of NAD$^+$ -Dependent Histone Deacetylases (Sirtuins) as Novel Therapeutic Targets. *Med. Res. Rev.* **2018**, *38*, 147–200.

(67) Ahuja, N.; Schwer, B.; Carobbio, S.; Waltregny, D.; North, B. J.; Castronovo, V.; Maechler, P.; Verdin, E. Regulation of insulin secretion by SIRT4, a mitochondrial ADP-ribosyltransferase. *J. Biol. Chem.* **2007**, *282*, 33583–33592.

(68) Laurent, G.; German, N. J.; Saha, A. K.; Boer, V. C. J. de; Davies, M.; Koves, T. R.; Dephoure, N.; Fischer, F.; Boanca, G.; Vaitheesvaran, B.*; et al.* SIRT4 coordinates the balance between lipid synthesis and catabolism by repressing malonyl CoA decarboxylase. *Mol. Cell* **2013**, *50*, 686–698.

(69) Nakagawa, T.; Lomb, D. J.; Haigis, M. C.; Guarente, L. SIRT5 deacetylates carbamoyl phosphate synthetase 1 and regulates the urea cycle. *Cell* **2009**, *137*, 560–570.

(70) Schuetz, A.; Min, J.; Antoshenko, T.; Wang, C.-L.; Allali-Hassani, A.; Dong, A.; Loppnau, P.; Vedadi, M.; Bochkarev, A.; Sternglanz, R.*; et al.* Structural basis of inhibition of the human NAD$^+$-dependent deacetylase SIRT5 by suramin. *Structure* **2007**, *15*, 377–389.

(71) Pan, P. W.; Feldman, J. L.; Devries, M. K.; Dong, A.; Edwards, A. M.; Denu, J. M. Structure and biochemical functions of SIRT6. *J. Biol. Chem.* **2011**, *286*, 14575–14587.

(72) Blank, M. F.; Grummt, I. The seven faces of SIRT7. *Transcription* **2017**, *8*, 67–74.

(73) Michishita, E.; McCord, R. A.; Berber, E.; Kioi, M.; Padilla-Nash, H.; Damian, M.; Cheung, P.; Kusumoto, R.; Kawahara, T. L. A.; Barrett, J. C.*; et al.* SIRT6 is a histone H3 lysine 9 deacetylase that modulates telomeric chromatin. *Nature* **2008**, *452*, 492–496.

(74) Du, J.; Zhou, Y.; Su, X.; Yu, J. J.; Khan, S.; Jiang, H.; Kim, J.; Woo, J.; Kim, J. H.; Choi, B. H.*; et al.* Sirt5 is a NAD-dependent protein lysine demalonylase and desuccinylase. *Science* **2011**, *334*, 806–809.

(75) Tan, M.; Peng, C.; Anderson, K. A.; Chhoy, P.; Xie, Z.; Dai, L.; Park, J.; Chen, Y.; Huang, H.; Zhang, Y.*; et al.* Lysine glutarylation is a protein posttranslational modification regulated by SIRT5. *Cell Metab.* **2014**, *19*, 605–617.

(76) Roessler, C.; Tüting, C.; Meleshin, M.; Steegborn, C.; Schutkowski, M. A Novel Continuous Assay for the Deacylase Sirtuin 5 and Other Deacetylases. *J. Med. Chem.* **2015**, *58*, 7217–7223.

(77) Haigis, M. C.; Mostoslavsky, R.; Haigis, K. M.; Fahie, K.; Christodoulou, D. C.; Murphy, A. J.; Valenzuela, D. M.; Yancopoulos, G. D.; Karow, M.; Blander, G.*; et al.* SIRT4 inhibits glutamate dehydrogenase and opposes the effects of calorie restriction in pancreatic beta cells. *Cell* **2006**, *126*, 941–954.

(78) Jiang, H.; Khan, S.; Wang, Y.; Charron, G.; He, B.; Sebastian, C.; Du, J.; Kim, R.; Ge, E.; Mostoslavsky, R.*; et al.* SIRT6 regulates TNF-α secretion through hydrolysis of long-chain fatty acyl lysine. *Nature* **2013**, *496*, 110–113.

(79) Teng, Y.-B.; Jing, H.; Aramsangtienchai, P.; He, B.; Khan, S.; Hu, J.; Lin, H.; Hao, Q. Efficient demyristoylase activity of SIRT2 revealed by kinetic and structural studies. *Sci. Rep.* **2015**, *5*, 8529.

(80) Mathias, R. A.; Greco, T. M.; Oberstein, A.; Budayeva, H. G.; Chakrabarti, R.; Rowland, E. A.; Kang, Y.; Shenk, T.; Cristea, I. M. Sirtuin 4 is a lipoamidase regulating pyruvate dehydrogenase complex activity. *Cell* **2014**, *159*, 1615–1625.

(81) Feige, J. N.; Auwerx, J. Transcriptional targets of sirtuins in the coordination of mammalian physiology. *Curr. Opin. Cell Biol.* **2008**, *20*, 303–309.

(82) Jing, H.; Lin, H. Sirtuins in epigenetic regulation. *Chem. Rev.* **2015**, *115*, 2350–2375.

(83) Richards, E. J.; Elgin, S. C.R. Epigenetic Codes for Heterochromatin Formation and Silencing. *Cell* **2002**, *108*, 489–500.

(84) Portran, D.; Schaedel, L.; Xu, Z.; Théry, M.; Nachury, M. V. Tubulin acetylation protects long-lived microtubules against mechanical ageing. *Nat. Cell Biol.* **2017**, *19*, 391–398.

(85) Xu, Z.; Schaedel, L.; Portran, D.; Aguilar, A.; Gaillard, J.; Marinkovich, M. P.; Théry, M.; Nachury, M. V. Microtubules acquire resistance from mechanical breakage through intralumenal acetylation. *Science* **2017**, *356*, 328–332.

(86) Nagai, T.; Ikeda, M.; Chiba, S.; Kanno, S.-I.; Mizuno, K. Furry promotes acetylation of microtubules in the mitotic spindle by inhibition of SIRT2 tubulin deacetylase. *J. Cell Sci.* **2013**, *126*, 4369–4380.

(87) Deng, C.-X. SIRT1, is it a tumor promoter or tumor suppressor? *Int. J. Biol. Sci.* **2009**, *5*, 147–152.

(88) He, X.; Nie, H.; Hong, Y.; Sheng, C.; Xia, W.; Ying, W. SIRT2 activity is required for the survival of C6 glioma cells. *Biochem. Biophys. Res. Commun.* **2012**, *417*, 468–472.

(89) Li, Y.'n.; Dai, D.; Lu, Q.; Fei, M.; Li, M.; Wu, X. Sirt2 suppresses glioma cell growth through targeting NF-κB-miR-21 axis. *Biochem. Biophys. Res. Commun.* **2013**, *441*, 661–667.

(90) Vaziri, H.; Dessain, S. K.; Eaton, E. N.; Imai, S.-i.; Frye, R. A.; Pandita, T. K.; Guarente, L.; Weinberg, R. A. hSIR2SIRT1 Functions as an NAD-Dependent p53 Deacetylase. *Cell* **2001**, *107*, 149–159.

(91) Heltweg, B.; Gatbonton, T.; Schuler, A. D.; Posakony, J.; Li, H.; Goehle, S.; Kollipara, R.; Depinho, R. A.; Gu, Y.; Simon, J. A.*; et al.* Antitumor activity of a small-molecule inhibitor of human silent information regulator 2 enzymes. *Cancer Res.* **2006**, *66*, 4368–4377.

(92) Lain, S.; Hollick, J. J.; Campbell, J.; Staples, O. D.; Higgins, M.; Aoubala, M.; McCarthy, A.; Appleyard, V.; Murray, K. E.; Baker, L.*; et al.* Discovery, in vivo activity, and mechanism of action of a small-molecule p53 activator. *Cancer Cell* **2008**, *13*, 454–463.

(93) Jin, Y.-H.; Kim, Y.-J.; Kim, D.-W.; Baek, K.-H.; Kang, B. Y.; Yeo, C.-Y.; Lee, K.-Y. Sirt2 interacts with 14-3-3 beta/gamma and down-regulates the activity of p53. *Biochem. Biophys. Res. Commun.* **2008**, *368*, 690–695.

(94) Li, L.; Wang, L.; Li, L.; Wang, Z.; Ho, Y.; McDonald, T.; Holyoake, T. L.; Chen, W.; Bhatia, R. Activation of p53 by SIRT1 inhibition enhances elimination of CML leukemia stem cells in combination with imatinib. *Cancer Cell* **2012**, *21*, 266–281.

(95) Chalkiadaki, A.; Guarente, L. The multifaceted functions of sirtuins in cancer. *Nat. Rev. Cancer* **2015**, *15*, 608–624.

(96) Wu, X.; Cao, N.; Fenech, M.; Wang, X. Role of Sirtuins in Maintenance of Genomic Stability: Relevance to Cancer and Healthy Aging. *DNA Cell Biol.* **2016**, *35*, 542–575.

(97) Yeung, F.; Hoberg, J. E.; Ramsey, C. S.; Keller, M. D.; Jones, D. R.; Frye, R. A.; Mayo, M. W. Modulation of NF-kappaB-dependent transcription and cell survival by the SIRT1 deacetylase. *EMBO J.* **2004**, *23*, 2369–2380.

(98) Rothgiesser, K. M.; Erener, S.; Waibel, S.; Lüscher, B.; Hottiger, M. O. SIRT2 regulates NF-κB dependent gene expression through deacetylation of p65 Lys310. *J. Cell Sci.* **2010**, *123*, 4251–4258.

(99) Tao, R.; Coleman, M. C.; Pennington, J. D.; Ozden, O.; Park, S.-H.; Jiang, H.; Kim, H.-S.; Flynn, C. R.; Hill, S.; Hayes McDonald, W.*; et al.* Sirt3-mediated deacetylation of evolutionarily conserved lysine 122 regulates MnSOD activity in response to stress. *Mol. Cell* **2010**, *40*, 893–904.

(100) Qiu, X.; Brown, K.; Hirschey, M. D.; Verdin, E.; Chen, D. Calorie restriction reduces oxidative stress by SIRT3-mediated SOD2 activation. *Cell Metab.* **2010**, *12*, 662–667.

(101) Xie, X.; Wang, L.; Zhao, B.; Chen, Y.; Li, J. SIRT3 mediates decrease of oxidative damage and prevention of ageing in porcine fetal fibroblasts. *Life Sci.* **2017**, *177*, 41–48.

(102) Sundaresan, N. R.; Gupta, M.; Kim, G.; Rajamohan, S. B.; Isbatan, A.; Gupta, M. P. Sirt3 blocks the cardiac hypertrophic response by augmenting Foxo3a-dependent antioxidant defense mechanisms in mice. *J. Clin. Invest.* **2009**, *119*, 2758–2771.

(103) Tu, L.-F.; Cao, L.-F.; Zhang, Y.-H.; Guo, Y.-L.; Zhou, Y.-F.; Lu, W.-Q.; Zhang, T.-Z.; Zhang, T.; Zhang, G.-X.; Kurihara, H.*; et al.* Sirt3-dependent deacetylation of COX-1 counteracts oxidative stress-induced cell apoptosis. *FASEB J.* **2019**, *33*, 14118–14128.

(104) Wang, Z.; Sun, R.; Wang, G.; Chen, Z.; Li, Y.; Zhao, Y.; Liu, D.; Zhao, H.; Zhang, F.; Yao, J.*; et al.* SIRT3-mediated deacetylation of PRDX3 alleviates mitochondrial oxidative damage and apoptosis induced by intestinal ischemia/reperfusion injury. *Redox Biol.* **2020**, *28*, 101343.

(105) Tang, X.; Li, Y.; Liu, L.; Guo, R.; Zhang, P.; Zhang, Y.; Zhang, Y.; Zhao, J.; Su, J.; Sun, L.*; et al.* Sirtuin 3 induces apoptosis and necroptosis by regulating mutant p53 expression in small-cell lung cancer. *Oncol. Rep.* **2020**, *43*, 591–600.

(106) Allison, S. J.; Milner, J. SIRT3 is pro-apoptotic and participates in distinct basal apoptotic pathways. *Cell Cycle* **2007**, *6*, 2669–2677.

(107) Mei, Z.; Zhang, X.; Yi, J.; Huang, J.; He, J.; Tao, Y. Sirtuins in metabolism, DNA repair and cancer. *J. Exp. Clin. Cancer Res.* **2016**, *35*, 182.

(108) Jiang, W.; Wang, S.; Xiao, M.; Lin, Y.; Zhou, L.; Lei, Q.; Xiong, Y.; Guan, K.-L.; Zhao, S. Acetylation regulates gluconeogenesis by promoting PEPCK1 degradation via recruiting the UBR5 ubiquitin ligase. *Mol. Cell* **2011**, *43*, 33–44.

(109) Schlicker, C.; Gertz, M.; Papatheodorou, P.; Kachholz, B.; Becker, C. F. W.; Steegborn, C. Substrates and regulation mechanisms for the human mitochondrial sirtuins Sirt3 and Sirt5. *J. Mol. Biol.* **2008**, *382*, 790–801.

(110) Rodgers, J. T.; Lerin, C.; Haas, W.; Gygi, S. P.; Spiegelman, B. M.; Puigserver, P. Nutrient control of glucose homeostasis through a complex of PGC-1alpha and SIRT1. *Nature* **2005**, *434*, 113–118.

(111) Caton, P. W.; Richardson, S. J.; Kieswich, J.; Bugliani, M.; Holland, M. L.; Marchetti, P.; Morgan, N. G.; Yaqoob, M. M.; Holness, M. J.; Sugden, M. C. Sirtuin 3 regulates mouse pancreatic beta cell function and is suppressed in pancreatic islets isolated from human type 2 diabetic patients. *Diabetologia* **2013**, *56*, 1068–1077.

(112) Zhang, H.-H.; Ma, X.-J.; Wu, L.-N.; Zhao, Y.-Y.; Zhang, P.-Y.; Zhang, Y.-H.; Shao, M.-W.; Liu, F.; Li, F.; Qin, G.-J. Sirtuin-3 (SIRT3) protects pancreatic β-cells from endoplasmic reticulum (ER) stress-induced apoptosis and dysfunction. *Mol. Cell. Biochem.* **2016**, *420*, 95–106.

(113) Bordone, L.; Motta, M. C.; Picard, F.; Robinson, A.; Jhala, U. S.; Apfeld, J.; McDonagh, T.; Lemieux, M.; McBurney, M.; Szilvasi, A.*; et al.* Sirt1 regulates insulin secretion by repressing UCP2 in pancreatic beta cells. *PLoS Biol.* **2006**, *4*, e31.

(114) Gomes, P.; Fleming Outeiro, T.; Cavadas, C. Emerging Role of Sirtuin 2 in the Regulation of Mammalian Metabolism. *Trends Pharmacol. Sci.* **2015**, *36*, 756–768.

(115) Picard, F.; Kurtev, M.; Chung, N.; Topark-Ngarm, A.; Senawong, T.; Machado De Oliveira, R.; Leid, M.; McBurney, M. W.; Guarente, L. Sirt1 promotes fat mobilization in white adipocytes by repressing PPAR-gamma. *Nature* **2004**, *429*, 771–776.

(116) Gerhart-Hines, Z.; Rodgers, J. T.; Bare, O.; Lerin, C.; Kim, S.-H.; Mostoslavsky, R.; Alt, F. W.; Wu, Z.; Puigserver, P. Metabolic control of muscle mitochondrial function and fatty acid oxidation through SIRT1/PGC-1alpha. *EMBO J.* **2007**, *26*, 1913–1923.

(117) Wang, F.; Tong, Q. SIRT2 suppresses adipocyte differentiation by deacetylating FOXO1 and enhancing FOXO1's repressive interaction with PPARgamma. *Mol. Biol. Cell* **2009**, *20*, 801–808.

(118) Purushotham, A.; Schug, T. T.; Xu, Q.; Surapureddi, S.; Guo, X.; Li, X. Hepatocyte-specific deletion of SIRT1 alters fatty acid metabolism and results in hepatic steatosis and inflammation. *Cell Metab.* **2009**, *9*, 327–338.

(119) Hirschey, M. D.; Shimazu, T.; Goetzman, E.; Jing, E.; Schwer, B.; Lombard, D. B.; Grueter, C. A.; Harris, C.; Biddinger, S.; Ilkayeva, O. R.*; et al.* SIRT3 regulates mitochondrial fatty-acid oxidation by reversible enzyme deacetylation. *Nature* **2010**, *464*, 121–125.

(120) Krishnan, J.; Danzer, C.; Simka, T.; Ukropec, J.; Walter, K. M.; Kumpf, S.; Mirtschink, P.; Ukropcova, B.; Gasperikova, D.; Pedrazzini, T.*; et al.* Dietary obesity-associated Hif1α activation in adipocytes restricts fatty acid oxidation and energy expenditure via suppression of the Sirt2-NAD$^+$ system. *Genes Dev.* **2012**, *26*, 259–270.

(121) Gomes, P.; Leal, H.; Mendes, A. F.; Reis, F.; Cavadas, C. Dichotomous Sirtuins: Implications for Drug Discovery in Neurodegenerative and Cardiometabolic Diseases. *Trends Pharmacol. Sci.* **2019**, *40*, 1021–1039.

(122) Donmez, G. The neurobiology of sirtuins and their role in neurodegeneration. *Trends Pharmacol. Sci.* **2012**, *33*, 494–501.

(123) Borra, M. T.; O'Neill, F. J.; Jackson, M. D.; Marshall, B.; Verdin, E.; Foltz, K. R.; Denu, J. M. Conserved enzymatic production and biological effect of *O*-acetyl-ADP-ribose by silent information regulator 2-like NAD$^+$-dependent deacetylases. *J. Biol. Chem.* **2002**, *277*, 12632–12641.

(124) Liou, G.-G.; Tanny, J. C.; Kruger, R. G.; Walz, T.; Moazed, D. Assembly of the SIR complex and its regulation by *O*-acetyl-ADP-ribose, a product of NAD-dependent histone deacetylation. *Cell* **2005**, *121*, 515–527.

(125) Lee, S.; Tong, L.; Denu, J. M. Quantification of endogenous sirtuin metabolite *O*-acetyl-ADP-ribose. *Anal. Biochem.* **2008**, *383*, 174–179.

(126) Lombardi, P. M.; Cole, K. E.; Dowling, D. P.; Christianson, D. W. Structure, mechanism, and inhibition of histone deacetylases and related metalloenzymes. *Curr. Opin. Struct. Biol.* **2011**, *21*, 735–743.

(127) Finnin, M. S.; Donigian, J. R.; Pavletich, N. P. Structure of the histone deacetylase SIRT2. *Nat. Struct. Biol.* **2001**, *8*, 621–625.

(128) Avalos, J. L.; Celic, I.; Muhammad, S.; Cosgrove, M. S.; Boeke, J. D.; Wolberger, C. Structure of a Sir2 Enzyme Bound to an Acetylated p53 Peptide. *Mol. Cell* **2002**, *10*, 523–535.

(129) Avalos, J. L.; Bever, K. M.; Wolberger, C. Mechanism of sirtuin inhibition by nicotinamide: altering the NAD(+) cosubstrate specificity of a Sir2 enzyme. *Mol. Cell* **2005**, *17*, 855–868.

(130) Borra, M. T.; Langer, M. R.; Slama, J. T.; Denu, J. M. Substrate specificity and kinetic mechanism of the Sir2 family of NAD$^+$-dependent histone/protein deacetylases. *Biochemistry* **2004**, *43*, 9877–9887.

(131) Feldman, J. L.; Dittenhafer-Reed, K. E.; Denu, J. M. Sirtuin catalysis and regulation. *J. Biol. Chem.* **2012**, *287*, 42419–42427.

(132) Hawse, W. F.; Hoff, K. G.; Fatkins, D. G.; Daines, A.; Zubkova, O. V.; Schramm, V. L.; Zheng, W.; Wolberger, C. Structural insights into intermediate steps in the Sir2 deacetylation reaction. *Structure* **2008**, *16*, 1368–1377.

(133) Avalos, J. L.; Boeke, J. D.; Wolberger, C. Structural Basis for the Mechanism and Regulation of Sir2 Enzymes. *Mol. Cell* **2004**, *13*, 639–648.

(134) Hoff, K. G.; Avalos, J. L.; Sens, K.; Wolberger, C. Insights into the sirtuin mechanism from ternary complexes containing NAD$^+$ and acetylated peptide. *Structure* **2006**, *14*, 1231–1240.

(135) Smith, B. C.; Denu, J. M. Sir2 deacetylases exhibit nucleophilic participation of acetyl-lysine in NAD$^+$ cleavage. *J. Am. Chem. Soc.* **2007**, *129*, 5802–5803.

(136) Smith, B. C.; Denu, J. M. Sir2 protein deacetylases: evidence for chemical intermediates and functions of a conserved histidine. *Biochemistry* **2006**, *45*, 272–282.

(137) Sauve, A. A.; Celic, I.; Avalos, J.; Deng, H.; Boeke, J. D.; Schramm, V. L. Chemistry of gene silencing: the mechanism of NAD$^+$-dependent deacetylation reactions. *Biochemistry* **2001**, *40*, 15456–15463.

(138) Tong, L.; Denu, J. M. Function and metabolism of sirtuin metabolite *O*-acetyl-ADP-ribose. *Biochim. Biophys. Acta* **2010**, *1804*, 1617–1625.

(139) Jackson, M. D.; Schmidt, M. T.; Oppenheimer, N. J.; Denu, J. M. Mechanism of nicotinamide inhibition and transglycosidation by Sir2 histone/protein deacetylases. *J. Biol. Chem.* **2003**, *278*, 50985–50998.

(140) Sanders, B. D.; Jackson, B.; Marmorstein, R. Structural basis for sirtuin function: what we know and what we don't. *Biochim. Biophys. Acta* **2010**, *1804*, 1604–1616.

(141) Rossmann, M. G.; Moras, D.; Olsen, K. W. Chemical and biological evolution of nucleotide-binding protein. *Nature* **1974**, *250*, 194–199.

(142) Hanukoglu, I. Proteopedia: Rossmann fold: A beta-alpha-beta fold at dinucleotide binding sites. *Biochem. Mol. Biol. Educ.* **2015**, *43*, 206–209.

(143) Min, J.; Landry, J.; Sternglanz, R.; Xu, R.-M. Crystal Structure of a SIR2 Homolog–NAD Complex. *Cell* **2001**, *105*, 269–279.

(144) Feldman, J. L.; Dittenhafer-Reed, K. E.; Kudo, N.; Thelen, J. N.; Ito, A.; Yoshida, M.; Denu, J. M. Kinetic and Structural Basis for Acyl-Group Selectivity and NAD(+) Dependence in Sirtuin-Catalyzed Deacylation. *Biochemistry* **2015**, *54*, 3037–3050.

(145) Robaa, D.; Monaldi, D.; Wössner, N.; Kudo, N.; Rumpf, T.; Schiedel, M.; Yoshida, M.; Jung, M. Opening the Selectivity Pocket in the Human Lysine Deacetylase Sirtuin2 - New Opportunities, New Questions. *Chem. Rec.* **2018**, *18*, 1701–1707.

(146) Zheng, W., Ed. *Sirtuins in health and disease*; *Prog. Mol. Biol. Trans. Sci.* **2018**, *154*.

(147) Bai, X.; Yao, L.; Ma, X.; Xu, X. Small Molecules as SIRT Modulators. *Mini Rev. Med. Chem.* **2018**, *18*, 1151–1157.

(148) Jiang, Y.; Liu, J.; Di Chen; Yan, L.; Zheng, W. Sirtuin Inhibition: Strategies, Inhibitors, and Therapeutic Potential. *Trends Pharmacol. Sci.* **2017**, *38*, 459–472.

(149) Napper, A. D.; Hixon, J.; McDonagh, T.; Keavey, K.; Pons, J.-F.; Barker, J.; Yau, W. T.; Amouzegh, P.; Flegg, A.; Hamelin, E.*; et al.* Discovery of indoles as potent and selective inhibitors of the deacetylase SIRT1. *J. Med. Chem.* **2005**, *48*, 8045–8054.

(150) Süssmuth, S. D.; Haider, S.; Landwehrmeyer, G. B.; Farmer, R.; Frost, C.; Tripepi, G.; Andersen, C. A.; Di Bacco, M.; Lamanna, C.; Diodato, E.*; et al.* An exploratory double-blind, randomized clinical trial with selisistat, a SirT1 inhibitor, in patients with Huntington's disease. *Br. J. Clin. Pharmacol.* **2015**, *79*, 465–476.

(151) AOP Orphan Pharmaceuticals AG. https://www.aoporphan.com/global_en/our-company/newsroom/aop-orphan-pharmaceuticals-ag-to-acquire-selisistat-a-clinical-stage-drug-candidate-for-the-treatment-of-huntingtons-disease-hd (accessed April 28, 2019).

(152) Suzuki, T.; Khan, M. N. A.; Sawada, H.; Imai, E.; Itoh, Y.; Yamatsuta, K.; Tokuda, N.; Takeuchi, J.; Seko, T.; Nakagawa, H.*; et al.* Design, synthesis, and biological activity of a novel series of human sirtuin-2-selective inhibitors. *J. Med. Chem.* **2012**, *55*, 5760–5773.

(153) Ai, T.; Wilson, D. J.; More, S. S.; Xie, J.; Chen, L. 5-((3-Amidobenzyl)oxy)nicotinamides as Sirtuin 2 Inhibitors. *J. Med. Chem.* **2016**, *59*, 2928–2941.

(154) Tatum, P. R.; Sawada, H.; Ota, Y.; Itoh, Y.; Zhan, P.; Ieda, N.; Nakagawa, H.; Miyata, N.; Suzuki, T. Identification of novel SIRT2-selective inhibitors using a click chemistry approach. *Bioorg. Med. Chem. Lett.* **2014**, *24*, 1871–1874.

(155) Cui, H.; Kamal, Z.; Ai, T.; Xu, Y.; More, S. S.; Wilson, D. J.; Chen, L. Discovery of potent and selective sirtuin 2 (SIRT2) inhibitors using a fragment-based approach. *J. Med. Chem.* **2014**, *57*, 8340–8357.

(156) Rumpf, T.; Schiedel, M.; Karaman, B.; Roessler, C.; North, B. J.; Lehotzky, A.; Oláh, J.; Ladwein, K. I.; Schmidtkunz, K.; Gajer, M.*; et al.* Selective Sirt2 inhibition by ligand-induced rearrangement of the active site. *Nat. Commun.* **2015**, *6*, 6263.

(157) Schiedel, M.; Rumpf, T.; Karaman, B.; Lehotzky, A.; Oláh, J.; Gerhardt, S.; Ovádi, J.; Sippl, W.; Einsle, O.; Jung, M. Aminothiazoles as Potent and Selective Sirt2 Inhibitors: A Structure-Activity Relationship Study. *J. Med. Chem.* **2016**, *59*, 1599–1612.

(158) Davis, P. D.; Hill, C. H.; Lawton, G.; Nixon, J. S.; Wilkinson, S. E.; Hurst, S. A.; Keech, E.; Turner, S. E. Inhibitors of protein kinase C. 1. 2,3-Bisarylmaleimides. *J. Med. Chem.* **1992**, *35*, 177–184.

(159) Davis, P. D.; Elliott, L. H.; Harris, W.; Hill, C. H.; Hurst, S. A.; Keech, E.; Kumar, M. K.; Lawton, G.; Nixon, J. S.; Wilkinson, S. E. Inhibitors of protein kinase C. 2. Substituted bisindolylmaleimides with improved potency and selectivity. *J. Med. Chem.* **1992**, *35*, 994–1001.

(160) Trapp, J.; Jochum, A.; Meier, R.; Saunders, L.; Marshall, B.; Kunick, C.; Verdin, E.; Goekjian, P.; Sippl, W.; Jung, M. Adenosine mimetics as inhibitors of NAD$^+$-dependent histone deacetylases, from kinase to sirtuin inhibition. *J. Med. Chem.* **2006**, *49*, 7307–7316.

(161) Hüll, K.; Morstein, J.; Trauner, D. In Vivo Photopharmacology. *Chem. Rev.* **2018**, *118*, 10710–10747.

(162) Paoletti, P.; Ellis-Davies, G. C. R.; Mourot, A. Optical control of neuronal ion channels and receptors. *Nat. Rev. Neurosci.* **2019**, *20*, 514–532.

(163) Ricart-Ortega, M.; Font, J.; Llebaria, A. GPCR photopharmacology. *Mol. Cell. Endocrin.* **2019**, *488*, 36–51.

(164) Quandt, G.; Höfner, G.; Pabel, J.; Dine, J.; Eder, M.; Wanner, K. T. First photoswitchable neurotransmitter transporter inhibitor: light-induced control of γ-aminobutyric acid transporter 1 (GAT1) activity in mouse brain. *J. Med. Chem.* **2014**, *57*, 6809–6821.

(165) Cheng, B.; Shchepakin, D.; Kavanaugh, M. P.; Trauner, D. Photoswitchable Inhibitor of a Glutamate Transporter. *ACS Chem. Neurosci.* **2017**, *8*, 1668–1672.

(166) Borowiak, M.; Nahaboo, W.; Reynders, M.; Nekolla, K.; Jalinot, P.; Hasserodt, J.; Rehberg, M.; Delattre, M.; Zahler, S.; Vollmar, A.*; et al.* Photoswitchable Inhibitors of Microtubule Dynamics Optically Control Mitosis and Cell Death. *Cell* **2015**, *162*, 403–411.

(167) Kim, D.; Nguyen, M. D.; Dobbin, M. M.; Fischer, A.; Sananbenesi, F.; Rodgers, J. T.; Delalle, I.; Baur, J. A.; Sui, G.; Armour, S. M.*; et al.* SIRT1 deacetylase protects against neurodegeneration in models for Alzheimer's disease and amyotrophic lateral sclerosis. *EMBO J.* **2007**, *26*, 3169–3179.

(168) Porquet, D.; Griñán-Ferré, C.; Ferrer, I.; Camins, A.; Sanfeliu, C.; Del Valle, J.; Pallàs, M. Neuroprotective role of *trans*-resveratrol in a murine model of familial Alzheimer's disease. *J. Alzheimer's Dis.* **2014**, *42*, 1209–1220.

(169) Yin, J.; Han, P.; Song, M.; Nielsen, M.; Beach, T. G.; Serrano, G. E.; Liang, W. S.; Caselli, R. J.; Shi, J. Amyloid-β Increases Tau by Mediating Sirtuin 3 in Alzheimer's Disease. *Mol. Neurobiol.* **2018**, *55*, 8592–8601.

(170) Ferretta, A.; Gaballo, A.; Tanzarella, P.; Piccoli, C.; Capitanio, N.; Nico, B.; Annese, T.; Di Paola, M.; Dell'aquila, C.; Mari, M. de*; et al.* Effect of resveratrol on mitochondrial function: implications in parkin-associated familiar Parkinson's disease. *Biochim. Biophys. Acta* **2014**, *1842*, 902–915.

(171) Outeiro, T. F.; Kontopoulos, E.; Altmann, S. M.; Kufareva, I.; Strathearn, K. E.; Amore, A. M.; Volk, C. B.; Maxwell, M. M.; Rochet, J.-C.; McLean, P. J.*; et al.* Sirtuin 2 inhibitors rescue alpha-synuclein-mediated toxicity in models of Parkinson's disease. *Science* **2007**, *317*, 516–519.

(172) Liu, L.; Peritore, C.; Ginsberg, J.; Kayhan, M.; Donmez, G. SIRT3 attenuates MPTP-induced nigrostriatal degeneration via enhancing mitochondrial antioxidant capacity. *Neurochem. Res.* **2015**, *40*, 600–608.

(173) Jeong, H.; Cohen, D. E.; Cui, L.; Supinski, A.; Savas, J. N.; Mazzulli, J. R.; Yates, J. R.; Bordone, L.; Guarente, L.; Krainc, D. Sirt1 mediates neuroprotection from mutant huntingtin by activation of the TORC1 and CREB transcriptional pathway. *Nat. Med.* **2011**, *18*, 159–165.

(174) Fu, J.; Jin, J.; Cichewicz, R. H.; Hageman, S. A.; Ellis, T. K.; Xiang, L.; Peng, Q.; Jiang, M.; Arbez, N.; Hotaling, K.*; et al.* *trans*-(-)-ε-Viniferin increases mitochondrial sirtuin 3 (SIRT3), activates AMP-activated protein kinase (AMPK), and protects cells in models of Huntington Disease. *J. Biol. Chem.* **2012**, *287*, 24460–24472.

(175) Naia, L.; Rosenstock, T. R.; Oliveira, A. M.; Oliveira-Sousa, S. I.; Caldeira, G. L.; Carmo, C.; Laço, M. N.; Hayden, M. R.; Oliveira, C. R.; Rego, A. C. Comparative Mitochondrial-Based Protective Effects of Resveratrol and Nicotinamide in Huntington's Disease Models. *Mol. Neurobiol.* **2017**, *54*, 5385–5399.

(176) Kitada, M.; Kume, S.; Kanasaki, K.; Takeda-Watanabe, A.; Koya, D. Sirtuins as possible drug targets in type 2 diabetes. *Curr. Drug Targets* **2013**, *14*, 622–636.

(177) Mariani, S.; Fiore, D.; Persichetti, A.; Basciani, S.; Lubrano, C.; Poggiogalle, E.; Genco, A.; Donini, L. M.; Gnessi, L. Circulating SIRT1 Increases After Intragastric Balloon Fat Loss in Obese Patients. *Obes. Surg.* **2016**, *26*, 1215–1220.

(178) Mariani, S.; Fiore, D.; Basciani, S.; Persichetti, A.; Contini, S.; Lubrano, C.; Salvatori, L.; Lenzi, A.; Gnessi, L. Plasma levels of SIRT1 associate with non-alcoholic fatty liver disease in obese patients. *Endocrine* **2015**, *49*, 711–716.

(179) Mariani, S.; Costantini, D.; Lubrano, C.; Basciani, S.; Caldaroni, C.; Barbaro, G.; Poggiogalle, E.; Donini, L. M.; Lenzi, A.; Gnessi, L. Circulating SIRT1 inversely correlates with epicardial fat thickness in patients with obesity. *Nutr. Metab. Cardiovasc. Dis.* **2016**, *26*, 1033–1038.

(180) Swyter, S.; Schiedel, M.; Monaldi, D.; Szunyogh, S.; Lehotzky, A.; Rumpf, T.; Ovádi, J.; Sippl, W.; Jung, M. New chemical tools for probing activity and inhibition of the NAD$^+$-dependent lysine deacylase sirtuin 2. *Philos. Trans. R. Soc. B* **2018**, *373*.

(181) Broichhagen, J.; Frank, J. A.; Trauner, D. A roadmap to success in photopharmacology. *Acc. Chem. Res.* **2015**, *48*, 1947–1960.

(182) Miyaura, N.; Yamada, K.; Suzuki, A. A new stereospecific cross-coupling by the palladium-catalyzed reaction of 1-alkenylboranes with 1-alkenyl or 1-alkynyl halides. *Tetrahedron Lett.* **1979**, *20*, 3437–3440.

(183) Milstein, D.; Stille, J. K. Palladium-catalyzed coupling of tetraorganotin compounds with aryl and benzyl halides. Synthetic utility and mechanism. *J. Am. Chem. Soc.* **1979**, *101*, 4992–4998.

(184) Heck, R. F. Palladium-Catalyzed Vinylation of Organic Halides. *Org. React. (Hoboken, NJ, U. S.)* **2004**, *27*; 345–390.

(185) Merino, E. Synthesis of azobenzenes: the coloured pieces of molecular materials. *Chem. Soc. Rev.* **2011**, *40*, 3835–3853.

(186) Baeyer, A. Nitrosobenzol und Nitrosonaphtalin. *Chem. Ber.* **1874**, *7*, 1638–1640.

(187) Mills, C. XCIII. Some new azo-compounds. *J. Chem. Soc., Trans.* **1895**, *67*, 925–933.

(188) Bamberger, E. Ueber die Einwirkung des Nitrosobenzols auf Amidoverbindungen. *Chem. Ber.* **1896**, *29*, 102–104.

(189) Yu, B.-C.; Shirai, Y.; Tour, J. M. Syntheses of new functionalized azobenzenes for potential molecular electronic devices. *Tetrahedron* **2006**, *62*, 10303–10310.

(190) Sonogashira, K. Development of Pd–Cu catalyzed cross-coupling of terminal acetylenes with sp2-carbon halides. *J. Organomet. Chem.* **2002**, *653*, 46–49.

(191) Heltweg, B.; Trapp, J.; Jung, M. In vitro assays for the determination of histone deacetylase activity. *Methods* **2005**, *36*, 332–337.

(192) Falenczyk, C.; Schiedel, M.; Karaman, B.; Rumpf, T.; Kuzmanovic, N.; Grøtli, M.; Sippl, W.; Jung, M.; König, B. Chromo-pharmacophores: photochromic diarylmaleimide inhibitors for sirtuins. *Chem. Sci.* **2014**, *5*, 4794–4799.

(193) Simeth, N. A.; Altmann, L.-M.; Wössner, N.; Bauer, E.; Jung, M.; König, B. Photochromic Indolyl Fulgimides as Chromo-pharmacophores Targeting Sirtuins. *J. Org. Chem.* **2018**, *83*, 7919–7927.

(194) Feringa, B. L. The Art of Building Small: From Molecular Switches to Motors (Nobel Lecture). *Angew. Chem. Int. Ed.* **2017**, *56*, 11060–11078.

(195) Feringa, B. L. Die Kunst, klein zu bauen: von molekularen Schaltern bis zu Motoren (Nobel-Aufsatz). *Angew. Chem.* **2017**, *129*, 11206–11226.

(196) Grathwol, C. W.; Wössner, N.; Swyter, S.; Hofstetter, R. K.; Bodtke, A.; Jung, M.; Link, A. Azologization and repurposing of a hetero-stilbene-based kinase inhibitor: towards the design of photoswitchable sirtuin inhibitors. *Beilstein J. Org. Chem.* **2019**, *15*, 2170–2183.

(197) Chung, J. W.; Yoon, S.-J.; An, B.-K.; Park, S. Y. Correction to “High-Contrast On/Off Fluorescence Switching via Reversible *E–Z* Isomerization of Diphenylstilbene Containing the α-Cyanostilbenic Moiety”. *J. Phys. Chem. C* **2017**, *121*, 26139.

(198) Guo, X.; Zhou, J.; Siegler, M. A.; Bragg, A. E.; Katz, H. E. Visible-light-triggered molecular photoswitch based on reversible *E*/*Z* isomerization of a 1,2-dicyanoethene derivative. *Angew. Chem. Int. Ed.* **2015**, *54*, 4782–4786.

(199) Kumar, S.; Bawa, S.; Gupta, H. Biological activities of quinoline derivatives. *Mini Rev. Med. Chem.* **2009**, *9*, 1648–1654.

(200) Hussaini, S. M. A. Therapeutic significance of quinolines: a patent review (2013-2015). *Expert Opin. Ther. Pat.* **2016**, *26*, 1201–1221.

(201) Kerry, M. A.; Boyd, G. W.; Mackay, S. P.; Meth-Cohn, O.; Platt, L. The synthesis of benzo[*h*]quinolines as topoisomerase inhibitors. *J. Chem. Soc. Perkin Trans. 1* **1999**, 2315–2321.

(202) Marzaro, G.; Dalla Via, L.; García-Argáez, A. N.; Dalla Via, M.; Chilin, A. Novel benzoquinoline derivatives via unpredicted condensation of ethyl propiolate and naphthylamines: Synthesis and topoisomerase inhibition activity. *Bioorg. Med. Chem. Lett.* **2016**, *26*, 4875–4878.

(203) Zhao, X.; Allison, D.; Condon, B.; Zhang, F.; Gheyi, T.; Zhang, A.; Ashok, S.; Russell, M.; MacEwan, I.; Qian, Y.*; et al.* The 2.5 Å crystal structure of the SIRT1 catalytic domain bound to nicotinamide adenine dinucleotide (NAD^+) and an indole (EX527 analogue) reveals a novel mechanism of histone deacetylase inhibition. *J. Med. Chem.* **2013**, *56*, 963–969.

(204) Gertz, M.; Fischer, F.; Nguyen, G. T. T.; Lakshminarasimhan, M.; Schutkowski, M.; Weyand, M.; Steegborn, C. Ex-527 inhibits Sirtuins by exploiting their unique NAD^+-dependent deacetylation mechanism. *Proc. Natl. Acad. Sci. U. S. A.* **2013**, *110*, E2772-81.

(205) Beharry, A. A.; Woolley, G. A. Azobenzene photoswitches for biomolecules. *Chem. Soc. Rev.* **2011**, *40*, 4422–4437.

(206) Hoorens, M. W. H.; Szymanski, W. Reversible, Spatial and Temporal Control over Protein Activity Using Light. *Trends Biochem. Sci.* **2018**, *43*, 567–575.

(207) Urner, L. H.; Schade, B.; Schulze, M.; Folmert, K.; Haag, R.; Pagel, K. Switchable Solubility of Azobenzene-Based Bolaamphiphiles. *ChemPhysChem* **2019**, *20*, 1690–1697.

(208) Szymanski, W.; Ourailidou, M. E.; Velema, W. A.; Dekker, F. J.; Feringa, B. L. Light-Controlled Histone Deacetylase (HDAC) Inhibitors: Towards Photopharmacological Chemotherapy. *Chemistry* **2015**, *21*, 16517–16524.

(209) Schehr, M.; Ianes, C.; Weisner, J.; Heintze, L.; Müller, M. P.; Pichlo, C.; Charl, J.; Brunstein, E.; Ewert, J.; Lehr, M.*; et al.* 2-Azo-, 2-diazocine-thiazols and 2-azo-imidazoles as photoswitchable kinase inhibitors: limitations and pitfalls of the photoswitchable inhibitor approach. *Photochem. Photobiol. Sci.* **2019**, *18*, 1398–1407.

(210) Matsumura, Y.; Ananthaswamy, H. N. Toxic effects of ultraviolet radiation on the skin. *Toxicol. Appl. Pharmacol.* **2004**, *195*, 298–308.

(211) Kalka, K.; Merk, H.; Mukhtar, H. Photodynamic therapy in dermatology. *J. Am. Acad. Dermatol.* **2000**, *42*, 389–413.

(212) Ash, C.; Dubec, M.; Donne, K.; Bashford, T. Effect of wavelength and beam width on penetration in light-tissue interaction using computational methods. *Laser Med. Sci.* **2017**, *32*, 1909–1918.

(213) Agostinis, P.; Berg, K.; Cengel, K. A.; Foster, T. H.; Girotti, A. W.; Gollnick, S. O.; Hahn, S. M.; Hamblin, M. R.; Juzeniene, A.; Kessel, D.*; et al.* Photodynamic therapy of cancer: an update. *Cancer J. Clin.* **2011**, *61*, 250–281.

(214) Frazier, C. C. Photodynamic therapy in dermatology. *Int. J. Dermatol.* **1996**, *35*, 312–316.

(215) Samanta, S.; Beharry, A. A.; Sadovski, O.; McCormick, T. M.; Babalhavaeji, A.; Tropepe, V.; Woolley, G. A. Photoswitching azo compounds in vivo with red light. *J. Am. Chem. Soc.* **2013**, *135*, 9777–9784.

(216) Yoon, I.; Li, J. Z.; Shim, Y. K. Advance in photosensitizers and light delivery for photodynamic therapy. *Clin. Endosc.* **2013**, *46*, 7–23.

(217) Bléger, D.; Hecht, S. Visible-Light-Activated Molecular Switches. *Angew. Chem. Int. Ed.* **2015**, *54*, 11338–11349.

(218) Bléger, D.; Hecht, S. Aktivierung molekularer Schalter mit sichtbarem Licht. *Angew. Chem.* **2015**, *127*, 11494–11506.

(219) Dong, M.; Babalhavaeji, A.; Samanta, S.; Beharry, A. A.; Woolley, G. A. Red-Shifting Azobenzene Photoswitches for in Vivo Use. *Acc. Chem. Res.* **2015**, *48*, 2662–2670.

(220) Iwahara, T.; Bonasio, R.; Narendra, V.; Reinberg, D. SIRT3 functions in the nucleus in the control of stress-related gene expression. *Mol. Cell. Biol.* **2012**, *32*, 5022–5034.

(221) Vaquero, A.; Sternglanz, R.; Reinberg, D. NAD$^+$-dependent deacetylation of H4 lysine 16 by class III HDACs. *Oncogene* **2007**, *26*, 5505–5520.

(222) Shogren-Knaak, M.; Ishii, H.; Sun, J.-M.; Pazin, M. J.; Davie, J. R.; Peterson, C. L. Histone H4-K16 acetylation controls chromatin structure and protein interactions. *Science* **2006**, *311*, 844–847.

(223) North, B. J.; Marshall, B. L.; Borra, M. T.; Denu, J. M.; Verdin, E. The Human Sir2 Ortholog, SIRT2, Is an NAD$^+$-Dependent Tubulin Deacetylase. *Mol. Cell* **2003**, *11*, 437–444.

(224) Chung, K.-T. Azo dyes and human health: A review. *J. Environ. Sci. Health Part C: Environ. Carcinog. Rev.* **2016**, *34*, 233–261.

(225) Ali, Y.; Hamid, S. A.; Rashid, U. Biomedical Applications of Aromatic Azo Compounds. *Mini Rev. Med. Chem.* **2018**, *18*, 1548–1558.

5 Manuskripte

5.1 Manuskript I

Azologisation and repurposing of a hetero-stilbene-based kinase inhibitor: towards the design of photoswitchable sirtuin inhibitors

Christoph W. Grathwol, Nathalie Wössner, Sören Swyter, Adam C. Smith, Enrico Tapavicza, Robert K. Hofstetter, Anja Bodtke, Manfred Jung, Andreas Link

Beilstein Journal of Organic Chemistry **2019**, *15*, 2170–2183.

DOI: 10.3762/bjoc.15.214

Beiträge der Autoren

Christoph W. Grathwol:	Konzipierung des Projekts
	Planung und Durchführung der Synthesen
	Analytische Charakterisierung
	Photochemische Evaluation
	Erstellen des Manuskripts
Nathalie Wössner:	Biologische Testung
Sören Swyter:	Biologische Testung
Adam C. Smith:	Quantenchemische Berechnungen
Enrico Tapavicza:	Quantenchemische Berechnungen
Robert K. Hofstetter:	Analytische Charakterisierung
Anja Bodtke:	Durchführung der HRMS-Messungen
Manfred Jung:	Betreuung des Projekts
Andreas Link:	Betreuung des Projekts
	Erstellen des Manuskripts

Christoph W. Grathwol

Andreas Link

BEILSTEIN JOURNAL OF ORGANIC CHEMISTRY

Azologization and repurposing of a hetero-stilbene-based kinase inhibitor: towards the design of photoswitchable sirtuin inhibitors

Christoph W. Grathwol[1], Nathalie Wössner[2], Sören Swyter[2], Adam C. Smith[3], Enrico Tapavicza[3], Robert K. Hofstetter[1], Anja Bodtke[1], Manfred Jung[2] and Andreas Link*[1]

Full Research Paper

Open Access

Address:
[1]Institute of Pharmacy, University of Greifswald, Friedrich-Ludwig-Jahn-Str. 17, 17489 Greifswald, Germany, [2]Institute of Pharmaceutical Sciences, University of Freiburg, Albertstr. 25, 79104 Freiburg, Germany and [3]Department of Chemistry and Biochemistry, California State University Long Beach, 1250 Bellflower Boulevard, Long Beach, CA, 90840 USA

Email:
Andreas Link* - link@uni-greifswald.de

* Corresponding author

Keywords:
azo compounds; epigenetics; photoswitch; sirtuins; stilbenes

Beilstein J. Org. Chem. **2019,** *15,* 2170–2183.
doi:10.3762/bjoc.15.214

Received: 28 June 2019
Accepted: 29 August 2019
Published: 16 September 2019

This article is part of the thematic issue "Molecular switches".

Guest Editor: W. Szymanski

Abstract

The use of light as an external trigger to change ligand shape and as a result its bioactivity, allows the probing of pharmacologically relevant systems with spatiotemporal resolution. A hetero-stilbene lead resulting from the screening of a compound that was originally designed as kinase inhibitor served as a starting point for the design of photoswitchable sirtuin inhibitors. Because the original stilbenoid structure exerted unfavourable photochemical characteristics it was remodelled to its heteroarylic diazeno analogue. By this intramolecular azologization, the shape of the molecule was left unaltered, whereas the photoswitching ability was improved. As anticipated, the highly analogous compound showed similar activity in its thermodynamically stable stretched-out (*E*)-form. Irradiation of this isomer triggers isomerisation to the long-lived (*Z*)-configuration with a bent geometry causing a considerably shorter end-to-end distance. The resulting affinity shifts are intended to enable real-time photomodulation of sirtuins in vitro.

Introduction

Sirtuins are protein deacylases that cleave off not only acetyl, but also other acyl groups from the ε-amino group of lysines in histones and many other substrate proteins. This class of lysine deacetylases (KDACs) is distinguished from others by their dependence on the cosubstrate NAD$^+$. In mammals, seven sirtuin isoforms have been identified to date [1]. These can be grouped into five classes (I, II, III, IV and V) according to their phylogenetic relationship [2]. The isoforms Sirt1, Sirt2 and Sirt3 originate from the same phylogenetic branch (class I), but differ in their subcellular localization. Although Sirt1 and Sirt2 were shown to shuttle between nucleus and cytoplasm in a cell-type and cell-cycle dependent manner, Sirt1 is mainly found in the nucleoplasm and Sirt2 in the cytoplasm [3-7]. Sirt3 primarily resides in the mitochondrion [8]. Facing the multitude of diseases that are associated with a dysregulation of sirtuin activity, they represent a promising target for pharmaceutical intervention. For example, selisistat (EX-527, **1**), a nanomolar and selective Sirt1 inhibitor, passed phase II clinical trials as a disease-modifying therapeutic for Huntington's disease (HD) and was acquainted by AOP Orphan Pharmaceuticals AG for phase III trials in 2017 [9,10]. Its structure comprises a carboxamide moiety, which mimics the amide group of the endogenous pan-sirtuin inhibitor nicotinamide (Figure 1). Likewise Sirt2 inhibition was shown to have beneficial effects in animal and cell models of neurodegenerative diseases like HD and Parkinson's disease [11,12]. Sirt3 activity recently was found to play an important role in cardiovascular diseases and extended ageing in humans [13-16]. Regarding tumorigenesis, the knowledge on the influence of sirtuins is inconsistent. Sirt1, Sirt2 and Sirt3 all have been reported to act either as tumor suppressors or promotors, depending on the particular cell type [1,17].

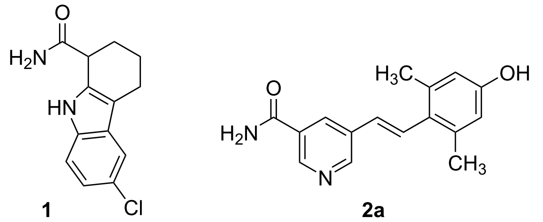

1

2a

Figure 1: Selisistat (**1**) and hit compound GW435821X (**2a**).

The ability to externally control the biological activity of small molecules in vitro or in vivo comprises numerous opportunities for example in the elucidation of biochemical pathways or the reduction of systemic side effects in drug therapy. Molecular photoswitches, i.e., compounds that undergo changes in their geometry and physicochemical properties upon irradiation with light, represent one major approach to this. One of the most common light-driven transformations exploited in molecular photoswitches is the *E*–*Z* isomerization of double bonds [18]. In this context, the photochemistry of stilbenes and the closely related azobenzenes has been studied intensely in the past [19-23]. Due to the multifaceted photoreactivity of unsubstituted stilbenes, an appropriate modification of the stilbene core is necessary to prevent unwanted irreversible side reactions [24,25]. On the contrary, the photochemical properties of azobenzenes are more convenient as already proven by their use as photoswitches in countless biological applications [26-30]. However, their heteroaromatic counterparts still seem underrepresented [31]. The approach to new chemotypes for sirtuin inhibition via known adenosine mimicking kinase inhibitors has already been fruitful in the past [32,33]. Therefore, a focused kinase inhibitor library from GlaxoSmithKline was screened for biological activity on human sirtuin isoforms Sirt1–Sirt3. Azastilbene derivative GW435821X (**2a,** Figure 1), initially published as c-RAF kinase inhibitor, was identified as a moderately active Sirt2 inhibitor with low selectivity [34,35]. In this work, the photoresponsiveness of the hetero-stilbene core structure is examined. Furthermore, an intramolecular azologization approach is performed in order to obtain photoswitchable sirtuin inhibitors, which could be useful tools in the further investigation of the biochemistry and pharmacology of sirtuins.

Results

Chemistry of azastilbenes

All azastilbene derivatives were synthesised by palladium-catalysed cross-coupling reactions using either commercially available 5-bromonicotinamide (**3a**) or methyl 5-bromonicotinate (**3b**). If **3b** was used, transformation to the nicotinamide was accomplished almost quantitatively by addition of a saturated solution of ammonia in anhydrous methanol and stirring in a closed vessel at 40 °C. Compounds **4a** and **b** could easily be obtained through Suzuki coupling with commercially available naphthalene-2-ylboronic acid or (3,4-dihydronaphthalen-2-yl)boronic acid (Scheme 1). The latter was synthesized according to a literature procedure [36].

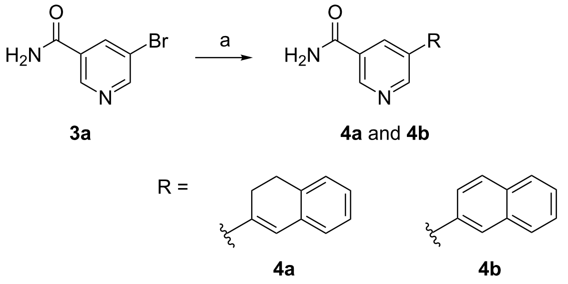

Scheme 1: Reagents and conditions: a) appropriate boronic acid, $Pd(PPh_3)_4$, Na_2CO_3, DMF, H_2O, microwave, 15 min, 150 °C, 43–64%.

Formation of compounds **2b**–**h** was accomplished through Heck coupling of aryl bromides with the appropriate styrenes (Scheme 2) [37].

Compounds **2b** and **2e** were obtained in moderate yield using **3a** as the aryl halide in the Heck reaction. The use of **3b** in the Heck reaction resulted in a substantial improvement of yield in the synthesis of **2g** but not for **2c**. Interchanging the roles by using 5-vinylnicotinamide (**5a**) or methyl 5-vinylnicotinate (**5b**) as alkene component had detrimental effects on the yields in the

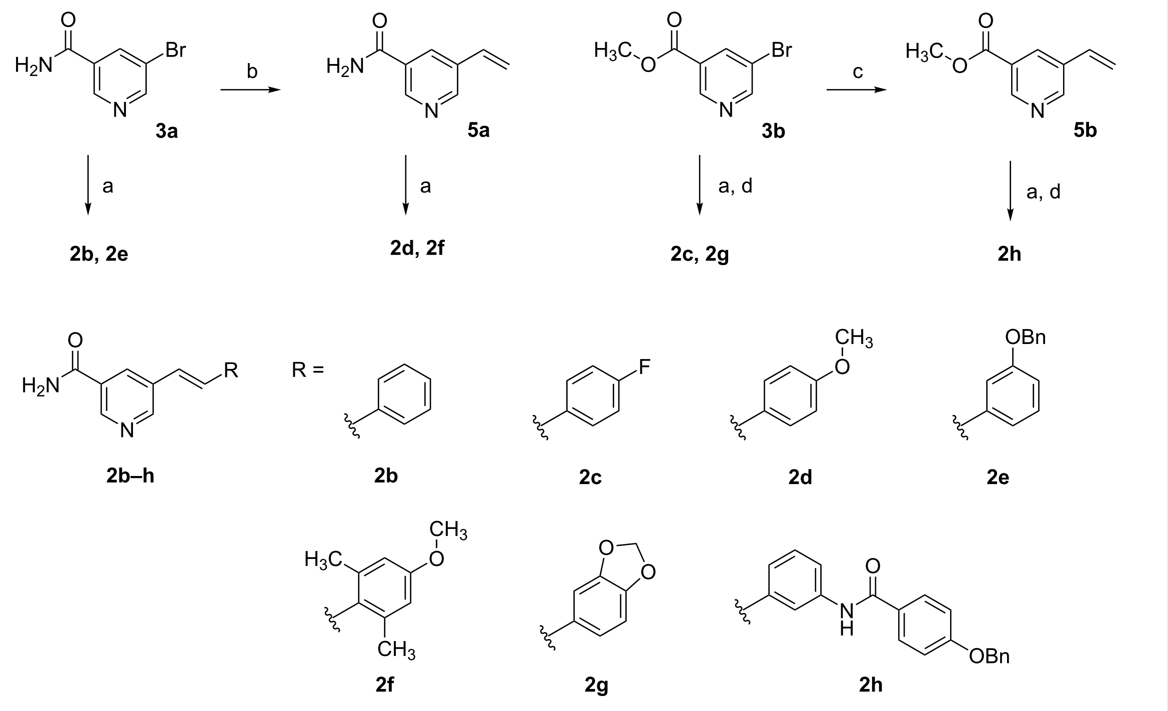

Scheme 2: Reagents and conditions: a) $Pd_2(dba)_3$ or $Pd(OAc)_2$, P(*o*-tol)$_3$, TEA, DMF, 120–140 °C, 0.7–24 h, 11–75%; b) potassium vinyltrifluoroborate, Cs_2CO_3, $PdCl_2(PPh_3)_2$, ACN, H_2O, 1.5 h, 120 °C, 78% c) tributylvinyltin, $Pd(PPh_3)_4$; toluene, reflux, 3 h, 76%; d) NH_3, MeOH, 40 °C, 3 d, 87–95%.

synthesis of **2d**, **2f** and **2h**. Intermediates **5a** and **5b** were accessible from **3a** and **3b** via Suzuki–Miyaura or Stille coupling [34].

Biology

The influence on deacetylase activity of three human sirtuin isoforms (Sirt1–3) was determined in a fluorescence-based assay, using *Z*-Lys(acetyl)-AMC (ZMAL) as a substrate [38]. Compared to the lead structure **2a**, all compounds except **2e**–**h** show increased inhibitory activity against Sirt2 (Table 1). Compound **2c** represents the most potent inhibitior with an IC_{50} value of about 7 µM. Moreover, a slight increase in selectivity for Sirt2 and Sirt3 over Sirt1 could be observed for **2c**, **4a** and **4b**. While none of the modifications provided complete isoenzyme specificity, **2c** preferentially inhibited Sirt2 (IC_{50} 6.6 ± 0.5) and Sirt3 (IC_{50} 7.5 ± 0.9 µM) compared to

Table 1: Sirt1–3 inhibition for compounds **2a–h**, **4a**/**4b** and **8a**.

Compound	Sirt1 inhibition[a]	Sirt2 inhibition[a]	Sirt3 inhibition[a]
2a	27% @ 50 µM	24.6 ± 2.8 µM[b]	41.7 ± 2.0 µM[b]
2b	71% @ 10 µM	8.7 ± 0.2 µM[b]	89% @ 50 µM
2c	51% @ 100 µM	6.6 ± 0.5 µM[b]	7.5 ± 0.9 µM[b]
2d	51% @ 10 µM	64% @ 10 µM	90% @ 50 µM
2e	61% @ 50 µM	69% @ 50 µM	60% @ 50 µM
2f	26% @ 10 µM	21% @ 10 µM	79% @ 50 µM
2g	52% @ 50 µM	62% @ 50 µM	87% @ 50 µM
2h	n.i.	9% @ 10 µM	n.i.
4a	n.i.	48% @ 10 µM	38% @ 10 µM
4b	n.i.	45% @ 10 µM	38% @ 10 µM
8a	n.i.	n.i.	n.i.

[a] Percent inhibition relative to controls at the indicated concentration, n.i. = no inhibition detected. [b] IC_{50} values (µM) with statistical limits; values are the mean ± SD of duplicate experiments.

Sirt1 (51% inhibition at 100 µM). Though not photoswitchable, compounds **4a** and **4b** were synthesized to test the influence of a rigid conformation around the C=C double bond on sirtuin inhibition. Interestingly, this increased rigidity provokes a complete loss of activity against Sirt1. Despite the fact, that all mammalian sirtuins possess profound similarity in their catalytic core domains, many isotype selective inhibitors have been developed in recent years [39-45]. In the case of Sirt2 it was shown that appropriate ligand binding can induce conformational changes of the enzyme, revealing a so-called selectivity pocket, which allows for isotype-specific interactions [46]. A recently developed fluorescence polarization (FP)-based assay enables mapping of ligand binding to this specific binding site [35]. For **2a** an interaction with the selectivity pocket was already implied in the same work. Additionally performed docking studies proposed a binding mode in which **2a** mimics the nicotinamide residue of NAD$^+$, whereas aromatic amino acid residues of the selectivity pocket stabilize the dimethylphenol ring [35]. As photoisomerization in stilbenes and azo dyes is accompanied by a perpendicular twist of the phenyl ring towards the former molecular plane, we assumed that this conformational change should provoke a differential binding situation at least for the dimethylphenol residue in **2a**. Unfortunately, binding of **2b** and **c** could not be localised in the vicinity of the selectivity pocket of Sirt2, so that the binding pose remains unclear.

Photochemistry of azastilbenes

The photochemical behaviour of stilbenes has been subject to intense investigation in the past. It is reported that unsubstituted stilbene undergoes *E*→*Z* photoisomerization [47], as well as photocyclization to dihydrophenanthrene upon UV irradiation, which is oxidized to phenantrene in the presence of oxygen [48]. In high concentrations, (*E*)-stilbene furthermore undergoes photocyclodimerization to cyclobutane derivatives [49]. Photoisomerization and photocyclization are also reported for 3-styrylpyridines, forming two regioisomeric dihydroazaphenanthrenes that are oxidized to 2- and 4-azaphenantrene (not shown), respectively [50].

Photochemistry of compounds **2b** and **2f** was investigated via UV–vis spectroscopy, LC–HRMS and NMR spectroscopy. Compound **2b** represents the core structure of the azastilbenes investigated, whereas in **2f** the influence of *ortho* methylation was intended to be examined. For UV–vis spectroscopy 50 µM solutions in 5% DMSO (v/v) in enzyme assay buffer were used, as this reflects the enzyme assay conditions. However, for LC-HRMS and NMR analysis, a higher concentration of 10 mM in methanol was necessary to receive reliable chromatograms and spectra.

Upon exposure of **2b** to radiation of 365 nm, changes in the UV–vis spectra proceeded slowly, due to the low absorbance of **2b** in this wavelength region. However, shorter wavelengths, i.e. 254 nm, revealed fast and dramatic changes (Figure 2). After an initial decline and blue shift of the absorption maximum, the UV–vis spectrum of **2b** developed a more complex structure with further illumination. The initial spectrum did not restore, neither thermally by standing in the dark nor photochemically when exposed to daylight. Regarding **2f**, 254 nm radiation was obligatory to obtain changes in the UV–vis spectrum. However even long-term radiation did not lead to a complex spectrum as with **2b**, yet no stationary state was reached in the examined time. As in the case of **2b**, the spectrum of **2f** was not altered by daylight, nor by standing several days in the dark at room temperature.

LC–HRMS analysis provided deeper insights and clarified the differential behaviour observed in the UV–vis spectra of **2b** and **2f** after UV irradiation. As anticipated, UV irradiation lead to *E*→*Z* isomerization of the C=C double bond in both compounds. The (*Z*)-isomers were found to be slightly more polar

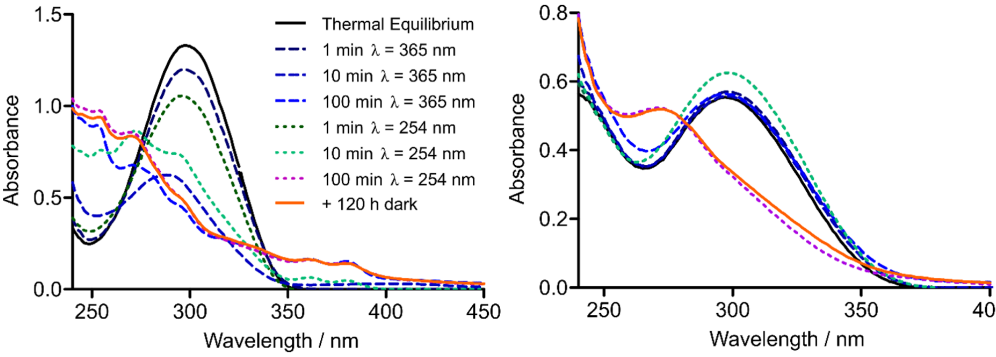

Figure 2: (Left) UV–vis spectrum of **2b** 50 µM in 5% DMSO (v/v) in assay buffer after varying durations of irradiation with 254 nm and 365 nm, respectively. (Right) UV–vis spectrum of **2f** 50 µM in 5% DMSO (v/v) in assay buffer after varying durations of UV radiation.

than the respective (*E*)-isomers and their absorption maxima appeared blue shifted as demonstrated by the UV–vis spectra extracted from the LC runs. Unfortunately, the amount of photoisomerization was only moderate, since after 100 minutes of continuous irradiation still substantial amounts of the (*E*)-isomers were present in the mixtures (Figure 3). Proton NMR analysis implied photostationary states comprising a relative percentage of 45% (*Z*)-**2b** and 57% (*Z*)-**2f**, respectively after 100 minutes of 254 nm irradiation. The NMR spectra can be found in Supporting Information File 1.

The degree of photoisomerization could not be enhanced by extended illumination. Instead, for **2b** prolonged irradiation resulted in the formation of several side products, so that after 10 hours the fractions containing (*E*)-**2b** and (*Z*)-**2b** had declined significantly. This decrease was primarily accompanied by an increase of the fractions containing the benzoquinoline carboxamide isomers **8a** and **b** formed by photocyclization and successive oxidation (Scheme 3). Furthermore, small amounts of cycloaddition products in two fractions were found, probably due to the high concentration of **2b** in the irradiated

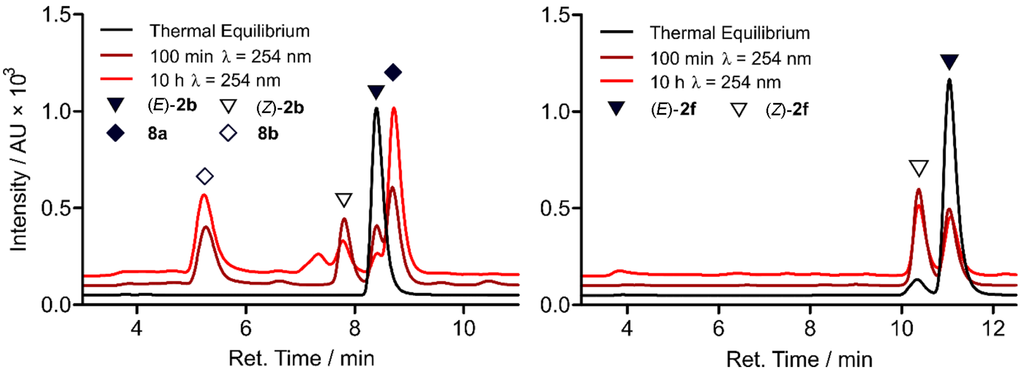

Figure 3: (Left) LC chromatogram of the LC–HRMS analysis of **2b** after varying durations of irradiation with 254 nm. Identity of **8a** was assigned by the reference compound synthesized and allowed differentiation of the two fractions containing photocyclized compounds, as indicated by mass spectra. (Right) LC chromatogram of the LC–HRMS analysis of **2f** after varying durations of irradiation with 254 nm.

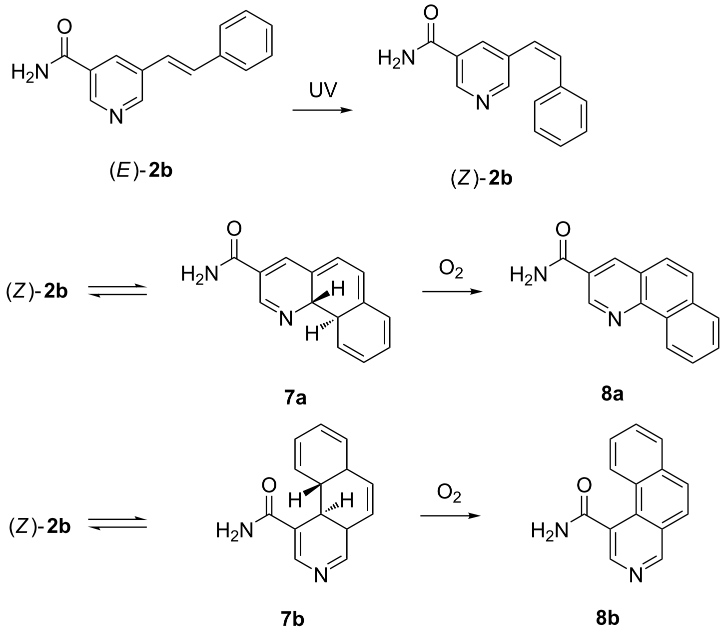

Scheme 3: Photocyclization and oxidation reaction of **2b** upon UV irradiation.

solution. In contrast, **2f** was remarkably stable to long-term UV radiation. Even though the ratio of the double bond isomers was left unaffected, only small traces of the cycloaddition product and some unidentified compounds were registered. No formation of benzoquinoline carboxamides was registered as in the case of **2b**. Hence, due to the sterically blocking *ortho* methyl groups in **2f**, intramolecular photocyclization could be prevented.

To verify the hypothetical structures derived from irradiation of **2b**, we carried out quantum chemical calculations of the double bond isomers (*E*)-**2b** and (*Z*)-**2b** as well as the oxidized compounds **8a** and **8b**. We used density functional theory (DFT) to optimize the ground state equilibrium structures of (*E*)-**2b**, (*Z*)-**2b**, **8a** and **8b**, and used time-dependent DFT (TDDFT) and high-level correlated methods to obtain UV–vis absorption energies and oscillator strengths. To obtain the simulated absorption spectrum and λ_{max} values, oscillator strengths were converted into molar decadic extinction coefficients using a Gaussian line shape with a full-width-at-half-maximum of 0.3 eV. The correlated methods used were second-order approximated coupled cluster singles and doubles (CC2) and its approximation, algebraic diagrammatic construction to second-order (ADC(2)) [51-53]. ADC2 calculations have also been carried out with the implicit solvent continuum model COSMO using a dielectricity constant and refractive index of a methanol/water mixture, which was used as solvent in the experimental UV–vis measurements of the LC-HRMS fractions [54,55]. Geometries for reactants (*E*)-**2b** and (*Z*)-**2b** were optimized for two different rotational isomers ((*E*)-**2b-A** and (*E*)-**2b-B**; (*Z*)-**2b-A** and (*Z*)-**2b-B**), defined in Supporting Information File 1. In the following, we report only the results for (*E*)-**2b-B** and (*Z*)-**2b-A**, since they possess lower ground state energies and therefore are expected to be the dominant species at room temperature. Energy differences of the ground state structures of two pairs of isomers, however, are less than 0.6 kcal/mol, and computed spectra differ only slightly. Extensive results of all structures and all applied computational methods are summarized in the Supporting Information. While TDDFT systematically underestimates the λ_{max} values of the lowest absorption of all compounds by 0.1–0.75 eV, CC2 and ADC(2) agree with the λ_{max} values of the lowest absorption bands with a maximum deviation of 0.15 eV, similar to the previously determined accuracy [56]. We notice a good agreement between ADC(2) gas phase calculations with CC2 gas phase calculations, which justifies the usage of the approximate ADC(2) method.

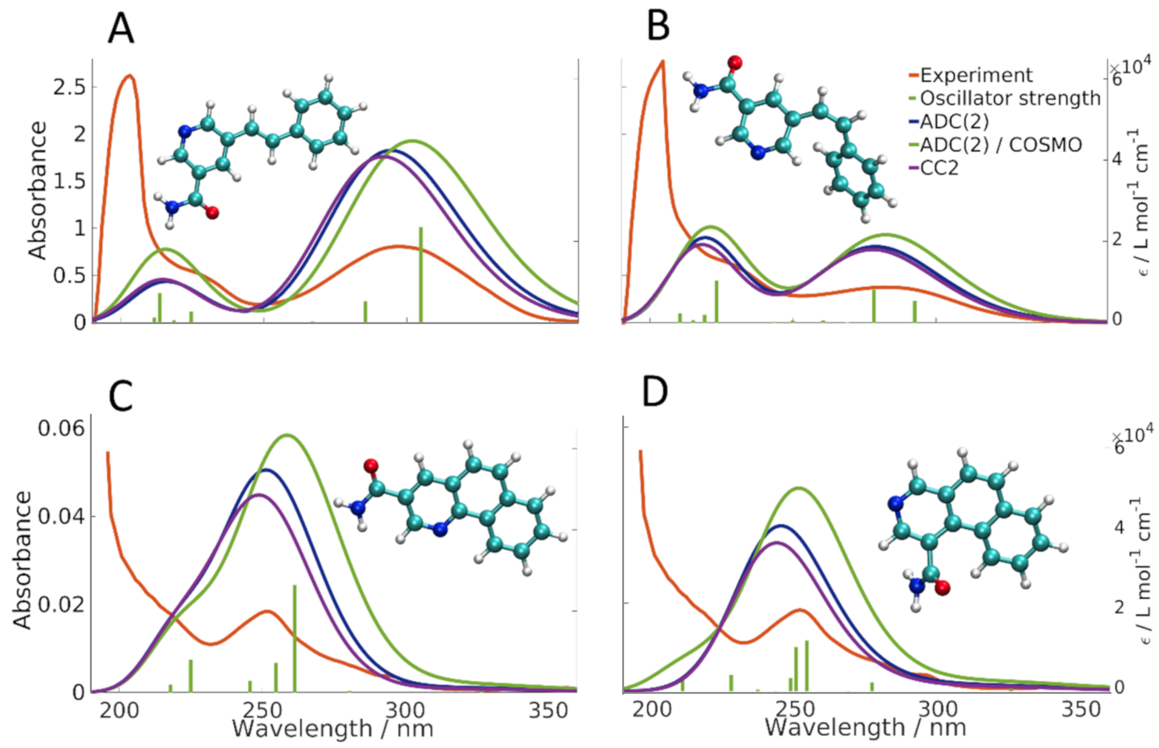

Figure 4: Calculated and experimental absorption spectra of compounds (*E*)-**2b-B** (A), (*Z*)-**2b-A** (B), and products **8a** (C) and **8b** (D). Oscillator strengths (green sticks) correspond to the ADC(2)/COSMO calculation.

Comparing the calculated absorption spectra for (*E*)-**2b-B** and (*Z*)-**2b-A** to the experimental spectra obtained from LC-HRMS (Figure 4A,B), we see that all calculations consistently confirm the experimentally found blue shift of about 15 nm (0.22 eV) for the λ_{max} value of the lowest absorption band. Blue shifts predicted by CC2, ADC(2), ADC(2)/COSMO are 14, 16, and 20 nm, respectively. Consistent with the experimental spectra, all theoretical methods predict the maximum extinction of the lowest absorption band of (*Z*)-**2b** to approximately one half of the one of (*E*)-**2b**. Since the maximum error of the methods (0.15 eV) is smaller than the observed blue shift (0.22 eV), we conclude that the computed λ_{max} values are meaningful and clearly support the successful formation of the *Z*-isomer. Regarding the spectra of the photocyclization and oxidation products **8a** and **8b** (Figure 4C,D), theoretical methods predict the λ_{max} value of the lowest absorption bands within 8 nm (≈0.15 eV) of the value of the experimental spectrum of the LC–HRMS, clearly confirming the experimentally found blue shift of 0.75 eV and 0.54 eV compared to compounds (*E*)-**2b** and (*Z*)-**2b**, respectively. Also here, we conclude that the calculations clearly support the formation of compounds **8a** and/or **8b**. However, due to the similarity of the spectra of **8a** and **8b**, calculations do not allow to predict which of the two isomers was present in the respective fraction analysed.

Regarding the high similarity between **8a**/**8b** and selisistat, it was likely that these cyclized compounds could possess biological activity against sirtuins, too. On the other hand they resemble a fixed (*Z*)-configuration of the stilbene double bond. Therefore, comparison with **2b** could provide information concerning differential biological activity of the two photoisomers. By applying Mallory reaction conditions to a solution of **2b** in methanol utilizing oxygen and iodine as oxidants we were able to isolate a preparative amount of **8a** and tested it for its biological activity against Sirt1, Sirt2 and Sirt3. Surprisingly, **8a** showed complete inactivity towards all sirtuins tested (Table 1). Hence it can be assumed that *E*→*Z* photoisomerization in similar compounds lowers inhibitory strength accordingly.

Synthesis and photochemistry of photoswitchable diazeno analogue

Even though the photochemical properties of *ortho* methylated azastilbenes like **2f** could be improved by preventing photocyclization, they were still unsuitable for the use as photoswitchable sirtuin inhibitors in the enzyme assay. The long irradiation periods that were necessary to obtain significant amounts of the (*Z*)-isomers did not permit switching of the inhibitors in the enzyme assay mixture, as the fluorescent substrate and the enzyme would be harmed by long-term UV radiation. We envisioned to replace the stilbene motive of selected stilbene **2c** by a diazeno group, because photoisomerization of azo dyes was anticipated to proceed fast and reversible by application of UV irradiation and visible light, respectively in this analogue.

5-Diazenylnicotinamide **11** was synthetically accessible in two steps through conversion of commercially available methyl 5-aminonicotinate (**9**) and 4-fluoroaniline to **10** under Mill's reaction conditions and subsequent ammonolysis of the methyl ester **10** to amide **11** (Scheme 4).

Photoswitching of (*E*)-**11** to a long-lived PSS ($t_{½}$ = 300 h) containing 84% of (*Z*)-**11** was possible by short term UV irradiation of 365 nm. The photoisomerization could be reversed by exposure to visible light, i.e. 452 nm, albeit the PSS at 452 nm still comprised about 25% of (*Z*)-**11** as determined by HPLC analysis using UV–vis detection at the isosbestic points (Table 2). Light of 500 nm could also reverse photoisomerization, but was not as effective as 452 nm radiation. 630 nm irradiation, in contrast, did not lead to an altered PSS composition

Table 2: Percentage of *E*/*Z*-isomers of **11** at the thermal equilibrium (Δ), and photostationary states (PSS) after 365 nm and 452 nm irradiation.

	Δ	PSS 5 min 365 nm	PSS 1 min 452 nm
(*E*)-**11**/(*Z*)-**11**	99:1	16:84	75:25

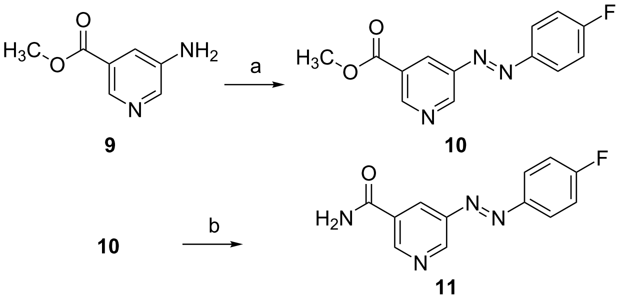

Scheme 4: Reagents and conditions: a) 4-fluoroaniline, oxone, HAc, 60 °C, 14 d, 42%; b) NH_3, MeOH, rt, 3 d, 98%.

obtained by UV irradiation of 365 nm. Switching between the two PSS could be repeated several times without any observable fatigue of the compound (Figure 5).

The photoswitchable diazeno compound **11** was subjected to biological evaluation to test the effect of photoisomerization on the inhibitory activity. The enzyme assay mixture containing **11** was exposed to 5 minutes of 365 nm radiation and compared with the results of a non-irradiated measurement. The applied radiation did not perturb the proper enzyme functioning as proved by an unaltered enzyme activity in the blank tests. Unfortunately, 365 nm radiation turned out to have only minor effects on the IC_{50} values of **11** (Table 3).

Table 3: Sirt1-3 inhibition for compound **11** at the thermal equilibrium (Δ) and the photostationary state (PSS) after 5 minutes of 365 nm irradiation.

Entry	Sirt1 inhibition[a]	Sirt2 inhibition[a]	Sirt3 inhibition[a]
Δ	35% @ 100 µM	18.9 ± 1.38 µM	27.5 ± 3.42 µM
PSS	19% @ 100 µM	24.1 ± 1.69 µM	29.9 ± 2.11 µM

[a]Percent inhibition relative to controls at the indicated concentration, n.i. = no inhibition detected.

Discussion

In recent years, photopharmacology has become a reputable strategy to optically control biochemical processes in the field of enzyme and ion channel modulation and recently 7TM-receptors also called GPCRs. Whereas in most approaches towards photoswitchable ligands the structure of the lead has to be changed considerable in order to incorporate a photoswitchable structural element, this was not the case with azastilbene-based lead structure **2a**. Unfortunately, due to several disadvantages the azastilbene moiety itself was unsuitable as photoswitchable element in this application. Even though competing azaphenantrene formation could be prevented by implementation of blocking *ortho* methyl groups in **2f**, the degree of photoisomerization in the two compounds observed was only moderate and required UV radiation over an extended period of time. Furthermore, the irreversibility of photoisomerization remained a major drawback and made an exchange with a diazeno group mandatory. Typically, it is not clear from the beginning, if the remodelling of the bioactive compounds will lead to an active diazeno derivative or not. The so-called azologization approach, moulded by Trauner et al., features a rational strategy for the design of photoswitchable compounds from established drug molecules through replacing certain core motives with an bioisosteric azobenzene moiety [57-59]. Recent examples have proven successful for receptor ligands by exchange of a linear alkinyl spacer for the zigzag shaped (*E*)-diazeno group [60,61]. In that instance, the geometry of the lead had to be changed considerably but careful design led to useful photoswitches. In the case of lead **2a** no such alteration of geometry was necessary and thus it seemed highly likely, that biological activity could be maintained. Indeed, this hypothesis could be proven. Exchange of the azastilbene double-bond with a diazeno bridge caused only a slight decrease in inhibitory potency against Sirt2 and Sirt3, and the selectivity profile of diazeno compound **11** equals the profile of its direct stilbene analogue **2c**. Concerning photoswitchability, **11** was superior to the stilbenoid structures, as it could be toggled reversibly between two states comprising high amounts of (*E*)-**11** and (*Z*)-**11**, respectively. The other part of the hypothesis was, that by this photoinduced isomerization a considerable drop of activity would occur due to the conformational change and the resulting changed geometry and polarity. However, this part of our hypothesis turned out to be wrong. The over-all conformational changes upon photoisomerization were too small or did not lead to a hindered binding, as antici-

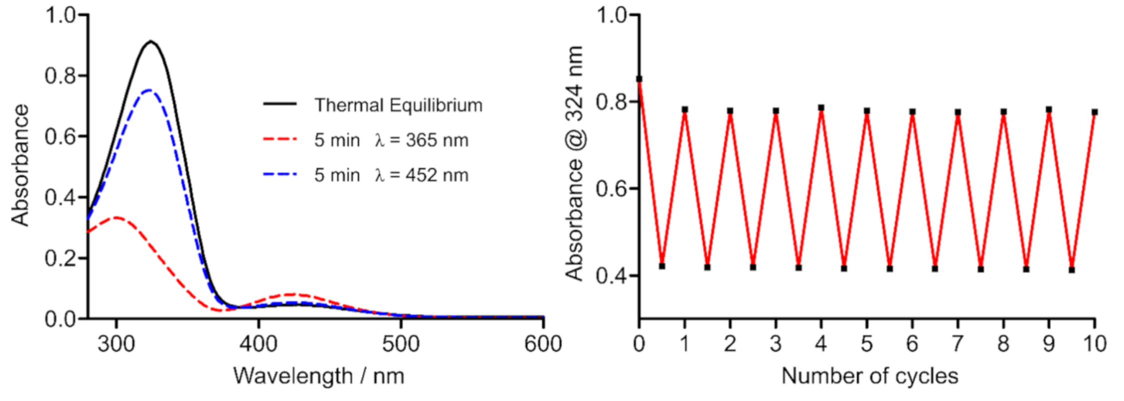

Figure 5: (Left) UV–vis spectrum of **11**, 50 µM in 5% DMSO (v/v), in assay buffer at the thermal equilibrium and the photostationary states (PSS) after 365 nm or 452 nm radiation. (Right) Fatigue resistance of **11**, 50 µM in 5% DMSO (v/v), in assay buffer over 10 cycles of alternating 365 nm and 452 nm radiation.

pated. This result is disappointing, because the photoswitchable sirtuin inhibitor **11** cannot be switched between active and inactive state, as envisioned. Possible reasons could be assigned to substituent effects as demonstrated by Simeth et al. [62]. As recently reported by Schehr et al., reducing agents like DTT, used to prevent enzyme oxidation in crystallization mixtures or in vitro assays, can reduce azo dyes to hydrazine derivatives very fast and thus disable photoisomerization [63]. However, in our enzyme assay no such reducing agents were present, which is why we assume that the photoswitchable diazeno group should still be intact in the enzyme assay mixture. Even if the change in space orientation does not alter binding after irradiation, we would have predicted, that at least the significant difference in polarity of (*E*)-**11** and (*Z*)-**11** should lead to marked differences of sirtuin engagement in vitro. However, recent results from a carefully designed azologization study performed by Rustler et al. led to comparable difficulties [64].

Conclusion

Based on lead structure GW435821X (**2a**) a small library of analogous azastilbene compounds was designed, synthesized and tested for their inhibitory activity against the human sirtuin isoforms Sirt1, Sirt2 and Sirt3. Compared to the lead structure the inhibitory potency could be increased to single digit µM potency for some compounds, while isoenzyme selectivity still remains an issue. The photochemistry of azastilbene compounds **2b** and **2f** was studied. For **2b**, besides photoisomerization, formation of benzoquinoline carboxamides by photocyclization and oxidation was indicated by high accuracy mass spectroscopy. Formation of 4-azaphenantrene derivative **8a** could be proven by isolation and characterization of a preparative sample. Theoretical UV–vis spectra for (*E*)-**2b**, (*Z*)-**2b** and two isomeric benzoquinoline carboxamides reproduced the experimental data. Compound **2f** was unsusceptible to photocyclization due to sterically blocking *ortho* methyl groups but could not be toggled between (*E*)- and (*Z*)-configuration. This lead to the synthesis of a first diazenyl derivative of the lead structure **2a** with promising photochemical characteristics for a new class of photoswitchable sirtuin inhibitors, but the activity difference for the (*E*)- and (*Z*)-isomers needs dramatic improvement before a useful molecular probe can be obtained by this approach.

Experimental

General remarks

All solvents and reagents were obtained from commercial suppliers and were used without purification. Anhydrous solvents were purchased from Acros Organics. Thin-layer chromatography (TLC) was executed on silica gel 60 F_{254} aluminium plates purchased from Merck. Visualization of the compounds was accomplished by UV-light (254 nm and 366 nm) and by staining with iodine, DNPH/H_2SO_4 (2 g 2,4-dinitrophenylhydrazine and 5 mL H_2SO_4 in 50 mL EtOH and 16 mL water) or vanillin/sulfuric acid (3.0 g vanillin and 0.5 mL H_2SO_4 in 100 mL EtOH) reagent. Synthesis was additionally monitored using high speed SFC/MS runs performed by a Nexera SFE-SFC/UHPLC switching system (Shimadzu Corporation, Kyoto, Japan) consisting of a pumping system (one LC-30ADSF for liquid CO_2 and two LC-20ADXR for modifier and make-up delivery), an on-line supercritical fluid extraction module (SFE-30A auto extractor equipped with 0.2 mL extraction vessels) for reaction monitoring, an autosampler (SIL-30AC) for purified compounds, a column thermostat (CTO-20AC) equipped with a Torus DIOL (Waters) or Phenomenex CSP (Lux Amylose-2, i-Amylose-3, i-Cellulose-5), a degasser (DGU-20A5R), a communications module (CBM-20A), and two back pressure regulators BPR A and B (SFC-30A). UV and MS spectra were recorded via photodiode array detection (SPD-M20A) and electrospray ionization single quadrupole MS (LCMS-2020) controlled by Shimadzu LabSolution software (Version 5.91). Chromatographic purification of products was performed by flash chromatography on silica gel (20–45 µm, Carl Roth) applying pressured air up to 0.8 bar. NMR spectra were recorded on a Bruker Avance III instrument (^{1}H NMR: 400 MHz, ^{13}C NMR: 100.6 MHz). Chemical shifts were referenced to tetramethylsilane (TMS) as internal standard in deuterated solvents and reported in parts per million (ppm). Coupling constants (*J*) are reported in Hz using the abbreviations: s = singlet, d = doublet, t = triplet, q = quartet, m = multiplet and combinations thereof, br = broad. Infrared (IR) spectra were recorded on a Bruker Alpha FT-IR spectrometer equipped with a diamond ATR unit and are indicated in terms of absorbance frequency [cm^{-1}]. Microwave synthesis was conducted in a Monowave 300 microwave synthesis reactor from Anton Paar equipped with appropriate sealed reaction vessels G10 (6 mL) or G30 (20 mL), applying a maximum initial power of 850 W to reach a given temperature (IR sensor) for a given time with stirring at 600 rpm. Melting points were measured in open capillary tubes using a Melting Point M-565 apparatus from Büchi and are uncorrected. High accuracy mass spectra were recorded on a Shimadzu LCMS-IT-TOF using ESI ionization. Purity of final compounds was determined by HPLC with DAD (applying the 100% method at 220 nm). Preparative and analytical HPLC were performed using Shimadzu devices CBM-20A, LC-20A P, SIL-20A, FRC-10A with SPD 20A UV–vis detector and an ELSD-LTII. In analytical mode a LiChroCART® (250 × 4 mm) and in preparative mode a Hibar® RT (250 × 25 mm) column, both containing LiChrospher® 100 RP-18e (5 µm), were used. An Elementar Vario MICRO cube was used for the experimental determination of elemental configurations of final pure products. UV–vis spectra were obtained using a Thermo Scientific Genesys 10S UV–vis spectrophotometer.

Synthesis

General procedure for synthesis of nicotinamides from methyl nicotinates: The respective methyl nicotinate was treated with a saturated solution of ammonia in anhydrous MeOH (30 mL) and stirred in a sealed vessel at 40 °C until thin layer chromatography indicated complete conversion of the starting material. The solvent was evaporated under reduced pressure and the residue washed sparingly with cold MeOH.

(*E*)-5-Styrylnicotinamide (2b): In a microwave reaction vessel **3a** (1.01 g, 5.00 mmol, 1.00 equiv) was mixed with styrene (651 mg, 6.25 mmol, 1.25 equiv), tris(*o*-tolyl)phosphine (61 mg, 0.20 mmol, 0.04 equiv), $Pd_2(dba)_3$ (92 mg, 0.10 mmol, 0.02 equiv) and NEt_3 (863 ML, 0.63 g, 6.25 mmol, 1.25 equiv) and suspended in anhydrous DMF (6 mL). The reaction was conducted at 120 °C for 40 min in a microwave reactor. After cooling to room temperature the mixture was taken up in EtOAc and filtered through a pad of Celite®. The filtrate was washed with water (3 × 30 mL) and sat. aq. NaCl solution (30 mL), dried over $MgSO_4$ and concentrated under reduced pressure. The formed precipitate was collected by filtration and recrystallized from EtOAc. The product was obtained as colourless crystals (0.55 g, 2.45 mmol, 49%): R_f = 0.25 (cyclohexane/THF 1:1); mp: 196.4 °C; ^1H NMR (400 MHz, DMSO-d_6) δ (ppm) 8.93 (d, *J* = 2.0 Hz, 1H), 8.90 (d, *J* = 2.1 Hz, 1H), 8.50 (pseudo-t, *J* = 2.0 Hz, 1H), 8.24 (s, br, 1H), 7.71–7.62 (m, 3H), 7.54–7.28 (m, 5H); ^{13}C NMR, DEPT135, HSQC, HMBC (75.5 MHz, DMSO-d_6) δ (ppm) 166.4, 150.4, 147.3, 136.4, 132.4, 131.4, 131.3, 129.6, 128.7, 128.2, 126.7, 124.2; IR (ATR) ν (cm^{-1}): 3372, 3168, 1649, 1619, 1492, 1394, 961, 746, 691, 568; HRESIMS: calcd for $[C_{14}H_{12}N_2O + H]^+$ 224.0950, found 224.0939; comp. purity (220 nm): 100 %; anal. calcd for $C_{14}H_{12}N_2O$: N, 12.49; C, 74.98; H, 5.39; found: N, 12.38; C, 74.81; H, 5.15.

Methyl (*E*)-5-(4-fluorostyryl)nicotinate: Synthesis was conducted according to the procedure of **2b** using **3b** (648 mg, 3.00 mmol, 1.00 equiv), 1-fluoro-4-vinylbenzene (550 mg, 4.50 mmol, 1.50 equiv), tris(*o*-tolyl)phosphine (183 mg, 0.60 mmol, 0.20 equiv), $Pd_2(dba)_3$ (67 mg, 0.30 mmol, 0.10 equiv) and NEt_3 (1.25 mL, 9.00 mmol, 3.00 equiv) in anhydrous DMF (4 mL). The reaction was conducted at 140 °C for 1.5 h. The raw product was purified by silica gel column chromatography (*n*-hexane/EtOAc 2:1) yielding a colourless solid (97 mg, 0.38 mmol, 13%): R_f = 0.50 (*n*-hexane/EtOAc 2:1); mp: 108.2 °C; ^1H NMR, H,H-COSY (400 MHz, $CDCl_3$) δ (ppm) 9.09 (d, *J* = 1.8 Hz, 1H), 8.90 (d, *J* = 2.1 Hz, 1H), 8.52 (pseudo-t, *J* = 2.0 Hz, 1H), 7.57–7.49 (m, 2H), 7.26 (d, *J* = 16.4 Hz, 1H), 7.13–7.06 (m, 2H), 7.03 (d, *J* = 16.4 Hz, 1H); 4.00 (s, 3H, H-8); ^{13}C NMR, DEPT135, HSQC, HMBC (75.5 MHz, $CDCl_3$) δ (ppm) 165.3, 163.2 (d, *J* = 249.4 Hz), 150.1, 147.7, 135.0, 134.0, 135.7, 132.4 (d, *J* = 3.4 Hz), 132.2, 128.8 (d, *J* = 8.2 Hz), 126.9, 122.9 (d, *J* = 2.3 Hz), 116.2 (d, *J* = 21.8 Hz), 52.9; IR (ATR) ν (cm^{-1}): 2957, 1718, 1508, 1433, 1299, 1230, 986, 821, 763; HRESIMS: calcd for $[C_{15}H_{12}NO_2F + H]^+$ 257.0852, found 257.0850.

(*E*)-5-(4-Fluorostyryl)nicotinamide (2c): Synthesis was conducted following the general procedure of nicotinamides from methyl nicotinates, using methyl (*E*)-5-(4-fluorostyryl)nicotinate (75 mg, 0.31 mmol, 1.00 equiv). The product was obtained as colourless solid (65 mg, 0.27 mmol, 87%): R_f = 0.48 (EtOAc/MeOH 95:5); mp: 205.6 °C; ^1H NMR, H,H-COSY (400 MHz, DMSO-d_6) δ (ppm) 8.91 (d, *J* = 1.9 Hz, 1H), 8.88 (d, *J* = 2.0 Hz, 1H), 8.47 (pseudo-t, *J* = 2.0 Hz, 1H), 8.22 (s, 1H), 7.76–7.68 (m, 2H), 7.49 (d, *J* = 16.6 Hz, 1H), 7.31 (d, *J* = 16.6 Hz, 1H), 7.29–7.22 (m, 2H); ^{13}C NMR, DEPT135, HSQC, HMBC (75.5 MHz, DMSO-d_6) δ (ppm) 166.4, 161.9, 150.3, 147.3, 133.1 (d, *J* = 3.2 Hz), 132.3, 131.4, 130.1, 129.7, 128.6 (d, *J* = 8.2 Hz), 124.1 (d, *J* = 2.2 Hz), 115.7 (d, *J* = 21.6 Hz); IR (ATR) ν (cm^{-1}): 3364, 3172, 1650, 1620, 1507, 1397, 1212, 968, 857, 601; HRESIMS: calcd for $[C_{14}H_{11}N_2OF + H]^+$ 242.0855, found 242.0844; comp. purity (220 nm): 100%; anal. calcd for $C_{14}H_{11}N_2OF$: N, 11.56; C, 69.41; H, 4.58; found: N, 11.53; C, 69.89; H, 4.51.

Methyl 5-[(4-fluorophenyl)diazenyl]nicotinate (10): 4-Fluoroaniline (444 mg, 4.00 mmol, 1.00 equiv) was dissolved in DCM (15 mL) and treated with a solution of oxone (4.92 g, 8.00 mmol, 2.00 equiv) in water (50 mL). The biphasic mixture was vigorously stirred until thin layer chromatography indicated complete consumption of the starting material. The watery phase was discarded and the organic phase washed with an aq. HCl-solution (1 M, 3 × 10 mL) and water (3 × 10 mL), then dried over $MgSO_4$. The solution was concentrated to a volume of 5 mL under reduced pressure and added to a solution of **9** (609 mg, 4.00 mmol, 1.00 equiv) in acetic acid (20 mL). The reaction mixture was stirred at 60 °C for two weeks, cooled to room temperature, poured onto ice cooled sat. aq. $NaHCO_3$-solution and extracted with EtOAc (3 × 50 mL). The combined organic extracts were washed with water (3 × 50 mL), sat. aq. NaCl solution (30 mL) and dired over $MgSO_4$. The solvent was evaporated under reduced pressure and the residue purified by silica gel column chromatography (cyclohexane/EtOAc 3:1). The product was obtained as orange solid (431 mg, 1.67 mmol, 42%): R_f = 0.52 (cyclohexane/EtOAc 3:1); mp: 103.6 °C; ^1H NMR, H,H-COSY (400 MHz, DMSO-d_6) δ (ppm) 9.34 (d, *J* = 2.3 Hz, 1H), 9.22 (d, *J* = 2.0 Hz, 1H), 8.50 (pseudo-t, *J* = 2.2 Hz, 1H), 8.09–8.01 (m, 2H), 7.52–7.44 (m, 2H), 3.95 (s, 3H); ^{13}C NMR, DEPT135, HSQC, HMBC (75.5 MHz, DMSO-d_6) δ (ppm) 164.5, 164.4 (d, *J* = 251.8 Hz), 151.8, 150.3, 148.5 (d, J = 2.8 Hz), 146.7, 126.4

(d, J = 6.7 Hz), 125.4 (d, J = 9.5 Hz), 116.6 (d, J = 23.2 Hz), 52.7; IR (ATR) ν (cm^{-1}): 3081, 1713, 1583, 1496, 1286, 1222, 1092, 1000, 843, 498.

5-[(4-Fluorophenyl)diazenyl]nicotinamide (11): Synthesis was conducted following the general procedure of nicotinamides from methyl nicotinates, using **10** (160 mg, 0.62 mmol, 1.00 equiv). The product was obtained as orange solid (149 mg, 0.61 mmol, 98%): R_f = 0.65 (EtOAc/MeOH 95:5); mp: 212.3 °C; ^{1}H NMR, H,H-COSY (400 MHz, DMSO-d_6) δ (ppm) 9.24 (d, J = 2.3 Hz, 1H), 9.20 (d, J = 2.0 Hz, 1H), 8.58 (pseudo-t, J = 2.2 Hz, 1H), 8.38 (s, br, 1H), 8.08–8.02 (m, 2H), 7.80 (s, br, 1H), 7.53–7.45 (m, 2H); ^{13}C NMR, DEPT135, HSQC, HMBC (75.5 MHz, DMSO-d_6) δ (ppm) 165.6, 164.3 (d, J = 251.4 Hz), 150.7, 148.6 (d, J = 2.8 Hz), 148.2, 146.7, 130.5, 125.7, 125.3 (d, J = 9.4 Hz), 116.6 (d, J = 23.2 Hz); IR (ATR) ν (cm^{-1}): 3359, 3125, 1669, 1628, 1496, 1398, 1136, 838, 808, 692; HRESIMS: calcd for $[C_{12}H_9N_4OF + H]^+$ 224.0760, found 224.0753; comp. purity (220 nm): 100%; anal. calcd for $C_{12}H_9N_4OF$: N, 22.94; C, 59.02; H, 3.71; found: N, 22.95; C, 59.46; H, 3.92.

Cloning, expression and purification of recombinant proteins: Expression and purification of $Sirt1_{133-747}$, $Sirt2_{56-356}$, and $Sirt3_{118-395}$ was carried out as described previously. Identity and purity were verified by SDS-PAGE [65]. Protein concentration was determined by the Bradford assay [66]. Deacylase activity of sirtuin isotypes could be inhibited with nicotinamide and was shown to be NAD^+-dependent.

Bioassay: The inhibitory effect of compounds **2a**–**h**, **4a**/**b**, **8a** and **11** on Sirt1–3 was detected via a previously reported fluorescence based assay [38]. The synthetic substrate *Z*-Lys(acetyl)-AMC (ZMAL) is deacetylated by sirtuins, followed by tryptic digestion and thereby release of 7-aminomethylcoumarin, leading to a fluorescent readout. Inhibition was determined by comparing percentage substrate conversion to a DMSO control after subtraction of the blank fluorescence signal. All compounds were tested at 100 µM, 50 µM and 10 µM, respectively. For compounds that showed more than 50% inhibition at 10 µM an IC_{50} value was determined. IC_{50} values were calculated with OriginPro 9.0 G using a non-linear regression to fit the dose response curve. An enzyme-free blank control and a 100% conversion control using AMC instead of ZMAL were measured as well. Inhibition measurements were performed in biological duplicates for all compounds.

Photochemistry: All photoisomerization experiments were conducted under ruby light of 630 nm. Illumination was executed using a Bio-Link 254 Crosslinker from Vilber-Lourmat equipped with six Vilber-Lourmat T8-C lamps (8 W, 254 nm) or six Vilber-Lourmat T8-L lamps (8W, 365 nm), respectively. Visible light radiation of 630 nm (red), 500 nm (green) and 452 nm (blue) was derived from a Paulmann FlexLED 3D strip. All compounds were irradiated in solution, using spectrophotometric grade solvents. Photoisomerization and UV–vis spectra measurement was conducted in quartz cuvettes at room temperature.

Computational details: All calculations were carried out using the TURBOMOLE version 7.2 quantum chemistry package [67]. Geometry optimizations of all compounds in different conformers were carried out using DFT with PBE approximation to the exchange-correlation (XC) functional and employing the SV(P) basis set [68,69]. The 10 lowest excitation energies and their oscillator strengths were computed using the SV(P) basis and the larger def2-TZVP basis set [69]. This was done using TDDFT with the hybrid approximation to the XC functional PBE0, CC2, and ADC(2) [51-53,70-72]. ADC(2) and CC2 calculations make use of the resolution-of-identity approximation [73]. ADC(2) calculations were also done using the continuum solvent model COSMO as previously described [54,55,74-76]. A dielectric constant of 62.14 and a refractive index of 1.3379 were used, which corresponds to a solvent of a 6/4-mixture of methanol/water, as experimentally determined [77,78]. Broadened absorption spectra were simulated by converting oscillator strengths to decadic extinction coefficients using a Gaussian line shape with a full-width-at-half-maximum of 0.3 eV [79-82].

Supporting Information

The Supporting Information features experimental and analytical data for the synthesis of intermediates and compounds **4a**, **4b**, **2c–2h** and **8a** and ^{1}H and ^{13}C NMR spectra for all synthesized compounds. Procedures of photochemical experiments and their analysis are described. Detailed summaries of electronic structure calculations for two conformers (A and B) of each double bond isomer ((*E*)-**2b** and (*Z*)-**2b**), photocyclization and oxidation products **8a** and **8b** are given.

Supporting Information File 1

Experimental procedures, analytical data and quantum chemical calulations.
[https://www.beilstein-journals.org/bjoc/content/supplementary/1860-5397-15-214-S1.pdf]

Acknowledgements

The Jung group thanks the Deutsche Forschungsgemeinschaft (DFG, Ju295/14-1 and RTG1976) for funding.

ORCID® iDs

Christoph W. Grathwol - https://orcid.org/0000-0003-0232-3279
Enrico Tapavicza - https://orcid.org/0000-0002-0640-0297
Robert K. Hofstetter - https://orcid.org/0000-0002-1077-9703
Manfred Jung - https://orcid.org/0000-0002-6361-7716
Andreas Link - https://orcid.org/0000-0003-1262-6636

Preprint

A non-peer-reviewed version of this article has been previously published as a preprint doi:10.3762/bxiv.2019.53.v1

References

1. Schiedel, M.; Robaa, D.; Rumpf, T.; Sippl, W.; Jung, M. *Med. Res. Rev.* **2018,** *38,* 147–200. doi:10.1002/med.21436
2. Frye, R. A. *Biochem. Biophys. Res. Commun.* **2000,** *273,* 793–798. doi:10.1006/bbrc.2000.3000
3. Vaziri, H.; Dessain, S. K.; Eaton, E. N.; Imai, S.-I.; Frye, R. A.; Pandita, T. K.; Guarente, L.; Weinberg, R. A. *Cell* **2001,** *107,* 149–159. doi:10.1016/s0092-8674(01)00527-x
4. Perrod, S.; Cockell, M. M.; Laroche, T.; Renauld, H.; Ducrest, A.-L.; Bonnard, C.; Gasser, S. M. *EMBO J.* **2001,** *20,* 197–209. doi:10.1093/emboj/20.1.197
5. Tanno, M.; Sakamoto, J.; Miura, T.; Shimamoto, K.; Horio, Y. *J. Biol. Chem.* **2007,** *282,* 6823–6832. doi:10.1074/jbc.m609554200
6. Rumpf, T.; Schiedel, M.; Karaman, B.; Roessler, C.; North, B. J.; Lehotzky, A.; Oláh, J.; Ladwein, K. I.; Schmidtkunz, K.; Gajer, M.; Pannek, M.; Steegborn, C.; Sinclair, D. A.; Gerhardt, S.; Ovádi, J.; Schutkowski, M.; Sippl, W.; Einsle, O.; Jung, M. *Nat. Commun.* **2015,** *6,* 6263. doi:10.1038/ncomms7263
7. North, B. J.; Verdin, E. *PLoS One* **2007,** *2,* e784. doi:10.1371/journal.pone.0000784
8. Schwer, B.; North, B. J.; Frye, R. A.; Ott, M.; Verdin, E. *J. Cell Biol.* **2002,** *158,* 647–657. doi:10.1083/jcb.200205057
9. AOP Orphan Pharmaceuticals AG. 2017; https://www.aoporphan.com/global_en/our-company/newsroom/aop-orphan-pharmaceuticals-ag-to-acquire-selisistat-a-clinical-stage-drug-candidate-for-the-treatment-of-huntingtons-disease-hd (accessed June 17, 2019).
10. Süssmuth, S. D.; Haider, S.; Landwehrmeyer, G. B.; Farmer, R.; Frost, C.; Tripepi, G.; Andersen, C. A.; Di Bacco, M.; Lamanna, C.; Diodato, E.; Massai, L.; Diamanti, D.; Mori, E.; Magnoni, L.; Dreyhaupt, J.; Schiefele, K.; Craufurd, D.; Saft, C.; Rudzinska, M.; Ryglewicz, D.; Orth, M.; Brzozy, S.; Baran, A.; Pollio, G.; Andre, R.; Tabrizi, S. J.; Darpo, B.; Westerberg, G.; the PADDINGTON Consortium. *Br. J. Clin. Pharmacol.* **2015,** *79,* 465–476. doi:10.1111/bcp.12512
11. Chopra, V.; Quinti, L.; Kim, J.; Vollor, L.; Narayanan, K. L.; Edgerly, C.; Cipicchio, P. M.; Lauver, M. A.; Choi, S. H.; Silverman, R. B.; Ferrante, R. J.; Hersch, S.; Kazantsev, A. G. *Cell Rep.* **2012,** *2,* 1492–1497. doi:10.1016/j.celrep.2012.11.001
12. Outeiro, T. F.; Kontopoulos, E.; Altmann, S. M.; Kufareva, I.; Strathearn, K. E.; Amore, A. M.; Volk, C. B.; Maxwell, M. M.; Rochet, J.-C.; McLean, P. J.; Young, A. B.; Abagyan, R.; Feany, M. B.; Hyman, B. T.; Kazantsev, A. G. *Science* **2007,** *317,* 516–519. doi:10.1126/science.1143780
13. Pillai, V. B.; Bindu, S.; Sharp, W.; Fang, Y. H.; Kim, G.; Gupta, M.; Samant, S.; Gupta, M. P. *Am. J. Physiol.: Heart Circ. Physiol.* **2016,** *310,* H962–H972. doi:10.1152/ajpheart.00832.2015
14. Lu, Y.; Wang, Y.-d.; Wang, X.-y.; Chen, H.; Cai, Z.-j.; Xiang, M.-x. *Int. J. Cardiol.* **2016,** *220,* 700–705. doi:10.1016/j.ijcard.2016.06.236
15. He, X.; Zeng, H.; Chen, J.-X. *Int. J. Cardiol.* **2016,** *215,* 349–357. doi:10.1016/j.ijcard.2016.04.092
16. Bellizzi, D.; Rose, G.; Cavalcante, P.; Covello, G.; Dato, S.; De Rango, F.; Greco, V.; Maggiolini, M.; Feraco, E.; Mari, V.; Franceschi, C.; Passarino, G.; De Benedictis, G. *Genomics* **2005,** *85,* 258–263. doi:10.1016/j.ygeno.2004.11.003
17. Serrano, L.; Martínez-Redondo, P.; Marazuela-Duque, A.; Vazquez, B. N.; Dooley, S. J.; Voigt, P.; Beck, D. B.; Kane-Goldsmith, N.; Tong, Q.; Rabanal, R. M.; Fondevila, D.; Muñoz, P.; Krüger, M.; Tischfield, J. A.; Vaquero, A. *Genes Dev.* **2013,** *27,* 639–653. doi:10.1101/gad.211342.112
18. Cameron, D.; Eisler, S. *J. Phys. Org. Chem.* **2018,** *31,* e3858. doi:10.1002/poc.3858
19. Suzuki, H. *Bull. Chem. Soc. Jpn.* **1952,** *25,* 145–150. doi:10.1246/bcsj.25.145
20. Bandara, H. M. D.; Burdette, S. C. *Chem. Soc. Rev.* **2012,** *41,* 1809–1825. doi:10.1039/c1cs15179g
21. Cammenga, H. K.; Emel'yanenko, V. N.; Verevkin, S. P. *Ind. Eng. Chem. Res.* **2009,** *48,* 10120–10128. doi:10.1021/ie900800q
22. Meier, H. *Angew. Chem., Int. Ed. Engl.* **1992,** *31,* 1399–1420. doi:10.1002/anie.199213993
23. Han, W.-G.; Lovell, T.; Liu, T.; Noodleman, L. *ChemPhysChem* **2002,** *3,* 167–178. doi:10.1002/1439-7641(20020215)3:2<167::aid-cphc167>3.0.co;2-g
24. Irie, M. *Chem. Rev.* **2000,** *100,* 1685–1716. doi:10.1021/cr980069d
25. Chung, J. W.; Yoon, S.-J.; An, B.-K.; Park, S. Y. *J. Phys. Chem. C* **2013,** *117,* 11285–11291. doi:10.1021/jp401440s
26. Lerch, M. M.; Hansen, M. J.; van Dam, G. M.; Szymanski, W.; Feringa, B. L. *Angew. Chem., Int. Ed.* **2016,** *55,* 10978–10999. doi:10.1002/anie.201601931
27. Hüll, K.; Morstein, J.; Trauner, D. *Chem. Rev.* **2018,** *118,* 10710–10747. doi:10.1021/acs.chemrev.8b00037
28. Hoorens, M. W. H.; Szymanski, W. *Trends Biochem. Sci.* **2018,** *43,* 567–575. doi:10.1016/j.tibs.2018.05.004
29. Tochitsky, I.; Kienzler, M. A.; Isacoff, E.; Kramer, R. H. *Chem. Rev.* **2018,** *118,* 10748–10773. doi:10.1021/acs.chemrev.7b00723
30. Szymański, W.; Beierle, J. M.; Kistemaker, H. A. V.; Velema, W. A.; Feringa, B. L. *Chem. Rev.* **2013,** *113,* 6114–6178. doi:10.1021/cr300179f
31. Crespi, S.; Simeth, N. A.; König, B. *Nat. Rev. Chem.* **2019,** *3,* 133–146. doi:10.1038/s41570-019-0074-6
32. Trapp, J.; Jochum, A.; Meier, R.; Saunders, L.; Marshall, B.; Kunick, C.; Verdin, E.; Goekjian, P.; Sippl, W.; Jung, M. *J. Med. Chem.* **2006,** *49,* 7307–7316. doi:10.1021/jm060118b
33. Falenczyk, C.; Schiedel, M.; Karaman, B.; Rumpf, T.; Kuzmanovic, N.; Grøtli, M.; Sippl, W.; Jung, M.; König, B. *Chem. Sci.* **2014,** *5,* 4794–4799. doi:10.1039/c4sc01346h
34. McDonald, O.; Lackey, K.; Davis-Ward, R.; Wood, E.; Samano, V.; Maloney, P.; Deanda, F.; Hunter, R. *Bioorg. Med. Chem. Lett.* **2006,** *16,* 5378–5383. doi:10.1016/j.bmcl.2006.07.063
35. Swyter, S.; Schiedel, M.; Monaldi, D.; Szunyogh, S.; Lehotzky, A.; Rumpf, T.; Ovádi, J.; Sippl, W.; Jung, M. *Philos. Trans. R. Soc., B* **2018,** *373,* 20170083. doi:10.1098/rstb.2017.0083
36. Buettelmann, B.; Alanine, A.; Bourson, A.; Gill, R.; Heitz, M.-P.; Mutel, V.; Pinard, E.; Trube, G.; Wyler, R. *Chimia* **2004,** *58,* 630–633. doi:10.2533/000942904777677579
37. Heck, R. F. *Palladium reagents in organic syntheses;* Academic Press: London, United Kingdom, 1990.

38. Heltweg, B.; Trapp, J.; Jung, M. *Methods* **2005,** *36,* 332–337. doi:10.1016/j.ymeth.2005.03.003
39. Cui, H.; Kamal, Z.; Ai, T.; Xu, Y.; More, S. S.; Wilson, D. J.; Chen, L. *J. Med. Chem.* **2014,** *57,* 8340–8357. doi:10.1021/jm500777s
40. Ai, T.; Wilson, D. J.; More, S. S.; Xie, J.; Chen, L. *J. Med. Chem.* **2016,** *59,* 2928–2941. doi:10.1021/acs.jmedchem.5b01376
41. Schiedel, M.; Rumpf, T.; Karaman, B.; Lehotzky, A.; Oláh, J.; Gerhardt, S.; Ovádi, J.; Sippl, W.; Einsle, O.; Jung, M. *J. Med. Chem.* **2016,** *59,* 1599–1612. doi:10.1021/acs.jmedchem.5b01517
42. Rumpf, T.; Schiedel, M.; Karaman, B.; Roessler, C.; North, B. J.; Lehotzky, A.; Oláh, J.; Ladwein, K. I.; Schmidtkunz, K.; Gajer, M.; Pannek, M.; Steegborn, C.; Sinclair, D. A.; Gerhardt, S.; Ovádi, J.; Schutkowski, M.; Sippl, W.; Einsle, O.; Jung, M. *Nat. Commun.* **2015,** *6,* 6263. doi:10.1038/ncomms7263
43. Suzuki, T.; Khan, M. N. A.; Sawada, H.; Imai, E.; Itoh, Y.; Yamatsuta, K.; Tokuda, N.; Takeuchi, J.; Seko, T.; Nakagawa, H.; Miyata, N. *J. Med. Chem.* **2012,** *55,* 5760–5773. doi:10.1021/jm3002108
44. Sundriyal, S.; Moniot, S.; Mahmud, Z.; Yao, S.; Di Fruscia, P.; Reynolds, C. R.; Dexter, D. T.; Sternberg, M. J. E.; Lam, E. W.-F.; Steegborn, C.; Fuchter, M. J. *J. Med. Chem.* **2017,** *60,* 1928–1945. doi:10.1021/acs.jmedchem.6b01690
45. Huang, S.; Song, C.; Wang, X.; Zhang, G.; Wang, Y.; Jiang, X.; Sun, Q.; Huang, L.; Xiang, R.; Hu, Y.; Li, L.; Yang, S. *J. Chem. Inf. Model.* **2017,** *57,* 669–679. doi:10.1021/acs.jcim.6b00714
46. Robaa, D.; Monaldi, D.; Wössner, N.; Kudo, N.; Rumpf, T.; Schiedel, M.; Yoshida, M.; Jung, M. *Chem. Rec.* **2018,** *18,* 1701–1707. doi:10.1002/tcr.201800044
47. Smakula, A. *Z. Phys. Chem.* **1934,** *25B,* 90–98. doi:10.1515/zpch-1934-2508
48. Buckles, R. E. *J. Am. Chem. Soc.* **1955,** *77,* 1040–1041. doi:10.1021/ja01609a073
49. Ciamician, G.; Silber, P. *Ber. Dtsch. Chem. Ges.* **1902,** *35,* 4128–4131. doi:10.1002/cber.19020350450
50. Lewis, F. D.; Kalgutkar, R. S.; Yang, J.-S. *J. Am. Chem. Soc.* **2001,** *123,* 3878–3884. doi:10.1021/ja0042027
51. Christiansen, O.; Koch, H.; Jørgensen, P. *Chem. Phys. Lett.* **1995,** *243,* 409–418. doi:10.1016/0009-2614(95)00841-q
52. Hättig, C.; Köhn, A. *J. Chem. Phys.* **2002,** *117,* 6939–6951. doi:10.1063/1.1506918
53. Hättig, C. *Adv. Quantum Chem.* **2005,** *50,* 37–60. doi:10.1016/s0065-3276(05)50003-0
54. Klamt, A.; Schüürmann, G. *J. Chem. Soc., Perkin Trans. 2* **1993,** 799–805. doi:10.1039/p29930000799
55. Lunkenheimer, B.; Köhn, A. *J. Chem. Theory Comput.* **2013,** *9,* 977–994. doi:10.1021/ct300763v
56. Send, R.; Kühn, M.; Furche, F. *J. Chem. Theory Comput.* **2011,** *7,* 2376–2386. doi:10.1021/ct200272b
57. Broichhagen, J.; Frank, J. A.; Trauner, D. *Acc. Chem. Res.* **2015,** *48,* 1947–1960. doi:10.1021/acs.accounts.5b00129
58. Schoenberger, M.; Damijonaitis, A.; Zhang, Z.; Nagel, D.; Trauner, D. *ACS Chem. Neurosci.* **2014,** *5,* 514–518. doi:10.1021/cn500070w
59. Morstein, J.; Awale, M.; Reymond, J.-L.; Trauner, D. *ACS Cent. Sci.* **2019,** *5,* 607–618. doi:10.1021/acscentsci.8b00881
60. Hauwert, N. J.; Mocking, T. A. M.; Da Costa Pereira, D.; Lion, K.; Huppelschoten, Y.; Vischer, H. F.; De Esch, I. J. P.; Wijtmans, M.; Leurs, R. *Angew. Chem., Int. Ed.* **2019,** *58,* 4531–4535. doi:10.1002/anie.201813110
61. Hauwert, N. J.; Mocking, T. A. M.; Da Costa Pereira, D.; Lion, K.; Huppelschoten, Y.; Vischer, H. F.; De Esch, I. J. P.; Wijtmans, M.; Leurs, R. *Angew. Chem.* **2019,** *131,* 4579–4583. doi:10.1002/ange.201813110
62. Simeth, N. A.; Bellisario, A.; Crespi, S.; Fagnoni, M.; König, B. *J. Org. Chem.* **2019,** *84,* 6565–6575. doi:10.1021/acs.joc.8b02973
63. Schehr, M.; Ianes, C.; Weisner, J.; Heintze, L.; Müller, M. P.; Pichlo, C.; Charl, J.; Brunstein, E.; Ewert, J.; Lehr, M.; Baumann, U.; Rauh, D.; Knippschild, U.; Peifer, C.; Herges, R. *Photochem. Photobiol. Sci.* **2019,** *18,* 1398–1407. doi:10.1039/c9pp00010k
64. Rustler, K.; Maleeva, G.; Bregestovski, P.; König, B. *Beilstein J. Org. Chem.* **2019,** *15,* 780–788. doi:10.3762/bjoc.15.74
65. Schiedel, M.; Herp, D.; Hammelmann, S.; Swyter, S.; Lehotzky, A.; Robaa, D.; Oláh, J.; Ovádi, J.; Sippl, W.; Jung, M. *J. Med. Chem.* **2018,** *61,* 482–491. doi:10.1021/acs.jmedchem.6b01872
66. Laemmli, U. K. *Nature* **1970,** *227,* 680–685. doi:10.1038/227680a0
67. *TURBOMOLE,* V7.2 2017; University of Karlsruhe and Forschungszentrum Karlsruhe GmbH, TURBOMOLE GmbH: Karlsruhe, Germany, 2007, http://www.turbomole.com.
68. Perdew, J. P.; Burke, K.; Ernzerhof, M. *Phys. Rev. Lett.* **1996,** *77,* 3865–3868. doi:10.1103/physrevlett.77.3865
69. Schäfer, A.; Horn, H.; Ahlrichs, R. *J. Chem. Phys.* **1992,** *97,* 2571–2577. doi:10.1063/1.463096
70. Perdew, J. P.; Ernzerhof, M.; Burke, K. *J. Chem. Phys.* **1996,** *105,* 9982–9985. doi:10.1063/1.472933
71. Bauernschmitt, R.; Ahlrichs, R. *Chem. Phys. Lett.* **1996,** *256,* 454–464. doi:10.1016/0009-2614(96)00440-x
72. Furche, F.; Ahlrichs, R. *J. Chem. Phys.* **2002,** *117,* 7433–7447. doi:10.1063/1.1508368
73. Eichkorn, K.; Weigend, F.; Treutler, O.; Ahlrichs, R. *Theor. Chem. Acc.* **1997,** *97,* 119–124. doi:10.1007/s002140050244
74. De Haan, D. O.; Tapavicza, E.; Riva, M.; Cui, T.; Surratt, J. D.; Smith, A. C.; Jordan, M.-C.; Nilakantan, S.; Almodovar, M.; Stewart, T. N.; de Loera, A.; De Haan, A. C.; Cazaunau, M.; Gratien, A.; Pangui, E.; Doussin, J.-F. *Environ. Sci. Technol.* **2018,** *52,* 4061–4071. doi:10.1021/acs.est.7b06105
75. Thompson, T.; Tapavicza, E. *J. Phys. Chem. Lett.* **2018,** *9,* 4758–4764. doi:10.1021/acs.jpclett.8b02048
76. Tapavicza, E.; Thompson, T.; Redd, K.; Kim, D. *Phys. Chem. Chem. Phys.* **2018,** *20,* 24807–24820. doi:10.1039/c8cp05181j
77. Mashimo, S.; Kuwabara, S.; Yagihara, S.; Higasi, K. *J. Chem. Phys.* **1989,** *90,* 3292–3294. doi:10.1063/1.455883
78. Herráez, J. V.; Belda, R. *J. Solution Chem.* **2006,** *35,* 1315–1328. doi:10.1007/s10953-006-9059-4
79. Epstein, S. A.; Tapavicza, E.; Furche, F.; Nizkorodov, S. A. *Atmos. Chem. Phys.* **2013,** *13,* 9461–9477. doi:10.5194/acp-13-9461-2013
80. Schalk, O.; Geng, T.; Thompson, T.; Baluyot, N.; Thomas, R. D.; Tapavicza, E.; Hansson, T. *J. Phys. Chem. A* **2016,** *120,* 2320–2329. doi:10.1021/acs.jpca.5b10928
81. Cisneros, C.; Thompson, T.; Baluyot, N.; Smith, A. C.; Tapavicza, E. *Phys. Chem. Chem. Phys.* **2017,** *19,* 5763–5777. doi:10.1039/c6cp08064b
82. Tapavicza, E.; Furche, F.; Sundholm, D. *J. Chem. Theory Comput.* **2016,** *12,* 5058–5066. doi:10.1021/acs.jctc.6b00720

License and Terms

5.2 Manuskript II

Crystal structure of benzo[*h*]quinoline-3-carboxamide

Christoph W. Grathwol, Nicolas Chrysochos, Benedict J. Elvers, Andreas Link,
Carola Schulzke

Acta Crystallographica Section E **2019**, *E75*, 1828–1832.

DOI: 10.1107/S2056989019014440

Beiträge der Autoren

Christoph W. Grathwol:	Planung und Durchführung der Synthesen Analytische Charakterisierung Photochemische Evaluation Erstellen des Manuskripts
Nicolas Chrysochos:	Aufnahme der Röntgenkristallstruktur
Benedict J. Elvers:	Aufnahme der Röntgenkristallstruktur
Andreas Link:	Erstellen des Manuskripts
Carola Schulzke:	Auswertung der Kristallstruktur, Erstellen des Manuskripts

Christoph W. Grathwol

Andreas Link

CRYSTALLOGRAPHIC COMMUNICATIONS

ISSN 2056-9890

Crystal structure of benzo[*h*]quinoline-3-carboxamide

Christoph W. Grathwol,[a] Nicolas Chrysochos,[b] Benedict J. Elvers,[b] Andreas Link[a]* and Carola Schulzke[b]*

[a]Institut für Pharmazie, Universität Greifswald, Friedrich-Ludwig-Jahn-Strasse 17, 17489 Greifswald, Germany, and [b]Institut für Biochemie, Felix-Hausdorff-Strasse 4, 17489 Greifswald, Germany. *Correspondence e-mail: link@uni-greifswald.de, carola.schulzke@uni-greifswald.de

Received 14 October 2019
Accepted 22 October 2019

Edited by J. Simpson, University of Otago, New Zealand

Keywords: crystal structure; benzoquinoline; nicotinamide derivative; photocyclization.

CCDC reference: 1960760

Supporting information: this article has supporting information at journals.iucr.org/e

The title compound, $C_{14}H_{10}N_2O$, crystallizes in the monoclinic space group $P2_1/c$ with four molecules in the unit cell. All 17 non-H atoms of one molecule lie essentially in one plane. In the unit cell, two pairs of molecules are exactly coplanar, while the angle between these two orientations is close to perfectly perpendicular at 87.64 (6)°. In the crystal, molecules adopt a 50:50 crisscross arrangement, which is held together by two nonclassical and two classical intermolecular hydrogen bonds. The hydrogen-bonding network together with off-centre π–π stacking interactions between the pyridine and outermost benzene rings, stack the molecules along the *b*-axis direction.

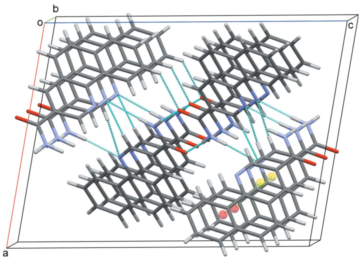

1. Chemical context

Quinoline and benzoquinoline scaffolds are common structural motifs in artificial, as well as natural products, and many of these compounds are of enormous value for pharmacotherapy. Their multifaceted biological efficacy is outstanding and ranges from cardiovascular (Ferlin *et al.*, 2002; Abouzid *et al.*, 2008) and anti-inflammatory effects (Kumar *et al.*, 2009; Hussaini, 2016) to antimicrobial (El Shehry *et al.*, 2018), as well as anticancer activity (Abdelsalam *et al.*, 2019; Haiba *et al.*, 2019; Jafari *et al.*, 2019; Musiol, 2017; Marzaro *et al.*, 2016). In a report on 3-(tetrazol-5-yl)quinolines with antiallergic potential, benzo[*h*]quinoline-3-carboxamide was mentioned as a synthetic intermediate, though its biological activity was not determined in that work (Erickson *et al.*, 1979). In our recent studies on photoswitchable sirtuin inhibitors, we obtained benzo[*h*]quinoline-3-carboxamide as a side product of aza-stilbene photoisomerization (Grathwol *et al.*, 2019). By UV radiation, (*E*)-5-styrylnicotinamide was transformed to its *Z* isomer as envisioned, but underwent photocyclization and successive oxidation, yielding two isomeric benzoquinoline derivatives; the identity of one of these was determined to be the benzo[*h*]quinoline derivative and its crystal structure is reported here.

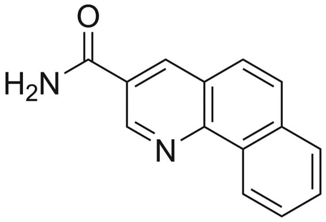

Table 1
Hydrogen-bond geometry (Å, °).

$D—\mathrm{H}\cdots A$	$D—\mathrm{H}$	$\mathrm{H}\cdots A$	$D\cdots A$	$D—\mathrm{H}\cdots A$
N1—H1$N\cdots$N2$^{\mathrm{i}}$	0.97 (3)	2.17 (3)	3.133 (3)	173 (2)
N1—H1$P\cdots$O1$^{\mathrm{ii}}$	0.93 (3)	1.96 (3)	2.895 (3)	175 (3)
C3—H3$\cdots$N2$^{\mathrm{i}}$	0.95	2.41	3.361 (3)	174
C7—H7$\cdots$O1$^{\mathrm{iii}}$	0.95	2.45	3.140 (3)	129

Symmetry codes: (i) $-x+1, y-\frac{1}{2}, -z+\frac{1}{2}$; (ii) $-x+1, -y-1, -z+1$; (iii) $x, -y+\frac{1}{2}, z-\frac{1}{2}$.

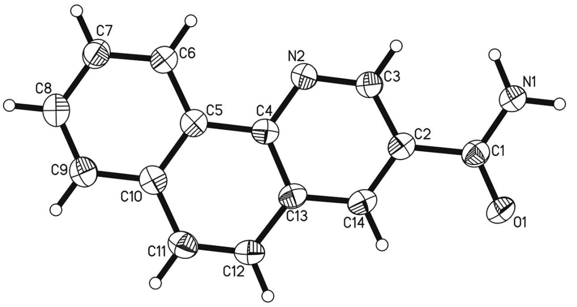

Figure 1
The molecular structure of benzo[*h*]quinoline-3-carboxamide. Displacement ellipsoids are shown at the 50% probability level.

2. Structural commentary

The title compound, benzo[*h*]quinoline-3-carboxamide, crystallizes in the monoclinic space group $P2_1/c$. Four molecules are present in the unit cell ($Z = 4$) and there is one molecule in the asymmetric unit. Benzo[*h*]quinoline-3-carboxamide consists of a nicotinamide unit being fused with a benzo[*h*]quinoline moiety, while the pyridine ring is shared between these two common structural building blocks (Fig. 1). The molecule is essentially flat, with a largest deviation from the plane through all 17 non-H atoms of 0.050 (2) Å (O1) and an r.m.s. deviation of 0.020 (2) Å. In the unit cell, the four molecules are arranged in two perfectly coplanar pairs, with a nearly perpendicular angle between the respective planes of the two pairs of 87.64 (6)° (Fig. 2). A plethora of crystal structures are known for compounds with one or other of the two building blocks that make up this molecule [for the nicotinamide scaffold, *ConQuest* finds over 2000 hits in the Cambridge Structural Database (CSD), while for benzoquinoline, there are over 500; Groom *et al.*, 2016]. However, the specific combination in the title compound is unprecedented. Comparing the title compound to the known structures of unsubstituted nicotinamides, its pronounced planarity is most notable. In the six published structures in the space groups $P2_1/c$ or $P2_1/a$, the angles between the aromatic plane (here C2/C3/N2/C4/C13/C14) and the amide substituent (here O1/N1/C1) range from 22.1 to 23.3° (general CSD refcode NICOAM; Wright & King, 1954; Miwa *et al.*, 1999; Fábián *et al.*, 2011; Jarzembska *et al.*, 2014), *i.e.* this angle is quite consistent. In the only distinct polymorph of a nicotinamide in the space group $P2/a$, four distinct molecules were refined with this angle ranging from 8.1 to 22.4° (Li *et al.*, 2011), *i.e.* they are not very consistent but still considerably larger than the corresponding angle found in the title compound, which is a mere 3.3 (4)°. This points toward an extension of the aromatic resonance systems to include the amide substituent. In the parent nicotinamide scaffolds, this does not occur. Similarly, the comparatively long C1═O1 distance of 1.238 (3) Å (average 1.23 Å) and the comparatively short C1—C2 distance of 1.491 (3) Å (average 1.50 Å in other nicotinamide structures) indicate some involvement of these atoms in resonance effects. In support of this extended resonance, in the nicotinamide structures, the aromatic C—C bonds are much less diverse (range 1.38–1.39 Å, indicating very strong aromaticity in the pyridine ring) than in the structure reported here. In fact, the C—C [range 1.376 (3)–1.414 (3) Å] and C—N [1.321 (3) and 1.360 (3) Å] bond lengths here are much

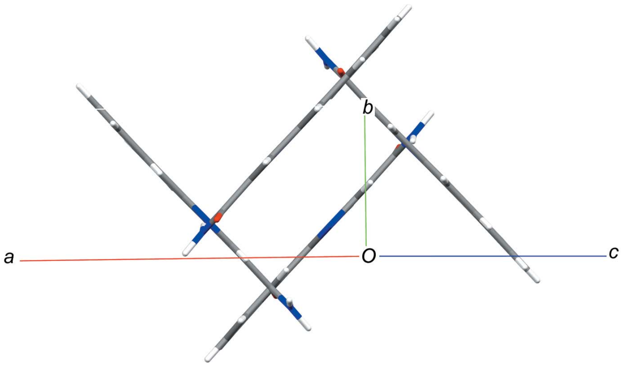

Figure 2
The unit cell of benzo[*h*]quinoline-3-carboxamide in $P2_1/c$, with its four molecules in a coplanar and perpendicular arrangement, viewed along the *ac* diagonal.

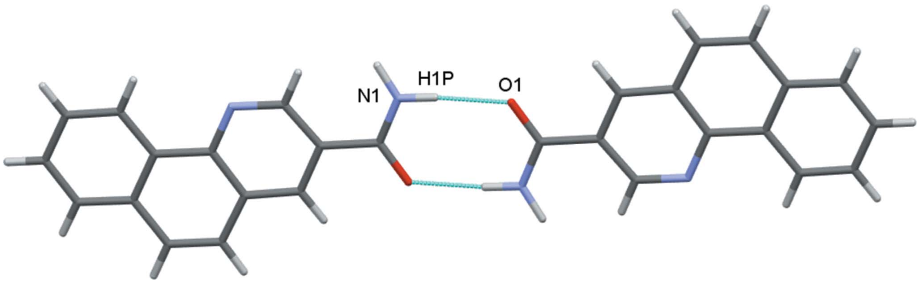

Figure 3
Dimers formed by N—H$\cdots$O hydrogen bonds.

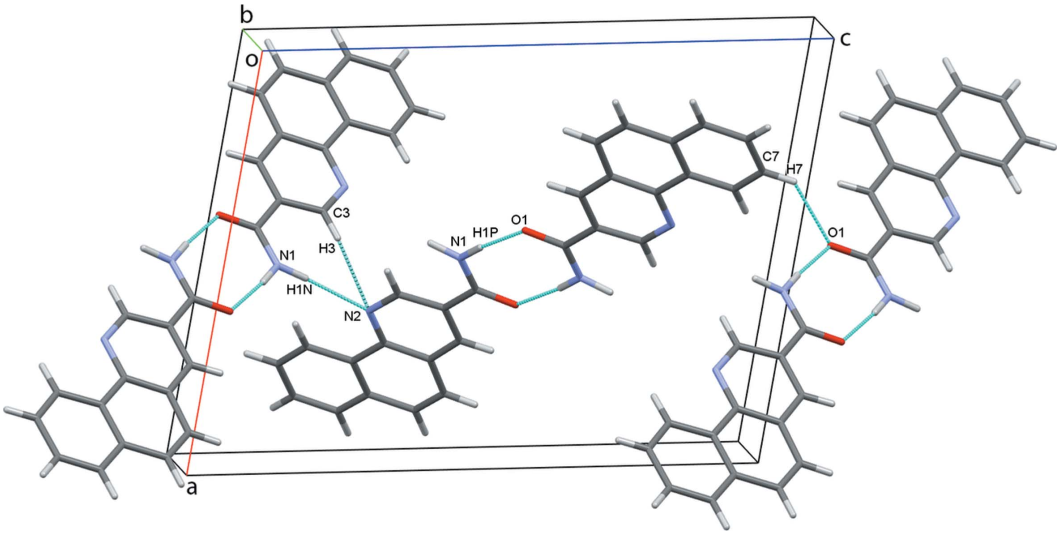

Figure 4
Chains of dimers along the *c*-axis.

more similar to the two known structures of 2-unsubstituted and 3-substituted benzo[*h*]quinolines (refcodes JAFVEU and SUDVES), with ranges of average C—C and C—N bond lengths of 1.38–1.42 and 1.32–1.36 Å, respectively (Martínez *et al.*, 1992; Luo *et al.*, 2015). The benzo[*h*]quinoline structural motif therefore dominates the observed metrical parameters of the molecule reported here, representing a fusion between a nicotinamide and a benzo[*h*]quinoline, with a partial extension of the aromaticity beyond the ring system and extending towards the amide substituent.

3. Supramolecular features

In the crystal, the planar molecules are all arranged in planes in two distinct orientations, which are nearly perpendicular to each other [angle 87.64 (6)°]. This forms a crisscross pattern when viewed along the *ac* diagonal (Fig. 2). Classical inversion-related N1—H1*P*···O1 hydrogen bonds form dimers and generate $R_2^2(8)$ ring motifs (Fig. 3). Each molecule forms two classical (N—H···O and N—H···N) and two nonclassical (C—H···N and C—H···O) hydrogen bonds (Table 1), and these contacts link adjacent dimers into zigzag chains along the *c*-axis direction (Fig. 4). The observed packing is further stabilized by off-centre π–π stacking between the pyridine and outermost benzene rings of each of the coplanar layers [centroid-to-centroid distance = 3.610 (1) Å] (Fig. 5). These contacts combine to stack the molecules along the *b*-axis direction (Fig. 6).

4. Synthesis and crystallization

A solution of (*E*)-5-styrylnicotinamide (673 mg, 3.00 mmol, 1.00 equiv.) in methanol (350 ml) was treated with a solution

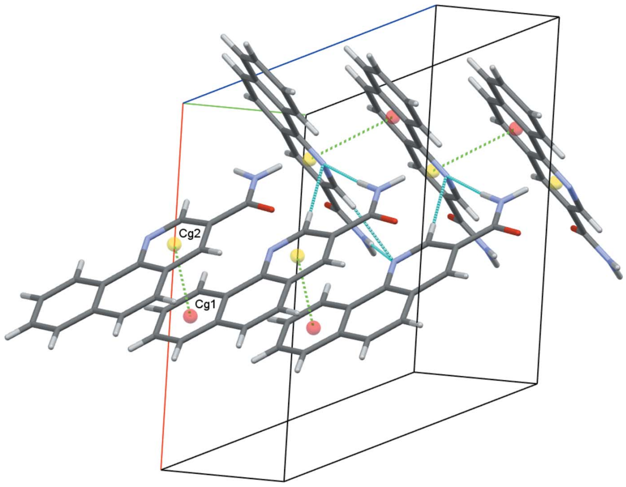

Figure 5
π–π stacking interactions, with centroids shown as coloured spheres. *Cg*1 and *Cg*2 are the centroids of the C5–C10 and C2/C3/N2/C4/C13/C14 rings, respectively.

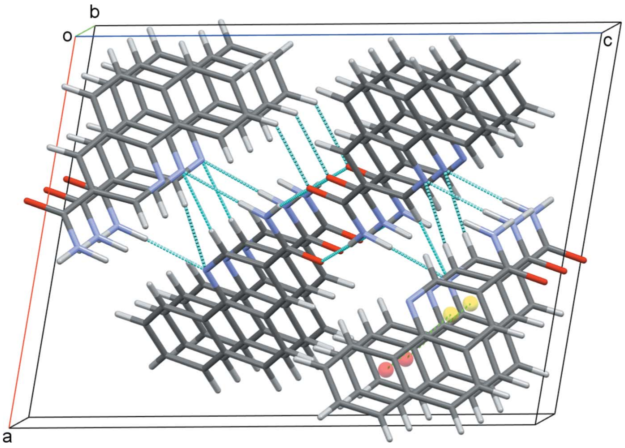

Figure 6
The overall packing of the title compound, viewed along the *b*-axis direction.

of iodine (38 mg, 0.15 mmol, 0.05 equiv.) in methanol (50 ml). A slow stream of compressed air was bubbled through the reaction mixture while it was irradiated with UV light (six Vilber-Lourmat T8-C lamps, 8 W, 254 nm). After complete consumption of the starting material (24 h), the solvent was removed under reduced pressure. Purification of the residue by silica-gel column chromatography (*n*-hexane/THF, 1:1 *v*/*v*) gave pure benzo[*h*]quinoline-3-carboxamide as a colourless solid (yield 80 mg, 0.36 mmol, 12%). Crystallization was accomplished by slow evaporation of a solution in THF (5 mg ml^{-1}) and yielded the title compound as colourless needles: R_F = 0.32 (*n*-hexane/THF, 1:1 *v*/*v*); m.p. 549.8 K (decomposition); ^{1}H NMR, H,H-COSY (400 MHz, DMSO-d_6): δ (ppm) 9.48 (*d*, *J* = 2.2 Hz, 1H, C3-H), 9.26–9.19 (*m*, 1H, C6-H), 8.89 (*d*, *J* = 2.1 Hz, 1H, C14-H), 8.36 (*s*, *br*, 1H, N1-H), 8.12–8.07 (*m*, 1H, C9-H), 8.03 (*d*, *J* = 8.9 Hz, 1H, C11-H), 7.95 (*d*, *J* = 8.9 Hz, 1H, C12-H), 7.85–7.78 (*m*, 2H, C7-H, C8-H), 7.74 (*s*, *br*, 1H, N1-H); ^{13}C NMR, DEPT135, HSQC, HMBC (101 MHz, DMSO-d_6): δ (ppm) 166.4 (C1), 147.8 (C3), 146.7 (C4), 135.5 (C14), 133.8 (C13), 130.3 (C5), 129.0 (C8), 128.1 (C9/C11), 128.0 (C9/C11), 127.8 (C2), 127.3 (C7), 125.8 (C12), 124.9 (C10), 124.1 (C6); IR (ATR): ν (cm^{-1}) 3336, 3136, 1686, 1482, 1395, 1295, 801, 691, 539, 489; ESI–HRMS calculated for $[C_{14}H_{10}N_2O + H]^+$ 222.0793, found 222.0796; compound purity (220 nm): 100%.

5. Refinement

Crystal data, data collection and structure refinement details are summarized in Table 2. All C-bound H atoms constitute aromatic protons, which were attached in calculated positions and treated as riding with $U_{iso}(H) = 1.2U_{eq}(C)$. The two amine H atoms were found and refined without any constraints or restraints.

Table 2
Experimental details.

Crystal data	
Chemical formula	$C_{14}H_{10}N_2O$
M_r	222.24
Crystal system, space group	Monoclinic, $P2_1/c$
Temperature (K)	170
a, b, c (Å)	12.634 (3), 4.9426 (10), 16.778 (3)
β (°)	100.53 (3)
V (Å^3)	1030.0 (4)
Z	4
Radiation type	Mo $K\alpha$
μ (mm^{-1})	0.09
Crystal size (mm)	0.37 × 0.07 × 0.04
Data collection	
Diffractometer	Stoe IPDS-2T
Absorption correction	Numerical face indexed
T_{min}, T_{max}	0.727, 0.997
No. of measured, independent and observed [$I > 2\sigma(I)$] reflections	10053, 2551, 1320
R_{int}	0.087
$(\sin \theta/\lambda)_{max}$ (Å^{-1})	0.667
Refinement	
$R[F^2 > 2\sigma(F^2)]$, $wR(F^2)$, S	0.055, 0.167, 0.98
No. of reflections	2551
No. of parameters	163
H-atom treatment	H atoms treated by a mixture of independent and constrained refinement
$\Delta\rho_{max}$, $\Delta\rho_{min}$ (e Å^{-3})	0.23, −0.27

Computer programs: *X-AREA* (Stoe & Cie, 2010), *SHELXT2018* (Sheldrick, 2015*a*), *SHELXL2018* (Sheldrick, 2015*b*), *XP* in *SHELXTL* (Sheldrick, 2008), *Mercury* (Macrae *et al.*, 2008), *CIFTAB* (Sheldrick, 2015*b*) and *publCIF* (Westrip, 2010).

Acknowledgements

The authors acknowledge support for the Article Processing Charge from the DFG (German Research Foundation) and the Open Access Publication Fund of the University of Greifswald.

Funding information

Funding for this research was provided by: Deutsche Forschungsgemeinschaft (grant No. 393148499).

References

Abdelsalam, E. A., Zaghary, W. A., Amin, K. M., Abou Taleb, N. A., Mekawey, A. A. I., Eldehna, W. M., Abdel-Aziz, H. A. & Hammad, S. F. (2019). *Bioorg. Chem.* **89**, 102985.

Abouzid, K., Abdel Hakeem, M., Khalil, O. & Maklad, Y. (2008). *Bioorg. Med. Chem.* **16**, 382–389.

El Shehry, M. F., Ghorab, M. M., Abbas, S. Y., Fayed, E. A., Shedid, S. A. & Ammar, Y. A. (2018). *Eur. J. Med. Chem.* **143**, 1463–1473.

Erickson, H. E., Hainline, C. F., Lenon, L. S., Matson, C. J., Rice, T. K., Swingle, K. F. & Van Winkle, M. (1979). *J. Med. Chem.* **22**, 816–823.

Fábián, L., Hamill, N., Eccles, K. S., Moynihan, H. A., Maguire, A. R., McCausland, L. & Lawrence, S. E. (2011). *Cryst. Growth Des.* **11**, 3522–3528.

Ferlin, M. G., Chiarelotto, G., Antonucci, F., Caparrotta, L. & Froldi, G. (2002). *Eur. J. Med. Chem.* **37**, 427–434.

Grathwol, C. W., Wössner, N., Swyter, S., Smith, A. C., Tapavicza, E., Hofstetter, R. K., Bodtke, A., Jung, M. & Link, A. (2019). *Beilstein J. Org. Chem.* **15**, 2170–2183.

Groom, C. R., Bruno, I. J., Lightfoot, M. P. & Ward, S. C. (2016). *Acta Cryst.* B**72**, 171–179.

Haiba, M. E., Al-Abdullah, E. S., Ahmed, N. S., Ghabbour, H. A. & Awad, H. M. (2019). *J. Mol. Struct.* **1195**, 702–711.

Hussaini, S. M. A. (2016). *Expert Opin. Ther. Pat.* **26**, 1201–1221.

Jafari, F., Baghayi, H., Lavaee, P., Hadizadeh, F., Soltani, F., Moallemzadeh, H., Mirzaei, S., Aboutorabzadeh, S. M. & Ghodsi, R. (2019). *Eur. J. Med. Chem.* **164**, 292–303.

Jarzembska, K. N., Hoser, A. A., Kamiński, R., Madsen, A., Durka, K. & Woźniak, K. (2014). *Cryst. Growth Des.* **14**, 3453–3465.

Kumar, S., Bawa, S. & Gupta, H. (2009). *Mini Rev. Med. Chem.* **9**, 1648–1654.

Li, J., Bourne, S. A. & Caira, M. R. (2011). *Chem. Commun.* **47**, 1530–1532.

Luo, C.-Z., Gandeepan, P., Wu, Y.-C., Chen, W.-C. & Cheng, C.-H. (2015). *RSC Adv.* **5**, 106012–106018.

Macrae, C. F., Bruno, I. J., Chisholm, J. A., Edgington, P. R., McCabe, P., Pidcock, E., Rodriguez-Monge, L., Taylor, R., van de Streek, J. & Wood, P. A. (2008). *J. Appl. Cryst.* **41**, 466–470.

Martínez, R., Toscano, R. A., Linzaga, I. E. & Sánchez, H. (1992). *J. Heterocycl. Chem.* **29**, 1385–1388.

Marzaro, G., Dalla Via, L., García-Argáez, A. N., Dalla Via, M. & Chilin, A. (2016). *Bioorg. Med. Chem. Lett.* **26**, 4875–4878.

Miwa, Y., Mizuno, T., Tsuchida, K., Taga, T. & Iwata, Y. (1999). *Acta Cryst.* B**55**, 78–84.

Musiol, R. (2017). *Exp. Opin. Drug Discov.* **12**, 583–597.
Sheldrick, G. M. (2008). *Acta Cryst.* A**64**, 112–122.
Sheldrick, G. M. (2015*a*). *Acta Cryst.* A**71**, 3–8.
Sheldrick, G. M. (2015*b*). *Acta Cryst.* C**71**, 3–8.
Stoe & Cie (2010). *X-AREA*. Stoe & Cie GmbH, Darmstadt, Germany.
Westrip, S. P. (2010). *J. Appl. Cryst.* **43**, 920–925.
Wright, W. B. & King, G. S. D. (1954). *Acta Cryst.* **7**, 283–288.

supporting information

Acta Cryst. (2019). E**75**, 1828-1832   [https://doi.org/10.1107/S2056989019014440]

Crystal structure of benzo[*h*]quinoline-3-carboxamide

Christoph W. Grathwol, Nicolas Chrysochos, Benedict J. Elvers, Andreas Link and Carola Schulzke

Computing details

Data collection: *X-AREA* (Stoe & Cie, 2010).; cell refinement: *X-AREA* (Stoe & Cie, 2010).; data reduction: *X-AREA* (Stoe & Cie, 2010).; program(s) used to solve structure: SHELXT2018 (Sheldrick, 2015a); program(s) used to refine structure: *SHELXL2018* (Sheldrick, 2015b); molecular graphics: *XP* in *SHELXTL* (Sheldrick, 2008) and *Mercury* (Macrae *et al.*, 2008); software used to prepare material for publication: CIFTAB (Sheldrick, 2015b) and *publCIF* (Westrip, 2010).

Benzo[*h*]quinoline-3-carboxamide

Crystal data

$C_{14}H_{10}N_2O$
$M_r = 222.24$
Monoclinic, $P2_1/c$
$a = 12.634\ (3)$ Å
$b = 4.9426\ (10)$ Å
$c = 16.778\ (3)$ Å
$\beta = 100.53\ (3)°$
$V = 1030.0\ (4)$ Å^3
$Z = 4$
$F(000) = 464$
$D_x = 1.433$ Mg m^{-3}
Mo $K\alpha$ radiation, $\lambda = 0.71073$ Å
Cell parameters from 11960 reflections
$\theta = 6.4–59.0°$
$\mu = 0.09$ mm^{-1}
$T = 170$ K
Needle, colourless
0.37 × 0.07 × 0.04 mm

Data collection

Stoe IPDS2T diffractometer
Radiation source: fine-focus sealed tube
Detector resolution: 6.67 pixels mm^{-1}
ω scans
Absorption correction: numerical face indexed
$T_{min} = 0.727$, $T_{max} = 0.997$
10053 measured reflections
2551 independent reflections
1320 reflections with $I > 2\sigma(I)$
$R_{int} = 0.087$
$\theta_{max} = 28.3°$, $\theta_{min} = 3.2°$
$h = -16 \rightarrow 16$
$k = -6 \rightarrow 6$
$l = -22 \rightarrow 22$

Refinement

Refinement on F^2
Least-squares matrix: full
$R[F^2 > 2\sigma(F^2)] = 0.055$
$wR(F^2) = 0.167$
$S = 0.98$
2551 reflections
163 parameters
0 restraints
Primary atom site location: dual
Secondary atom site location: difference Fourier map
Hydrogen site location: mixed
H atoms treated by a mixture of independent and constrained refinement
$w = 1/[\sigma^2(F_o^2) + (0.086P)^2]$ where $P = (F_o^2 + 2F_c^2)/3$
$(\Delta/\sigma)_{max} < 0.001$
$\Delta\rho_{max} = 0.23$ e Å^{-3}
$\Delta\rho_{min} = -0.27$ e Å^{-3}

Extinction correction: SHELXL2018
(Sheldrick, 2015b),
$Fc^{*}=kFc[1+0.001xFc^{2}\lambda^{3}/\sin(2\theta)]^{-1/4}$
Extinction coefficient: 0.019 (4)

Special details

Geometry. All esds (except the esd in the dihedral angle between two l.s. planes) are estimated using the full covariance matrix. The cell esds are taken into account individually in the estimation of esds in distances, angles and torsion angles; correlations between esds in cell parameters are only used when they are defined by crystal symmetry. An approximate (isotropic) treatment of cell esds is used for estimating esds involving l.s. planes.

Fractional atomic coordinates and isotropic or equivalent isotropic displacement parameters (Å²)

	x	y	z	U_{iso}*/U_{eq}
O1	0.60103 (14)	−0.2438 (3)	0.51392 (9)	0.0364 (4)
N2	0.63400 (15)	0.2758 (4)	0.28016 (11)	0.0304 (5)
N1	0.48278 (17)	−0.3250 (4)	0.39872 (12)	0.0331 (5)
C1	0.56558 (19)	−0.1907 (4)	0.44191 (13)	0.0312 (5)
C2	0.61839 (18)	0.0252 (4)	0.40098 (12)	0.0287 (5)
C3	0.58725 (19)	0.0909 (4)	0.31880 (13)	0.0311 (5)
H3	0.528010	−0.004871	0.288573	0.037*
C4	0.71867 (17)	0.4149 (4)	0.32278 (12)	0.0274 (5)
C5	0.77008 (18)	0.6182 (4)	0.28123 (13)	0.0292 (5)
C6	0.7362 (2)	0.6735 (5)	0.19826 (13)	0.0332 (5)
H6	0.678537	0.573337	0.167687	0.040*
C7	0.7858 (2)	0.8702 (5)	0.16151 (14)	0.0360 (6)
H7	0.762331	0.905703	0.105414	0.043*
C8	0.8707 (2)	1.0200 (5)	0.20521 (15)	0.0375 (6)
H8	0.904089	1.157365	0.178843	0.045*
C9	0.90571 (19)	0.9702 (5)	0.28530 (14)	0.0346 (6)
H9	0.963477	1.073076	0.314661	0.041*
C10	0.85689 (18)	0.7665 (4)	0.32529 (13)	0.0305 (5)
C11	0.8935 (2)	0.7074 (5)	0.40961 (14)	0.0350 (6)
H11	0.952662	0.805664	0.438992	0.042*
C12	0.84594 (19)	0.5161 (5)	0.44794 (13)	0.0329 (5)
H12	0.872211	0.481242	0.503736	0.039*
C13	0.75657 (17)	0.3646 (4)	0.40605 (12)	0.0291 (5)
C14	0.70365 (19)	0.1668 (4)	0.44428 (13)	0.0307 (5)
H14	0.726853	0.130640	0.500358	0.037*
H1N	0.449 (2)	−0.279 (6)	0.344 (2)	0.059 (9)*
H1P	0.452 (2)	−0.464 (6)	0.4246 (16)	0.054 (8)*

Atomic displacement parameters (Å²)

	U^{11}	U^{22}	U^{33}	U^{12}	U^{13}	U^{23}
O1	0.0445 (10)	0.0389 (9)	0.0247 (8)	−0.0018 (8)	0.0036 (7)	0.0056 (7)
N2	0.0311 (11)	0.0302 (10)	0.0293 (9)	−0.0018 (8)	0.0037 (8)	0.0005 (8)
N1	0.0373 (12)	0.0331 (11)	0.0280 (10)	−0.0018 (9)	0.0036 (9)	0.0020 (8)
C1	0.0351 (13)	0.0302 (11)	0.0285 (11)	0.0031 (10)	0.0064 (10)	0.0001 (9)

C2	0.0310 (12)	0.0281 (11)	0.0275 (10)	0.0048 (9)	0.0068 (9)	0.0004 (9)
C3	0.0333 (12)	0.0306 (11)	0.0286 (11)	−0.0012 (10)	0.0033 (9)	0.0002 (9)
C4	0.0278 (11)	0.0261 (11)	0.0279 (11)	0.0029 (9)	0.0036 (9)	−0.0021 (9)
C5	0.0299 (12)	0.0276 (11)	0.0307 (11)	0.0034 (10)	0.0068 (9)	−0.0007 (9)
C6	0.0345 (13)	0.0355 (13)	0.0295 (11)	−0.0024 (10)	0.0058 (10)	0.0009 (9)
C7	0.0372 (14)	0.0387 (13)	0.0327 (11)	−0.0005 (11)	0.0082 (10)	0.0042 (10)
C8	0.0367 (13)	0.0348 (13)	0.0428 (13)	−0.0015 (11)	0.0124 (11)	0.0025 (11)
C9	0.0325 (13)	0.0324 (12)	0.0393 (13)	0.0003 (10)	0.0079 (10)	−0.0006 (10)
C10	0.0291 (12)	0.0280 (11)	0.0351 (11)	0.0030 (9)	0.0079 (9)	−0.0021 (9)
C11	0.0319 (13)	0.0379 (13)	0.0342 (12)	−0.0024 (10)	0.0037 (10)	−0.0063 (10)
C12	0.0324 (12)	0.0372 (12)	0.0274 (11)	0.0009 (10)	0.0009 (9)	−0.0027 (9)
C13	0.0303 (12)	0.0302 (11)	0.0260 (10)	0.0045 (10)	0.0033 (9)	0.0006 (9)
C14	0.0352 (13)	0.0312 (12)	0.0248 (10)	0.0053 (10)	0.0034 (9)	0.0009 (9)

Geometric parameters (Å, º)

O1—C1	1.238 (3)	C6—H6	0.9500
N2—C3	1.321 (3)	C7—C8	1.396 (3)
N2—C4	1.360 (3)	C7—H7	0.9500
N1—C1	1.335 (3)	C8—C9	1.358 (3)
N1—H1N	0.97 (3)	C8—H8	0.9500
N1—H1P	0.93 (3)	C9—C10	1.413 (3)
C1—C2	1.491 (3)	C9—H9	0.9500
C2—C14	1.376 (3)	C10—C11	1.436 (3)
C2—C3	1.401 (3)	C11—C12	1.346 (3)
C3—H3	0.9500	C11—H11	0.9500
C4—C13	1.414 (3)	C12—C13	1.428 (3)
C4—C5	1.443 (3)	C12—H12	0.9500
C5—C6	1.406 (3)	C13—C14	1.404 (3)
C5—C10	1.411 (3)	C14—H14	0.9500
C6—C7	1.364 (3)		

C3—N2—C4	118.11 (19)	C6—C7—H7	119.6
C1—N1—H1N	124.6 (17)	C8—C7—H7	119.6
C1—N1—H1P	117.5 (17)	C9—C8—C7	120.2 (2)
H1N—N1—H1P	118 (2)	C9—C8—H8	119.9
O1—C1—N1	122.2 (2)	C7—C8—H8	119.9
O1—C1—C2	119.3 (2)	C8—C9—C10	120.5 (2)
N1—C1—C2	118.55 (19)	C8—C9—H9	119.7
C14—C2—C3	117.0 (2)	C10—C9—H9	119.7
C14—C2—C1	119.62 (19)	C5—C10—C9	119.1 (2)
C3—C2—C1	123.4 (2)	C5—C10—C11	119.4 (2)
N2—C3—C2	125.0 (2)	C9—C10—C11	121.5 (2)
N2—C3—H3	117.5	C12—C11—C10	121.5 (2)
C2—C3—H3	117.5	C12—C11—H11	119.3
N2—C4—C13	121.5 (2)	C10—C11—H11	119.3
N2—C4—C5	118.57 (19)	C11—C12—C13	121.0 (2)
C13—C4—C5	119.92 (19)	C11—C12—H12	119.5

C6—C5—C10	119.0 (2)	C13—C12—H12	119.5
C6—C5—C4	122.1 (2)	C14—C13—C4	118.1 (2)
C10—C5—C4	118.95 (19)	C14—C13—C12	122.68 (19)
C7—C6—C5	120.3 (2)	C4—C13—C12	119.3 (2)
C7—C6—H6	119.9	C2—C14—C13	120.37 (19)
C5—C6—H6	119.9	C2—C14—H14	119.8
C6—C7—C8	120.9 (2)	C13—C14—H14	119.8

Hydrogen-bond geometry (Å, º)

D—H···*A*	*D*—H	H···*A*	*D*···*A*	*D*—H···*A*
N1—H1*N*···N2^{i}	0.97 (3)	2.17 (3)	3.133 (3)	173 (2)
N1—H1*P*···O1^{ii}	0.93 (3)	1.96 (3)	2.895 (3)	175 (3)
C3—H3···N2^{i}	0.95	2.41	3.361 (3)	174
C7—H7···O1^{iii}	0.95	2.45	3.140 (3)	129

Symmetry codes: (i) $-x+1, y-1/2, -z+1/2$; (ii) $-x+1, -y-1, -z+1$; (iii) $x, -y+1/2, z-1/2$.

5.3 Manuskript III

Activation of Sirt2 Inhibitors Employing Photoswitchable Geometry and Aqueous Solubility

Christoph W. Grathwol, Nathalie Wössner, Steven Behnisch-Cornwell, Lukas Schulig, Lin Zhang, Oliver Einsle, Manfred Jung, Andreas Link

ChemMedChem **2020**, *15*, Early View.

DOI: 10.1002/cmdc.202000148

Beiträge der Autoren

Christoph W. Grathwol:	Konzipierung des Projekts Planung und Durchführung der Synthesen Analytische Charakterisierung Photochemische Evaluation Erstellen des Manuskripts
Nathalie Wössner:	Biologische Testung
Steven Behnisch-Cornwell:	Biologische Testung
Lukas Schulig:	Molekulares Docking
Lin Zhang:	Expression rekombinanter Sirtuine
Oliver Einsle:	Expression rekombinanter Sirtuine
Manfred Jung:	Betreuung des Projekts
Andreas Link:	Betreuung des Projekts Erstellen des Manuskripts

Christoph W. Grathwol

Andreas Link

Activation of Sirtuin 2 Inhibitors Employing Photoswitchable Geometry and Aqueous Solubility

Christoph W. Grathwol,[a] Nathalie Wössner,[b] Steven Behnisch-Cornwell,[a] Lukas Schulig,[a] Lin Zhang,[c] Oliver Einsle,[c] Manfred Jung,[b] and Andreas Link*[a]

Because isoenzymes of the experimentally and therapeutically extremely relevant sirtuin family show high similarity, addressing the unique selectivity pocket of sirtuin 2 is a promising strategy towards selective inhibitors. An unrelated approach towards selective inhibition of isoenzymes with varied tissue distribution is targeted drug delivery or spatiotemporal activation by photochemical activation. Azologization of two nicotinamide-mimicking lead structures was undertaken to combine both approaches and yielded a set of 33 azobenzenes and azopyridines that have been evaluated for their photochemical behaviour and bioactivity. For some compounds, inhibitory activity reached the sub-micromolar range in their thermodynamically favoured *E* form and could be decreased by photoisomerization to the metastable *Z* form. Besides, derivatization with long-chain fatty acids yielded potent sirtuin 2 inhibitors, featuring another intriguing aspect of azo-based photoswitches. In these compounds, switching to the *Z* isomer increased aqueous solubility and thereby enhanced biological activity by up to a factor of 21. The biological activity of two compounds was confirmed by hyperacetylation of sirtuin specific histone proteins in a cell-based activity assay.

Introduction

Sirtuins refer to a family of NAD$^+$-dependent lysine deacylases that are highly conserved and found throughout all domains of life. Usually, sirtuins are classified as histone deacetylases (class III HDACs), but also an increasing number of non-histone proteins were identified as native substrates. In sum, sirtuin-promoted deacylation is involved in the regulation of various cellular processes such as DNA repair, gene transcription, aging, metabolism, and apoptosis representing an auspicious target for pharmacological intervention.[1] In human cells, seven sirtuin isotypes (Sirt1–7) have been identified. Sirt1–3 are phylogenetically closely related (class I sirtuins) exhibiting high similarity in their amino acid sequence especially along the catalytic cleft, which comprises the binding sites of the acyl-lysine substrate and the cofactor NAD$^+$.[2] Nevertheless, these three isotypes show differences in their substrate recognition as well as their enzymatic activity. In addition to a robust deacetylation ability, Sirt2 efficiently binds and cleaves myristoylated peptides, whereas *in vivo* histone decrotonylation has been reported for Sirt3.[3] During sirtuin-catalysed protein deacylation, the by-product nicotinamide functions as an endogenous pan-sirtuin inhibitor.[4] Hence, nicotinamide-mimicking compounds (Figure 1) act as eligible sirtuin inhibitors demonstrated by the potently active Sirt1 inhibitor selisistat (**1**), which was announced to be intended for evaluation in a long term phase III study for the treatment of Huntington's disease.[5] Furthermore, 5-[(3-amidobenzyl)oxy]nicotinamides (**2**) exert robust Sirt2 inhibition evincing promising effects in the therapy of neurodegenerative diseases or cancer.[6] In our hands, an *in vitro* activity screening of a pooled kinase inhibitor library revealed 5-styrylnicotinamide **3** as a moderate inhibitor of Sirt2.[7] Based on this structure, azologization resulted in a reversible photo-

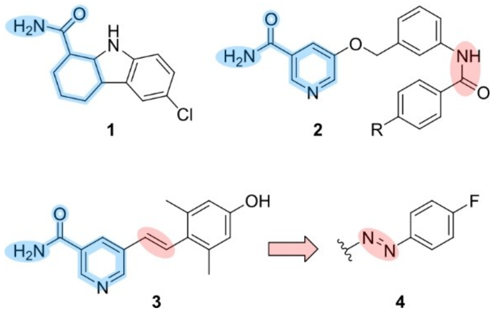

Figure 1. Nicotinamide-mimicking sirtuin inhibitors: Selisistat (**1**), 5-[(3-amidobenzyl)oxy]nicotinamides (**2**) and the structurally related 5-styrylnicotinamide **3**. Exchange of the amide bond in **2** and the stilbene C,C-double bond in **3** allows for incorporation of a photoswitchable azo moiety while maintaining the original shape of the parent molecules.

---

[a] C. W. Grathwol, Dr. S. Behnisch-Cornwell, L. Schulig, Prof. Dr. A. Link
Institute of Pharmacy
University of Greifswald
Friedrich-Ludwig-Jahn-Str. 17
17489 Greifswald (Germany)
E-mail: link@uni-greifswald.de
[b] N. Wössner, Prof. Dr. M. Jung
Institute of Pharmaceutical Sciences
University of Freiburg
Albertstr. 25, 79104 Freiburg, Germany
[c] Dr. L. Zhang, Prof. Dr. O. Einsle
Institute of Biochemistry
University of Freiburg
Albertstr. 21, 79104 Freiburg, Germany

Supporting information for this article is available on the WWW under https://doi.org/10.1002/cmdc.202000148

switch (**4**) exhibiting comparable inhibitory activity of its stretched out *E* form.[8,9]

Over the past decade, molecular photoswitches have permitted light-mediated control over a vast scope of biological targets such as ion channels, transporters, GPCRs, and various enzymes.[10] A common strategy to achieve light-sensitivity of certain biological target structures is the design of photochromic ligands (PCLs) by insertion of photoswitchable moieties into known bioactive small molecules.[11] Upon irradiation with appropriate wavelengths, PCLs undergo reversible photoisomerization reactions, accompanied by marked changes in shape and physicochemical properties of the ligand. As the target affinity of a ligand is strongly influenced by its structure and electron distribution, distinct photoisomers often show an altered binding behaviour and consequently exert differential bioactivity.[12] As a matter of fact, the first PCLs targeting an epigenetic regulator have been photoswitchable sirtuin inhibitors based on a diarylmaleimide photoswitch.[13] Using an indolyl fulgimide core instead improved the photochemical behaviour of the sirtuin photoswitch under physiological conditions.[14] Besides, azobenzene-based photoswitches have been designed for the light-mediated modulation of human Zn^{2+}-dependent HDACs as well as related bacterial amidohydrolases, offering promising perspectives concerning highly selective antineoplastic and antimicrobial chemotherapy.[15] Among the known molecular photoswitches, azo dyes hold a prominent role combining a comfortable way of synthesis with finely tuneable photophysical properties. By treatment with UV radiation, (*E*)-azobenzene segues in a metastable photostationary state (PSS) comprising high amounts of the *Z* isomer followed by slow thermal relaxation of (*Z*)-azobenzene back to the more stable *E* isomer in the dark. Blue light radiation accelerates *Z*→*E* isomerization, while complete transformation is only obtained thermally.[16] Wavelength of maximal absorption, half-life of the metastable *Z* isomer, and photoisomer distribution (PSD) are strongly influenced by different substitutions at the azobenzene core or the incorporation of heteroaromatic moieties affecting also other physicochemical properties, ultimately determining absorption and distribution.[17]

Building on our previous efforts in the design of photoswitchable sirtuin inhibitors, we now present the synthesis of various azopyridine-based photoswitches in analogy to compound **4**.[8] Furthermore, another azologization approach yielded azobenzene-based photoswitches derived from recently published 5-benzyloxynicotinamides (**2**).[6] The photophysical and photochemical properties of the obtained azo dyes were studied and adjusted to long thermal half-lives of the metastable *Z* isomers (>300 h) under physiological conditions. The biological activity of the compounds was determined *in vitro* applying a fluorescence-based enzyme assay and could also be proven in a urinary cancer cell line.

Results and Discussion

Synthesis

Starting from commercially available methyl 5-aminonicotinate (**5**), a first set of heteroaryl azo dyes was easily accessible in two steps. Diazotization and azo coupling of **5** with phenols and anilines gave the respective methyl 5-diazenylnicotinates (**6a**–**f**) in moderate yields. Quantitative transformation to nicotinamides was accomplished by successive ammonolysis, providing phenols **7a**–**d** and anilines **7e** and **7f** in satisfying overall yield (Scheme 1). Although, ammonolysis of **5** prior to derivatization by azo coupling might be more beneficial in the synthesis of a compound library, we generally performed ammonolysis at the final step because of more efficient chromatographic purification of methyl nicotinates in comparison to 5-diazenylnicotinamides.

Aniline **6f** was converted to several amides (**8a**–**k**, structures not shown) by reaction with acyl chlorides resulting in compounds **9a**–**k** after final ammonolysis (Scheme 2). As nucleophilic attack of the amino group in **6f** is hampered by the two neighbouring methyl groups, amide formation required long reaction times (1–3 days) and gave only modest yields.

Derivatization to *N*-alkyl nicotinamides (**12a**–**d**) was achievable by aminolysis of ethyl nicotinate **11** using the respective primary alkylamines (Scheme 3). On the contrary, *N*-alkyl nicotinamides could not be obtained through aminolysis of the

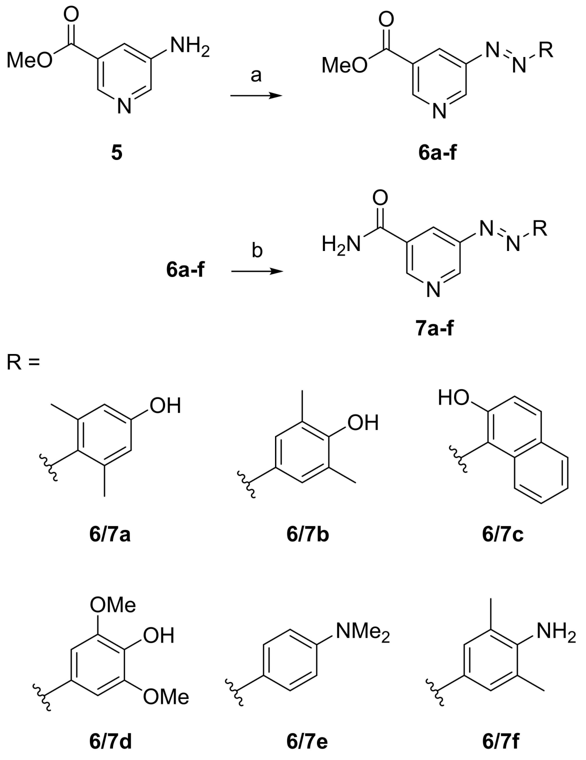

Scheme 1. a) 1. $NaNO_2$, HCl, H_2O, 0 °C; 2. phenols or anilines, NaOH, H_2O, 0 °C to RT, 31–65 %; b) NH_3, MeOH, RT, 1–4 d, quant.

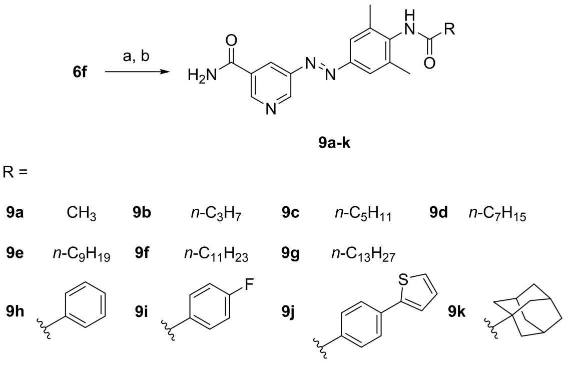

Scheme 2. a) acyl chloride, pyridine or DIPEA, THF, 0 °C to RT, 1–3 d, 26–58 %; b) NH_3, MeOH, RT, 1–4 d, quant.

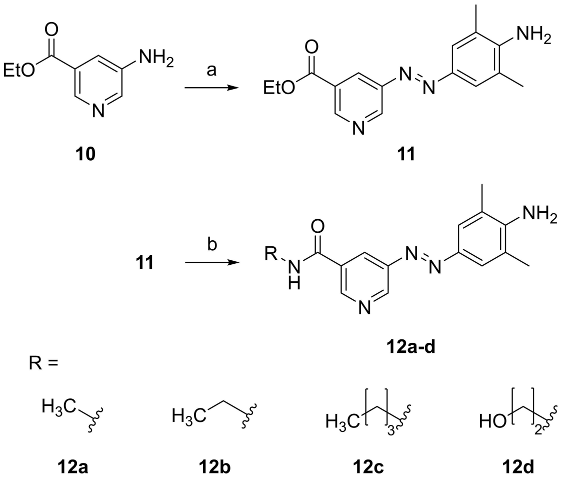

Scheme 3. a) 1. $NaNO_2$, HCl, H_2O, 0 °C; 2. 2,6-dimethylaniline, NaOH, H_2O, 0 °C to RT, 42 %; b) R-NH_2, MeOH, 40–110 °C, 4 d, 88–98 %.

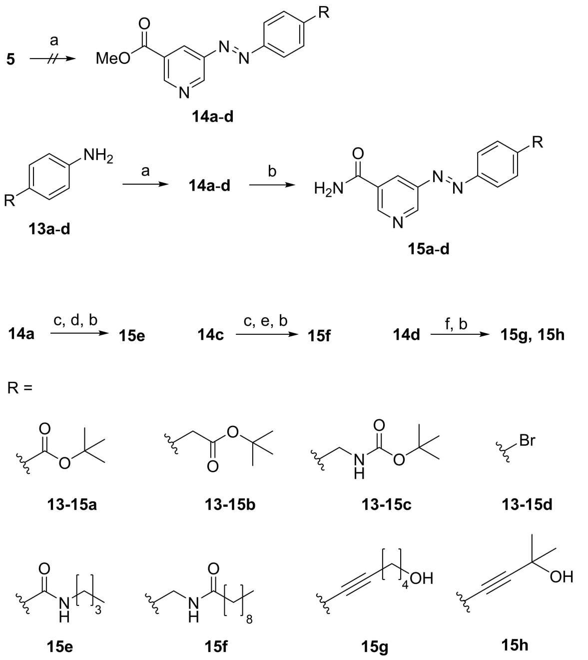

Scheme 4. a) 1. oxone, CH_2Cl_2, H_2O, RT, 4–48 h; 2. anilines **13a–d** or **5**, HAc, 40 °C, 2–14 d, 7–43 %; b) NH_3, MeOH, RT, 4 d, quant. c) TFA, CH_2Cl_2, RT, 12 h, quant. d) *n*Bu-NH_2, HATU, DIPEA, DMF, RT, 56 % e) decanoyl chloride, DIPEA, THF, RT, 80 % f) alkyne, $Pd(PPh_3)_4$, CuI, NEt_3, THF or CH_2Cl_2, 50–85 °C, 24 h, 20 %.

corresponding methyl nicotinate **6f** due to an insufficient reactivity of the methyl ester with primary alkylamines.

A greater diversity of 5-diazenylnicotinamides was realizable exerting Mills reaction for the synthesis of unsymmetrical azo dyes by reaction of aromatic nitroso derivatives with anilines in glacial acetic acid. Aromatic nitroso compounds were obtained by oxidation of anilines with potassium peroxymonosulfate (oxone) yielding the methyl 5-diazenylnicotinates **14a–d** after condensation with **5** (Scheme 4). In the first place, we tried to transform the electron-deficient aminopyridine **5** to its nitroso derivative in order to use the electron-rich anilines **13a–d** as nucleophiles in the following condensation reaction. However, transformation of **5** to its nitroso derivative by potassium peroxymonosulfate failed, probably due to the oxidative susceptibility of amino pyridines towards formation of *N*-oxides. Consequently, we interchanged the roles of the reagents, treated **13a–d** with oxone, and used the less suitable aminopyridine **5** as nucleophile in the condensation reaction. Normally, Mills reaction provides good yields in the synthesis of azobenzenes, but in the case of methyl 5-diazenyl-nicotinates, yields were often poor and required long reaction times caused by the said reduced nucleophilicity of **5**. Compounds **15a–d** were obtained by successive ammonolysis. In the case of **14a** and **14c**, further derivatization was performed by acidic cleavage of the *tert*-butyl-based protective group, followed by amide formation and ammonolysis to **15e** and **15f**. Sonogashira-type coupling of arylbromide **14d** with terminal alkynes resulted in formation of methyl nicotinates **14g** and **14h** (structure not shown) in modest yield, which were transformed to **15g** and **15h** as described above.

Based on closely related 5-[(amidobenzyl)oxy]-nicotinamides (**2**), we additionally synthesized a small set of analogous azobenzene photoswitches.[6,18] Compound **18** was prepared similarly to the original procedure and was converted to azo compounds **20a–d** applying Mills reaction and subsequent ammonolysis (Scheme 5).

Photochemistry

The design of photoswitchable drugs requires careful consideration of their photophysical and photochemical properties under physiological conditions. With water being the solvent of choice for all pharmaceutically relevant systems, it had to be considered that hydrogen bonding in polar solvents strongly affects thermal relaxation rates and may lead to rapid thermal

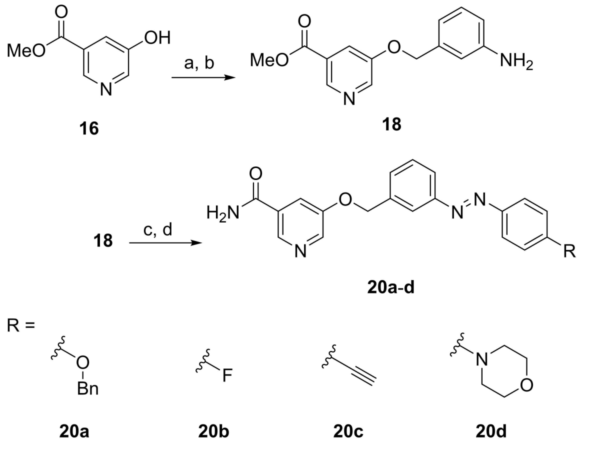

Scheme 5. a) 3-Nitrobenzyl bromide, Cs_2CO_3, DMF, RT, 61 %; b) Raney-Ni, H_2, THF, RT, 85 %; c) 1. Oxone, CH_2Cl_2, H_2O, 2–14 h; 2. R-NH_2, HAc, 40 °C, 1–7 d, 23–42 %; d) NH_3, MeOH, RT, 4 d, quant.

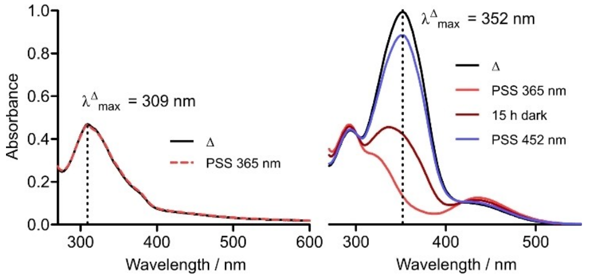

Figure 2. Left: **20 a** (50 μM) in assay buffer (5 % DMSO, *v/v*) at thermal equilibrium (Δ) and PSS after 365 nm irradiation (red). Due to aggregation of the chromophore, general light absorption is diminished and λ^{Δ}_{max} appears blue-shifted. Right: **20 a** (50 μM) in assay buffer (50 % DMSO, *v/v*) at thermal equilibrium (Δ), directly after 365 nm illumination (red) as well as additional 15 h in the dark (dark red). After 452 nm irradiation (blue) PSS displays almost complete transformation to thermal equilibrium (Δ). Under these conditions, aggregation of the compound is prevented, and photoisomerization proceeds unhindered.

Table 1. Absorption maxima of azo dyes **9 a–k**, **15 a–h**, and **20 a–c** at thermal equilibrium (Δ), half-lives of thermal *Z*→*E* isomerization and PSD after 365 nm and 452 nm irradiation.

	λ^{Δ}_{max} [nm][a]	$t_{1/2}$ [h][a]	*E/Z* [%][e]	
			@ 365 nm	@ 452 nm
9 a[b]	329	6	12/88	90/10
9 b[b]	332	8	10/90	86/14
9 c[c]	339	16	9/91	87/13
9 d[d]	345	21	9/91	88/12
9 e[d]	344	22	10/90	90/10
9 f[d]	346	21	10/90	91/9
9 g[d]	345	26	14/86	87/13
9 h[c]	337	0.7	14/86	91/9
9 i[c]	337	0.6	12/88	91/9
9 j[c]	330	0.6	29/71	93/7
9 k[c]	339	7	14/86	89/11
15 a[c]	325	178	31/69	94/6
15 b[c]	332	23	6/94	90/10
15 c[b]	329	319	11/89	86/14
15 d[b]	332	220	9/91	91/9
15 e[c]	326	254	40/60	89/11
15 f[d]	333	102	5/95	79/21
15 g[c]	355	50	25/75	89/11
15 h[c]	350	77	23/77	92/8
20 a[c]	352	33	4/96	80/20
20 b[c]	324	166	2/98	83/17
20 c[c]	340	63	14/86	85/15

[a] Solutions in DMSO/assay buffer (50 μM): [b] 5 % DMSO (*v/v*), [c] 50 % DMSO (*v/v*), [d] 90 % DMSO, (*v/v*); [e] PSD determined by HPLC analysis in MeOH/water mixtures applying isocratic conditions and evaporative light-scattering detection (ELSD).

Z→*E* isomerization in certain classes of azobenzenes.[16] Though this can be desirable in some applications, in our case slow thermal *Z*→*E* isomerization was obligatory in order to retain the impact of short term UV irradiation.

According to their substitution pattern and spectral properties, phenylazopyridines **7 a–d** (2-/4-OH) as well as **7 e** and **f** (4-NR_2) can be classified as amino-azobenzenes (aAB). In this sort of heteroarylic azo dyes, the rate of thermal isomerization is intensively increased by hydrogen bonding and tautomerization. Consequently, aAB undergo thermal *Z*→*E* isomerization within milliseconds to seconds in aqueous solution.[19] Such rapid transformations could not be captured by our experimental set-up. Noteworthy, in aprotic and less polar acetonitrile thermal *Z*→*E* isomerization of compound **7 a** was notably decelerated, showing a half-life of 94 min in contrast to its constitutional isomer **7 b**, that exerted rapid thermal isomerization. We suggest that the *ortho* methyl groups in **7 a** impeded isomerization leading to delayed thermal relaxation.

In order to increase the thermal half-life of the *Z* isomers, we performed additional structural modifications on the phenylazopyridine scaffold. However, investigation of thermal *Z*→*E* isomerization kinetics could not be performed in the exact solvent composition of the enzyme assay (i.e., 5 % DMSO (*v/v*) in assay buffer) for most of the synthesized compounds due to their high lipophilicity. In fact, many of them were prone for aggregation indicated by blue-shifted maxima and notably decreased absorption in the UV-Vis spectra.[20] As a consequence, photoisomerization was hampered in the respective compounds. Higher amounts of DMSO prevented aggregation and enabled determination of *Z* isomer stability in aqueous environment as exemplified for compound **20 a** (Figure 2).

Acylation of **7 f** yielded compounds **9 a–k**, adopting PSS sufficiently stable for acquisition (Table 1). PSD of these compounds was approximately 90 % of the respective photoisomers, thus enabling almost perfect toggling between *Z* and *E* form. Regarding the *Z* isomer half-life, amides **9 h–j** obtained from aromatic carboxylic acid chlorides were inferior to amides **9 a–g** and **9 k** prepared from aliphatic counterparts.

By inverting the amide bond, we received compound **15 a** and its derivative **15 e**. As reflected by strongly increased half-lives of the thermal *Z*→*E* isomerization, inversion of the amide bond was beneficial for the thermal stability of the *Z* isomer, while PSD after 365 nm radiation was only about 60–70 % of the respective *Z* isomer. Insertion of a methylene bridge instead of the amide bond yielded **15 b**, **15 c**, and **15 f** exhibiting slow thermal *Z*→*E* isomerization kinetics as well as efficient switching between both states. Half-life of the respective *Z* isomers and PSD for the ethinyl substituted **15g** and **15h** were still sufficient, but not as valid as in the methylene bridged compounds **15c** and **15f**.

Azobenzene-based compounds **20a**–**c** also elicited slow thermal *Z*→*E* isomerization in combination with an appropriate PSD of the respective photoisomers. Especially **20a** and **20b** demonstrated almost quantitative transformation to their *Z* isomers upon 365 nm irradiation. Contrarily, amino-azobenzene (aAB) **20d** showed rapid thermal *Z*→*E* isomerization due to 4-NR_2 substitution.

Conclusively, the half-lives of the thermal *Z*→*E* isomerization as well as the PSD are not necessarily reflecting the situation in the enzyme assay mixture due to the discrepancies in the solvent compositions.[21] Nevertheless, an approximate estimation of *Z* isomer half-life in aqueous solutions was possible.

Biochemistry

The effect of the compounds on deacetylase activity of three human sirtuin isotypes (Sirt1–3) was investigated by a homogeneous fluorescence-based assay, using (*Z*)-Lys(acetyl)-AMC (ZMAL) as substrate. In order to determine the impact of photoisomerization, the respective compounds were irradiated (365 nm, 5 min) in DMSO prior to incubation in the enzyme assay mixture. The results of the irradiated probes were finally compared to non-irradiated measurements. For compounds displaying rapid thermal isomerization in aqueous solution (**7a**–**7f**, **11**, **12a**–**d**, **20d**) only non-irradiated probes were tested.

As previously published, lead **3** exhibited moderate potency for Sirt2 inhibition ($IC_{50} = 25\ \mu M$), but at the same time represented the least-selective hit, as Sirt3 activity was also notably affected (Table 1).[7] Azologization of **3** yielded the direct azo analogue **7a**. As the geometry of the molecule was unaltered by this structural modification, we expected **7a** to display a biological activity comparable to the lead. In fact, exchange of the ethylene bridge by the azo group even improved inhibitory potency to the single digit μM range. However, isoenzyme selectivity remained unsatisfactory. In general, 5-diazenylnicotinamides primarily inhibited Sirt2/Sirt3, whereas a distinct inhibition between Sirt2 and Sirt3 was harder to achieve. The existence and position of the two methyl groups on the phenyl substructure was found to be virtually irrelevant for biological activity as well as isoenzyme selectivity, as both the isomers **7a**/**7b** and compound **7e** exerted similar activity and selectivity profiles. However, exchange of the methyl groups with methoxy ethers in **7d** resulted in slightly improved isoenzyme selectivity with decreased Sirt3 inhibition, whereas Sirt2 inhibition was unaltered. Interestingly, aniline **7f** exhibited the highest activity with an IC_{50} of 6 μM against Sirt2 and 9 μM against Sirt3, whereas methylation of the amino group provoked a slight decrease of Sirt2 inhibition in *N*,*N*-dimethyl aniline derivative **7e** indicating the relevance of the amino group for polar target interactions.

Compounds **6f**, **11** and **12a**–**d** confirmed that the primary amide group of the nicotinamide partial structure was essential for affinity towards Sirt1–3, as modifications on this residue provoked a dramatic loss of activity (Table 1). Hence, binding of compounds **7a**–**f** was highly likely to occur in a fashion similar to nicotinamide itself. Nicotinamide is known to bind to the enzymatic C-site, which is part of the catalytic cleft and is contained in all sirtuin isotypes. Thus, further interactions with specific domains were necessary in order to improve isoenzyme selectivity.

In the case of Sirt2, a hydrophobic selectivity pocket adjacent to the C-site presents new possibilities for specific interactions.[22] This unique binding pocket is typically formed after binding of the highly potent and selective sirtuin-rearranging ligands (SirReals) by a conformational change to the so-called locked open conformation. This conformational change is also observed upon binding of numerous other compounds as myristoylated substrates, for instance.[23] A recently developed fluorescence polarization (FP)-based binding assay was utilized to determine whether our compounds are able to prevent binding of a fluorescently labelled SirReal to the catalytic core of Sirt2.[7] Serendipitously, competition with the fluorescent probe could be confirmed for **7f** (Table S3). Hence, one could hypothesize that **7f** exerts a binding mode similar to that of the SirReals and possibly is also able to introduce the same conformational change to the locked open conformation that was observed upon SirReals binding. Therefore, this scaffold seemed to be a promising structure for further derivatization.

Comparable to **7f**, the acetylated derivative **9a** may induce an opening of the selectivity pocket (Table S3). However, acetylation of the amino group caused a notable loss of inhibitory potency supporting the assumption that the amino group is involved in polar target interactions (Table 2). Nevertheless, as Sirt2 is known to bind and process myristoylated substrates, we anticipated a Sirt2 selective inhibition by long-chain fatty acyl derivatives of **7f**. In fact, extension of the acyl

Table 2. Influence of stilbenoid lead **3** and **6f**, **7a**–**f**, **11**, **12a**–**d**, and **20d** on the deacetylase activity of human sirtuin isotypes Sirt1–3 determined in the fluorescence-based ZMAL activity assay.

	Sirt1 inhibition[a]	Sirt2 inhibition[a]	Sirt3 inhibition[a]
3	27% @ 50 μM	24.6 ± 2.8 μM[b]	41.7 ± 2.0 μM[b]
6f	n.i.	n.i.	n.i.
7a	14% @ 50 μM	7.9 ± 0.6 μM[b]	9.5 ± 0.9 μM[b]
7b	19% @ 50 μM	10.8 ± 0.6 μM[b]	7.9 ± 0.5 μM[b]
7c	n.i.	55% @ 10 μM	64% @ 10 μM
7d	10% @ 10 μM	62% 10 μM	39% @ 50 μM
7e	17% @ 10 μM	54% @ 10 μM	66% @ 10 μM
7f	47% @ 100 μM	5.8 ± 0.7 μM[b]	9.4 ± 0.7 μM[b]
11	n.i.	n.i.	n.i.
12a	33% @ 100 μM	45% @ 100 μM	45% @ 100 μM
12b	n.i.	16% @ 10 μM	11% @ 10 μM
12c	n.i.	17% @ 10 μM	11% @ 10 μM
12d	n.i.	43% @ 100 μM	43% @ 100 μM
20d	n.i.	49% @ 10 μM	33% @ 10 μM

[a] Percent inhibition relative to controls at the indicated concentration, [b] IC_{50} values (μM) with statistical limits; values are mean ± SD of duplicate experiments, n.i.: no inhibition detected (< 30% @ 100 μM).

chain (**9 b**–**g**) enhanced inhibition of Sirt2 and yielded a potent myristic acid derivative **9 g**. However, with an increasing length of the fatty acyl chain, aqueous solubility obviously became a major concern. Indeed, Sirt3 stability was affected by **9 d**–**g** potentially due to substance precipitation during the activity assay (Table 3).

Depending on the lipophilicity, UV irradiation (365 nm) showed varying effects on the biological activity of **9 a**–**g**. The three less lipophilic compounds **9 a**–**9 c** did not exhibit major differences in target engagement, yet a slight decrease of affinity towards Sirt2 and Sirt3 was observable. In contrast, **9 d** displayed an about fivefold increase of Sirt2 inhibition, which is most likely caused by the improved aqueous solubility and higher abundance of the *Z* isomer in the enzyme assay mixture. Irradiation of **9 g** even yielded sub-micromolar inhibition of Sirt2 ($IC_{50} = 0.9$ μM), yet differential target engagement is less pronounced compared to **9 d** as affinity for Sirt2 is also increased in the *E* form of **9 g**.

In order to test the influence of nonpolar, bulky substituents, we synthesized compounds **9 h**–**k**. None of these compounds exerted potent inhibition, neither in their non-irradiated *E* form nor after 365 nm irradiation. Consequently, a certain degree of flexibility in the hydrophobic substructure is regarded crucial for target affinity.

Despite the detrimental effects of bulky hydrophobic substituents, we found a potent inhibition of Sirt2 and Sirt3 by *tert*-butyl ester **15 a**. According to the previously mentioned low amount of *Z* isomers at the PSS after 365 nm irradiation, we found only negligible differences in target engagement of the irradiated probe. By insertion of a methylene bridge, we attempted to improve the photochemical behaviour of the chromophore and at the same time enhance flexibility of the hydrophobic acyl group. Indeed, **15 b** and **15 c** demonstrated both a stronger inhibition and a larger impact of irradiation compared to **15 a**. Boc-protected 4-aminomethyl derivative **15 c** inhibited Sirt2 within the sub-micromolar range ($IC_{50} = 0.9$ μM). Upon irradiation, the IC_{50} value is diminished three- and fourfold for Sirt2 and Sirt3, respectively. Pharmacophore-guided docking studies indicated binding of the voluminous *tert*-butyl group to the hydrophobic acetyl-lysine channel. However, photoisomerization is not expected to lead to substantially altered target interactions (Figure 3).

Inspired by the beneficial influence of a methylene bridge on biological activity and photochemical properties, we synthesized a methylene bridged derivative of **9 g**. In order to reduce lipophilicity, the fatty acyl chain had to be shortened by four links. Albeit, the resulting compound **15 f** exerted excellent isoenzyme selectivity, the strength of Sirt2 inhibition was dramatically diminished by this modification compared to **9 g**. However, illumination provoked a 23-fold increase of inhibitory potency ($IC_{50} = 1.6$ μM). Besides better aqueous solubility, molecular docking studies implied favourable binding of (*Z*)-**15 f** to be responsible for this remarkable improvement of biological activity (Figure 4).

Although insertion of a methylene bridge increased target affinity, gained flexibility at the same time reduced the overall net structural changes provoked by photoisomerization. Insertion of a more rigid ethinyl spacer instead was expected to enhance these structural changes and thus increase the impact of light-switching.[24] Furthermore, a polar hydroxyl group was integrated in compounds **15 g** and **15 h** in order to address the excessive lipophilicity of most compounds. However, this failed

Table 3. Influence of azo dyes **9 a**–**k**, **15 a**–**h**, and **20 a**-**c** on the deacetylase activity of human sirtuin isotypes Sirt1–3, determined by the fluorescence-based ZMAL activity assay. Biological activity was investigated at the thermal equilibrium (Δ) and the PSS after 5 min of UV irradiation (365 nm).

	Sirt1 inhibition[a]		Sirt2 inhibition[a]		Sirt3 inhibition[a]	
	Δ	PSS [365 nm]	Δ	PSS [365 nm]	Δ	PSS [365 nm]
9 a	n.i.	n.i.	17 % @ 10 μM	11 % @ 10 μM	68 % @ 100 μM	52 % @ 100 μM
9 b	n.i.	n.i.	30 % @ 10 μM	4 % @ 10 μM	80 % @ 100 μM	52 % @ 100 μM
9 c	n.i.	n.i.	40 % @ 10 μM	24 % @ 10 μM	20 % @ 10 μM	3 % @ 10 μM
9 d	n.i.	n.i.	44.0 ± 9.5 μM[b] (26 % @ 10 μM)	7.9 ± 0.7 μM[b] (54 % @ 10 μM)	u.i.	u.i.
9 e	n.i.	n.i.	26 % @ 10 μM	78 % @ 10 μM	u.i.	u.i.
9 f	n.i.	n.i.	46 % @ 10 μM	65 % @ 10 μM	u.i.	u.i.
9 g	n.i.	n.i.	2.2 ± 0.3 μM[b]	0.9 ± 0.2 μM[b]	u.i.	u.i.
9 h	n.i.	n.i.	27 % @ 100 μM	52 % @ 100 μM	n.i.	32 % @ 100 μM
9 i	n.i.	n.i.	15 % @ 10 μM	15 % @ 10 μM	n.i.	n.i.
9 j	n.i.	n.i.	80 % @ 100 μM	59 % @ 100 μM	u.i.	u.i.
9 k	n.i.	n.i.	43 % @ 100 μM	71 % @ 100 μM	n.i.	n.i.
15 a	n.i.	7 % @ 10 μM	6.0 ± 1.1 μM[b]	6.8 ± 0.4 μM[b]	42 % @ 10 μM	45 % @ 10 μM
15 b	35 % @ 100 μM	44 % @ 100 μM	3.9 ± 0.2 μM[b]	6.9 ± 0.6 μM[b]	58 % @ 10 μM	30 % @ 10 μM
15 c	n.i.	6 % @ 10 μM	0.88 ± 0.06 μM[b]	2.8 ± 0.1 μM[b]	1.1 ± 0.2 μM[b]	4.0 ± 0.7 μM[b]
15 d	n.i.	47 % @ 100 μM	7.5 ± 0.5 μM[b]	8.4 ± 0.9 μM[b]	8.2 ± 1.4 μM[b]	13.0 ± 2.2 μM[b]
15 e	n.i.	10 % @ 10 μM	51 % @ 10 μM	61 % @ 10 μM	54 % @ 10 μM	49 % @ 10 μM
15 f	n.i.	n.i.	36.6 ± 9.3 μM[b]	1.6 ± 0.2 μM[b]	n.i.	n.i.
15 g	60 % @ 100 μM	54 % @ 100 μM	7.2 ± 0.5 μM[b]	11.8 ± 1.0 μM[b]	64 % @ 10 μM	22 % @ 10 μM
15 h	n.i.	n.i.	15.2 ± 1.8 μM[b]	37.5 ± 5.2 μM[b]	42 % @ 10 μM	18 % @ 10 μM
20 a	n.i.	n.i.	0.70 ± 0.21 μM[b]	1.6 ± 0.2 μM[b]	23 % @ 10 μM	24 % @ 10 μM
20 b	n.i.	n.i.	3.2 ± 0.5 μM[b]	6.4 ± 0.5 μM[b]	34 % @ 10 μM	47 % @ 10 μM
20 c	45 % @ 100 μM	62 % @ 100 μM	u.i.	6.2 ± 0.54 μM[b]	u.i.	17.2 ± 1.57 μM[b]

[a] Percent inhibition relative to controls at the indicated concentration. [b] IC_{50} values (μM) with statistical limits; values are mean ± SD of duplicate experiments. n.i.: no inhibition detected (< 30 % @ 100 μM), u.i.: unspecific interactions.

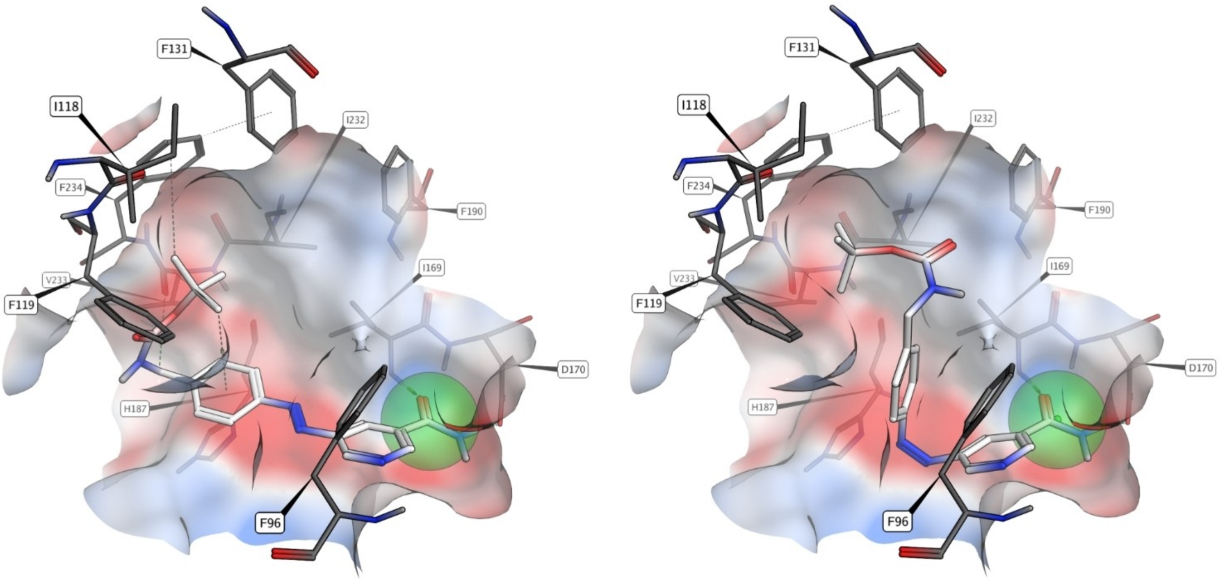

Figure 3. Binding pose for compound **15 c** in the *E* (left) and *Z* (right) configurations from pharmacophore-guided docking. Because compound **15 c** is not selective for Sirt2, and modification of the primary amide group leads to complete loss of activity, binding of the nicotinamide moiety to residues I169 and D170 like NAD$^+$is expected (C-site). For (*E*)-**15 c**, the *tert*-butyl group points towards the hydrophobic acetyl-lysine channel while exposing the polar carbamate towards the solvated entrance region. After photoisomerization, the phenyl group shifts to the more hydrophobic binding site, leading to unfavourable interactions for the carbamate; this might explain the decrease in activity. However, the binding of the nicotinamide moiety is not expected to be affected. The conformation of (*Z*)-**15 c** was validated by analyses of potential energies in relation the CCNN-dihedral angles (Figure S7). The pharmacophore region for an amide group is shown as green sphere.

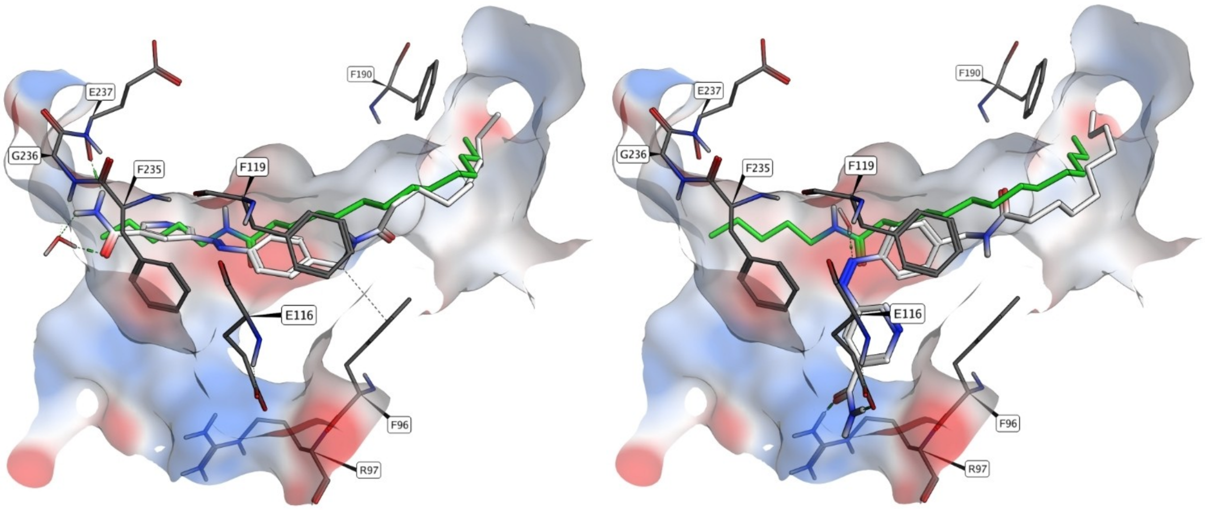

Figure 4. Binding pose for compound **15 f** in the *E* (left) and *Z* (right) configurations from molecular docking. The position of the decanoyl chain is in good agreement with the crystallized myristoylated lysine side chain (green) which opens the selectivity pocket (PDB ID: 4Y6L). Through photoisomerization, hydrophilicity is increased, and the polar (*Z*)-azo group is accessible for hydrogen bond interactions with water molecules, while hiding the pyridine ring in a more hydrophobic pocket and conceiving two strong hydrogen bonds to the charged side chains of R97 and E116.

to enhance differential target engagement: Sirt2 inhibition is diminished by a factor of 1.6 for **15 g** and 2.5 for **15 h**. A similar influence is indicated regarding Sirt3.

Azologization of lead **2** yielded azobenzene-based photoswitches **20 a-d**. As in the case of lead **3**, the azo group could be inserted under full maintenance of the parent molecules geometry. Hence, we expected **20 a**–**d** to possess comparable biological activities. In fact, we obtained active sirtuin inhibitors also by this azologization approach, though not in every case the azo analogues maintained the biological activity of the respective lead structure: Compound **20 a** showed Sirt2 inhibition with an IC_{50} of 0.7 μм (Table 3), consistent with the originally published value of 0.1 μм for the respective derivative of **2** (R=OBn). Besides, inhibition of Sirt1 and Sirt3 was almost negligible, so that **20 a** approximates the excellent properties of its *N*-arylbenzamide counterpart. On the contrary, inhibitory potency and isoenzyme selectivity of **20 b** is significantly decreased. In fact, the IC_{50} of **20 b** regarding Sirt2 inhibition is off by a factor of 100 compared to the parent structure (**2**, R=F). Also **20 c** and **20 d** did not resemble their parent compounds. Whereas the *N*-arylbenzamides inhibit Sirt2 in the nanomolar range, **20 d** displayed Sirt2 inhibition with an IC_{50} value of about 10 μм (Table 1). In the case of **20 c**, unspecific interactions were indicated by a rather linear than sigmoidal dose response curve in the Sirt2 and Sirt3 activity assay. As this was not detected for irradiated probes of **20 c**, we assumed that solubility issues were responsible for the observed interference. In terms of their photochemical behaviour, **20 a** and **20 b** seemed promising as their PSS after UV irradiation displayed high amounts of the respective *Z* isomers. Still, both compounds did not exceed a twofold decrease of Sirt2 inhibition after illumination.

Cell-based activity assay

Bioactivity towards a human urinary cancer cell line (RT-4) was studied for the three most active inhibitors **15 c**, **15 f** (after UV illumination) and **20 a**. RT-4 cells showed the highest expression of Sirt2 in our cellular inventory and therefore have been chosen for the cell-based activity determination. In order to prove a general effect of the compounds inside the cells, we conducted preliminary studies solely for irradiated probes, since the enzyme-based activity assay indicated either comparable activities of both photoisomers (**15 c**, **20 a**), or a higher activity of the *Z* isomer. Reductive stability of **15 c**, **15 f** and **20 a** in the presence of the cellular reductant glutathione (5 mм) was confirmed by HPLC analysis (Figure S5, Table S2). For the cell-based activity assay, we illuminated the compounds solved in DMSO with UV light (365 nm) prior to incubation with the cells. The compiled western blots displayed that all three compounds (**20 a**, **15 c**, **15 f**) had no effect on the expression of total histone H3 and total α-tubulin protein but in contrast, a slight increase of total H4 was detectable (Figure 5). As expected, **15 c** and **15 f** increased the levels of acetylated lysines H3K18 and H3K56, which are both affirmed substrates of Sirt2. In addition, we found H4K8 hyperacetylation even though this site is usually not affected by sirtuin catalysed deacetylation, indicating a further mode of action. In contrast, none of the compounds influenced the acetylation level of α-tubulin, which is frequently consulted as it is specifically processed by Sirt2. However, also in a cell-based activity assay of the highly potent Sirt2 inhibitor SirReal2 the degree of α-tubulin hyperacetylation was less pronounced when examined by western blot technique. Instead, applying an immunofluorescence assay yielded clearer results.[22] Surprisingly, compound **20 a** did not exert any activity regarding the examined substrates. In Figure 6, we show the relative results, whereby the acetylation product was related to total target protein and to the vehicle control. Again, we found an increase in acetylated histones induced by **15 c** and **15 f** which proves activity of these two compounds in living cells.

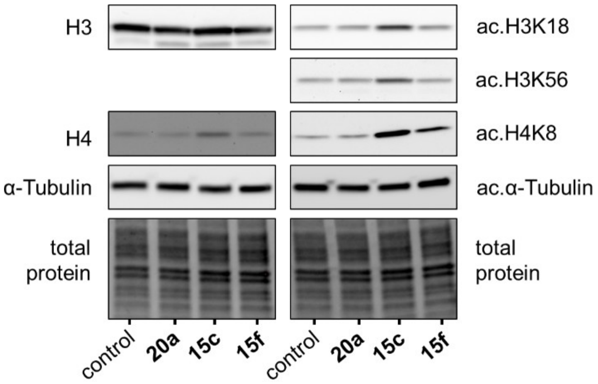

Figure 5. Representative western blots for total H3 resp. H4, α-tubulin as well as specific histone acetylation sites. Compounds were irradiated by UV light (365 nm) prior to incubation with cells.

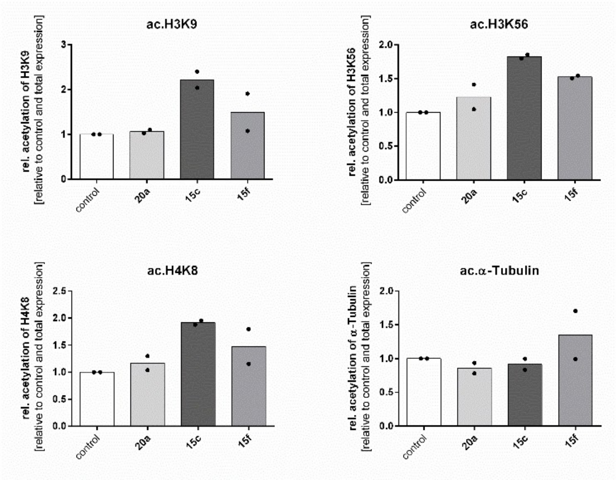

Figure 6. Relative acetylation levels of protein targets after incubation with compounds at 50 μм for 24 h in urinary bladder cancer cell line RT-4 (mean of $n=2$).

Conclusions

In this work, azologization of two different lead structures was performed in order to obtain azobenzene and azopyridine-based photoswitchable sirtuin inhibitors. Despite the high potential of diarylmaleimides and indolylfulgides as photoswitchable sirtuin inhibitors, we anticipated azo dyes to be more convenient, as this class of molecular photoswitches is known to possess reliable and highly tuneable photophysical properties also under physiological conditions. Indeed, azologization proved successful, since we obtained biologically active compounds, whose configuration could be reversibly toggled between *E* and *Z* form by UV (365 nm) or blue (452 nm) light irradiation. However, differential target engagement of the respective photoisomers was not as profound as anticipated. Whereas several photoswitchable drugs show a ten- to 50-fold difference in activity, in our case differential inhibition did not exceed a factor of 3–4 for most compounds.[25] Our docking studies implied that, despite the considerable structural change in the azo core, flexibility of the overall ligand structure could be responsible for the minor differences in bioactivity of the photoisomers. Furthermore, photoisomerization did not result in clearly unfavourable interactions between the ligand and residues of the sirtuins active site. Consequently, further rigidification and the introduction of sterically demanding groups could potentially be favourable in this regard. In contrast, pronounced effects were observed by photoswitching of highly lipophilic derivatives. Due to poor aqueous solubility, **15f** exerted only moderate, yet selective Sirt2 inhibition (IC_{50}= 37 µм) in its thermally stable *E* form. Since polarity is significantly enhanced by photoisomerization, biological activity of **15f** could be raised by a factor of 23 (IC_{50} = 1.6 µм) for Sirt2 inhibition. Additionally, activity of (*Z*)-**15f** was confirmed by increased acetylation levels of Sirt2 specific histones. Obviously, this effect is caused rather by a light-mediated improvement of the aqueous solubility than by altered binding affinity, as anticipated in the classical sense of photoswitchable drugs. This aspect of azo-based photoswitches has been studied recently and was exploited in the use of photochromic azo-combrestatin A-4 analogues.[26] In the latter case, photoswitching to the bioactive *Z* isomers provoked an up to 550-fold increase of bioactivity. Interestingly, in the same work the authors observed a longer *Z* isomer half-life of less soluble compounds in watery environment, potentially contributing to the remarkable impact of photoisomerization.

Even though photoisomerization of **15f** and other lipophilic compounds was hampered by chromophore aggregation in aqueous environment, solubility of these compounds should be enhanced in physiological media as blood, mediated by binding to albumin proteins. In this case, switching of an albumin-bound compound to the *Z* isomer could provoke its liberation in this specific area, thereby enabling tissue specific pharmacotherapy.

Experimental Section

General procedure for azo coupling of phenols: Methyl 5-aminonicotinate (1.0 equiv.) was suspended in aqueous HCl (6 м, 3.0 equiv.) and cooled to 0 °C. An aqueous solution of $NaNO_2$ (2.5 м, 1.0 equiv.) was added dropwise, so that the temperature did not exceed 5 °C. The resulting yellow solution was added slowly under stirring to the appropriate phenol (1.1 equiv.) dissolved in aqueous NaOH (2 м). If necessary, aqueous NaOH (2 м) was added to keep the resulting solution alkaline. After complete addition, the reaction mixture was acidified with aqueous HCl (6 м) and extracted with EtOAc. The combined organic extracts were washed with brine, dried over $MgSO_4$, filtrated and freed from solvent. The crude product was purified by silica gel column chromatography.

General procedure for azo coupling of anilines: Diazotization of methyl 5-aminonicotinate was carried out as described above. The yellow solution containing the diazonium salt was added slowly under stirring to the appropriate aniline (1.1 equiv.) dissolved in HCl (1 м). After complete addition, the reaction mixture was stirred for 10 min, then basified by using a saturated aqueous solution of Na_2CO_3 and extracted with EtOAc. The combined organic extracts were washed with brine, dried over $MgSO_4$, filtered and freed from solvent. The crude product was purified by silica gel column chromatography.

General procedure for synthesis of nicotinamides from methyl nicotinates: The respective methyl nicotinate was treated with a saturated solution of ammonia in anhydrous MeOH (30 mL) and stirred in a sealed vessel at 40 °C until thin layer chromatography indicated complete conversion of the starting material (three to four days). The solvent was evaporated under reduced pressure and the residue washed sparingly with cold acetonitrile.

Photochemistry: All photoisomerization experiments were conducted under ruby light of 630 nm and total exclusion of daylight. Illumination was executed using a Bio-Link 254 Crosslinker from Vilber-Lourmat equipped with six Vilber-Lourmat T8-L lamps (8 W, 365 nm). Visible light radiation of 630 nm (ruby) and 452 nm (blue) was derived from a Paulmann FlexLED 3D strip. All compounds were irradiated in solution using spectrophotometric grade solvents. Photoisomerization and UV/Vis-spectra measurement was conducted in quartz glass cuvettes (114-QS, Hellma Analytics) at room temperature.

Cloning, expression and purification of recombinant proteins: Expression and purification of $Sirt1_{133-747}$, $Sirt2_{56-356}$, and $Sirt3_{118-395}$ was carried out as described previously.[27] Identity and purity were verified by SDS-PAGE. Protein concentration was determined by the Bradford assay.[28] Deacylase activity of sirtuin isotypes could be inhibited with nicotinamide and was shown to be NAD^+-dependent.

Fluorescence-based activity assay: The inhibitory effect of compounds on Sirt1–3 was detected *via* a previously reported fluorescence-based assay.[29] The synthetic substrate (*Z*)-Lys(acetyl)-AMC (ZMAL) is deacetylated by sirtuins, followed by tryptic digestion and thereby release of 7-aminomethylcoumarin, leading to a fluorescent readout. Inhibition was determined by comparing percentage substrate conversion to a DMSO control after subtraction of the blank fluorescence signal. All compounds were tested at 100 or 50 µм and 10 µм respectively. For compounds that showed more than 70% inhibition at 10 µм an IC_{50} value was determined. IC_{50} values were calculated with OriginPro 9.0 G using a non-linear regression to fit the dose response curve (Figure S6). An enzyme-free blank control and a 100% conversion control using AMC instead of ZMAL were measured as well. Inhibition measurements were performed in biological duplicates for all compounds.

Molecular modelling: All calculations were performed by using the Molecular Operating Environment (MOE) software suite (version 2019.01).[30] If not explicitly stated otherwise, default settings and parameters were used.

General preparation: For molecular docking of ligands to human Sirt2, a crystal structure with open-state selectivity pocket and bound ligand was used (PDB IDs: 5MAT, 4RMG). Both systems were prepared by applying AMBER14 force field parameters, adding hydrogen atoms and protonation with Protonate3D (pH 7.4). Missing flexible protein loops were rebuilt, followed by a restraint minimization of the protein-ligand complex.

Molecular docking: Ligands used for docking experiments were prepared by generating three-dimensional structures from SMILES, taking into account possible protonation states and both *E*/*Z* isomers for azo groups. AM1-BCC charges were applied. The binding site was defined as all residues within 4.5 Å of the bound ligand in the crystal structure. Docking was performed using a two-stage protocol with placement of 30 poses by Triangle Matcher and London dG scoring, followed by an Induced Fit refinement and more accurate MM/GBVI scoring. For each ligand, a total of 10 final poses were obtained and visually inspected. For pharmacophore-guided molecular docking, a sphere with 1.7 Å was placed on the amide group of NAD$^+$(PDB: 4RMG), which was encoded by the SMARTS expression "[#7X3H2][#6X3](=[#8X1])[#6]".

Acknowledgements

The Jung group thanks the Deutsche Forschungsgemeinschaft (DFG, JU295/14-1 and 235777276/GRK1976) for funding, O.E. acknowledges support by grant DFG CRC 922.

Conflict of Interest

The authors declare no conflict of interest.

Keywords: azo dyes · epigenetics · photopharmacology · photoswitches · sirtuins

[1] a) J. N. Feige, J. Auwerx, *Curr. Opin. Cell Biol.* **2008**, *20*, 303–309; b) M. C. Haigis, L. P. Guarente, *Genes Dev.* **2006**, *20*, 2913–2921; c) E. Verdin, M. D. Hirschey, L. W. S. Finley, M. C. Haigis, *Trends Biochem. Sci.* **2010**, *35*, 669–675.

[2] a) R. A. Frye, *Biochem. Biophys. Res. Commun.* **2000**, *273*, 793–798; b) S. Greiss, A. Gartner, *Mol. Cells* **2009**, *28*, 407–415; c) M. Schiedel, D. Robaa, T. Rumpf, W. Sippl, M. Jung, *Med. Res. Rev.* **2018**, *38*, 147–200.

[3] Y.-B. Teng, H. Jing, P. Aramsangtienchai, B. He, S. Khan, J. Hu, H. Lin, Q. Hao, *Sci. Rep.* **2015**, *5*, 8529.

[4] K. J. Bitterman, R. M. Anderson, H. Y. Cohen, M. Latorre-Esteves, D. A. Sinclair, *J. Biol. Chem.* **2002**, *277*, 45099–45107.

[5] a) AOP Orphan Pharmaceuticals AG, to be found under https://www.aoporphan.com/global_en/our-company/newsroom/aop-orphan-pharmaceuticals-ag-to-acquire-selisistat-a-clinical-stage-drug-candidate-for-the-treatment-of-huntingtons-disease-hd, **2017**; b) S. D. Süssmuth, *Br. J. Clin. Pharmacol.* **2015**, *79*, 465–476.

[6] T. Ai, D. J. Wilson, S. S. More, J. Xie, L. Chen, *J. Med. Chem.* **2016**, *59*, 2928–2941.

[7] S. Swyter, M. Schiedel, D. Monaldi, S. Szunyogh, A. Lehotzky, T. Rumpf, J. Ovádi, W. Sippl, M. Jung, *Philos. Trans. R. Soc. B* **2018**, *373*.

[8] C. W. Grathwol, N. Wössner, S. Swyter, R. K. Hofstetter, A. Bodtke, M. Jung, A. Link, *Beilstein J. Org. Chem.* **2019**, *15*, 2170–2183.

[9] C. W. Grathwol, N. Chrysochos, B. J. Elvers, A. Link, C. Schulzke, *Acta Crystallogr. Sect. E* **2019**, *75*, 1828–1832.

[10] a) P. Leippe, J. A. Frank, *Curr. Opin. Struct. Biol.* **2019**, *57*, 23–30; b) P. Paoletti, G. C. R. Ellis-Davies, A. Mourot, *Nat. Rev. Neurosci.* **2019**, *20*, 514–532; c) H. Cheng, J. Yoon, H. Tian, *Coord. Chem. Rev.* **2018**, *372*, 66–84; d) K. Hüll, J. Morstein, D. Trauner, *Chem. Rev.* **2018**, *118*, 10710–10747; e) I. Tochitsky, M. A. Kienzler, E. Isacoff, R. H. Kramer, *Chem. Rev.* **2018**, *118*, 10748–10773; f) M. Zhu, H. Zhou, *Org. Biomol. Chem.* **2018**, *16*, 8434–8445; g) M. M. Lerch, M. J. Hansen, G. M. van Dam, W. Szymanski, B. L. Feringa, *Angew. Chem. Int. Ed.* **2016**, *55*, 10978–10999; *Angew. Chem.* **2016**, *128*, 11140–11163; *Angew. Chem.* **2016**, *128*, 11140–11163; *Angew. Chem. Int. Ed.* **2016**, *55*, 10978–10999.

[11] a) J. Broichhagen, J. A. Frank, D. Trauner, *Acc. Chem. Res.* **2015**, *48*, 1947–1960; b) W. Szymański, J. M. Beierle, H. A. V. Kistemaker, W. A. Velema, B. L. Feringa, *Chem. Rev.* **2013**, *113*, 6114–6178.

[12] W. A. Velema, W. Szymanski, B. L. Feringa, *J. Am. Chem. Soc.* **2014**, *136*, 2178–2191.

[13] C. Falenczyk, M. Schiedel, B. Karaman, T. Rumpf, N. Kuzmanovic, M. Grøtli, W. Sippl, M. Jung, B. König, *Chem. Sci.* **2014**, *5*, 4794–4799.

[14] N. A. Simeth, L.-M. Altmann, N. Wössner, E. Bauer, M. Jung, B. König, *J. Org. Chem.* **2018**, *83*, 7919–7927.

[15] a) W. Szymanski, M. E. Ourailidou, W. A. Velema, F. J. Dekker, B. L. Feringa, *Chemistry* **2015**, *21*, 16517–16524; b) S. A. Reis, *Nat. Chem. Biol.* **2016**, *12*, 317–323; c) C. E. Weston, A. Krämer, F. Colin, Ö. Yildiz, M. G. J. Baud, F.-J. Meyer-Almes, M. J. Fuchter, *ACS Infect. Dis.* **2017**, *3*, 152–161.

[16] H. M. D. Bandara, S. C. Burdette, *Chem. Soc. Rev.* **2012**, *41*, 1809–1825.

[17] a) S. Crespi, N. A. Simeth, B. König, *Nat. Rev. Chem.* **2019**, *3*, 133–146; b) D. Cameron, S. Eisler, *J. Phys. Org. Chem.* **2018**, *31*, e3858; c) M. Dong, A. Babalhavaeji, S. Samanta, A. A. Beharry, G. A. Woolley, *Acc. Chem. Res.* **2015**, *48*, 2662–2670; d) N. A. Simeth, A. Bellisario, S. Crespi, M. Fagnoni, B. König, *J. Org. Chem.* **2019**; e) J. Calbo, C. E. Weston, A. J. P. White, H. S. Rzepa, J. Contreras-García, M. J. Fuchter, *J. Am. Chem. Soc.* **2017**, *139*, 1261–1274.

[18] H. Cui, Z. Kamal, T. Ai, Y. Xu, S. S. More, D. J. Wilson, L. Chen, *J. Med. Chem.* **2014**, *57*, 8340–8357.

[19] a) A. A. Blevins, G. J. Blanchard, *J. Phys. Chem. B* **2004**, *108*, 4962–4968; b) W. R. Brode, J. H. Gould, G. M. Wyman, *J. Am. Chem. Soc.* **1952**, *74*, 4641–4646.

[20] a) M. Shimomura, R. Ando, T. Kunitake, *Ber. Bunsen-Ges.* **1983**, *87*, 1134–1143; b) J. M. Kuiper, J. B. F. N. Engberts, *Langmuir* **2004**, *20*, 1152–1160; c) L. H. Urner, B. Schade, M. Schulze, K. Folmert, R. Haag, K. Pagel, *ChemPhysChem* **2019**, *20*, 1690–1697.

[21] N. A. Simeth, S. Crespi, M. Fagnoni, B. König, *J. Am. Chem. Soc.* **2018**, *140*, 2940–2946.

[22] T. Rumpf, *Nat. Commun.* **2015**, *6*, 6263.

[23] D. Robaa, D. Monaldi, N. Wössner, N. Kudo, T. Rumpf, M. Schiedel, M. Yoshida, M. Jung, *Chem. Rec.* **2018**, *18*, 1701–1707.

[24] A. A. Beharry, G. A. Woolley, *Chem. Soc. Rev.* **2011**, *40*, 4422–4437.

[25] M. W. H. Hoorens, W. Szymanski, *Trends Biochem. Sci.* **2018**, *43*, 567–575.

[26] a) S. K. Rastogi, *Eur. J. Med. Chem.* **2018**, *143*, 1–7; b) M. Ishikawa, T. Ohzono, T. Yamaguchi, Y. Norikane, *Sci. Rep.* **2017**, *7*, 6909.

[27] M. Schiedel, D. Herp, S. Hammelmann, S. Swyter, A. Lehotzky, D. Robaa, J. Oláh, J. Ovádi, W. Sippl, M. Jung, *J. Med. Chem.* **2018**, *61*, 482–491.

[28] U. K. Laemmli, *Nature* **1970**, *227*, 680–685.

[29] B. Heltweg, J. Trapp, M. Jung, *Methods* **2005**, *36*, 332–337.

[30] Molecular Operating Environment (MOE), 2019.01; Chemical Computing Group ULC, 1010 Sherbrooke St. West, Suite #910, Montreal, QC, H3A 2R7, **2019**.

Manuscript received: March 6, 2020
Revised manuscript received: April 20, 2020
Accepted manuscript online: April 21, 2020
Version of record online: ■■, ■■■

FULL PAPERS

Switched into action: Besides fine-tuning molecular geometry for enzyme inhibition, photoinduced isomerization of azopyridine-based nicotinamide mimics results in improved aqueous solubility, enforcing the effect on target protein sirtuin 2. The resulting Sirt2 inhibitor could be used to study binding events in cellular systems with spatiotemporal control by two independent molecular and supramolecular effects.

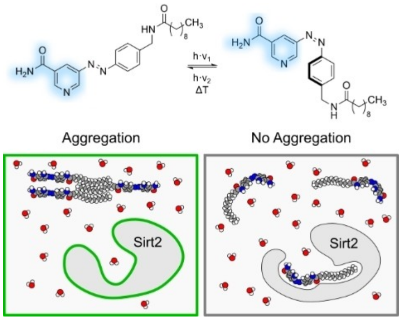

*C. W. Grathwol, N. Wössner, Dr. S. Behnisch-Cornwell, L. Schulig, Dr. L. Zhang, Prof. Dr. O. Einsle, Prof. Dr. M. Jung, Prof. Dr. A. Link**

1 – 11

Activation of Sirtuin 2 Inhibitors Employing Photoswitchable Geometry and Aqueous Solubility

5.4 Manuskript IV

Correlations between the expression of 10 histone deacetylases (HDACs) and the sensitivities of 23 anticancer drugs in 17 human cancer cell lines and the influence of various HDAC inhibitors on cisplatin, lomustin and topotecan cytotoxicity

Steven Behnisch-Cornwell, Christoph W. Grathwol, Lukas Schulig, Anika Voigt, Andreas Link, Patrick J. Bednarski

FEBS Journal **2020**, zur Begutachtung eingereicht.

Beiträge der Autoren

Steven Behnisch-Cornwell:	Konzipierung des Projekts Biologische Testung Erstellen des Manuskripts
Christoph W. Grathwol:	Synthese untersuchter Verbindungen Erstellen des Manuskripts
Lukas Schulig:	Durchführung der Korrelationsanalysen
Anika Voigt:	Biologische Testung
Andreas Link:	Betreuung des Projekts
Patrick J. Bednarski:	Betreuung des Projekts

Christoph W. Grathwol

Andreas Link

ORIGINAL ARTICLE

Journal Section

Correlations between the expression of 10 histone deacetylases (HDACs) and the sensitivities of 23 anticancer drugs in 17 human cancer cell lines and the influence of various HDAC inhibitors on cisplatin, lomustin and topotecan cytotoxicity

Steven Behnisch-Cornwell, Dr. | Christoph W. Grathwol | Lukas Schulig | Anika Voigt | Andreas Link, Prof. | Patrick J. Bednarski, Prof.

Correspondence
Steven Behnisch-Cornwell
Tel. +49 3834 4204860
Email: steven.behnisch@uni-greifswald.de
(until september 2020)

Present address
University of Greifswald, Institute of Pharmacy, Friedrich-Ludwig-Jahn-Str. 17, 17489 Greifswald, Germany

Funding information
We acknowledge support for the Article Processing Charge from the DFG (German Research Foundation, 393148499) and the Open Access Publication Fund of the University of Greifswald, as well as we thank the University of Greifswald for funding this project with a start-up grant.

The modulation of histone deacetylase (HDAC) activity is a contemporary strategy in anticancer therapy. However, until now the relation between HDAC protein expression and anticancer drug sensitivity of cancer cells has not been investigated. In the current work, we investigated the relative expression profiles of 10 HDAC isoenzymes of the classes I–III (HDAC1/2/4/6; Sirt1/2/3/5/6/7) in a set of 17 cancer cell lines, including various breast, cervix, oesophageal, lung, oral squamous, pancreas, as well as urinary bladder carcinoma cells. Correlations between the mRNA expression data for these same enzymes obtained from the NCI 60 cancer cell line program were also done. Next, we performed univariate analysis between the HDACs expression patterns with the sensitivity of cancer cell lines towards several anticancer drugs. In a univariate correlation analysis, we found a strong relation between Sirt2 expression and cytotoxicity caused by busulfan, etoposide and hydroxyurea. Another correlation was identified between Sirt5 and oxaliplatin or topotecan as well as between HDAC4 expression and the same two drugs. Correlations between the mRNA expression data for enzymes with the potencies of the same anticancer agents obtained from the NCI 60 cancer cell line program were also performed. Additionally, we report here the combination effects of the approved HDAC inhibitors vorinostat and trichostatin A, as well as newer stilbene and diazeno based inhibitors on cisplatin, lomustin and topotecan potency. For all three anticancer drugs, we found a significantly enhanced cytotoxicity when co-incubated with HDAC inhibitors, demonstrating a potentially beneficial influence of HDAC inhibition in anticancer drug treatment.

KEYWORDS
histone deacetylases, sirtuins, anticancer drugs, correlation analysis, HDAC inhibitors, sirtuin inhibitors

1 | INTRODUCTION

The epigenetic modulation of protein expression can have a broad influence on tumor progression and prognosis and can cause cancer recurrence as well as malfunction of anticancer therapy. [1, 2, 3] Epigenetic regulation is often an effect of post–translational protein modification through processes of methylation/demethylation or

---

Abbreviations: CGI, relative combination growth inhibition at $50\,\%$; GI_{50}, growth inhibition at $50\,\%$; HDAC, histone deacetylase; NCI, National Cancer Institute; SAHA, suberanilohydroxamic acid (Vorinostat); TSA, trichostatin–A acetylation/deacetylation, just to name but a few. The histone proteins are one of the major epigenetic targets, which are responsible for the DNA compaction in the nucleus. Post–translational acetylation of lysine residues in histone tails causes an "open" chromatin conformation leading to a better accessibility of DNA binding sites for transcription factors and enhanced RNA polymerase activity in that area. Instead, methylation of lysines in histone tales causes denser chromatin structures, with the result of a reduced transcriptional activity. Key players of these posttranslational histone modifications are histone deacetylases (HDAC) and acetyltransferases. As epigenetic alterations are characterised to be reversible, intervention into epigenetic regulation mechanism ranks among contemporary strategies in antineoplastic therapy.

The super family of HDAC enzymes is subdevided into four classes according to sequence homologies and cofactor dependencies. The classes I, II and IV mediate their hydrolysis activity through a zinc depending mechanism and are designated as "classical" HDACs. The zinc ion stabilises the acetylated substrate in the catalytic center and polarises the carbonyl group, thereby facilitating the nucleophilic attack of the carbonyl group by a water molecule. The class I HDACs (HDAC1, HDAC2 HDAC3 and HDAC8) share a common domain of the yeast transcriptional regulator RPD3 and are located in nuclear compartments. The class II HDACs are subdivided into class IIa (HDAC4, HDAC5, HDAC7 and HDAC9), which share a large C-terminus and into class IIb (HDAC6 and HDAC10) that contain two acetylase domains. In general, class II HDACs possess just a minor or limited enzymatic activity. In the cell, these enzymes migrate between cytosol and nucleus. HDAC11 is the only member of class IV and exhibits features of both, the classes I and II HDACs. However, the specificity of classical HDACs towards single core histones is very low and ambiguously discussed.[4, 5, 6]

Class III HDACs, the so-called sirtuins, distinguish themselves from classical HDACs by their dependency on the cofactor NAD$^+$. Interestingly, these enyzmes do not use NAD$^+$ as a redox active co-factor; rather during the enzymatic reaction, the acetyl group is transferred to NAD$^+$, releasing nicotinamide and a mixture of 2'- and 3'-*O*-acetyl-ADP-ribose (*O*AADPR) as by-products. In humans, seven sirtuin isoenzymes have been identified (Sirt1–7) and were assigned to four different groups, according to their phylogenetic relationship. Class I includes the isoenzymes Sirt1–3, the class IV includes Sirt6 and Sirt7, whereas the isoenyzmes Sirt4 and Sirt5 are assigned to class II and class III, respectively. The various sirtuin isoenzymes differ in their subcellular localisation, enzymatic activities as well as substrate specificities. Sirt1, Sirt6 and Sirt7 are usually localised in the nucleus, Sirt2 is mainly cytosolic. Except for Sirt4 and Sirt5, *in vivo* deacetylation of core histone proteins is reported for all human sirtuin isoenzymes. However, enyzmatic activity is not limited to histone deacetylation; whereas the class I isotypes Sirt1–3 show a robust deacetylase activity, the mono-ADP-ribosyltransferase activity of Sirt4 and Sirt6 is more profound. Furthermore, other acyl groups than acetyl are recognized and cleaved by certain isotypes. In this regard, Sirt5 is associated with the removal of acyl groups derived from dicarboxylic acids (malonyl, glutaryl and succinyl) and Sirt6 as well as Sirt2 with the cleavage of long-chain fatty acyl groups such as myristoyl. Besides their function as epigenetic regulators *via* histone deacetylation, nearly all HDAC isoenzymes possess additional non-histone targets, such as p53, NF-κB or HIF-1α explaining their overarching role in apoptosis, cell cycle progression, and ultimately tumorigenesis.[7, 8, 9]

HDAC inhibitors are currently under intensive investigation because of their promising potential in antineoplastic chemotherapy. Inhibitors of the classical HDAC isotypes can be classified into four groups according to their structural features: i) hydroxamic acids as vorinstat, belinostat, panabinostat or trichostatin A (for some, see Figure 1), ii) short chain fatty acids such as valproic acid, iii) 2-aminobenzamides like etinostat and iv) cyclic tetrapeptides such as romidepsin. All these compounds share a common mechanism of action, which is based on their tendency to form highly stable chelate complexes with the HDACs active site zinc ion, ultimately causing loss of enzymatic functionality.

In recent years, the unselective HDAC inhibitors vorinostat, panabinostat, belinostat as well as the HDAC6 selective inhibitor romidepsin have been approved as drugs for the treatment of haematological malignancies as well as various solid tumors.[5, 6] Additionally, a whole range of further HDAC inhibitors such as valproic acid and roclinostat are currently undergoing clinical trials. Regarding sirtuins, several compounds have been identified as potent inhibitors, even though none of them have yet reached market maturity. Besides analogues of the endogenous pan-sirtuin inhibitor nicotinamide, several other compounds where found to inhibit the sirtuin-catalyzed deacetylation. These include NAD$^+$ mimics, hydroxynaphthaldehyde derivatives as sirtinol and cambinol, splitomicins, thiobarbiturates, SirReals and numerous structurally divers compounds such as suramin, tenovin and aristoforin. The screening of kinase inhibitor libraries has often proven successful in the search for novel sirtuin inhibitors and yielded the Sirt2-selective inhibitor AGK2, for instance. The highly potent and selective Sirt1 inhibitor selisistat (EX-527) represents the most advanced sirtuin-targeting drug candidate and is currently tested in phase-III clinical trials as disease-modifying agent in Huntington's disease.[9, 10, 11]

Recently, we reported on the design of photoswitchable sirtuin inhibitors based on the moderately active, but unselective stilbenoid lead structure GW435821X. By structural modifications, the bioactivity of the parent compound was increased to the lower micro-molar range and isotype selectivity towards Sirt2 and Sirt3 could be improved.[12] Furthermore, replacement of the stilbene C,C-double bond with a diazeno group yielded a series of analogous phenylazopyridines that enabled light-mediated modulation of the sirtuin-catalysed deacetylation (see Figure 1).[13]

Herein, we present a comprehensive study of the HDAC expression profiles in a panel of 17 human cancer cell lines from various tumor origins, along with univariate correlation analyses to anticancer drug potency. Furthermore, we investigated the combination effects of HDAC inhibition on the potency exerted by the approved anticancer drugs cisplatin, lomustin and topotecan.

2 | METHODS

2.1 | Chemicals

Compounds **1a-5c** were synthesised as recently described.[12, 13] All other chemicals were purchased from Sigma Aldrich (Taufkirchen, Germany) except for lomustin, temozolomid and topotecan, which were obtained from biomol (Hamburg, Germany). Imatinib mesylate was purchased from Selleckchem (Munich, Germany). The cell culture medium RPMI1640, as well as the penicillin/streptomycin were obtained from PAN Biotech (Aidenbach, Germany), whereas foetal bovine serum was from Sigma Aldrich.

2.2 | Cell culture

All cell lines were obtained from Deutsche Sammlung von Mikroorganismen und Zellkulturen (DSMZ) and cultured in RMPI 1640 cell culture medium supplemented with $10\,\%$ foetal bovine serum and $1\,\%$ penicillin/streptomycin in a humidified incubator at $37\,^{\circ}\mathrm{C}$ with $5\,\%$ CO_2 atmosphere. All cell lines were passaged weekly (nearly reaching confluence) and routinely tested for mycoplasma.

2.3 | GI_{50} determination (inhibition of proliferation)

Growth inhibition (GI) was determined by the crystal violet assay as previously described.[16] In brief, per well of a 96-well plate, 1000 cells were seeded out in $100\,\mu\mathrm{L}$ culture medium and allowed to attach for $24\,\mathrm{h}$. Subsequently, cells in the rapid phase of cell growth were exposed to serial dilutions of compounds, added to the medium of the 1000-fold concentrated stock solution in DMSO. After an incubation period of $96\,\mathrm{h}$, cells were fixed with an $1\,\%$ glutaraldehyde solution in Dulbecco's buffer for $20\,\mathrm{min}$. After washing with Dulbecco's buffer a staining procedure was performed, using a $0.2\,\%$ crystal violet solution in water for $30\,\mathrm{min}$. Plates were washed with water and stored for $15\,\mathrm{min}$ in water to remove unbound crystal violet. Bound crystal violet was eluted with $70\,\%$ ethanol for $2\,\mathrm{h}$ on a plate shaker, followed by determination of optical density at $\lambda = 570\,\mathrm{nm}$ utilizing a SpectraMax Plus 384 plate reader. The optical density of cells at time point zero of compound exposure (T_0 control) was subtracted from treated cells and related to untreated control (T/C). The GI_{50} value was calculated with GraphPad Prism Software 6.0 by interpolation of the inhibited proliferation at $50\,\%$.

2.4 | Determination of expression profiles

HDAC expression profiles were analysed *via* western blot technique, following the instructions of Biorad (Munich, Germany) by using precast "Cirterion TGX Stain-Free Gels" and the corresponding "Trans-Blots Turbo Pack Midi" PVDF membranes. All antibodies were purchased from Cell Signaling Technology (United Kingdom): anti-HDAC1 (#5356), anti-HDAC2 (#5113), anti-HDAC4 (#7628), anti-HDAC6 (#7558), anti-Sirt1 (#9475), anti-Sirt2 (#12650), anti-Sirt3 (#5490), anti-Sirt5 (#8782), anti-Sirt6 (#12486), anti-Sirt7 (#5360), anti-mouse HRP-linked (#7076) and anti-rabbit HRP-linked (#7074).

The culture cells were grown in T_{75} flasks and samples were collected when confluency of $80\,\%$ were reached and lysed on ice for $30\,\mathrm{min}$ with a buffer containing $50\,\mathrm{mM}$ Tris (pH 7.4), $100\,\mathrm{mM}$ NaCl, $100\,\mathrm{mM}$ NaF, $5\,\mathrm{mM}$ EDTA, $0.2\,\mathrm{mM}$ Na_3VO_3, $0.1\,\%$ Triton-X and freshly

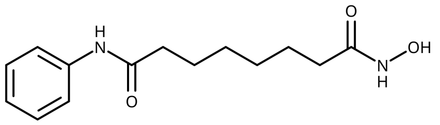

SAHA

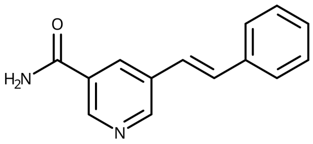

1a

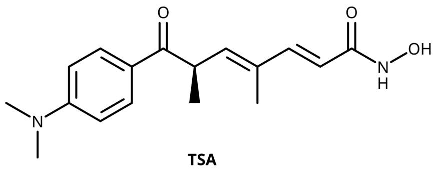

TSA

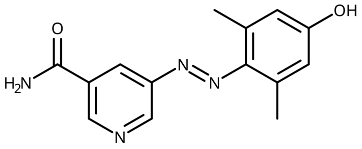

2a

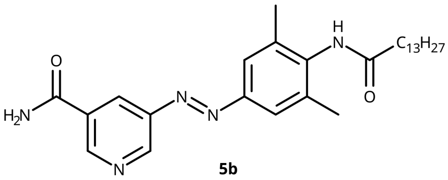

5b

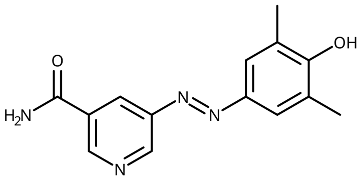

3a

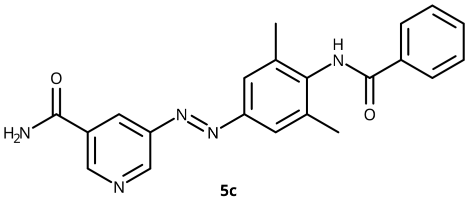

5c

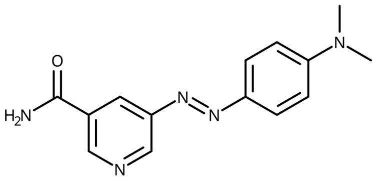

4a

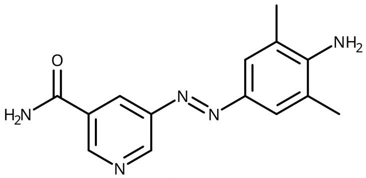

5a

	Sirt1	Sirt2	Sirt3
1a	71 % [10 µM]	8.7 ± 0.2 µM	89 % [50 µM]
2a	14 % [50 µM]	7.9 ± 0.6 µM	9.5 ± 0.9 µM
3a	19 % [50 µM]	10.8 ± 0.6 µM	7.9 ± 0.5 µM
4a	17 % [10 µM]	54 % [10 µM]	66 % [10 µM]
5a	47 % [100 µM]	5.8 ± 0.7 µM	9.4 ± 0.7 µM
5b	n. i.	2.4 ± 0.4 µM	n. i.
5c	n. i.	n. i.	n. i.

FIGURE 1 Structures and IC_{50} values in µM or inhibition in % at fixed concentration of HDAC inhibitors, n.i.: no inhibition detected (< 30 % at $100\,\mu M$).[12, 13, 14, 15]

added $1\,\%$ protease inhibitor cocktail (Sigma Aldrich, Germany), followed by a sonication for $10\,\mathrm{min}$. After centrifugation at $18\,000\,\mathrm{g}$ for $10\,\mathrm{min}$ at $4\,°\mathrm{C}$, the protein concentration was quantified via Bradford method against bovine serum albumin (BSA) as standard. Protein samples were stored at $-80\,°\mathrm{C}$ until analysis.

For the electrophoretic separation, $30\,\mu\mathrm{g}$ of total protein were diluted in $22.5\,\mu\mathrm{L}$ aqua purificata and $7.5\,\mu\mathrm{L}$ 4x laemmli buffer containing $0.65\,\mathrm{mM}$ 1,4-dithiothreitol, $18.66\,\mu\mathrm{M}$ bromophenol blue, $0.25\,\mathrm{mM}$ Tris (pH 6.8), sodium lauryl sulfate $7.5\,\%$, and $37.5\,\%$ glycerol in water. Each slot of the precast gels was loaded with protein samples and blotted onto PVDF-membranes after electrophoretic separation. Blots were blocked with $10\,\%$ non-fat milk powder in Tris buffered saline / tween buffer (TBST) containing $0.02\,\mathrm{mM}$ Tris, $0.145\,\mathrm{mM}$ NaCl and $0.5\,\%$ Tween 20 in water for $2\,\mathrm{h}$ and incubated with primary antibody dilution (1:1000) in TBST plus $1\,\%$ BSA over night at $4\,°\mathrm{C}$. After washing procedure with TBST, blots were incubated with horse radish peroxidase conjugated secondary antibody dilution (1:5000) in TBST plus $1\,\%$ BSA for $2\,\mathrm{h}$ at room temperature. Protein bands were detected with Clarity Western ECL Substrate (Biorad, Germany) and recorded with an Advanced Fluorescence Imager (INTAS, Germany). Band intensity was related to internal standard signals of the TGX Stain-Free gels as loading control and to the mean of each target protein signal.

2.5 | Data from National Cancer Institute 60 cell line program

The data from NCI were downloaded from dtp.cancer.gov in May 2020. For the expression of mRNA following experiment ID numbers were used: HDAC1 #GC29185, HDAC2 #GC15516, HDAC4 #GC28681, HDAC6 #GC12671, Sirt1 #GC64431, Sirt2 #GC16536, Sirt3 #GC91754, Sirt5 #GC13785, Sirt6 #GC78925, Sirt7 #GC46856. Following experiment NSC identifiers and experiment ID numbers were used for anticancer drug potency (GI_{50} values): methotrexate NSC740 #25554, colchicine NSC757 #333742, busulfan NSC750 #442014, chlorambucil NSC3088 #281369, thiotepa NSC6396 #244838, melphalan NSC8806 #257999, 5–fluorouracil NSC19893 #112657, podophyllotoxin NSC24818 #284040, hydroxyurea NSC32065 #66393, vinblastine NSC49842 #377648, lomustin NSC79037 #48835, camptothecin NSC94600 #15291, azacitidine NSC102816 #242610, cisplatin NSC119875 #103078, doxorubicin NSC123127 #442278, paclitaxel NSC125973 #32427, etoposide NSC141540 #178907, carboplatin NSC241240 #35161, oxaliplatin NSC266046 #145880, topotecan NSC609699 #35531, bortezomib NSC681239 #167040, vorinostat NSC701852 #238689, imatinib NSC743414 #96705.

2.6 | Statistics

For the statistical evaluation and visualization the Python packages statsmodels v0.11.1 [17], Matplotlib v.3.1.3 [18] and GraphPad Prism v6.0 Software were used. Pearson correlation, *R* were calculated by using ordinary least squares (OLS).

For the statistical analysis of the influence of HDAC inhibitors on anticancer drug potency (subsection 3.4) an ordinary one-way ANOVA was performed with Dunnett's multiple comparison test adaption against the control. In general, the mean of a determination is imaged ± SD and the level of significance is pictured as $^{*}p < 0.05$, $^{**}p < 0.01$, $^{***}p < 0.001$ and $^{****}p < 0.0001$.

3 | RESULTS

3.1 | Determination of expression profiles of HDAC isoenzymes in a panel of 17 cell lines and the correlation analysis of their expression

A representative set of corresponding western blots of the expression of the HDAC/Sirt in 17 cancer cell lines is pictured in Figure 2 and the relative protein expression profiles are compiled in Figure 3. Table 1 provides the underlying dataset to Figure 3. For HDAC1, expression is most pronounced in the cell lines MCF-7, BHY and A278, whereas the urinary bladder cancer cell lines 5637, RT-4 and RT-112 show the lowest expression. Among the tested cell lines, HDAC2 expression is less varying than for HDAC1, as the relative expression lies between 0.7 and 1.3 for the most cell lines. Compared to the mean, only YAPC, RT-4 and RT-112 possess lower levels, whereas Kyse-510 as well as EFM-19 cells show higher levels. Regarding HDAC4, the highest expression was found in DanG, YAPC and A427, whereas BHY, MCF-7 and LCLC-103H cells showed the lowest expression. In case of HDAC6, the relative expression of protein varies much more compared to the other HDAC isoenzymes tested. The highest relative levels of 3.45, 2.55 and 2.19 are found in A427, YAPC and SiSo cells, whereas the lowest levels of 0.16, 0.19 and 0.46 were detected in DanG, Kyse-520 and Pa-Tu-8902, respectively.

For Sirt1, the highest expression was found in A427 cells, whereas EFM-19, DanG, 5637, RT-4 and RT-112 cells showed low relative protein expression with values under 0.65. The total Sirt2 protein consists of two isoforms, one with $43\,\mathrm{kDa}$ and a smaller variant with $39\,\mathrm{kDa}$. For the relative expression profile determination, both isoforms were used in sum. The highest Sirt2 expression was found in RT-4 and EFM-19 cell lines and the lowest level was determined in Pa-Tu-8902 cells. Noticeable, all of the oesophageal carcinoma and lung carcinoma cell lines showed a lower protein expression than the mean of all tested cell lines. A427, MT-3 and Kyse-70 cells showed the highest expression for Sirt3, whereas RT-112, EFM–19 and 5637 cells showed the lowest expression. For Sirt5 we found the lowest protein expression in 5637 cells, followed by EFM-19, SiSo and LCLC-103H cells with the same range of protein expression. The highest amount of Sirt5 was detected in DanG cells, followed by Kyse-510 and Kyse-70. The Sirt6 levels, also in sum of two isoforms, fluctuated notably in tested cells lines with highest expression in A427 cells, followed by Kyse-70 and 5637 cells with values above 2. The pancreas carcinomas cell lines Pa-Tu-8902, YAPC and DanG expressed the weakest Sirt6 expression, with values under 0.41. Regarding the expression of Sirt7, we detected values between 0.55 for Kyse-70 cells and 1.71 for A427 cells. In relation to all sirtuin isotypes, Sirt7 was most equally balanced among the tested cell lines.

Pearson-*R* correlation analysis was performed to detect potential correlations between protein expression of various HDAC isoenzymes. Figure 4 illustrates the results in a correlation matrix, whereas corresponding *R* and *p*-values are compiled in Table S1. No correlations were detected among HDAC isoenzymes of class I and II. However, a clearly positive and significant correlation was detected between HDAC1 and HDAC6 with Sirt1 ex-

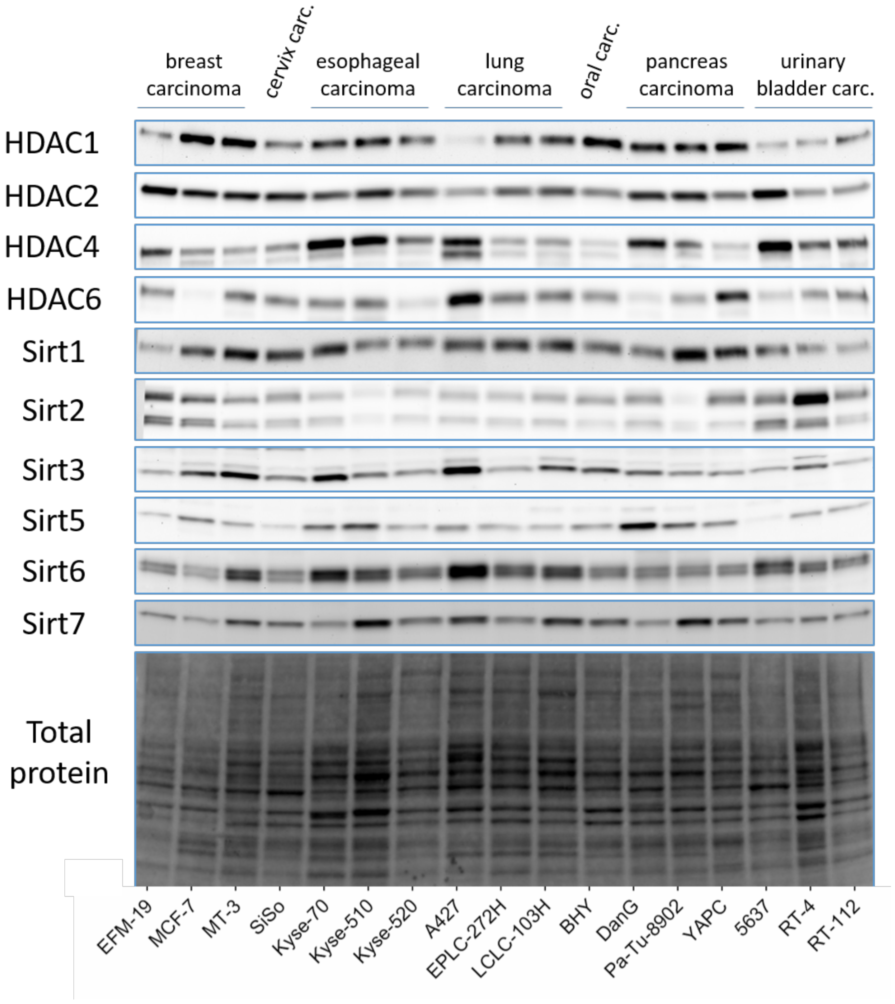

FIGURE 2 Representative western blots of protein expression for HDAC-isoenzymes in various cancer cell lines.

pression, HDAC4 with Sirt5, as well as HDAC1 with Sirt3 and Sirt7 expression. We detected a significant inverse correlation between HDAC2 and Sirt2 as well as a borderline significant correlation between HDAC1 and Sirt2. Within the group of sirtuins a significant positive correlations were detected among each other for Sirt1 with Sirt3, Sirt6 and Sirt7 as well as Sirt3 with Sirt6 and Sirt7 (borderline).

3.2 | Analogous correlation analysis of mRNA expression data from the National Cancer Institute 60 cancer cell line program

By using data made available by the National Cancer Institute (NCI) 60 cancer cell line program, we performed analogous correlation analysis with mRNA expression data for the corresponding HDACs and Sirts. The NCI ID numbers of the enzymes that were used are listed in the methods section, and the univariate correlation matrix of mRNA expression is shown in Figure 5 and data values compiled in Table S2. In the comparison of the mRNA expression data from 60 cell lines, positive correlations between HDAC1 mRNA expression was found between HDAC2 and HDAC6, with significant R-values of 0.354 and 0.364, respectively. Further significant correlations between the HDAC isoenzymes mRNA expression were not identified.

3.3 | Determination of antiproliferative activity of SAHA and TSA and correlation analysis of their activity with the protein expression of zinc dependent HDAC isoenzymes

To test whether the potency of the HDAC inhibitors SAHA and TSA correlates with the expression of zinc dependent HDAC isoenzymes, we determined the potency of both compounds in various cancer cell lines, expressed

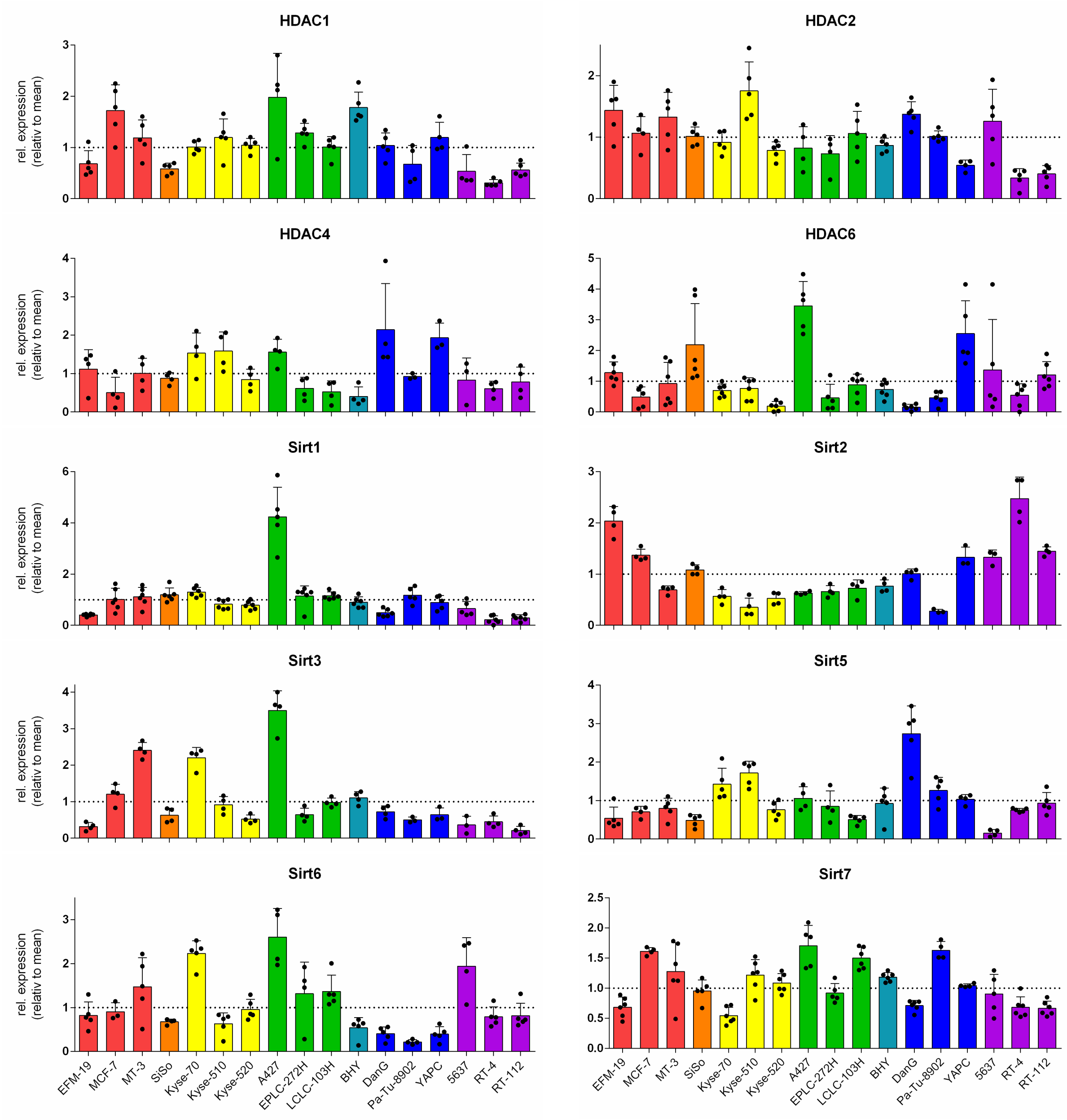

FIGURE 3 . Relative protein expression profiles of HDAC isoenzymes in various cancer cell lines (relative to the mean expression) [mean ± SD of $n > 3$ of independent determinations; breast carcinoma, cervix carcinoma, oesophageal carcinoma, lung carcinoma, oral squamous carcinoma, pancreas carcinoma, urinary bladder carcinoma]

TABLE 1 Relative HDAC isoenzyme protein expression of various cancer cell lines (relative to the mean expression) [mean± SD of n = 3 of independent determinations].

	breast carcinoma			cerv. carc.	oesophageal carcinoma			lung carcinoma			oral carc.	pancreas carcinoma			urinary bladder carcinoma		
	EFM-19	MCF-7	MT-3	SiSo	Kyse-70	Kyse-510	Kyse-520	A427	EPLC-272H	LCLC-103H	BHY	DanG	Pa-Tu-8902	YAPC	5637	RT-4	RT-112
HDAC1	0.681 0.257	1.718 0.503	1.186 0.352	0.584 0.108	1.011 0.117	1.196 0.361	1.043 0.133	1.978 0.859	1.284 0.186	1.010 0.203	1.780 0.301	1.037 0.246	0.673 0.367	1.195 0.295	0.536 0.323	0.308 0.065	0.560 0.133
HDAC2	1.436 0.409	1.065 0.271	1.328 0.401	1.015 0.153	0.917 0.177	1.755 0.472	0.784 0.142	0.822 0.348	0.732 0.293	1.061 0.361	0.867 0.118	1.374 0.202	1.015 0.087	0.544 0.087	1.260 0.521	0.338 0.152	0.404 0.137
HDAC4	1.114 0.511	0.503 0.401	1.009 0.393	0.876 0.148	1.532 0.523	1.586 0.497	0.844 0.269	1.559 0.332	0.615 0.286	0.526 0.284	0.406 0.248	2.141 1.203	0.926 0.073	1.932 0.383	0.833 0.574	0.608 0.192	0.785 0.383
HDAC6	1.281 0.346	0.490 0.330	0.923 0.694	2.192 1.331	0.702 0.210	0.768 0.343	0.190 0.149	3.454 0.791	0.461 0.442	0.881 0.349	0.735 0.268	0.157 0.095	0.458 0.229	2.550 1.066	1.369 1.643	0.548 0.370	1.208 0.432
Sirt1	0.405 0.047	1.016 0.435	1.109 0.367	1.189 0.272	1.297 0.179	0.825 0.183	0.785 0.164	4.236 1.154	1.139 0.400	1.158 0.148	0.902 0.206	0.490 0.146	1.176 0.310	0.890 0.269	0.653 0.280	0.219 0.155	0.294 0.116
Sirt2	2.037 0.283	1.368 0.120	0.692 0.076	1.081 0.098	0.564 0.136	0.352 0.179	0.523 0.119	0.629 0.030	0.660 0.113	0.725 0.162	0.767 0.118	1.010 0.089	0.277 0.038	1.327 0.202	1.326 0.144	2.472 0.421	1.446 0.088
Sirt3	0.318 0.110	1.204 0.274	2.406 0.215	0.629 0.196	2.202 0.281	0.914 0.229	0.521 0.112	3.497 0.539	0.645 0.178	0.976 0.124	1.104 0.173	0.724 0.163	0.502 0.075	0.641 0.191	0.363 0.240	0.448 0.159	0.212 0.113
Sirt5	0.539 0.291	0.708 0.140	0.794 0.267	0.482 0.155	1.424 0.413	1.715 0.310	0.761 0.212	1.054 0.302	0.848 0.405	0.508 0.103	0.924 0.404	2.736 0.719	1.261 0.343	1.032 0.126	0.155 0.089	0.752 0.045	0.932 0.276
Sirt6	0.822 0.305	0.905 0.207	1.473 0.666	0.679 0.060	2.232 0.288	0.634 0.246	0.960 0.231	2.604 0.656	1.319 0.717	1.367 0.372	0.542 0.231	0.409 0.152	0.217 0.051	0.400 0.168	1.943 0.652	0.792 0.223	0.814 0.286
Sirt7	0.685 0.169	1.613 0.064	1.278 0.479	0.955 0.182	0.546 0.138	1.218 0.259	1.087 0.157	1.705 0.337	0.920 0.159	1.500 0.178	1.185 0.076	0.712 0.086	1.629 0.145	1.044 0.028	0.905 0.325	0.683 0.173	0.666 0.120

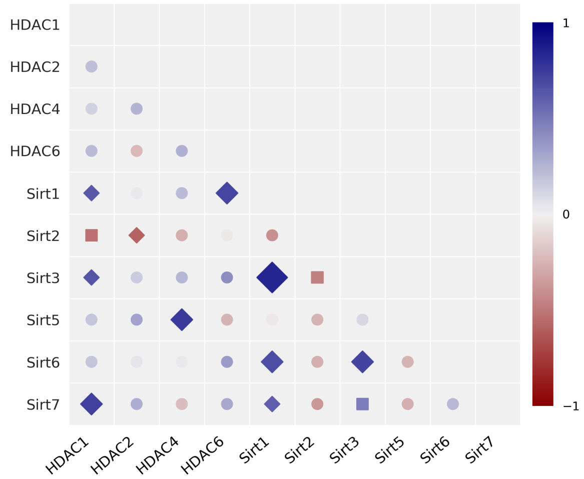

FIGURE 4 Univariate correlation matrix for HDAC isoenzyme protein expression [statistics: ♦ $p < 0.05$, ■ $p < 0.1$, • not significant]. Positive correlations are in blue, negative in red (see scale-bar)

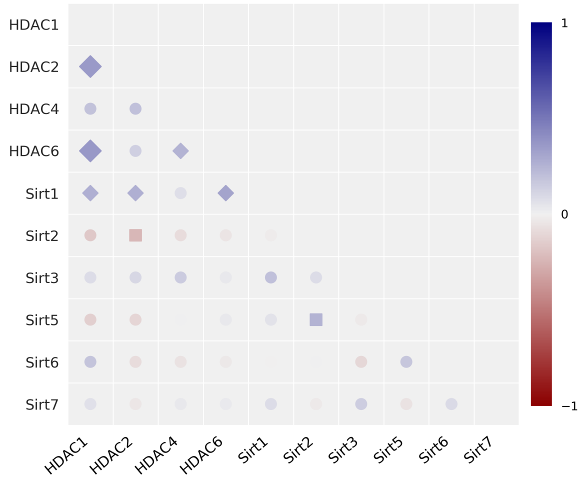

FIGURE 5 Univariate correlation matrix for HDAC isoenzyme mRNA expression with data of NCI 60 cancer cell line program [statistics: ♦ $p < 0.05$, ■ $p < 0.1$, • not significant]. Positive correlations are in blue, negative in red (see scale-bar)

as $50\,\%$ growth inhibitory values (GI_{50}). Table 2 shows the determined GI_{50} values as well as the relative GI_{50} (GI_{50} value related to the mean of all tested cell lines). For SAHA the GI_{50} values were in the single-digit micromolar scale, whereas the GI_{50} values for TSA were approximately ten times lower. To assess whether SAHA and TSA act by the same mechanism of action a Pearson correlation analysis was performed with the corresponding graph illustrated in Figure 6. A highly significant correlation was identified between the potency of both compounds in the various cancer cell lines, with R-values of 0.852 ($p < 0.0001$). The most sensitive cell line towards zinc dependent HDAC inhibitors was A427 followed by MCF-7 and LCLC-103H, whereas the cell lines Kyse-510 and Pa-Tu-8902 were the least sensitive.

We hypothesize that the toxicity of SAHA and TSA could correlate with the expression of zinc dependent HDAC isoenzymes. To clarify this situation, a Pearson correlation analysis was performed with the GI_{50} values of SAHA or TSA in every cell line to the corresponding relative protein expression of zinc dependent HDAC isoenzymes (data not shown). However, no correlation was detected between these two variables, with R-values between -0.44 and 0.30 and corresponding p-values beyond 0.1.

3.4 | Correlation analysis of standard anticancer drugs potency in cancer cells and the doubling time of cancer cells with the HDAC protein expression

To test whether there is a connection between the HDAC protein expression and the cytotoxic effect of selected anticancer drugs, a univariate correlation analysis was performed with the relative GI_{50} values of the anticancer drugs of each cell line to the corresponding relative protein expression of the HDAC isoenzyme.

The GI_{50} values for most of the anticancer drugs in 14 of the cell lines were taken from our earlier investigations [16], while the GI_{50} values of imatinib, lomustin, temozolomide, bortezomib, and topotecan were newly determined for the present study. The GI_{50} values are given in Table 3, and corresponding relative GI_{50} can also be found in the supporting information.

In the case of imatinib, the cell line A427 and DanG were quite sensitive with GI_{50} values of $6.5 \pm 5.6\,\mu\mathrm{M}$ and $6.8 \pm 1.2\,\mu\mathrm{M}$, respectively. The highest GI_{50} was found in Pa-Tu-8902 with a value of $16.6 \pm 0.7\,\mu\mathrm{M}$. For lomustin, the most sensitive cell line was MT-3 with a GI_{50} of $3.5 \pm 0.4\,\mu\mathrm{M}$ The average GI_{50} in every cell line was $28.3\,\mu\mathrm{M}$. Relative to the mean GI_{50}, the GI_{50} in MT-3 cells is 8-times lower. In the case of temozolomide, it was not possible to determine an GI_{50} value below

TABLE 2 GI$_{50}$ values of SAHA and TSA for proliferation inhibition in various cancer cell lines [mean ± SD of $n < 3$ of independent determinations] and their relative GI$_{50}$ values (relative to the mean GI$_{50}$).

	SAHA		TSA			SAHA		TSA	
cell line	GI$_{50}$ (nM)	rel.GI$_{50}$	GI$_{50}$ (nM)	rel.GI$_{50}$	cell line	GI$_{50}$ (nM)	rel.GI$_{50}$	GI$_{50}$ (nM)	rel.GI$_{50}$
MCF7	527.8 79.4	0.64	33.55 14.41	0.45	BHY	598.7 136.3	0.73	52.36 7.20	0.71
MT3	689.6 114.9	0.84	77.74 14.48	1.05	DanG	586.1 35.7	0.72	71.90 11.33	0.97
SiSo	909.3 126.6	1.11	60.13 3.56	0.81	Pa-Tu-8902	1536.6 248.5	1.88	123.92 9.36	1.67
Kyse-70	602.0 67.5	0.74	50.56 7.69	0.68	YAPC	1210.4 228.9	1.48	72.83 38.57	0.98
Kyse-510	1862.6 210.3	2.28	174.83 40.01	2.36	5637	667.2 239.4	0.82	78.71 38.98	1.06
Kyse-520	501.5 45.4	0.61	78.14 29.97	1.06	RT-4	873.6 115.5	1.07	98.75 22.38	1.33
A427	228.3 158.0	0.28	24.89 24.26	0.34	RT-112	825.9 106.6	1.01	92.68 16.12	1.25
LCL-103H	511.8 74.2	0.63	38.72 13.13	0.52	A2780	964.9 165.0	1.18	54.47 6.98	0.74

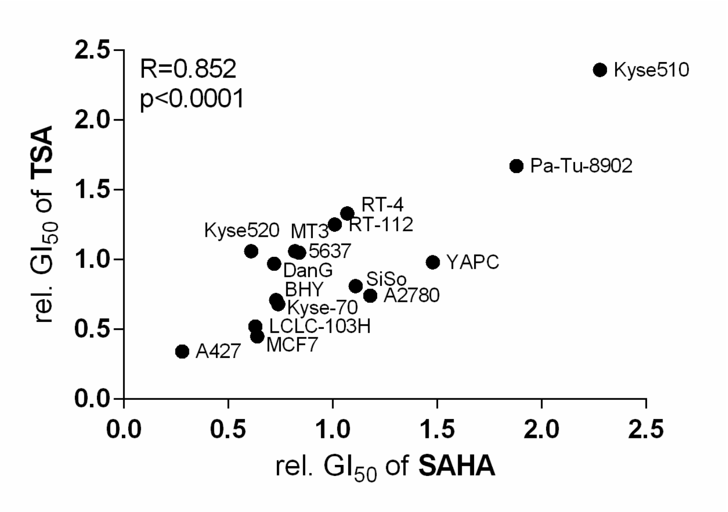

FIGURE 6 Univariate correlation analysis of SAHA with TSA potency expressed as relative GI$_{50}$ values in various cancer cells lines [$R = 0.852$, $p < 0.0001$].

$400\,\mu\mathrm{M}$ for the most cell lines; only A427 showed a low GI$_{50}$ around $6.1\,\mu\mathrm{M}$, followed by LCLC–103H ($71.3\,\mu\mathrm{M}$) and Pa-Tu-8902 cells ($211.9\,\mu\mathrm{M}$). The GI$_{50}$ values of bortezomib ranged from $4.1\,\mathrm{nM}$ (Pa-Tu-8902) to $9.0\,\mathrm{nM}$ (Kyse–510) in tested cell lines. The potency of paclitaxel was unspecific, with the GI$_{50}$ values ranging only between $1.0\,\mathrm{nM}$ and $1.7\,\mathrm{nM}$, except for MT-3 cells, where an increased GI$_{50}$ value around $3.6\,\mathrm{nM}$ was detected. In contrast, the antiproliferative potency of topotecan fluctuates much more in tested cell lines, with a ca. 5-fold difference between the most sensitive cell line MT-3 $10.4 \pm 4.15\,\mathrm{nM}$ and the least sensitive Kyse-510 $56.3 \pm 1.36\,\mathrm{nM}$.

The correlation matrix for the correlation of the relative protein expression and corresponding anticancer drug potency (expressed as GI$_{50}$ value) are shown in Figure 7, with the corresponding R and p-values compiled in Table S3. A positive correlation means high protein expression correlates with high GI$_{50}$ values (direct correlation), whereas a negative correlation (inverse correlation) means high protein expression correlates with low GI$_{50}$ values. For the zinc dependent HDAC2 isoenzyme, we found borderline significance ($p < 0.1$) for an inverse correlation with carboplatin, cisplatin, hydroxyurea and a positive correlation with topotecan. For HDAC4, a highly significant positive correlation was detected with oxali-

TABLE 3 GI_{50} values of several anticancer drugs in various cancer cell lines [mean ± SD of n = 3].

	MCF-7	MT-3	Kyse-510	Kyse-520	A427	LCLC-103H	BHY	DanG	Pa-Tu-8902	YAPC	5637
Imatinib (μM)	11.61	11.49	13.38	9.24	6.47	9.29	13.20	6.78	16.56	11.77	12.98
	3.75	0.27	1.16	1.30	5.63	3.97	0.91	1.21	0.71	1.14	1.66
Lomustin (μM)	55.83	3.51	23.30	16.03	11.47	22.29	41.00	39.40	37.45	46.04	15.14
	8.63	0.35	1.16	4.91	3.06	6.24	4.65	10.80	1.97	5.86	3.75
Temozolomid (μM)	>400	>400	22.82	>400	6.07	71.27	>400	>400	211.92	>400	>400
			2.23		0.52	7.40			35.32		
Bortezomib (nM)	4.51	6.16	9.00	8.69	7.79	5.69	4.89	6.24	4.10	6.34	8.65
	2.03	1.46	4.21	3.39	0.78	1.37	1.58	0.51	0.28	1.09	1.22
Paclitaxel (nM)	1.22	3.61	1.68	1.19	1.42	1.17	1.24	1.01	1.46	1.63	1.23
	0.33	0.70	0.31	0.18	0.36	0.04	0.11	0.26	0.17	0.08	0.04
Topotecan (nM)	18.71	10.24	56.30	11.70	21.98	15.41	21.02	52.95	12.12	20.67	13.04
	2.82	4.15	1.36	1.66	7.20	0.88	1.33	2.08	0.98	1.12	0.81

platin and topotecan and for HDAC6 a negative correlation with chlorambucil and vinblastine.

Significant relations were also found between NAD^+-dependent HDAC expression and anticancer drug potency. A positive significant correlation was indicated between Sirt2 expression and potency mediated by busulfan, etoposide, 5-fluorouracil, and hydroxyurea as well as a borderline significance regarding potency caused by thiotepa. The Sirt5 expression correlates positive significantly with oxaliplatin and topotecan. For Sirt6 an inverse significant correlation was detected with oxaliplatin and for Sirt7 a borderline significance with podophyllotoxin.

Additionally, a Pearson correlation analysis was done to detect a potential connection of the doubling time of cancer cells with the HDAC isoenzyme expression. The doubling time of cancer cells was determined during the weekly transfer of cells into new cell culture flask by counting the cells and seeding out a specific cell number to the new flasks. The doubling time was calculated *via* the following equation.

$$\text{doubling time (h)} = \frac{t\ \text{(h)}}{\log_2\left(\frac{\text{cell number } t}{\text{cell number } t_0}\right)} \qquad (1)$$

The calculated doubling times of the cancer cell lines are compiled in Table S5; the data for correlation analysis is shown in Figure 7. The correlation analysis rules out a linear correlation between the expressions of various HDAC isoforms with the doubling time. Only concerning Sirt2 a borderline significance was detected that linked a high Sirt2 expression with a longer doubling time.

3.5 | Analogues correlation analysis of standard anticancer drugs potency in cancer cells and the mRNA expression with data from the National Cancer Institute 60 cancer cell line program

Analogous correlation analysis of HDAC isoenzyme mRNA expression and the potency of anticancer drugs was performed with data from the NCI 60 cancer cell line program. The univariate correlation matrix of mRNA expression is shown in Figure 8 and corresponding values in Table S4. In total, the data from 60 cell lines were compared. In general, a few significant correlations were found, but the R-values were below -0.370; this is because of the very large number of cell lines still makes such correlations significant. Remarkably, only inverse correlations were detected between enzyme mRNA expression and GI_{50} values: i.e., HDAC1 mRNA expression with 5-fluorouracil and methotrexate, HDAC2 with colchicine, HDAC6 and Sirt1 with lomustin, Sirt2 with camptothecin, chlorambucil, oxaliplatin, thiotepa and topotecan and between Sirt6 mRNA expression with etoposide potency. This is in contrast to our data in the 17 cancer cell line panel with protein expression, where both negative and positive correlations were found (Figure 8).

3.6 | Combination effect of HDAC inhibition on anticancer drug potency

The stilbenoid compound **1a** and the other azo-based sirtuin inhibitors **2b-5c** did not display potency in tested cell lines up to $100\,\mu\mathrm{M}$ (data not shown). Only in case of **2a**, GI_{50} values were determined with: $4.6 \pm 2.1\,\mu\mathrm{M}$, $10.8 \pm 0.4\,\mu\mathrm{M}$, $8.8 \pm 1.7\,\mu\mathrm{M}$, $5.4 \pm 1.5\,\mu\mathrm{M}$ and $7.1 \pm 4.1\,\mu\mathrm{M}$

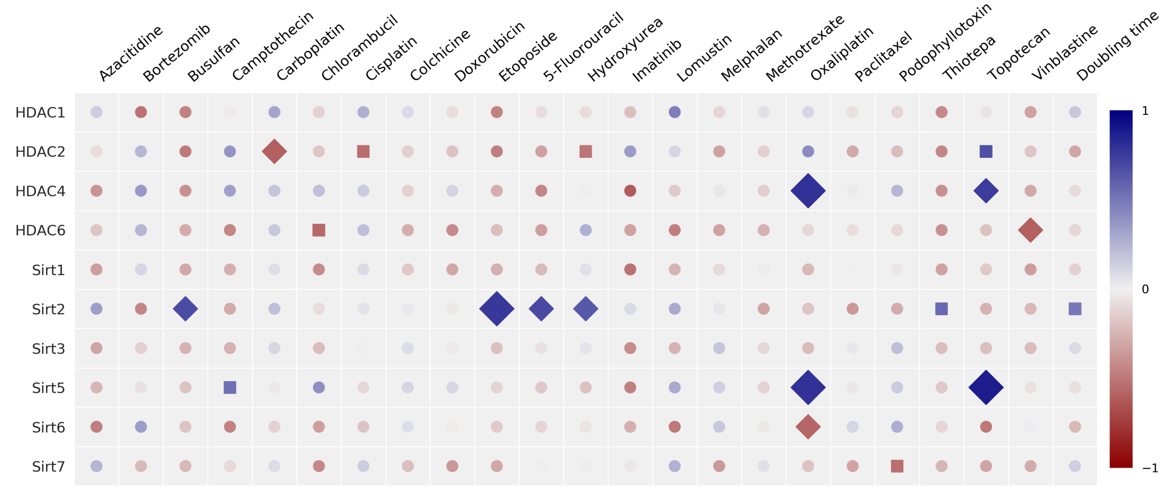

FIGURE 7 Univariate correlation of HDAC isoenzyme protein expression with anticancer drug potency expressed as GI_{50} values and the doubling time of cancer cells [statistics: ♦ $p < 0.05$, ■ $p < 0.1$, • not significant]

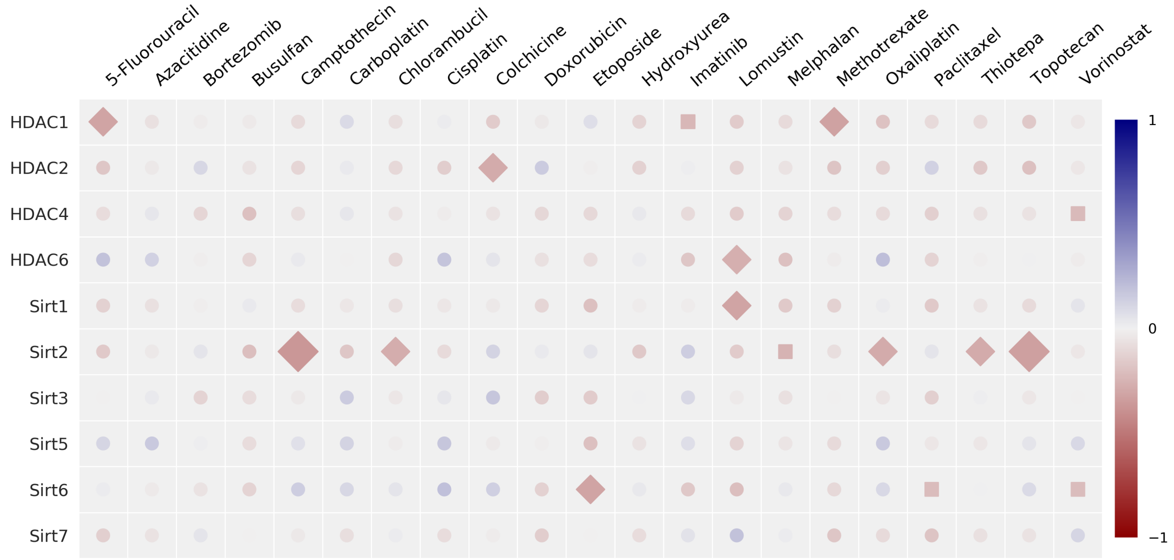

FIGURE 8 Univariate correlation of HDAC isoenzyme protein expression with anticancer drug potency expressed as GI_{50} values and the doubling time of cancer cells [statistics: ♦ $p < 0.05$, ■ $p < 0.1$, • not significant]

in the 5637, SiSo, Kyse-70, RT-4 and RT-112 cell lines, respectively. Due to the minor cytotoxicity of the sirtuin inhibitors we did not perform a correlation analysis according to subsection 3.3 and 3.4 for these compounds. To assess whether HDAC inhibitors can affect the potency of the anticancer drugs, SiSo cells were used because of a balanced protein expression of all tested HDAC isoenzymes. SiSO cells were exposed to inhibitors at fixed, non-toxic concentrations (SAHA: $0.3\,\mu\mathrm{M}$, TSA: $0.03\,\mu\mathrm{M}$, **2a**: $5\,\mu\mathrm{M}$, **1a** and **3a-5c**: $50\,\mu\mathrm{M}$) in combination with serial dilutions of anticancer drugs and the GI_{50} values for the inhibition proliferation were determined. The combination effect is expressed as relative combination growth inhibition at $50\,\%$ (CGI), which is the value of the quotient of the GI_{50} in combination (drug + the HDAC-inhibitor) divided by the control GI_{50} (drug alone). A CGI < 1 indicates enhanced anticancer drug potency as a result of the HDAC inhibitor, a CGI > 1 indicates diminished potency and with CGI $= 1$ the HDAC-inhibitor has no effect on the potency of the anticancer drug.

Figure 9 shows the results for CGI determination for the combinations of various HDAC-inhibitors with the anticancer drugs cisplatin, lomustin and topotecan in the SiSo cell line, while the raw GI_{50} and CGI values are compiled in Table 4. The combination of cisplatin with several HDAC inhibitors resulted in an enhanced cisplatin potency in some cases. For instance, the combination of cisplatin with SAHA and TSA showed just a slightly decreased GI_{50} with CGI values of 0.81 and 0.91. Similar results were obtained in combinations with **2a** (0.88), **4a** (0.86) and **5c** (0.89). For the combination of cisplatin with **1a**, **3a**, and **5a**, a significantly enhanced potency of cisplatin was detected, with decreased GI_{50} values from 238 to 135, 184 and $121\,\mathrm{nM}$ respectively, corresponding to CGI values of 0.43, 0.61 and 0.57, respectively. SAHA and TSA had no effect on the potency of lomustin on SiSo cells. Compared to the control GI_{50}, the GI_{50} values determined in combination were virtually unaffected. Instead, the GI_{50} decreased significantly in combination with **1a**, **3a**, and **5a** to values of 2.4, 2.3 and $2.9\,\mu\mathrm{M}$ respectively, and with CGI values of 0.50, 0.47 and 0.59, respectively. In combination with **2a** and **4a**, the CGI were only slightly decreased (0.85 and 0.83) and left unaffected in the case of **5b** and **5c** (0.93 and 1.07).

For the combination with SAHA or TSA with topotecan, a significant enhancement of topotecan potency was detected. The combination with SAHA and TSA resulted in decreases in the GI_{50} of topotecan from 20.2 to 16.3 and $16.5\,\mathrm{nM}$ respectively, with CGI values of 0.63 and 0.80, respectively. The combination with stilbenoid compound **1a** or azo-based sirtuin inhibitors resulted in a significantly enhanced topotecan potency, except for **5b**. The GI_{50} value of topotecan decreased significantly, in some cases by half, to 13.5, 10.0, 11.2, 14.6, 12.8, and $15.4\,\mathrm{nM}$ when co-incubated with **1a**, **2a**, **3a**, **4a**, **5a** and **5c**, respectively. Corresponding CGI values range from 0.52 to 0.79.

4 | DISCUSSION AND CONCLUSIONS

In previous studies we sought associations between antiproliferative activity of 19 anticancer drugs with the activity of various antioxidative enzymes in a similar panel of human cancer cell lines.[19] In the present work, correlations between the HDAC expression profiles in various cancer cell lines and the potency of anticancer drug potency were investigated. HDACs represent a family of key epigenetic modulators. It has been reported that the expression of zinc dependent HDACs can be significantly increased in neoplastic tissues compared to healthy tissues [20, 21]. However, expression of sirtuins in cancer would seem to be much more complex. Various studies report an upregulation of sirtuins in cancer cells, while others demonstrate a downregulation in comparison to normal tissues [22]. Thus, the role of sirtuins in cancer cells may be double-edged because of tumor suppression and on the other hand, oncogenic properties.

For our studies, we expected an irregular protein expression of HDAC isoenzymes across the tested cell lines and assumed that a low protein expression of a certain isoenzyme could be compensated by an increase in the expression of another isoenzyme, reflected by a significant inverse correlation. However, we found no evidence to confirm this hypothesis. Except for HDAC2 with Sirt2, no inverse correlations were apparent. Instead, a few positive correlations were detected. We found positive correlations between HDAC1 with Sirt1, Sirt3 and Sirt7, HDAC4 with Sirt5, HDAC6 with Sirt1, Sirt1 with Sirt3, Sirt6 and Sirt7 as well as Sirt6 with Sirt7. The genes for the HDAC isoenzymes are spread widely across the chromosomes; an overview of the localisation is given in Table S6. This fact rules out that significant positive correlations are due to adjacent or closely localized genes on the same chromosome. To the best of our knowledge, there are no comparable studies in literature that report similar findings.

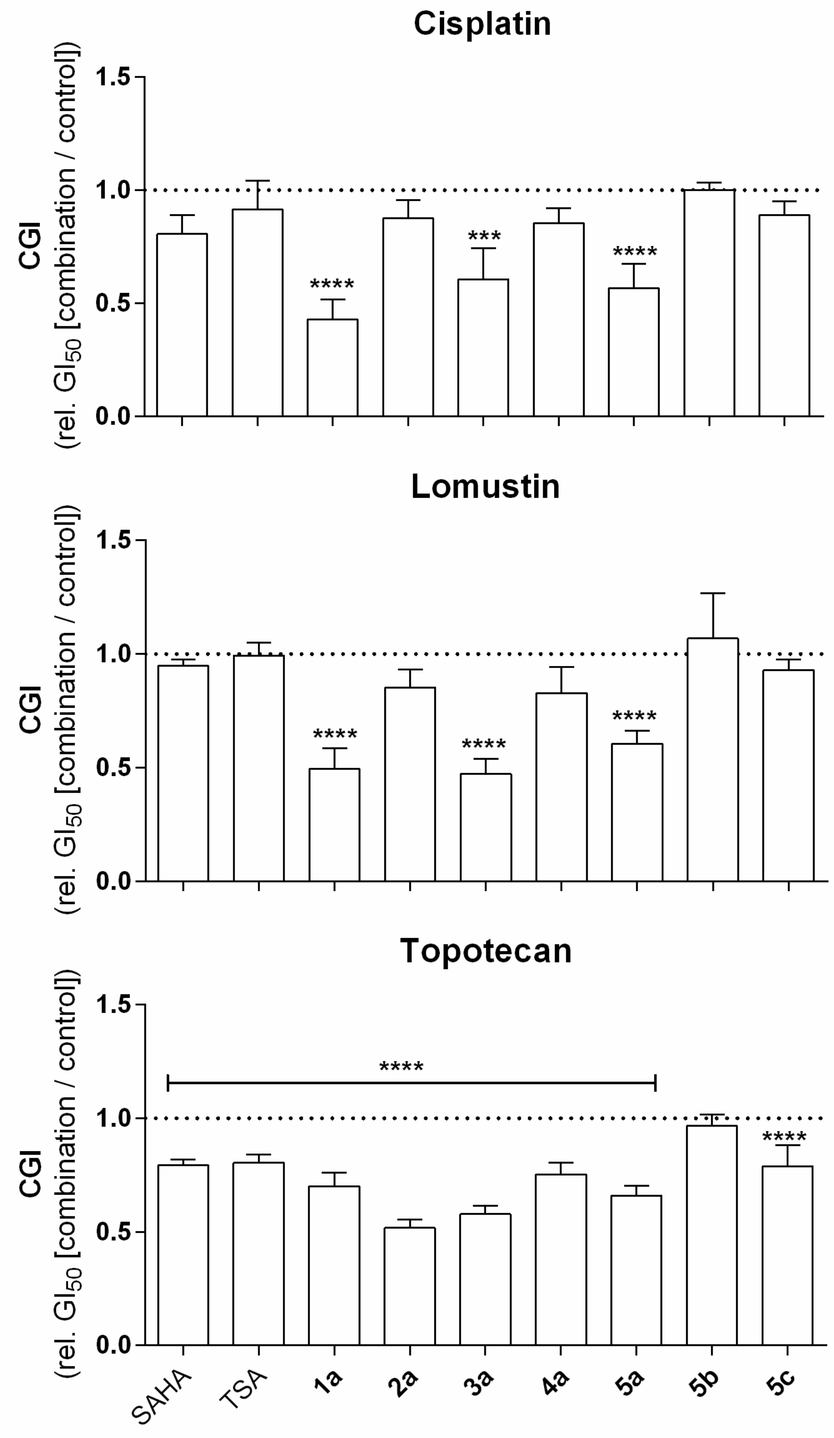

FIGURE 9 Relative GI_{50} values of cisplatin, lomustin and topotecan in combination with HDAC inhibitors (SAHA: $0.3\,\mu M$, TSA: $0.03\,\mu M$, **2a**: $5\,\mu M$, **1a** and **3a–5c**: $50\,\mu M$) related to the GI_{50} of the respective anticancer drug without inhibitor (CGI) in SiSo cell line; dotted lines mark the control without inhibitor incubation [mean + SD of $n > 3$; statistics: one way ANOVA, Dunnett's multiple comparisons test; $^{***}p < 0.001$, $^{****}p < 0.0001$]

TABLE 4 GI$_{50}$ and relative GI$_{50}$ values (CGI) for cisplatin, lomustin and topotecan in combination with HDAC inhibitors (SAHA: $0.3\,\mu\mathrm{M}$, TSA: $0.03\,\mu\mathrm{M}$, A1a: $5\,\mu\mathrm{M}$, A2a-A7a: $50\,\mu\mathrm{M}$) in SiSo and Kyse-70 cells [mean ± SD of $n > 3$, statistics: $p < \mathbf{0.001}$].

	Cisplatin		Lomustin		Topotecan	
	GI$_{50}$ (μM)	CGI	GI$_{50}$ (μM)	CGI	GI$_{50}$ (nM)	CGI
W/O	237.9	1.000	4.93	1.000	20.15	1.000
	60.8		0.61		2.03	
SAHA	156.3	0.805	4.90	0.948	16.31	**0.634**
	18.2	0.070	0.36	0.023	1.26	0.318
TSA	177.5	0.914	5.15	0.995	16.52	**0.804**
	25.6	0.103	0.50	0.045	0.94	0.032
1a	134.9	**0.428**	2.40	**0.495**	13.54	**0.700**
	50.9	0.072	0.28	0.074	0.58	0.050
2a	184.2	0.875	4.10	0.853	10.03	**0.518**
	13.7	0.066	0.99	0.069	0.59	0.029
3a	189.7	**0.606**	2.31	**0.473**	11.20	**0.578**
	70.8	0.112	0.40	0.055	0.80	0.029
4a	265.3	0.855	4.05	0.828	14.64	**0.754**
	64.4	0.053	0.70	0.092	1.44	0.041
5a	120.6	**0.566**	2.85	**0.591**	12.83	**0.659**
	31.8	0.089	0.72	0.042	1.68	0.035
5b	308.0	1.002	5.18	1.068	18.84	0.967
	47.5	0.025	0.76	0.164	2.68	0.039
5c	275.3	0.890	4.56	0.929	15.44	**0.790**
	55.0	0.048	0.72	0.039	3.12	0.074

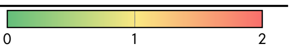

Analogous correlation analyses were performed with data from the NCI 60 cancer cell line program. The NCI collects data of mRNA expression for genes as well as antiproliferative potencies (GI$_{50}$) of a large number of small molecules such as anticancer drugs in a panel of 60 various cancer cells lines of differing tumor origin. Compiled datasets are available free of charge to the public by an internet-based data bank. Unfortunately, data with protein expression profiles are not available, probably because of the high expense and effort such protein analysis by western blotting would entail. Here, we have performed correlation analysis with protein expression, which we believe more accurately mirrors the cellular epigenomic functionality comparable to data obtained from mRNA analysis. Interestingly, none of the correlations we found between the HDAC/Sirt enzyme expression were found in the corresponding NCI data, and *vica versa*. Likewise, none of the correlations we found between HDAC/Sirt enzyme expression and anticancer drug potencies in the 17 cell line panel were present in the corresponding NCI data, and *vice versa*. While the two panels of cancer cell lines have different sizes and different cancer cell lines, in a previous study where we compared relative potencies of anticancer drugs in these two panels, many of the same correlations could be confirmed in both panels.[14] On the other hand, when we compared the relative enzyme activities of various antioxidative enzymes with the corresponding mRNA expression in the 60 cell NCI panel, no apparent correlations were found.[19] Thus, we believe that the reason for these discrepancies in the present study are due to differences in comparing protein expression with mRNA expression data.

Further analysis of the protein expression of the HDAC isoenzymes in relation to the potency of several anticancer drugs revealed numerous coherencies. For the anticancer drugs busulfan and hydroxyurea, we detected a significant positive correlation with Sirt2 levels. As a result, cancer cells that possessed lower levels of Sirt2 protein were more sensible to the cytotoxic effects of the respective drugs and *vice versa*. In the literature, a connection between Sirt2 protein expression and busulfan as well as hydroxyurea potency has not yet been described. Further studies need to be conducted to confirm this finding. Moreover, we detected a significant positive correlation between the 5–fluorouracil mediated toxicity and Sirt2 expression. Combination studies of unspecific zinc dependent HDAC inhibitors, as well as sirtuin inhibitors, have been performed by several groups, who found a positive combination effect between 5–fluorouracil and various HDACs[23, 24]. Similarly, we determined significant positive correlations between the topoisomerase inhibitors etoposide and Sirt2 protein expression as well as topotecan with HDAC4 and Sirt5 and an inverse correlation of the vinca alkaloid vinblastine with HDAC6. While the beneficial effect of a combination of class I HDAC inhibitors with etoposide, topotecan and vinca alkaloids has already been reported [25, 26, 27], a correlation between these drugs and Sirt2 protein expression is new. Interestingly, Grohmann et al. showed that the inhibition of nicotinamide phosphoribosyltransferase, that causes leakage of NAD$^+$, leads to an increased sensitivity of cells towards etoposide via a Sirt2 dependent mechanism.[28] Likewise, Hoffmann et al. showed that etoposide potency is increased due to Sirt2 inhibition. [29] The connection between HDAC6 functionality and vinca alkaloid activity was shown by Tu et al.[30] Inhibition of HDAC isoenzymes by SAHA or the HDAC6 specific inhibitor MPT0G211 has been reported to lead to an increased vinblastine toxicity. [30, 31] For the platinum complexes cisplatin and carboplatin, we detected an inverse correlation with HDAC2 protein expression in cancer cells, while the potency of oxaliplatin inversely correlates with Sirt6 protein expression and with HDAC4 and Sirt5 in a positive manner. Several studies have shown that various HDAC inhibitors such as SAHA and other hydroxamic acid derivatives increase cisplatin toxicity in cancer cells or can circumvent cisplatin resistance [32, 33, 34, 35, 36], supporting the association between the activity of cisplatin or carboplatin and the expression of HDAC2. Interestingly, for another clinically used platinum complex, oxaliplatin, we detected a reverse correlation with the HDAC2 expression (not significant) as well as a significant positive correlation with HDAC4 and Sirt5 expression. Analogous searches for correlations between anticancer drug potency and mRNA expression of HDACs and Sirts with data from the NCI 60 cancer cell program were not in accordance with our results. We believe that our results are especially relevant because protein expression more closely characterises the epigenomic functionality of cancer cells. Importantly, on the basis of the current study, we were able to gain new insights into the relationships between HDAC protein expression and anticancer drug sensitivity, which should be useful for investigating possible drug combination therapies.

Another goal of our work was to seek possible connections between the potency of the unselective zinc depending HDAC inhibitors SAHA and TSA and the expression profiles of class I and II HDAC isoenzymes. In the first step, the antiproliferative activity of both was determined in 16 cell lines. Evidence suggested a strong correlation between their activity profiles, revealing the same mode of action in our panel of cancer cells. However, no connection between HDAC expression profiles and the SAHA and TSA potency was detected in the univariate correlation analysis. One interpretation suggests that the toxicity of both drugs is not primarily associated with an inhibition of HDACs. While it is known that both SAHA and TSA induce apoptosis [37, 38, 39], their exact effect mechanism of killing cancer cells has not yet been elucidated.

Besides the correlation analysis of HDAC protein expression and anticancer drug potency, we performed combination analysis of HDAC inhibitors with several anticancer drugs. These studies focussed on the effect of SAHA and TSA as well as the newer sirtuin inhibitors on cisplatin, lomustin and topotecan potency. For the combination analysis, the GI_{50} values of the anticancer drugs were determined in the presence and absence of non-toxic concentrations of HDAC inhibitors. Due to the high cytotoxicity of SAHA and TSA, the concentration used was quite low, i.e., $0.30\,\mu\mathrm{M}$ and $0.03\,\mu\mathrm{M}$, respectively. For combinations with lomustin, no effect on anticancer drug potency was detected. In contrast, Staberg et al. reported an increase in lomustin potency with the co-treatment of TSA in glioblastoma cell lines.[40] As mentioned previously, it is known that SAHA as well as TSA can increase potency of cisplatin. Our combination studies of the hydroxamic acid derivative TSA showed just a small effect on the cisplatin induced potency, but this modest effect may be just due to the low concentration of TSA used in the assay. On the other hand, we detected a significant enhancement in topotecan potency when co-incubated with SAHA or TSA in the cervix carcinoma cell line SiSo. These results are consistent with previous publications on other cell lines.[41, 42] Even more interesting, we detected a highly significant enhancement in the antiproliferative potency of cisplatin and lomustin when SiSo cells were co-incubated with **1a**, **3a**, and **5a**. This is the first report of a positive effect of HDAC inhibition on lomustin toxicity. Furthermore, all tested sirtuin inhibitors (except **5b**) increased topotecan potency.

In summary, insight has been gained into the connection of HDAC protein expression and anticancer drug sensitivity. These studies provide important tools for the optimisation of the anticancer drug therapy. With the current work, we have shown that the expression of several HDAC isoenzymes correlates with the sensitivity towards a number of anticancer drugs, such as platinum compounds, topoisomerase inhibitors or other cytostatic agents of natural origin. In most cases a positive correlation to the relative protein expression with the GI_{50} values of the drug was detected, indicating that cancer cells with a low enzyme expression are especially sensitive to anticancer drug treatment. Based on these new findings, we now hypothesize that tumors with a high Sirt2 expression could respond particularly well on Sirt2 inhibition in combination with busulfan, etoposide or 5-fluorouracil. Furthermore, we demonstrated that the inhibition of Sirt2 significantly increased cisplatin, lomustin and topotecan potency *in vitro*. Based on this observation, a set of recently discovered Sirt2 inhibitors were used to gained first insights into their potential benefit in combination with such anticancer drugs. Future studies will focus on the promising combination of the drugs busulfan, etoposide, or 5–fluorouracil with Sirt2 inhibitors in a set of cancer cells with especially high and low Sirt2 expression to help prove our hypothesis.

Acknowledgements

We are grateful to Anne Schüttler for technical assistance with the cell culture.

Conflict of Interest

The authors declare that there is no conflict of interest.

References

[1] Timp W, Feinberg AP. Cancer as a dysregulated epigenome allowing cellular growth advantage at the expense of the host. Nature reviews Cancer 2013;13(7):497–510.

[2] Vilcinskas A. The role of epigenetics in host–parasite coevolution: lessons from the model host insects Galleria mellonella and Tribolium castaneum. Zoology 2016;119(4):273–280.

[3] Zhao Z, Shilatifard A. Epigenetic modifications of histones in cancer. Genome Biol 2019;20(1):245.

[4] Seto E, Yoshida M. Erasers of histone acetylation: the histone deacetylase enzymes. Cold Spring Harb Perspect Biol 2014;6(4):a018713.

[5] Yoon S, Eom GH. HDAC and HDAC Inhibitor: From Cancer to Cardiovascular Diseases. Chonnam Med J 2016;52(1):1–11.

[6] Eckschlager T, Plch J, Stiborova M, Hrabeta J. Histone Deacetylase Inhibitors as Anticancer Drugs. Int J Mol Sci 2017;18(7).

[7] Hu J, Jing H, Lin H. Sirtuin inhibitors as anticancer agents. Future Med Chem 2014;6(8):945–66.

[8] Gomes ID, Pflum MKH. Optimal Substrate-Trapping Mutants to Discover Substrates of HDAC1. ChemBioChem 2019;20(11):1444–1449.

[9] Schiedel M, Robaa D, Rumpf T, Sippl W, Jung M. The Current State of NAD+-Dependent Histone Deacetylases (Sirtuins) as Novel Therapeutic Targets. Medicinal Research Reviews 2018;38(1):147–200.

[10] Schemies J, Uciechowska U, Sippl W, Jung M. NAD+-dependent histone deacetylases (sirtuins) as novel therapeutic targets. Medicinal Research Reviews 2010;30(6):861–889.

[11] Kazantsev AG, Thompson LM. Therapeutic application of histone deacetylase inhibitors for central nervous system disorders. Nature Reviews Drug Discovery 2008;7(10):854–868.

[12] Grathwol CW, Wossner N, Swyter S, Smith AC, Tapavicza E, Hofstetter RK, et al. Azologization and repurposing of a hetero-stilbene-based kinase inhibitor: towards the design of photoswitchable sirtuin inhibitors. Beilstein J Org Chem 2019;15:2170–2183.

[13] Grathwol CW, Wossner N, Behnisch-Cornwell S, Schulig L, Zhang L, Einsle O, et al. Activation of sirtuin 2 inhibitors employing photoswitchable geometry and aqueous solubility. ChemMedChem 2020;.

[14] Rumpf T, Schiedel M, Karaman B, Roessler C, North BJ, Lehotzky A, et al. Selective Sirt2 inhibition by ligand-induced rearrangement of the active site. Nature Communications 2015;6(1):6263.

[15] Swyter S, Schiedel M, Monaldi D, Szunyogh S, Lehotzky A, Rumpf T, et al. New chemical tools for probing activity and inhibition of the NAD(+)-dependent lysine deacylase sirtuin 2. Philos Trans R Soc Lond B Biol Sci 2018;373(1748).

[16] Bracht K, Boubakari, Grunert R, Bednarski PJ. Correlations between the activities of 19 anti-tumor agents and the intracellular glutathione concentrations in a panel of 14 human cancer cell lines: comparisons with the National Cancer Institute data. Anticancer Drugs 2006;17(1):41–51.

[17] Seabold S, Perktold J. statsmodels: Econometric and statistical moldeing with python. 9th Python in Science Conference; 2010.

[18] Hunter JD. Matplotlib: A 2D graphics environment. Computing in Science & Engineering 2007;9(3):90–95.

[19] Bracht K, Liebeke M, Ritter CA, Grunert R, Bednarski PJ. Correlations between the activities of 19 standard anticancer agents, antioxidative enzyme activities and the expression of ATP-binding cassette transporters: comparison with the National Cancer Institute data. Anticancer Drugs 2007;18(4):389–404.

[20] Weichert W. HDAC expression and clinical prognosis in human malignancies. Cancer Letters 2009;280(2):168–176.

[21] Li Y, Seto E. HDACs and HDAC Inhibitors in Cancer Development and Therapy. Cold Spring Harbor perspectives in medicine 2016;6(10):a026831.

[22] Zhao E, Hou J, Ke X, Abbas MN, Kausar S, Zhang L, et al. The Roles of Sirtuin Family Proteins in Cancer Progression. Cancers (Basel) 2019;11(12).

[23] Hosokawa M, Tanaka S, Ueda K, Iwakawa S. Different Schedule-Dependent Effects of Epigenetic Modifiers on Cytotoxicity by Anticancer Drugs in Colorectal Cancer Cells. Biol Pharm Bull 2017;40(12):2199–2204.

[24] Tan YJ, Lee YT, Petersen SH, Kaur G, Kono K, Tan SC, et al. BZD9L1 sirtuin inhibitor as a potential adjuvant for sensitization of colorectal cancer cells to 5-fluorouracil. Ther Adv Med Oncol 2019;11:1758835919878977.

[25] Gray J, Cubitt CL, Zhang S, Chiappori A. Combination of HDAC and topoisomerase inhibitors in small cell lung cancer. Cancer Biol Ther 2012;13(8):614–22.

[26] Unland R, Clemens D, Heinicke U, Potratz JC, Hotfilder M, Fulda S, et al. Suberoylanilide hydroxamic acid synergistically enhances the antitumor activity of etoposide in Ewing sarcoma cell lines. Anticancer Drugs 2015;26(8):843–51.

[27] Wu WC, Liu YM, Lin MH, Liao YH, Lai MJ, Chuang HY, et al. Design, synthesis, and evaluation of N-phenyl-4-(2-phenylsulfonamido)-benzamides as microtubule-targeting agents in drug-resistant cancer cells, displaying HDAC inhibitory response. Eur J Med Chem 2020;192:112158.

[28] Grohmann T, Penke M, Petzold-Quinque S, Schuster S, Richter S, Kiess W, et al. Inhibition of NAMPT sensitizes MOLT4 leukemia cells for etoposide treatment through the SIRT2-p53 pathway. Leuk Res 2018;69:39–46.

[29] Hoffmann G, Breitenbucher F, Schuler M, Ehrenhofer-Murray AE. A novel sirtuin 2 (SIRT2) inhibitor with p53-dependent pro-apoptotic activity in non-small cell lung cancer. J Biol Chem 2014;289(8):5208–16.

[30] Tu HJ, Lin YJ, Chao MW, Sung TY, Wu YW, Chen YY, et al. The anticancer effects of MPT0G211, a novel HDAC6 inhibitor, combined with chemotherapeutic agents in human acute leukemia cells. Clin Epigenetics 2018;10(1):162.

[31] Chao MW, Lai MJ, Liou JP, Chang YL, Wang JC, Pan SL, et al. The synergic effect of vincristine and vorinostat in leukemia in vitro and in vivo. J Hematol Oncol 2015;8:82.

[32] Mutze K, Langer R, Becker K, Ott K, Novotny A, Luber B, et al. Histone deacetylase (HDAC) 1 and 2 expression and chemotherapy in gastric cancer. Ann Surg Oncol 2010;17(12):3336–43.

[33] Beck A, Eberherr C, Hagemann M, Cairo S, Haberle B, Vokuhl C, et al. Connectivity map identifies HDAC inhibition as a treatment option of high-risk hepatoblastoma. Cancer Biol Ther 2016;17(11):1168–1176.

[34] Chen JH, Zheng YL, Xu CQ, Gu LZ, Ding ZL, Qin L, et al. Valproic acid (VPA) enhances cisplatin sensitivity of non-small cell lung cancer cells via HDAC2 mediated down regulation of ABCA1. Biol Chem 2017;398(7):785–792.

[35] Pflieger M, Hamacher A, Oz T, Horstick-Muche N, Boesen B, Schrenk C, et al. Novel alpha,beta-unsaturated hydroxamic acid derivatives overcome cisplatin resistance. Bioorg Med Chem 2019;27(19):115036.

[36] Asfaha Y, Schrenk C, Alves Avelar LA, Lange F, Wang C, Bandolik JJ, et al. Novel alkoxyamide-based histone deacetylase inhibitors reverse cisplatin resistance in chemoresistant cancer cells. Bioorg Med Chem 2020;28(1):115108.

[37] Shi XY, Ding W, Li TQ, Zhang YX, Zhao SC. Histone Deacetylase (HDAC) Inhibitor, Suberoylanilide Hydroxamic Acid (SAHA), Induces Apoptosis in Prostate Cancer Cell Lines via the Akt/FOXO3a Signaling Pathway. Med Sci Monit 2017;23:5793–5802.

[38] Natarajan U, Venkatesan T, Radhakrishnan V, Samuel S, Rathinavelu A. Differential Mechanisms of Cell Death Induced by HDAC Inhibitor SAHA and MDM2 Inhibitor RG7388 in MCF-7 Cells. Cells 2018;8(1).

[39] Gilardini Montani MS, Granato M, Santoni C, Del Porto P, Merendino N, D'Orazi G, et al. Histone deacetylase inhibitors VPA and TSA induce apoptosis and autophagy in pancreatic cancer cells. Cell Oncol (Dordr) 2017;40(2):167–180.

[40] Staberg M, Michaelsen SR, Rasmussen RD, Villingshoj M, Poulsen HS, Hamerlik P. Inhibition of histone deacetylases sensitizes glioblastoma cells to lomustine. Cell Oncol (Dordr) 2017;40(1):21–32.

[41] Bruzzese F, Rocco M, Castelli S, Di Gennaro E, Desideri A, Budillon A. Synergistic antitumor effect between vorinostat and topotecan in small cell lung cancer cells is mediated by generation of reactive oxygen species and DNA damage-induced apoptosis. Mol Cancer Ther 2009;8(11):3075–87.

[42] Sato A, Asano T, Horiguchi A, Ito K, Sumitomo M, Asano T. Antitumor effect of suberoylanilide hydroxamic acid and topotecan in renal cancer cells. Oncol Res 2011;19(5):217–23.

6 Publikationen und Posterbeiträge

Peer-Review-Artikel

R. K. Hofstetter, M. Hasan, G. M. Fassauer, C. Bock, A. S. Surur, S. Behnisch, C. W. Grathwol, F. Potlitz, T. Oergel, W. Siegmund und A. Link, „Simultaneous quantification of acidic and basic flupirtine metabolites by supercritical fluid chromatography according to European Medicines Agency validation“, *J. Chromatogr. A* **2019**, *1603*, 338–347.

C. W. Grathwol, N. Wössner, S. Swyter, A. C. Smith, E. Tapavicza, R. K. Hofstetter, A. Bodtke, M. Jung und A. Link, „Azologisation and repurposing of a hetero-stilbene-based kinase inhibitor: towards the design of photoswitchable sirtuin inhibitors”, *Beilstein J. Org. Chem.* **2019**, *15*, 2170–2183.

C. W. Grathwol, N. Chrysochos, B. J. Elvers, A. Link und C. Schulzke, „Crystal structure of benzo[*h*]quinoline-3-carboxamide”, *Acta Cryst.* **2019**, *E75*, 1828–1832.

C. W. Grathwol, N. Wössner, S. Behnisch-Cornwell, L. Schulig, M. Jung und A. Link, „Activation of Sirt2 inhibitors employing photoswitchable geometry and aqueous solubility”, *ChemMedChem* **2020**, *15*, Early View.

Q. Tang, Y. M. Vianney, K. Weisz, C. W. Grathwol, A. Link, U. T. Bornscheuer und I. V. Pavlidis, „Influence of substrate binding residues on the substrate scope and regioselectivity of a plant *O*-methyltransferase against flavonoids”, *ChemCatChem* **2020**, *12*, Early View.

S. Behnisch-Cornwell, C. W. Grathwol, L. Schulig, A. Voigt, A. Link und P. J. Bednarski „Correlations between the expression of 10 histone deacetylases (HDACs) and the sensitivities of 23 anticancer drugs in 17 human cancer cell lines and the influence of various HDAC inhibitors on cisplatin, lomustin and topotecan cytotoxicity”, *FEBS J.* **2020**, submitted.

Poster

C. W. Grathwol, S. Swyter, N. Wössner, M. Jung und A. Link, „5-Phenyldiazenylnicotinamides as photoswitchable Sirt2 and Sirt3 inhibitors”, Frontiers in Medicinal Chemistry Jena, 11. – 13.03.2018.

C. W. Grathwol, S. Swyter, N. Wössner, M. Jung und A. Link, „Photoswitchable Sirt2/3 inhibitors derived from Aza-Stilbene Lead Structure”, DPhG-Doktorandentagung Bad Dürkheim, 14. – 16.03.2018.

C. W. Grathwol, N. Wössner, M. Jung und A. Link, „c-RAF Kinase Inhibitor as Lead to Photoswitchable Sirtuin Inhibition”, EFMC-ACSMEDI Medicinal Chemistry Frontiers Krakau, 10. – 13.06.2019.

Eigenständigkeitserklärung

Hiermit erkläre ich, dass diese Arbeit bisher von mir weder an der Mathematisch-Naturwissenschaftlichen Fakultät der Universität Greifswald noch einer anderen wissenschaftlichen Einrichtung zum Zwecke der Promotion eingereicht wurde.

Ferner erkläre ich, dass ich diese Arbeit selbstständig verfasst und keine anderen als die darin angegebenen Hilfsmittel und Hilfen benutzt und keine Textabschnitte eines Dritten ohne Kennzeichnung übernommen habe.

Ort, Datum	Unterschrift

Lebenslauf

PERSÖNLICHE DATEN

Name	Christoph Werner Grathwol
Geburtsdatum, -ort	20.05.1988 in Donaueschingen
Staatsangehörigkeit	deutsch

BILDUNGSWEG UND BERUFLICHER WERDEGANG

02/2016 – jetzt	**Promotion, Universität Greifswald** Institut für Pharmazie Lehrstuhl für Pharmazeutische/Medizinische Chemie Prof. Dr. Andreas Link Titel: Synthese und Charakterisierung *E*/*Z*-photoisomerisierbarer Inhibitoren zur reversiblen Modulation der Deacetylase-Aktivität von Sirtuinen
10/2014 – 07/2015	**Wissenschaftlicher Mitarbeiter, Johannes-Gutenberg-Universität Mainz** Institut für Pharmazie und Biomedizinische Wissenschaften Lehrstuhl für Pharmazeutische/Medizinische Chemie Prof. Dr. Tanja Schirmeister Projekt: Entwicklung von Cystein-Protease-Inhibitoren mit Aziridinstruktur
01/2013 – 10/2013	**Diplomarbeit, Johannes-Gutenberg-Universität Mainz** Institut für Pharmazie und Biomedizinische Wissenschaften Lehrstuhl für Pharmazeutische/Medizinische Chemie Prof. Dr. Tanja Schirmeister Titel: Synthese und Testung von Phenylvinylsulfonen als Cystein-Protease-Inhibitoren
10/2008 – 12/2012	**Studium der Biomedizinischen Chemie, Johannes-Gutenberg-Universität Mainz**
09/2007 – 05/2008	**Zivildienst, DRK-Kreisverband Villingen-Schwenningen**
09/1998 – 06/2007	**Allgemeine Hochschulreife, Gymnasium am Hoptbühl, Villingen-Schwenningen**

LEHRERFAHRUNG

04/2020 – jetzt	**Betreuung Praktikum „Allgemeine und analytische Chemie der anorganischen Arznei-, Hilfs- und Schadstoffe inkl. Arzneibuchmethoden“**
08/2019 – 04/2020	**Betreuung Diplomarbeit Larissa Heyen** Titel: Synthese und Testung photoisomerisierbarer Sirtuin-Inhibitoren
02/2016 – 03/2020	**Betreuung Praktikum „Chemie der organischen Arznei-, Hilfs- und Schadstoffe“**

Danksagung

An dieser Stelle möchte ich mich von ganzem Herzen bei den vielen Menschen bedanken, die zum Gelingen dieser Arbeit beigetragen haben.

Allen voran danke ich Herrn Prof. Dr. Andreas Link, meinem Doktorvater, für die Aufnahme in seine Arbeitsgruppe und seine uneingeschränkte fachliche sowie menschliche Unterstützung in den darauffolgenden Jahren.

Mein aufrichtiger Dank gilt außerdem Frau Prof. Dr. Tanja Schirmeister für ihre freundliche Empfehlung im Vorfeld.

Besonders danken möchte ich Herrn Prof. Manfred Jung für die durchgehend hervorragende Zusammenarbeit sowie Nathalie Wössner für ihre unerschütterliche Geduld bei der Durchführung der Enzymassays.

Eine ausgesprochene Freude hat mir die enge Zusammenarbeit mit meinen Kollegen und Freunden Dr. Steven Behnisch-Cornwell, Robert K. Hofstetter, Lukas Schulig sowie Dr. Enrico Tapavicza bereitet. Vielen Dank für euer großes Engagement und die tatkräftige Unterstützung beim Publizieren.

Ebenso möchte ich Frau Prof. Dr. Carola Schulzke und ihren Mitarbeitern Dr. Nicolas Chrysochos und Benedict Elvers für die „Express“-Röntgenstrukturanalysen und die reibungslose Zusammenarbeit bei der Verfassung des Manuskripts danken.

Bei Dr. Anja Bodtke, Maria Hühr und Michael Eccius möchte ich mich für die Messung zahlreicher NMR-, IR-, und Massenspektren bedanken. Des Weiteren danke ich Larissa Heyen, die mit ihrer Diplomarbeit einen hilfreichen Beitrag zur Synthese der untersuchten Verbindungen geleistet hat.

Meinen lieben Freunden Dr. Stefanie König, Dr. Thomas Emmrich und Dr. Marco Nebe ein herzliches Dankeschön für deren selbstverständliche Bereitschaft diese Arbeit Korrektur zu lesen.

Mein besonderer Dank gilt außerdem Dr. Nicole Rüger, Dr. Christian Bock, Dr. Abdrrhahman S. Surur und Konrad W. Wurm, mit denen ich Abzug an Abzug plaudern, staunen, lachen und fluchen durfte. Vielen Dank auch, dass die Tür zwischen B20.14 und B20.15 trotz Diskrepanzen bezüglich des Musikgeschmackes nie geschlossen war. Auch all den übrigen Kollegen der Pharmazeutischen/Medizinischen Chemie, die mich während meiner Zeit am Institut begleitet haben, möchte ich für das angenehme Arbeitsklima danken.

Schließlich möchte ich mich bei meinen großartigen Eltern und Geschwistern bedanken, denen kein Weg zu weit war und die mir immer den notwendigen mentalen Rückhalt geboten haben.

Mein allergrößter Dank gilt jedoch meiner lieben Nonie. Ohne ihre Geduld, ihre aufopferungsvolle Unterstützung und ihre unzähligen motivierenden Worte wäre diese Arbeit nicht möglich gewesen.